



ScuDo

Scuola di Dottorato ~ Doctoral School

WHAT YOU ARE, TAKES YOU FAR



Doctoral Dissertation  
Doctoral Program in Materials Science and Technology (34<sup>th</sup> Cycle)

# **Nanofibrous polymeric membranes by coupling electrospinning and photo- induced crosslinking**

**Parnian Kianfar**

\* \* \* \* \*

## **Supervisors**

Prof. Roberta Bongiovanni, Supervisor  
Dr. Alessandra Vitale, Co-Supervisor

## **Doctoral Examination Committee:**

Dr. Maila Castellano , Referee, University of Genoa  
Dr. Sandra Schlögl, Referee, Polymer Competence Center Leoben

Politecnico di Torino  
February 12, 2022

This thesis is licensed under a Creative Commons License, Attribution - Noncommercial - NoDerivative Works 4.0 International: see [www.creativecommons.org](http://www.creativecommons.org). The text may be reproduced for non-commercial purposes, provided that credit is given to the original author.

I hereby declare that, the contents and organisation of this dissertation constitute my own original work and does not compromise in any way the rights of third parties, including those relating to the security of personal data.

.....

Parnian Kianfar  
Turin, February 12, 2022





# Abstract

The main goal of the present doctoral work was to prepare innovative polymeric fibrous membranes and to tailor their physico-chemical, mechanical and thermal properties coupling electrospinning and various photo-induced crosslinking chemistries.

Electrospinning was used as unique processing of polymers for the fabrication of non woven mats made of fine fibers with diameters ranging from tens of nanometers to micrometers. Photo-induced crosslinking reactions were selected due to their numerous advantages, such as short conversion times, low-energy consumption, ambient temperature operations, and selective curing with control both in time and space. The light irradiation to trigger the crosslinking reaction was performed either on the fabricated electrospun fibrous membranes or *in-situ* during the fiber formation. In the presence of photoactive agents (e.g., photoinitiators and photo-crosslinkers), covalent bonds between polymer chains were formed, building a crosslinked network. The electrospinning process, the chemistry of the systems and the irradiation conditions were optimized to produce defect-free fibrous membranes and to assure an efficient crosslinking degree in order to increase their solvent and temperature resistance, as well as controlling morphology. The coupling of photo-crosslinking and electrospinning processes was proved to solve the issue of electrospun fibers shape instability over storage time, upon solvent exposure, or temperature changes. Moreover, the processes were performed at ambient condition (room temperature) and water was mainly used as a solvent, limiting the use of toxic and harmful substances: the research aimed to develop methods raising the least possible environmental and health concerns.

This new approach was successfully applied to different polymeric systems, namely chitosan-based, polyethylene oxide-based and polybutadiene-based materials. Accordingly, different polymeric fibrous membranes with enhanced properties and thus improved applicability were fabricated: uniform and defect free chitosan-based membranes resistant to solvent and potentially promising for packaging application; polyethylene oxide-based membranes resistant to solvent and heat applicable as solid-solid shape stable phase change material in heat management; polybutadiene-based membranes, obtained from either free solvent electrospinning or aqueous suspension electrospinning, promising for water/oil separation.

The overall results demonstrate that the proposed approach (i.e., coupling of electrospinning and photo-induced crosslinking) was successful. Being sustainable and highly versatile by changing photo-crosslinking chemistry, it can be applied to the development of advanced membranes from a variety of polymeric systems.

# Acknowledgments

I would like to express my sincere gratitude to my group POLYMAT at Politecnico di Torino. I truthfully felt that I have been surrounded by brilliant people who were my second family members in Italy.

I would like to show my heartfelt appreciation to Professor Roberta Bongiovanni, who trusted me after being away from academia and having different background. I will always feel honored that I have pursued my Ph.D. with her, and both professionally and personally learnt valuable lessons from her. During these years, especially during the COVID-19 pandemic, her inclusive support encouraged me to do my utmost.

My profound gratitude goes to Dr. Alessandra Vitale, my co-supervisor. She gave me insight and the right way of thinking; as a young Professor, she is exceptionally wise, committed and professional. I truly value her patience and knowledge in teaching me the required skills to step into the academia as a researcher.

During this doctoral program, I was indeed lucky to get to know great people. I acknowledge Dr. Sara Dalle Vacche for sharing her knowledge and experience and helping me in experimental works and data analysis. I thank Professor Pegoretti and Dr. Fredi from the University of Trento for showing me how to look at scientific results from different perspectives. I would like to thank also the senior Ph.D. students and researchers, Giuseppe, Samantha, Angelo, Gustavo, Luigi, for sharing their experiences and helping me through the struggles of everyday life of a Ph.D. student. Moreover, working with younger students, Quan, Thu, Mariagrazia, Mara, Riccardo, Yaren, and Elvan, was a great opportunity to learn and to face new and unbiased questions to widen my thinking horizon. I send my special thanks to my reviewers, Professor Castellano and Professor Schlögl, for accepting and considering reviewing my thesis.

Here, I express my deepest gratitude to my parents and my sister. My achievements undoubtedly could not be attained without their sacrifice and affection. Their day-to-day caring words and wholehearted support gave me the strength to continue.

And above all, I would like to express my inmost appreciation and love to my husband, Navid. From the beginning of this journey, he truly believed in me and never let me give up no matter what would happen. During these years, his passion inspired and forced me to fight for my dreams. I cannot be thankful enough for all of his understandings, sacrifices and devotions.

# Contents

1. Introduction .....	1
2. State of the art.....	5
2.1 Electrospinning .....	5
2.1.1 Electrospinning process.....	7
Taylor cone formation .....	7
Stretching of the jet.....	8
Bending instability.....	8
Beaded fibers .....	10
Solidification of the jet .....	10
Deposition of the fibers.....	10
2.1.2 Mathematical and empirical models.....	11
Taylor cone .....	12
Jet elongation and pathway – straight regime.....	12
Bending and whipping instabilities.....	13
2.1.3 Electrospinning parameters .....	15
Effect of applied voltage.....	15
Effect of flow rate.....	15
Effect of distance and needle diameter .....	15
Effect of polymer concentration and solution viscosity .....	16
Effect of solution conductivity .....	17
Role of solvents .....	17
Effect of humidity and temperature .....	18
2.1.4 Types of electrospinning process .....	19



Melt electrospinning .....	19
Suspension and emulsion electrospinning .....	20
Oligomer electrospinning .....	21
2.1.5 Electrospinning setups.....	21
Electrospun fibers morphology.....	23
2.1.6 Materials subjected to electrospinning .....	24
Blends and multicomponent fibers .....	26
Composite fibers.....	27
2.1.7 Applications.....	27
2.1.8 Scaling up.....	28
2.2 Photo-induced reactions .....	29
2.2.1 Photoinitiated free radical polymerization .....	31
Photoinitiators.....	32
Unsaturated polyesters/styrene systems.....	33
Acrylate monomers.....	33
Thiol-ene monomers .....	34
Oxygen inhibition .....	35
2.2.2 Photoinitiated cationic polymerization.....	36
2.2.3 Photo-induced crosslinking .....	37
2.2.4 Applications.....	39
2.3 Photo-induced reactions coupled with electrospinning.....	39
3. Chitosan-based photo-crosslinked electrospun membrane .....	44
3.1 Abstract .....	44
3.2 Introduction .....	44
3.3 Materials and methods .....	46
3.3.1 Materials.....	46
3.3.2 Electrospinning procedure.....	47
3.3.3 Photo-curing process .....	47
3.3.4 Characterizations .....	48
3.4 Results and discussion.....	48
3.4.1 Electrospinning of CS/PEO blend.....	49
3.4.2 Photo-crosslinking of CS/PEO electrospun fibers .....	51

3.4.3	Characterization of photo-crosslinked CS/PEO electrospun fibers	55
3.5	Conclusions	57
4.	Polyethylene oxide-based photo-crosslinked electrospun membranes	60
4.1	Abstract	60
4.2	Introduction	61
4.3	Materials and methods	64
4.3.1	Materials	64
4.3.2	Sample preparations	64
4.3.3	Electrospinning procedure	65
4.3.4	Film Casting	65
4.3.5	Photo-curing process	65
4.3.6	Characterization	65
4.4	Results and discussion	68
4.4.1	Study and optimization of the PEO-based fibrous membranes	68
Electrospun mat morphology		69
Photo-curing of fibrous mats		71
Characterization of the photo-cured fibrous mats		76
4.4.2	Optimized PEO-based fibrous membranes as PCMs	81
Control of the crosslinking efficiency and mat morphology		82
Mechanical and dynamic-mechanical analysis		84
Heat storage and long-term stability		87
4.6	Conclusions	90
5.	Polybutadiene-based photo-crosslinked electrospun membranes	93
5.1	Abstract	93
5.2	Introduction	94
5.3	Materials and method	97
5.3.1	Materials	97
5.3.2	Sample preparation	98
5.3.3	Characterizations	99
5.4	Results and discussion	101
5.4.1	Electrospinning of liquid polybutadienes and their <i>in-situ</i> photo-curing	101

Study of the polybutadienes photo-curing process .....	102
Optimization of electrospinning process and characterization of the photo-cured electrospun mats .....	106
5.4.2 Styrene-butadiene-based materials fiber fabrication .....	110
SBR/PEO fiber production by electrospinning.....	111
Photo-crosslinking of SBR/PEO electrospun fibers .....	112
Characterization of the photo-crosslinked SBR/PEO electrospun membranes .....	115
Characterization of the photo-crosslinked SBR electrospun membranes after PEO removal .....	117
5.5 Conclusions .....	123
6. General conclusions and future perspectives .....	126
7. References .....	131
8. Appendix A .....	154
9. Appendix B.....	166
10. List of publication.....	166



# List of Tables

Table 2-1 Common parameters used for mathematical models .....	11
Table 2-2 The most studied polymeric materials for electrospun fiber fabrication.....	25
Table 3-1 Composition of the solutions used for the electrospinning process. ....	47
Table 3-2 Comparison of the composition of the investigated CS/PEO blends before (starting solution) and after (fiber mat) the electrospinning process, based on TGA data. ....	51
Table 3-3 Melting temperature and crystallization degree of CS/PEO electrospun fibers, based on DSC data.....	56
Table 4-1 Composition details of the investigated samples. ....	64
Table 4-2 C=C conversion and insoluble fraction of PEO/PEGDA and PEO/TMPTA photo-cured fibrous membranes.....	75
Table 4-3 Crosslinking density $\nu$ of PEO/PEGDA and PEO/TMPTA photo-cured fibrous membranes by considering the membranes as plain films. ....	76
Table 4-4 Thermal properties of PEO/PEGDA and PEO/TMPTA photo-cured fibrous membranes, as well as pure PEO, obtained by DMTA, DSC and TGA analyses.....	77
Table 4-5 Mechanical properties of the electrospun fibrous membranes.....	79
Table 4-6 List of prepared samples with nominal composition, processing and obtained form.....	82
Table 4-7 Results of C=C conversion (calculated by Eq 1) and gel content measurement.....	82
Table 4-8 Glass transition temperature for different samples.....	87
Table 4-9 Main results of DSC tests on the prepared samples. ....	87
Table 5-1 Properties of the liquid polybutadienes, provided by the supplier .	97

Table 5-2 Tack free time of PB and maleinized PB in two curing atmospheres (air and nitrogen).....	102
Table 5-3 Effect of TPO photoinitiator and TRIS crosslinker on the tack-free time of thin films of PB and PB-15MA due to UV irradiation in air.....	105
Table 5-4 Composition of the latex-based formulations used for electrospinning .....	110
Table 5-5 Theoretical amount of PEO in the electrospun fibers, the soluble fraction of the photo-cured electrospun fibers after water treatment and their insoluble fraction after chloroform treatment.....	114
Table 5-6 Theoretical and calculated PEO concentration, melting enthalpy ( $\Delta H_m$ ), melting temperature ( $T_m$ ) and glass transition temperature ( $T_g$ ) of the SBR/PEO photo-cured fibers, and of pristine SBR and PEO films, from DSC measurements .....	117
Table 5-7 Static water and hexadecane contact angle values of the photo-cured electrospun mats after PEO removal, and of SBR and PEO films.....	122

# List of Figures

Figure 2-1 Timeline of evolution of electrospinning technique [9].....	6
Figure 2-2 The growing number of publications per year for the electrospinning technique (source Scopus.com with “Electrospinning” as keyword).....	6
Figure 2-3 a. Conventional electrospinning setup; b. example of an electrospun fibrous membrane.....	7
Figure 2-4 Taylor cone evolution over time under applied electric field .....	8
Figure 2-5 Schematic representation of the primary bending of moving jet due to excess like sign charges.....	9
Figure 2-6 a. Schematic representation of trajectory of moving electrified jet of polymer b. images obtained by CCD camera of the electrospinning process, c. imaging of travelling jet of polymer with different exposure time .....	10
Figure 2-7 The morphology of the electrospun beaded fibers made of PEO solution .....	10
Figure 2-8 Reneker viscoelastic Maxwellian model for the electrified liquid jet [5] .....	14
Figure 2-9 The chain entanglement number equation for solution and the plot of the calculated entanglement number $n_e$ versus the concentration of PS in THF solvent, with three different morphology regimes during the electrospinning process.....	17
Figure 2-10 a. Melt-electrospinning setup; b.various process parameter in designing of the melt-electrospinning setups [ 56].....	20
Figure 2-11 Schematic illustration of the suspension electrospinning .....	20
Figure 2-12 Schematic representation of emulsion electrospinning.....	21
Figure 2-13 Schematic diagrams of rotating collectors for electrospinning. Blunt collectors: a) mandrel, b) wire drum, and c) drum with wire around it. Sharp edge collectors: d) disk, e) rotating tube collector with knife-edge electrodes (to induce more alignment on the tube collector) below, and f) rotating drum with a	

sharp pin (to fabricate arrayed fibers) inside it. Parallel collectors: g) parallel electrodes, h) electrode array, i) blades placed in line, and j) ring collectors placed in parallel (placed between the tip of the needle and the collector to control the surrounding electrical field in which the traveling jet pass through) [75]. ..... 23

Figure 2-14 Microcopy images of: a. PEO beaded fibers [18], b. poly(vinyl pyrrolidone) (PVP) aligned nanofibers collected across an airgap between two silicon strips [71], c. PLA porous electrospun fibers obtained by binodal phase separation [77], d. co-axial electrospun fibers of PVDF and Teflon Amorphous Fluoropolymer in core and sheath, respectively [78], e. hollow fibers of PVDF-HFP and PVP, where PVP is deposited on the inner wall of the PVDF-HFP shell[79] f. spider-net in electrospun nylon 6 nanofiber mat containing NaCl [43], g. polytetrafluoroethylene (PTFE) electrospun fibers obtained by PTFE/PEO blend electrospinning and subsequent sintering [80], h. electrospun nanofibers of ionomer with catalyst nanoparticles (NP)separately electro-sprayed onto them [81], i. electrospun fibers of polyvinylpyrrolidone/ammonium metatungstate (PVP/AMT) with a ribbon shape [82], j. PVDF cactus-like fibers (rough and porous) [83], k. wrinkled fibers of PS obtained at relative humidity of 15% [45], l. electrospun fibers of ZnO/TiO<sub>2</sub> on TiO<sub>2</sub> fibers obtained by calcination and ZnO nanorods [84]..... 24

Figure 2-15 Potential applications of electrospun membranes ..... 27

Figure 2-16 Schematic illustration of a. chromophores photophysical and photochemical reaction as a result of photoexcitation [59], b. the Jablonski diagram., showing that the singlet state S<sub>1</sub> by intersystem crossing can enter the triplet state T<sub>1</sub>, which can trigger photochemical reactions [160,161], c. the primary photochemical reactions including the isomerization, bond forming reaction and bond breaking reaction [59]..... 29

Figure 2-17 a. Schematic representation of free radical photopolymerization including three steps of initiation, propagation and termination, b. example of free radical polymerization of a monomer M containing a C=C double bond. .... 31

Figure 2-18 Norrish type I (direct photocleavage) and Norrish type II (hydrogen abstraction) radical photoinitiating system..... 32

Figure 2-19 Unsaturated polyesters/styrene photoinduced polymerization and crosslinking..... 33

Figure 2-20 Simple example of photopolymerization of an acrylate monomer in presence of a Norrish type I photoinitiator during UV irradiation..... 34

Figure 2-21 General thiol-ene photopolymerization process [188]..... 35

Figure 2-22 Both photoinitiator systems (Norrish type I and II) are used in thiol-ene chemistry..... 35



Figure 2-23 Molecular orbital diagram for ground state oxygen, singlet oxygen, superoxide radical anion and peroxide ion [198].	36
Figure 2-24 Oxygen inhibition on photoinitiation and polymerization reaction [171].	36
Figure 2-25 Examples of cationic photoinitiated reactions of a. epoxy monomer and b. vinyl ether monomer.	37
Figure 2-26 General mechanisms and schematic of free radical photo-crosslinking reactions: a. chain polymerization of polymers containing reactive double bonds, b. thiol-ene reaction between polymer chains with ene functionalities and a thiol crosslinker, c. photo-oxidation via benzoyl groups [201].	38
Figure 3-1 Generation of radical species on PEO chain in presence of a photoinitiator (i.e., benzophenone) upon UV irradiation	46
Figure 3-2 molecular structure of CS, PEO and benzophenone, used as photoinitiator	46
Figure 3-3 Schematic illustration of the electrospinning and photo-crosslinking procedure	48
Figure 3-4 The FE-SEM image of electrospun PEO fibers prepared by 5 wt.% aqueous solution	49
Figure 3-5 FE-SEM images and fiber size distribution of electrospun mats of CS/PEO blend solutions of a. 50/50, b.70/30 and c.90/10 composition ratio.	50
Figure 3-6 TGA (a) and first derivative DTGA (b) results of pure CS, pure PEO, and electrospun fibers with CS/PEO 50/50, 70/30 and 90/10 composition ratio.	50
Figure 3-7 Photo-DSC thermograms of: a. CS/PEO blend irradiated by low UV and high UV (7 mW/cm <sup>2</sup> and 70 mW/cm, respectively) b. CS/PEO irradiated by low UV (the baseline is shown by dash line), c. CS irradiated by low UV and high UV and d. PEO irradiated by both UV intensities after baseline subtraction.	52
Figure 3-8 FTIR spectra of a.CS/PEO and b PEO before UV irradiation and after UV with two intensities.	53
Figure 3-9 The area of characteristic peaks of CS/PEO obtained from FTIR spectroscopy before and after UV irradiation; the peak areas were normalized to peak 845 cm <sup>-1</sup> as the least affected peak during the UV irradiation.	54
Figure 3-10 . FE-SEM images of CS/PEO electrospun fiber mats after photo-crosslinking with a. low UV dose and b. high UV dose.	55
Figure 3-11 Thermal properties of the CS/PEO samples, a. TGA and first derivative b. DTGA results of pure CS, pure PEO, and the UV-cured CS/PEO with low UV and high UV, and c. carbonyl peak area obtained from FTIR experiments.	56

Figure 3-12 . FE-SEM images of CS/PEO fiber mats photo-crosslinked with low UV dose (a) and high UV dose (b), after water contact. ....	57
Figure 4-1 radical generation upon UV irradiation of PEO in the presence of a photo-initiator (e.g., benzophenone) .....	62
Figure 4-2 Molecular structure of PEO polymer, PEGDA and TMPTA acrylic crosslinkers, and benzophenone photo-initiator. ....	64
Figure 4-3 Schematic illustration of the electrospinning solution preparation, the electrospinning process and the photo-curing process .....	69
Figure 4-4 Morphology of the PEO-based photo-cured electrospun fibrous mats with different type of crosslinker and different composition ratio of PEO/crosslinker (L-PEGDA, M-PEGDA, H-PEGDA and L-TMPTA, M-TMPTA, H-TMPTA). (a) FE-SEM images of the front side (top surface) of the membranes. (b) FE-SEM images of the back side (bottom surface) of the membranes. ....	70
Figure 4-5 (a) Fiber diameters distribution of the top surface of the electrospun mats. (b) Surface porosity of both sides of the fibrous membranes. ....	71
Figure 4-6 a. Photo-DSC of PEO/PEGDA and PEO/TMPTA blends as well as pure PEO, pure PEGDA and pure TMPTA, in presence of photoinitiator, at isothermal condition of 25°C under inert atmosphere of N <sub>2</sub> and irradiation with light intensity of 200 mW/cm <sup>2</sup> . b. reports the photo-DSC curves for the first 120 seconds of irradiation .....	72
Figure 4-7 Scheme of free-radical photo-crosslinking in presence of an acrylic monomer.....	73
Figure 4-8 ATR-FTIR spectroscopic analyses Spectra of pure PEO, and of M-PEGDA and M-TMPTA electrospun fibrous membranes prior (uncured) and after (UV-cured) UV irradiation. ....	75
Figure 4-9 DMTA curves of PEO/PEGDA and PEO/TMPTA samples. ....	76
Figure 4-10 DSC scans of PEO/PEGDA and PEO/TMPTA samples .....	78
Figure 4-11 TGA thermograms of the PEO/PEGDA and PEO/TMPTA systems .....	78
Figure 4-12 Mechanical tensile characterization of photo-cured fibrous mats of PEO/PEGDA and PEO/TMPTA: stress vs. strain curves; one curve for each sample is reported as an example. ....	80
Figure 4-13 Water permeability of the photo-cured electrospun membranes of PEO/PEGDA and PEO/TMPTA. (a) Water weight loss as a function of time. (b) Average measurement of the water vapor transmission WVT after two weeks. ...	80
Figure 4-14 FE-SEM images of the photo-cured electrospun fibrous membranes of PEO/PEGDA and PEO/TMPTA after water treatment. ....	81
Figure 4-15 FTIR spectra of the PEO-PI, M-TMPTA and M-TMPTA-C .....	83

Figure 4-16 FE-SEM images of the PEO-PI (a,b) and M-TMPTA (c,d) fibers after UV-irradiation and after water treatment, the insets are the size distribution of the fibers.....	84
Figure 4-17 a. strain vs. stress curve and b. Young's modulus, ultimate tensile strength (UTS) and elongation at the breaking point obtained from tensile tests of PEO-PI, M-TMPTA and M-MPTA-C samples.....	85
Figure 4-18 Results of DMTA tests. Storage modulus ( $E'$ ), loss modulus ( $E''$ ) and $\tan\delta$ as a function of temperature. $E''$ and $\tan\delta$ have been smoothed.....	86
Figure 4-19 Results of DSC tests on the prepared samples: (a) first heating scan; (b) cooling scan; (c) second heating scan.....	87
Figure 4-20 Results of 50-cycles DSC tests on the sample M-TMPTA. a. thermograms of cycles #1, #2, #5, #20 and #50 are colored and indicated with an arrow, while all the other cycles are black. B. values of melting and crystallization enthalpy for all cycles.....	88
Figure 4-21 Macroscopic view of the (a) M-TMPTA-C, (b) M-TMPTA and (c) PEO-PI electrospun samples at 25 °C (as prepared) and (d) M-TMPTA-C, (e) M-TMPTA and (f) PEO-PI after thermal treatment at 100 °C for 2 min, and FE-SEM images of PEO-PI electrospun sample at 25 °C and 100 °C.....	89
Figure 4-22 FE-SEM micrograph of M-TMPTA sample as prepared (a) and after 1 (b), 20 (c), and 80 (d) thermal cycles in the climatic chamber; the insets are FE-SEM images in greater magnification. e. size distribution of fibers before (#0) and after (#1, #20, and #80) thermal cycles. f. fiber diameters, FWHM and surface porosity of the electrospun mats, obtained by DiamaterJ, after thermal cycling ..	90
Figure 5-1 a. Thiol-ene reaction in presence of free radicals, b. schematic representation of the crosslinked polybutadiene based network in presence of trifunctional thiol monomer [159,362].....	95
Figure 5-2 Scheme of chemical structure of materials used in this study including polybutadiene (PB), maleinized polybutadiene (PB-MA), SBR, PEO, TRIS thiol crosslinker, TPO and Darocur 1173 photoinitiators.....	98
Figure 5-3 a. Scheme of the electrospinning process with <i>in-situ</i> photocuring of liquid polybutadienes. b. Optical microscope image of PB-MA after electrospinning and <i>in-situ</i> photocuring. c. Optical microscope image of PB-MA–2%TPO–3%TRIS fibers obtained by electrospinning and <i>in-situ</i> photocuring. .	101
Figure 5-4 FTIR spectra of PB (a) and PB-15MA (b) prior (irradiation time = 0 min), during (irradiation time = 5 min) and after (irradiation time = 15 min) UV irradiation .....	103
Figure 5-5 Scheme of the photo-induced crosslinking reactions of PB (a) and maleinized PB (b), and of polybutadienes in the presence of the trifunctional thiol	

crosslinker TRIS (R(SH) <sub>3</sub> ) and the photoinitiator TPO (c), occurring during UV irradiation in air. ....	104
Figure 5-6 FTIR spectra of 12 μm thick film of a.PB and b.PB-15MA containing 2 wt.% photoinitiator and 3 wt.% crosslinker (PB-2TPO-3TRIS and PB-15MA-2TPO-3TRIS, respectively) prior (irradiation time = 0 s) and after UV irradiation (irradiation time = 10 s) in air.....	106
Figure 5-7 Viscosity vs. shear rate of PB-15MA and of the PB-15MA-2TPO-3TRIS formulations used in electrospinning with 0, 3, 5 and 9 wt.% OA. ....	107
Figure 5-8 Fiber morphology by optical microscope images of PB-MA-2TPO-3TRIS formulations with 0 (a), 3 (b), 5 (c) and 9 (d) wt.% OA and (e) their size distribution.....	107
Figure 5-9 Insoluble fraction of photo-cured electrospun PB-15MA-2TPO-3TRIS samples with 0, 3, 5 and 9 wt.% OA.....	108
Figure 5-10 a. TGA thermograms of liquid PB-15MA and crosslinked electrospun PB-MA-2TPO-3TRIS systems containing 0, 3, 5 and 9 wt.% OA. b.Average fiber diameter of photocured electrospun PB-MA-2TPO-3TRIS with 3 wt.% OA after a thermal treatment. The insets show the fiber morphology by optical microscope images, c.DMTA results on photo-cured electrospun mats of PB-MA-2TPO-3TRIS without (0OA), with 3 wt.% (3OA) and 5 wt.% (5OA) of oleic acid as polar additive.....	109
Figure 5-11 Contact angle with water (WCA) of the photocured electrospun mats of PB-15MA-2TPO-3TRIS with 0, 3, 5 and 9 wt.% OA. ....	110
Figure 5-12 Schematic illustration of SBR/PEO fibers and their photo-crosslinking: SBR particles are dispersed in PEO template upon electrospinning and subjected to thiol-ene crosslinking by UV irradiation; then a water treatment is applied to remove the uncured PEO, leaving crosslinked rubber fibers formed by SBR nanoparticles .....	111
Figure 5-13 FE-SEM images of electrospun membrane of (a) SBR/PEO, with the diameter distribution in the range of 670 to 1000 nm, and of (b) PEO, with the diameter distribution in the range of 160 to 540 nm. ....	111
Figure 5-14 ATR FTIR spectra of SBR cast film, PEO film and SBR/PEO electrospun fibers. The triple peak associated to ether bond in PEO, the -CH <sub>2</sub> -CO rocking of PEO backbone at ~840 cm <sup>-1</sup> and the peak at 699 cm <sup>-1</sup> related to aromatic ring in SBR are shown with blue, green and red frames, respectively.....	112
Figure 5-15 a. Schematic of three double bond isomers of trans-1,4, vinyl-1,2 and cis-1,4 in polybutadiene b. vinyl and c. trans conversion for SBR/PEO fibers containing three different contents of TRIS upon UV irradiation and c. S-H and	

vinyl conversion for the sample SBR/PEO/50%TRIS upon UV irradiation. The conversion data were obtained by real time FTIR spectroscopy.....	113
Figure 5-16 FE-SEM images of the photo-cured electrospun membranes made of PEO/SBR with a. 3 wt.% and b.10 wt.% of the thiol crosslinker and 1 wt.% of TPO:Darocur 1173 1:1 photoinitiator system, and their fiber diameters distribution. ....	115
Figure 5-17 a. DSC scans (cooling and second heating) of the prepared electrospun samples and pristine SBR, b. zoom of the DSC scans to better show the T <sub>g</sub> of the SBR/PEO samples, c. TGA thermograms of the SBR/PEO photo-cured fibers as well as of pristine PEO and SBR .....	116
Figure 5-18 FTIR spectra of SBR-based photo-cured electrospun samples (a. SBR/PEO/3%TRIS and b. SBR/PEO/10%TRIS) before and after water treatment for PEO removal.....	118
Figure 5-19 FE-SEM images of SBR-based photo-cured electrospun fibers with a. 3 wt.% TRIS and b.10 wt.% TRIS after water treatment, their fiber diameters distribution, and the distributions of the rubber particles that form the fibers. ...	119
Figure 5-20 DMTA results on photo-cured SBR/PEO electrospun mats containing 3 and 10 wt.% TRIS a. prior and b. after water treatment, c. example of a tensile test measurement on SBR/PEO/10%TRIS photo-cured fibrous membrane after water treatment.....	120
Figure 5-21 TGA thermograms and first derivative of the TGA of electrospun fibers of SBR/PEO/3%TRIS and SBR/PEO/10%TRIS after water treatment....	121
Figure 5-22 a. photograph of the electrospun membrane of SBR/PEO/10wt.%TRIS after water treatment, b. schematic representation of the filtration setup for water/oil separation experiment, c. the experimental setup for the water/oil filtration.....	122
Figure 5-23 Water contact angle versus time for SBR/PEO/3%TRIS-WT and SBR/PEO/10%TRIS-WT .....	123
Figure A-1 The C=C conversion obtained through real-time FTIR, while the cast film (on the silicon wafer as substrate) of the formulations were subjected to UV irradiation while the silicon wafer and cast film covered by PP transparent layer (initially the background spectrum was collected in presence of the silicon wafer and the PP layer).....	156
Figure A-2 FTIR-ATR spectra of the L-TMPTA fibers prior and after UV irradiation, the consumption of the C=C can be observed .....	157
Figure A-3 FTIR-ATR spectra of the M-TMPTA fibers prior and after UV irradiation, the consumption of the C=C can be observed .....	157

Figure A-4 FTIR-ATR spectra of the H-TMPTA fibers prior and after UV irradiation, the consumption of the C=C can be observed .....	158
Figure A-5 FTIR-ATR spectra of the M-PEGDA fibers prior and after UV irradiation, the consumption of the C=C can be observed .....	158
Figure A-6 The FTIR spectra of L-PEGDA, M-PEGDA, H-PEGDA, L-TMPTA, M-TMPTA and H-TMPTA fibers prior and after UV-irradiation. The C=C conversion can be obtained by tracking the band at $1640\text{ cm}^{-1}$ by considering the peak of C=O as a reference at wave number $1720\text{ cm}^{-1}$ .....	159
Figure A-7 FE-SEM image of the cross-section of a H-TMPTA electrospun sample. The fibers along the thickness show a homogenous structure.....	160
Figure A-8 FE-SEM image of cross-section of H-PEGDA samples, the film formation on backside of the fibers can be seen.....	161
Figure A-9 FE-SEM image of cross-section of the thick H-PEGDA samples, the film formation on the side near the aluminum foil (the substrate) can be observed .....	162
Figure A-10 FTIR spectra of N4-5000 during the UV irradiation at different time intervals. ....	163
Figure A-11 FTIR spectra of N4-5000-10MA during the UV irradiation at different time intervals. ....	163
Figure A-12 FTIR spectra of N4-5000-15MA during the UV irradiation at different time intervals. ....	164
Figure A-13 FTIR spectra of PM4 during the UV irradiation at different time intervals. ....	164
Figure A-14 FTIR spectra of PM4-7.5MA during the UV irradiation at different time intervals. ....	165



# Chapter 1

## Introduction

Electrospinning is a unique and versatile technique for fine polymer fibers fabrication with diameters in the range of nanometers to micrometers from a variety of polymers both natural and synthetic. The electrospun fibrous structures offer extraordinary properties such as high surface area to volume ratio, high porosity with interconnected pores, flexibility and light weight. Nanofibrous membranes prepared by electrospinning thus show a tremendous potential for application in several areas, such as filtration, biomedical, energy and sensing fields. The versatility of the technique provides the possibility for further developments. Therefore, nowadays novel and innovative setups and materials are developed to fabricate nanofibers and nanofibrous membranes tackling the conventional problems.

The ultimate properties of an electrospun membrane depend on the intrinsic properties of the polymer itself, in addition to the properties due to the fibrous structure and its morphology. Therefore, the electrospinning process has to be optimized and in many cases, obstacles related to intrinsic properties of the selected materials (e.g., shape instability) need to be addressed for allowing the successful application of the fabricated electrospun membranes. In this work, different photo-induced crosslinking reactions, which are characterized by low energy consumption, ambient temperature operations, high throughput, and high reaction rate, were applied in order to enhance the properties of electrospun polymeric fibrous membranes, such as their morphology stability, and solvent and heat resistance. In particular, the present thesis describes three interconnected topics of research in the field of the coupling of electrospinning process and photo-induced crosslinking reactions, applying the proposed strategy to different polymeric systems and fabricating photo-crosslinked electrospun membranes based on:

- i) chitosan (CS);
- ii) polyethylene oxide (PEO);
- iii) polybutadiene (PB).



The state of the art on the electrospinning process and on photo-induced polymerization/crosslinking reactions, together with the current solutions present in the literature for the coupling of electrospinning and photoinduced processes are described in Chapter 2.

Then, the main results of the experimental research work on the different polymeric systems are presented in three separate chapters, each one encompassing the description of the optimization of the electrospinning process and of the photo-induced crosslinking reaction, the selection of the preferable polymer formulation, and the characterization of the obtained photo-cured electrospun membranes.

In Chapter 3, the fabrication of CS-based electrospun fibrous membranes is reported. Chitosan is the main derivative of the natural polysaccharide chitin, and is characterized by biocompatibility, biodegradability, antibacterial properties, and nontoxicity, with a wide application potential. However, CS suffers from challenging processability particularly in electrospinning, mainly due to its polycationic nature. Thus, for fabricating CS-based electrospun membranes, PEO as an easily electrospinnable polymer was used, and acidic water-based CS/PEO blend solutions were subjected to electrospinning. The CS/PEO electrospinning process has been investigated and optimized. Then, the photo-induced crosslinking reaction by UV irradiation in presence of a suitable photo-initiator was applied to the electrospun membranes to increase the solvent resistance and to stabilize the CS/PEO fibrous structure. Both the CS/PEO composition ratio and the light irradiation conditions were optimized. The promising results showed that upon UV irradiation, the fibrous morphology as well as the thermal and structural properties of CS-based electrospun membranes can be enhanced, making them suitable for a wide range of applications, in which CS in the form of a membrane with nanoscale features and a high available surface area is required.

In Chapter 4, water-based PEO solutions containing a multifunctional acrylic monomer and a photo-initiator were subjected to electrospinning and subsequent photo-induced crosslinking of the fibrous mats. It is worth noting that PEO is soluble in almost all organic solvents including water and has a melting temperature  $T_m$  around 60°C; hence, the fibrous morphology of PEO electrospun membranes can be easily destroyed when in contact with a solvent or at temperatures higher than  $T_m$ . As a result, the solubility and the morphology instability issue suppresses the potential application in many fields of this polymer, which is characterized by excellent properties such as biocompatibility, inertness and thermal stability. Consequently, the photo-induced crosslinking reaction was applied to form a stable polymer network, and an acrylic monomer was introduced to the formulation in order to accelerate the curing reaction. Different types and concentrations of acrylic monomer were investigated. A comprehensive characterization of the electrospinning and photo-crosslinking reaction was performed, and the properties of the photo-cured electrospun membranes were fully studied. As a result, solvent resistant electrospun PEO fibrous structures retaining their morphology when in contact with solvents were obtained. Then, the optimum PEO formulation was selected for further thermal and mechanical characterizations. The results showed that UV-cured PEO fibers can also withstand elevated temperatures, above the

melting point of PEO. The newly fabricated PEO-based electrospun membranes with enhanced solvent and thermal resistance, and superior morphology stability were thus demonstrated to be suitable as novel solid-solid phase change materials.

In Chapter 5, the coupling of electrospinning and photo-crosslinking of PB-based rubbers were investigated. PBs are characterized by high extensibility, elasticity, elastic recovery, and resilience, but they suffer from cold flow at room temperature, due to their very low glass transition temperature. Therefore, PB-based fibers tend to flow over time and lose their overall morphology. The shape stability can be enhanced by the application of a crosslinking reaction. For instance, PB-based materials can undergo photo-induced crosslinking thanks to the presence of the C=C double bonds, and it has been shown that thiol-ene chemistry is the most efficient approach to induce the crosslinking of these polymers. This section of the work was dedicated to the development of two distinct environmentally friendly processes based on the coupling of electrospinning and photo-induced thiol-ene crosslinking involving polybutadiene-based materials, meaning liquid polybutadienes with low molecular weight and styrene-butadiene rubber (SBR) latexes. The liquid polybutadienes were subjected to electrospinning without using any solvent and *in-situ* UV-curing (i.e., during the fiber formation), while the SBR latexes were subjected to suspension electrospinning (i.e., using water as the only solvent) and post-modification of the electrospun membranes by UV irradiation. Both systems were examined and optimized, by tailoring the PB formulation containing a multifunctional thiol crosslinker and a suitable photoinitiator system, and tuning the process conditions. As a result, successfully electrospun rubber fibrous membranes were obtained, and the coupling of the electrospinning process and the thiol-ene crosslinking chemistry was demonstrated to be an interesting approach to fabricate stable polybutadiene-based electrospun fibers in an environmentally friendly way. Shape-stable rubber fine fibrous membranes can find applications in several fields where a high surface area together with the rubber intrinsic properties are required, such as filtration and water/oil separation.

Finally, Chapter 6 contains the general conclusions of the research work and presents its future perspectives.



# Chapter 2

## State of the art

Electrospinning is a unique technique to produce fine submicrometric fibers and nonwoven mats from polymer solution or melt through the application of high electrostatic forces. The deep impact of electrospinning and its wide application potential are related to the possibility to process a large set of polymers, both natural and synthetic. Nanomaterials prepared by electrospinning have tremendous potential for application in several areas, from filtration to sensing and biomedical devices.

Photoinduced processes are employed for the synthesis, curing, and modification of polymers and are recognized as ecofriendly approaches. In fact, they present short conversion times and high efficiency, low-energy consumption, ambient temperature operations, no need of solvents, and selective curing with a precise control both in time and space. Photoinduced reactions find widespread applications in coating industries, lithography, biomedical area, and surface modification.

This chapter briefly describes the state of the art on the electrospinning process, illustrating the process fundamentals and focusing on its governing parameters, the different types and setups of electrospinning, the main materials employed and applications, and the current scaling up of the technique.

Photoinduced reactions are then presented, including free radical polymerization and crosslinking processes, which are particularly applied in this study by different routes in presence of photoinitiators and acrylic or thiol crosslinkers.

Finally, the current solutions for the coupling of electrospinning and photoinduced processes are shown.

### 2.1 Electrospinning

Electrospinning is a unique and versatile technique for fine fiber fabrication with diameters ranging from tens of nanometers to micrometers from polymer solution or melt [1–4]. During electrospinning process, the electrified jet of polymer solution or melt is generated from the liquid droplet and consecutively under the applied high electric field (10–30 kV) the jet is stretched, elongated and solidified as fine fibers. [5]. This technique has gained a momentum in recent decades in a variety of applications [1–4].

Electrospinning technique dates back to 1887 [6], when it was found that fibers could be drawn from a viscoelastic liquid when electric field is applied. In fact, the

concept of electrospinning was raised much earlier, in 1600 the formation of conical shape of water in presence of external electric field was reported, later the electrospaying of water passing through the charged vessel was observed.

**Figure 2-1** demonstrates the timeline of the evolution of the electrospinning process. In 1882 Lord Rayleigh studied the behavior of the charged liquid droplet and ejection of liquid jet from the charged droplet [7]. Then Sir G. Taylor in 1969 mathematically and experimentally explained the conical shaped at the tip of the liquid droplet in presence of electric field and eventually ejection of fine jets from the conical shape. In the introduction of his published scientific work, it is stated that:

*“Fine jets of slightly conducting viscous fluids and thicker jets or drops of less viscous ones can be drawn from conducting tubes by electric forces. As the potential of the tube relative to a neighboring plate rises, viscous fluids become nearly conical and fine jets come from vertices.”*[8]

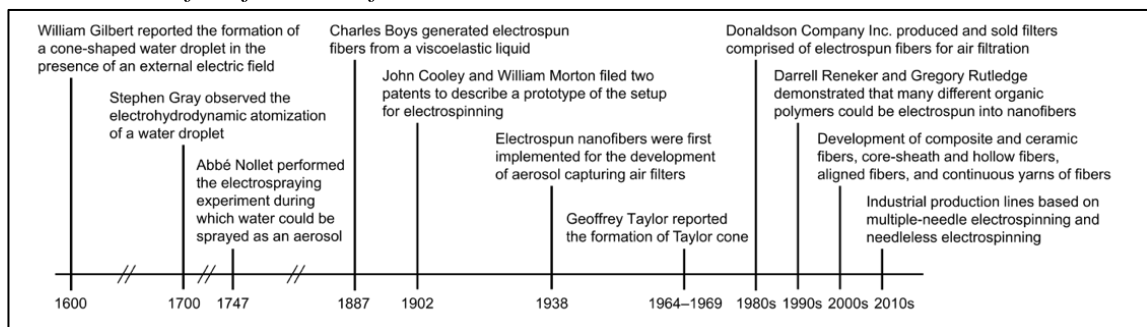


Figure 2-1 Timeline of evolution of electrospinning technique [9]

Electrospinning technique received a great attention in both industry and academia since 1990; more than 44,000 publication (**Figure 2-2**) and nearly 20,000 patents are issued up to now (2021) reporting technique development and new and innovative material fiber fabrications.

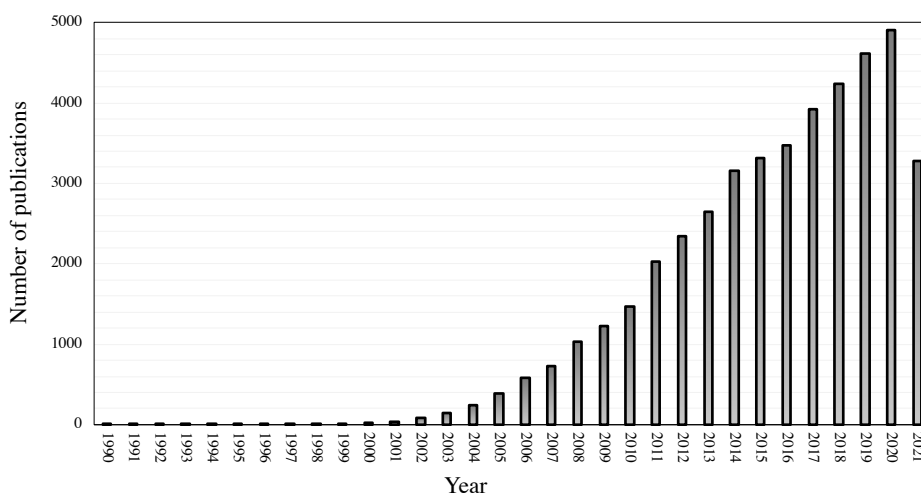


Figure 2-2 The growing number of publications per year for the electrospinning technique (source Scopus.com with “Electrospinning” as keyword)

Conventionally, an electrospinning setup consists of three major components: a high voltage power supply, an electrically conducting spinneret and a collector at a defined distance (working distance) from the spinneret (**Figure 2-3a**). This technology has been changing over time and, as will be described below, in recent decades innovative electrospinning setups are introduced in which unconventional setup components are used (e.g., needleless electrospinning setups, liquid type collectors) [10–14]. **Figure 2-3b** displays a typical fibers morphology obtained from polymer solution electrospinning.

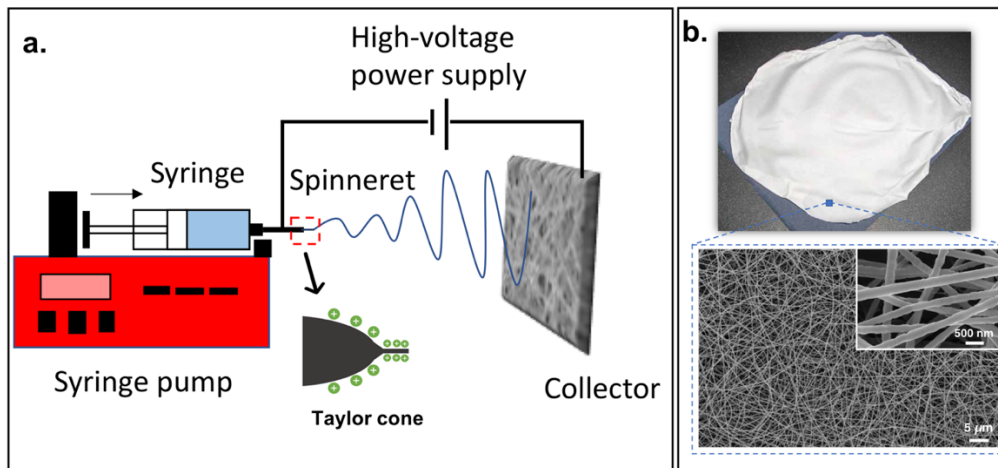


Figure 2-3 a. Conventional electrospinning setup; b. example of an electrospun fibrous membrane

### 2.1.1 Electrospinning process

Electrospinning process encompasses a complex interaction between surfaces properties, rheology and electrical charges to yield an electrified jet and consecutively to shape the solid fibers. The different steps of the process are described in the following.

#### Taylor cone formation

Basically, during the electrospinning process, a high voltage is applied to the conductive spinneret containing the polymer solution or melt; consequently, the surface of the liquid droplet (polymer solution or melt) at the tip of the needle gets electrostatically charged. Then the transformation of the droplet into a conical shape, called Taylor cone, at a certain voltage occurs (**Figure 2-4**) [5]. When the electrical repulsive forces overcome the surface tension holding the droplets, the continuous charged jet of polymer solution or melt is generated. In other words, upon application of the electrical charges, ions carrying the charges travel to the surface and when the electrical potential on the surface reaches a certain value, the surface energy holding the droplet in sphere shape is overcome and the electrified jet is formed. This phenomenon takes place at a certain intensity of the electrical field. [11].

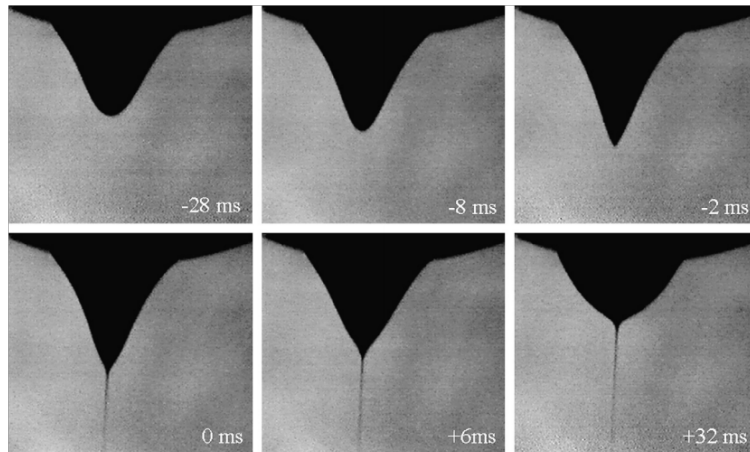


Figure 2-4 Taylor cone evolution over time under applied electric field [11]

### Stretching of the jet

The ejected electrified jet of liquid polymer initially follows a straight line, in which the viscoelastic properties of the jet should satisfy the jet entanglement to prevent the Rayleigh instability, which leads the jet to break into drops. In the straight segment, the diameter of the jet gradually decreases by moving away from the tip of the cone. The jet segment leaving the Taylor cone tip is pulled by the Coulomb forces between the charges, acting against the surface tension, towards the collector. After the jet is formed, the radial component of the Coulomb force causes the excess ions to migrate to the surface of the liquid polymer to provide the equilibrium conditions; it can be said that inside the flowing jet the electric field should be equal to zero. The jet velocity, the straight segment length and the diameter of the moving jet in the straight segment can be mathematically calculated [15–17]. The monotonic stretching continues before the electrical bending instability starts.

### Bending instability

After the stretching along a straight line, the generated charged jet undergoes the vigorous whipping motion because of the growth of electrical bending or whipping instability due to stronger electric field. As the jet elongates and becomes very thin, the charges demand longer time to redistribute along the jet length. The excess charge present on the liquid polymer surface or inside the flying jet tend to deform the straight trajectory of the polymer jet. As a result, the bending of the jet from its straight pathway starts (**Figure 2-5**), and other deformations of the polymer jet in a way to favor the repulsive forces of like sign charges take place. In fact, the Coulomb forces between excess charges acts against the axial component of viscoelastic stress.

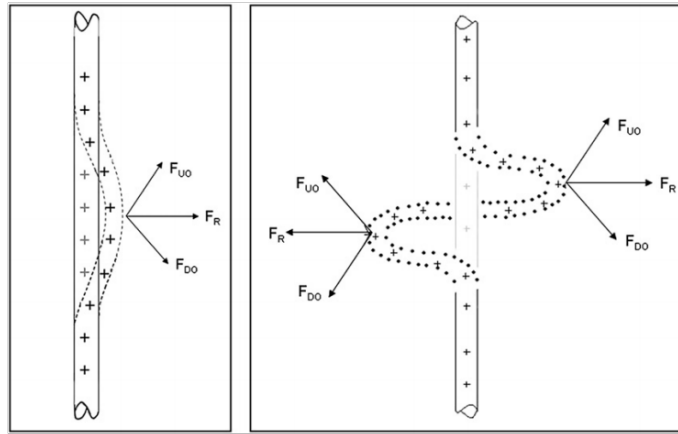


Figure 2-5 Schematic representation of the primary bending of moving jet due to excess like sign charges [11]

Upon the bending instabilities or perturbations due to excess charges, the jet movement resembles a three-dimensional coil with increasing diameter moving toward the collector. This shape permits the major elongation/stretching of the polymer jet (generally of 10,000 times) in a small space unit. The coil pathway allows the decrease of the fiber diameters leading to an increased surface area per volume ratio. It is worth noting that the velocity of moving jet on the onset of bending instability is reported to be 1-5 m/s. Expectedly, thinning of liquid polymer jet advancing the coil-shaped trajectory exacerbates the bending instabilities and reportedly three or more other bending instabilities stages take place before the fiber solidification and deposition on the collector. As shown in **Figure 2-6a**, the liquid polymer jet undergoes several bending instabilities, and each time a smaller coiled path is formed permitting the solvent evaporation and/or fiber solidification (**Figure 2-6b** and **6c** display the images obtained by CCD camera of a jet trajectory).

Moreover, during electrospinning process other instabilities can be also observed such as branching, flat ribbons or beaded fiber formation. Branching is more frequent in system characterized by a high concentration or viscosity, particularly when a higher electrical field than the required potential is applied.

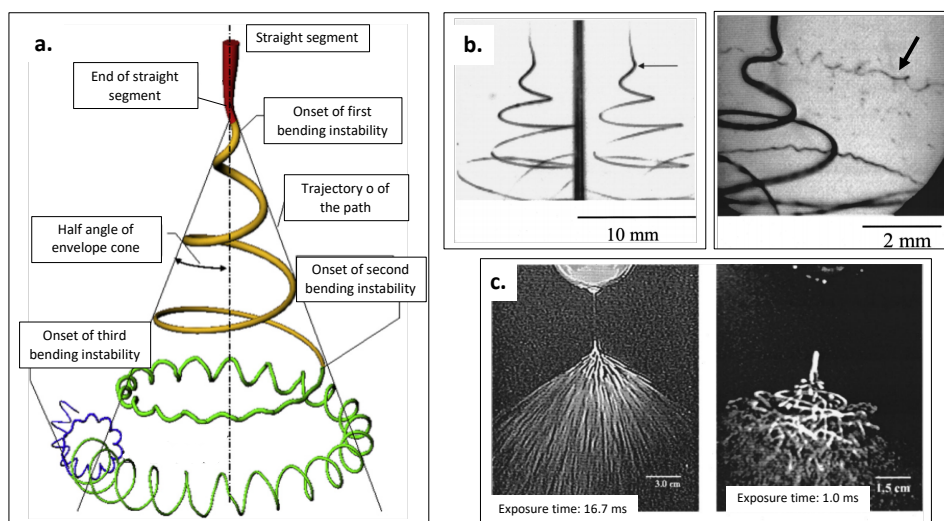




Figure 2-6 a. Schematic representation of trajectory of moving electrified jet of polymer b. images obtained by CCD camera of the electrospinning process, c. imaging of travelling jet of polymer with different exposure time [11]

### Beaded fibers

It has been previously described that the excess electrical charges cause the elongation of the jet. While the capillary instability leads to the breaking of the cylindrical jet into droplets. This phenomenon has been explained by Lord Rayleigh: the surface energy of a fluid in the form of a cylindrical jet is higher than that of a sphere with the same volume. During the capillary instability, charges are more stable on the surface of a sphere and are well-distributed; as the excess charges overcome the surface energy of the sphere, a jet is emanated from the sphere. This pattern can be periodically repeated and results in the so-called bead-on-string structure (**Figure 2-7**) [18,19].

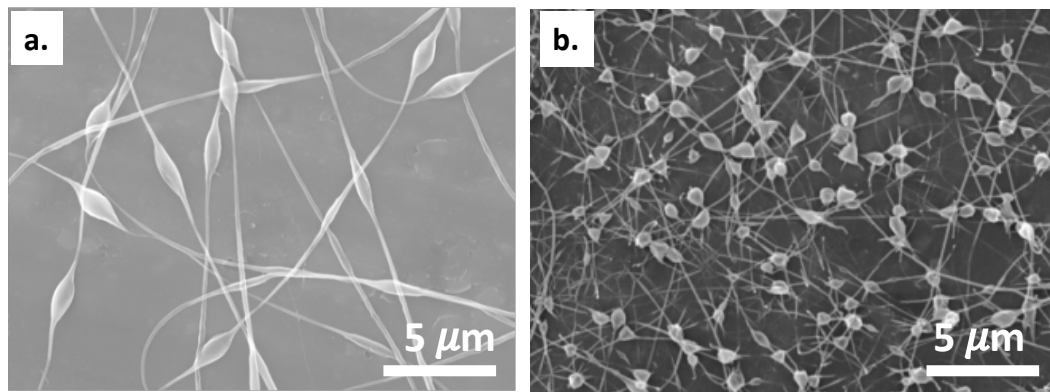


Figure 2-7 The morphology of the electrospun beaded fibers made of PEO solution [18]

### Solidification of the jet

Upon this complicated process of elongation and bending instabilities, the solvent is evaporated, or the melt polymer cools down and the solidification of the jet takes place. Slower is the evaporation process of the polymer solution, thinner the deposited fibers are [7,20].

### Deposition of the fibers

The fiber morphology and diameters can be defined by the bending instability stage (or also the straight regime), depending on at which stage fibers are deposited. Fibers in the first bending instability can be collected as nonwoven mat, while the second, third or further bending instabilities yield a more complicated fiber deposition in form of coil or wavy morphology. Most of the charges on the fibers after deposition are dissipated through the grounded collector; it should be taken into consideration that polymers are mostly poorly conductive, thus, fully depletion of the charges does not occur. The residue of the charges on the deposited fibers can repels the depositing fibers to further distance and as a result mainly in lab scale efforts the thickness of the electrospun membrane is restricted to 0.5-1 mm [21].

In the course of electrospinning, materials (solution/melt) parameters, process parameters and also ambient parameters interact and define the electrospinning fate and final fiber morphology and characteristics. In fact, the formation of the Taylor cone, the generation of a stable liquid polymer jet, the bending instabilities and the solidification all depend on these parameters and their interactions. The governing parameters in electrospinning process have been comprehensively studied and reviewed [7,22,23]. In general, these parameters are categorized into three main groups:

- solution/melt parameters (i.e., *viscosity, conductivity, molecular weight, and surface tension*),
- process parameters (i.e., *applied electric field, working distance and feed rate*),
- ambient parameters (i.e., *temperature and humidity of the surroundings*).

Each of the above-mentioned parameters can affect the outcome of the electrospinning process, and thus the fiber morphology and fiber diameter can be tuned by optimizing these parameters.

The electrospinning mathematical models and simulations are not the purpose and subject of the present work. Though, in the following section some useful equations and relationship of the major parameters in electrospinning are briefly explained.

### 2.1.2 Mathematical and empirical models

In last few decades, electrospinning process has been profoundly studied and mathematically modeled. Different phenomena such as Taylor cone formation, stretching of the polymer jet in straight line, bending, whipping and Rayleigh instabilities are studied through application of fluid mechanics, electromagnetism and rheology, by using momentum or force balance considering several parameters. In general, the electrospinning process can be considered to occur in two main flight zones: zone I, where the jet is near the solution with slower acceleration, and zone II, where the flying jet undergoes fast acceleration and is near the collector. The literature studies are mainly attributed to the so-called zone I in electrospinning, where the events are more predictable and thus much is known about this zone; whereas, the zone II, where the chaos and complex instabilities are taking place, is not fully understood. In the following section, some of the most known theories on electrospinning process are brought (**Table 2-1** reports the common parameters used for mathematical models of the electrospinning process).

Table 2-1 Common parameters used for mathematical models

Parameter	Symbol
Liquid flow rate	Q
Liquid electrical conductivity	K
Liquid-gas surface tension	$\gamma$
Fluid density	$\rho$

Electrical permittivity of vacuum	$\epsilon_0$
Jet radius	$r$
Electrical current	$I$
Applied electric field	$E$
Surface charge	$\sigma$

### Taylor cone

In 1969, Sir Geoffrey Taylor [8] proposed an expression for the critical voltage at which the conical shape known as Taylor cone is formed:

$$V_c^2 = \frac{4H^2}{h^2} \left( \ln \left( \frac{2h}{R} \right) - 1.5 \right) (2\pi R \gamma \cos \varphi) \quad \text{Eq1}$$

H, h, R and  $\gamma$  are the distance between the tip of the needle and the collector, the length of the spinneret, the outer radius of the spinneret and the surface tension of the liquid polymer, respectively. According to Taylor empirical and mathematical treatment in 1964, a conducting liquid under external electrical potential can be in conical shape and in state of balance only when the semi-vertical angle  $\varphi$  is 49.3 ° [24]. It is worth noting that in 2001, Yarin et al. experimentally and theoretically showed that as the liquid surface tends to develop a critical cone shape, the configuration is close to  $\varphi$  equals to 33.5° rather than 49.3 °[25].

Upon electrospinning process, the critical voltage at which the conical shape is formed depends greatly on the liquid properties. In case of viscous liquids (e.g., polymer liquids in form of solution or melt), a critical voltage is needed to provide sufficient repulsion to overcome the surface tension of the liquid.

### Jet elongation and pathway – straight regime

The formation of the electrified jet has also been studied and mathematically modelled by several research groups [12,16,19,26–32].

For instance, Gañán-Calvo in 1997 [16] reported an analytical model for the multidisciplinary problem of a spraying liquid under an applied electric field. By considering the cone-jet mode, he proposed his model to solve the electrohydrodynamic process of a liquid and the electrified jet emission from the cone. In this approach, considerations are the perfectly conical equilibrium shape (i.e, same as the Tylor results and considerations) and an infinite thin jet emanated from the cone apex. As a result, Eq2 and Eq3 for the total electric current (I) (driven by both surface charge motion and the bulk electric conduction) and droplet diameter (d) were proposed, respectively.

$$I = 4.25 \left( \frac{QK\gamma}{\ln \left( \frac{Q}{Q_0} \right)} \right)^{1/2} = 4 \left( \frac{QK\gamma}{L_0} \right)^{1/2} \quad \text{Eq2}$$

$$d = 2 \times 1.89 R_0 f_b = 3.78 \pi^{-2/3} Q^{1/2} \left( \frac{\rho \epsilon_0}{\gamma K} \right)^{1/6} f_b \quad \text{Eq3}$$

In the proposed relations, I and d are a function of the liquid flow rate (Q), the liquid electrical conductivity (K), the non-dimensional flow rate ( $\frac{Q}{Q_0}$ ), the surrounding liquid-gas surface tension ( $\gamma$ ), the dimensionless number

$\mathcal{L}_0 = \ln\left(\frac{Q}{Q_0}\right)^{1/2}$ , the density of the fluid ( $\rho$ ), the electrical permittivity of vacuum ( $\varepsilon_0$ ), the typical jet radius  $R_0 = d_0\left(\frac{Q}{Q_0}\right)^{1/2}$ , and  $f_b$ , which is a nondimensional quantity (obtained equal to  $\sim 0.6$ ).

In 1998, Spivak and Dzenis [28] analyzed the decay of the polymer jet radius at a large distance from the cone apex and as a result a differential equation for the jet radius variation with axial coordinate was driven. By applying a numerical solution, they showed that in accordance with earlier experimental work on several fluids, at long distance a power-law asymptote approximation of the jet radius  $r$  with exponent  $1/4$  can be obtained ( $r \sim Z^{-1/4}$ ).

### Bending and whipping instabilities

In 2003, Fridrikh et al. [12] proposed an analytical model for the stretching of a charged viscous fluid, also in whipping instabilities regime, subjected to an electric field. This model predicts the final polymer jet diameter ( $d_t$ ) by solving the equation of motion, driven from the force balance between surface tension and electrostatic charge repulsion, as a function of material properties (e.g., conductivity, dielectric permittivity, dynamic viscosity, surface tension, and density) and operating parameters (e.g., flow rate, applied electric field and current).

$$d_t = \left( \gamma \bar{\varepsilon} \frac{Q^2}{I^2} \frac{2}{\pi(2\ln\chi-3)} \right)^{1/3} \quad \text{Eq4}$$

The parameter  $\chi \sim R/d$ , in which  $R$  is jet curvature radius and  $d$  is the jet diameter, is a dimensionless wavelength of the instability regime responsible for the normal displacements.

Similarly, in 2005, He et al. [17] proposed a model for predicting the length of the straight segment of the jet  $L$ . Where  $E$  is the applied electric field and  $\sigma$  is the surface charge and  $k$  is a dimensionless conductivity of the liquid.

$$L = \frac{4kQ^3}{\pi\rho^2I^2} [R_0^{-2} - r_0^{-2}] \quad \text{Eq5}$$

$$R_0 = \left( \frac{2\sigma Q}{\pi k \rho E} \right)^{1/3} \quad \text{Eq6}$$

In 2004, Wan et al. [33] proposed a model considering the coupled effect of temperature, electricity and hydrodynamics in electrospinning process. Hence, heat flux and also materials properties dependent on temperature were considered in this model. Performing melt electrospinning at elevated temperature, these considerations become vital for understanding the process.

Bending instabilities of electrically charged liquids were also studied and modelled by Reneker [5] and Yarin [34]. Reneker et al. [5] imaged the region of starting point of the coil (bending instability) by a CCD camera with 2000 frames per second and modelled the segment of electrified jet by a viscoelastic dumbbell (**Figure 2-8**), proposing a viscoelastic Maxwellian model for the liquid jet.

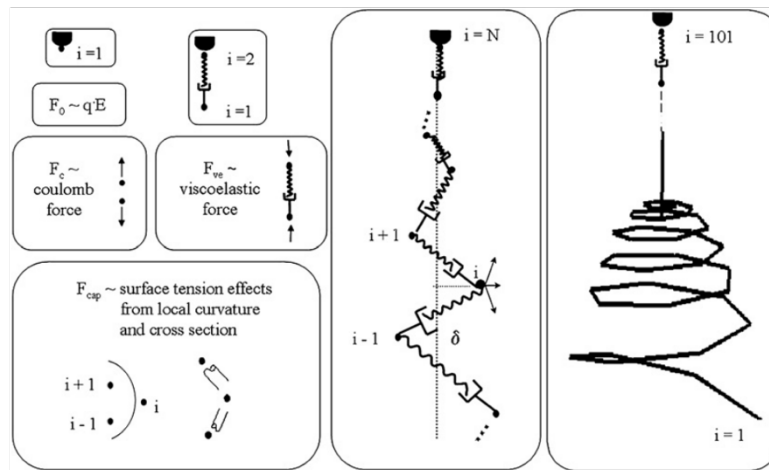


Figure 2-8 Reneker viscoelastic Maxwellian model for the electrified liquid jet [5]

In 2001, Shin et al. [20] theoretically and experimentally investigated the effect of electrospinning parameters. Then, Hohman and Shin [31,32] in their paper series extensively studied the stability problem modifying the existing theories, developed the theory for whipping instability, examined the competition between instabilities (axisymmetric and whipping instabilities) and ultimately applied their findings to the experimental work.

In 2005, Zou et al. [35] experimentally examined the effect of applied voltage, solution surface tension and conductivity on bead formation during electrospinning process as a result of the axisymmetric instability. Their experimental studies were in well-accordance with the theoretical models based on axisymmetric instability. In this regard, the applied voltage and feeding rate were reported as key parameters in different morphology development. Other parameters determining the fiber morphology were conductivity and surface tension.

Deitzel et al. [29,30] experimentally studied the effect of electrospinning parameters (specially, applied voltage and solution concentration) on the fiber morphology. They claimed that the morphology of the nanofibers is strongly affected by the feed rate of the polymer solution, the applied voltage and the solution properties, such as viscosity and surface tension. They systematically studied the relationship of the fibers (number and average diameters) to the solution concentration and applied voltage. The general conclusions were that the increasing of the polymer solution concentration led to the increasing in fiber diameter, and that higher voltages changed the instability regimes that can yield beaded fibers or droplets.

The surface tension of the liquid and distribution of the ions on the liquid surface has been described by partial differential equations. Both analytical solution and numerical solutions have been proposed [5,18,36,37].

In 2005, Theron et al. [38] performed another systematic study on governing parameters of different polymer solutions, namely polyethyleneoxide (PEO), polyacrylic acid (PAA), polyvinyl alcohol (PVA), polyurethane (PU) and polycaprolactone (PCL). The experiments were designed to determine the dependence of electric current ( $I$ ) and volume charge density as a response to

variation in solution volumetric flow rate, polymer molecular weight, nozzle to collector distance, applied voltage as well as solvent type. They found that the charge density exhibited a power law dependence on applied voltage, concentration, molecular weight and volumetric flow rate, all studied polymers showing the same trend of responses. While the electric current showed diverse response to the same governing parameter for different polymers. For instance, by increasing the flow rate the electric current for some polymers increased, for PCL decreased and for PAA showed no changes.

### **2.1.3 Electrospinning parameters**

By all of the previously described models, one can define the involving parameters under consideration for electrospinning process associated to liquid polymer properties, ambient parameters and process parameters. In this section, some general observations according to the effect of electrospinning parameters on fiber diameter and morphology are briefly explained.

#### Effect of applied voltage

It is generally accepted that the critical voltage is different for one polymer to another. Smaller fibers can be obtained by increasing the voltage and this is mainly due to the stretching of the polymer solution because of the growth of bending instabilities and the repulsion of the same sign charges. However, after a certain voltage value (which depends on the polymer) defective and beaded fibers can also be formed.

#### Effect of flow rate

The flow rate of the liquid polymer can also define the morphology of the fibers. Beaded fibers can be generated when a flow rate higher than critical value, which varies for different polymers, is applied. Additionally, increasing of the fiber diameter and the pore size can arise from higher feed rates. The formation of ribbon like fibers is another consequence of the increasing of the flow rate. Having lower flow rate can induce the formation of receded jets, in which the liquid polymer jet is continuously replaced by new ones; therefore, a wide range of fiber diameters is obtained. It is worth mentioning here that Theron et al. [39] showed the relation between flow rate and electrical current. They demonstrated that by increasing the flow rate, the electric current simultaneously increases, and the surface charge decreases.

#### Effect of distance and needle diameter

The needle to collector distance determines the fiber diameter and morphology, depending on at which stage the fibers are deposited. The morphology of the fibers can be affected by the evaporation rate, the deposition time, and the instability stages. For having smooth and defect-free fibers a critical distance should be selected, in which the fibers beforehand have undergone enough stretching and

elongation. However, in general studies on the effect of the working distance resulted in different conclusions: either increasing the distance leads to decreasing the fiber diameter or there is no effect [40].

### Effect of polymer concentration and solution viscosity

Basically, the electrospinning process relies on the stretching of the electrified charged jet of polymer solution/melt. In case of polymer solutions, the concentration plays a crucial role. Low concentration (below a critical value) cannot provide the required chain entanglements during the jet flying time and as a result fragmented and defective fibers instead of uniform continuous fibers are obtained. Increasing the concentration (above the critical value) hampers the flow of polymer liquid and consequently prevents the electrospinning or ultimately results in defective and beaded fibers. Likewise, viscosity of the solution/melt affects the morphology of electrospun fibers. By increasing viscosity up to a critical value, round-shaped beads (in solutions with low-viscosity) turn into the ellipse-shape fibers and ultimately to beadless smooth fibers (sufficient viscosity). Depending on the polymer type, the required viscosity can be varied: for instance, PEO ( $M_w=1450000$  g/mol) can be electrospun into smooth fibers by solution viscosity of 8-40 dPa s, while for a polymer with different molecular weight the range of effective viscosity changes. Therefore, using a parameter defining the required concentration, or viscosity, and molecular weight is essential. In this regard, chain entanglement is a parameter that can significantly affect the fiber formation during the electrospinning. Shenoy et al. [41] in their study investigated the role of chain entanglement number ( $n_e$ ) in fiber fabrication. In a polymer melt, at a certain critical molecular weight ( $M_c$ ), the overlapping of the chains is initiated; in this regard the physical bonds act similarly to the chemical covalent bonds and crosslinks. The entanglement molecular weight ( $M_e$ ), which refers to the average molecular weight between the junctions, can be obtained by viscosity or plateau modulus or steady-state compliance measurements. Analogously, in a polymer solution, below the critical concentration value, chains are not overlapping leading to no chain entanglement. During the electrospinning process, the chain entanglement in a sufficiently concentrated solution ( $\geq$  critical polymer concentration) provides the jet stability/continuity by preventing the jet breakdown. By defining the solution/melt  $n_e$  as the ratio of polymer molecular weight ( $M_w$ ) and  $M_e$ , one can predict the electrospinnability of a solution/melt. Accordingly, for a concentrated solution, the chain entanglement number can be determined by the polymer volume fraction ( $\phi_p$ ) of a polymer melt (validated by experimental observations). For instance, **Figure 2-9** displays the calculated entanglement number for polystyrene (PS) with different molecular weight (i.e., 50k, 100k, 190k and 300k) and varied solution concentrations, with three morphology regimes (meaning beads, bead and fibers, fibers only). At  $n_e \geq 2$ , the change in morphology takes place, in fact,  $n_e$  equal to 2 means that for two involving chains there are two entanglements (or one entanglement per each chain).

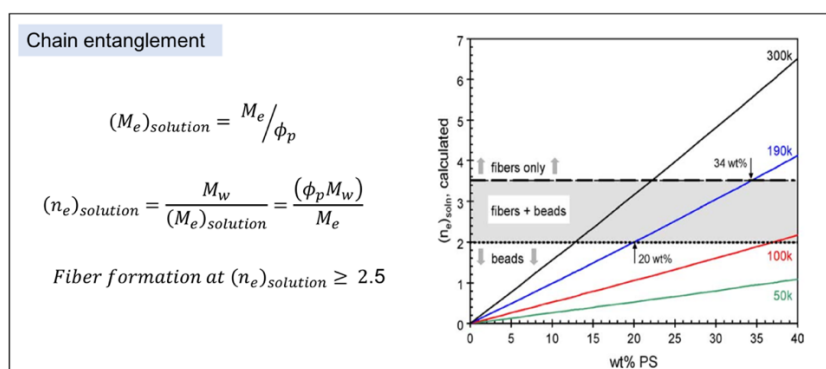


Figure 2-9 The chain entanglement number equation for solution and the plot of the calculated entanglement number  $n_e$  versus the concentration of PS in THF solvent, with three different morphology regimes during the electrospinning process [41]

### Effect of solution conductivity

Solution conductivity, as another important solution/melt parameter, affects the Taylor cone formation and also the fiber morphology and diameter. Similar to other parameters involved in the electrospinning process, the solution conductivity has an effective window. Increasing the conductivity of the solution (above a minimum critical value) leads to the increase of the number of charges on the surface of the droplet, favoring the Taylor cone formation and subsequently higher stretching and elongation of the polymer jet. Increasing the conductivity beyond a maximum critical value can hinder the electrospinning process. In general, the conductivity of the polymer solution can be tailored by addition of additives such as salts. Addition of the salts, in one hand, increases the number of ions leading to higher charge mobility and surface charge density, and in another hand, increases the conductivity of the polymer solution. Increasing the polymer liquid conductivity leads to the decrease in electrostatic forces (acting against the surface tension) along the droplet surface and adversely affect the Taylor cone formation. The addition of the salts has been shown to result in fiber formation with smaller diameter [40].

Accordingly, spider net can be considered as another phenomenon during electrospinning that can arise by internal modification of the polymers by addition of strong salts (e.g., NaCl, KBr, CaCl<sub>2</sub> and H<sub>2</sub>PtCl<sub>6</sub>) [42,43]. When ions are present in the polymer solution or in case of cationic polymers such as chitosan, the netting between main fibers due to the ions can take place. In fact, different charges due to the ions distributed in the solution generate electric poles leading to formation of joints between the main fibers. Actually, the formation of the joints become vital to keep the ionic balance [43].

### Role of solvents

The solvent selection in the solution electrospinning is indeed a key factor for fabricating defect-free and smooth fibers. Two primarily concerns in selecting a solvent are: first, the selected solvent should fully solubilize the polymer, and second, the solvent should be sufficiently volatile (the solvent evaporation directly



depends on the vapor pressure of the polymer). Too volatile solvents might result in fast evaporation of the solvent even at the tip of the needle hindering the electrospinning process. Expectedly low volatile solvents lead to the deposition of wet fibers on the collector. Using a solvent system composed of more than one solvent has been practiced for different polymers. For instance, using a bicomponent solvent system with different evaporation rates permits the production of highly porous electrospun structures, while another possibility is to use a solvent providing the required evaporation rate, and another one playing a role in the conductivity of the whole solution.

#### Effect of humidity and temperature

Humidity, which is generally reported as relative humidity (RH) (depending on the temperature and air pressure), can affect the electrospinning process by influencing the solvent evaporation rate or the solidification rate, leading to different fiber structures. During the electrospinning process, evaporation takes place in two zones of electrospinning, in vicinity of the needle and solution reservoir and during the whipping motions, by diffusion and convection, respectively. During the second evaporation phase (during the bending instability phases), the longer pathway, higher jet velocity and accordingly higher air velocity favor the evaporation. In this regard, humidity can slow down the evaporation of the solvent, particularly when hydrophilic polymers are used in aqueous solution. Consequently, the solidification rate decreases, and fibers can undergo higher elongation and stretching. Inversely, in case of hydrophobic polymers, the increase in humidity leads to faster solidification.

Tripatanasuwana et al. [44] systematically investigated the ambient parameters, meaning humidity and temperature, on fiber diameter and morphology. The experiments were carried out in a closed chamber by controlling the humidity and the temperature. It was shown that solidification and solvent evaporation rate affect the fiber morphology and diameter. Increasing the humidity led to decreasing fiber diameter of PEO (as a hydrophilic polymer): by slowing down the evaporation, smaller diameters were obtained. Increasing the humidity above a threshold led to beads formation on thinner fibers.

Pai et al. [45] in their study investigated the effect of humidity on PS (a hydrophobic polymer) electrospinning when DMF was used as solvent. It has been demonstrated that at higher humidity, the solidification of PS was faster (because the water absorbed from the air into the jet acts as a non-solvent for PS) and for instance at RH 24% smooth fibers were obtained. While at lower humidity (at RH 15% and lower), the solidification was delayed and as a result wrinkled or collapsed structures (composed of both fibers and beads) were obtained. The origin of the wrinkles can be due to the evaporation of the solvent from the core of the jet and consequently buckling of the polymer jet shell under compressive radial stress or from the contraction from the axial tensile stress as a result of continuous stretching.

## 2.1.4 Types of electrospinning process

In addition to the most common solution electrospinning, in which a polymer solution is processed and the solvent evaporates during the flying of the jet towards the collector, other types of electrospinning have been developed, and they are briefly described in the following.

### Melt electrospinning

Electrospun fibers can be directly obtained from polymer melt specially for polymers that are poorly soluble, for instance polyethylene (PE) [46] or polypropylene (PP) [47] can be named.

Upon melt electrospinning, the polymer should be in its molten state in the spinneret, and subsequently a heating device such as an electrical heating tape, a circulating fluid, or a laser is necessitated (**Figure 2-10**). In the course of electrospinning, electrified molten polymer jet accelerates towards the collector and during this journey, it cools down and solidifies and it is deposited as solid fibers.

In general, the polymer melt exhibits lower electrical conductivity with higher viscosity. Due to the lower conductivity leading to lower surface charge density, together with higher viscosity and the absence of the solvent, the bending and whipping instabilities are mainly suppressed in melt electrospinning and the stretching is not taking place like in solution electrospinning. The depositing fibers in melt electrospinning do not experience the repulsion by the former deposited fibers, and in general the placement of fibers on the collector is more predictable than in solution electrospinning; this makes the melt electrospinning a suitable approach for direct write techniques [48].

Melt electrospinning is advantageous over solution electrospinning also thanks to its much higher throughput and to the fact that excluding the use of solvents is a greener process. However, more complicated setups and larger fiber diameters are restricting factors for melt electrospinning. Additionally, long term exposure to heat can lead to polymer degradation and generally this method is not applicable to biomolecules, proteins and thermally unstable polymers.

In order to develop and facilitate the melt electrospinning process, particular configurations can be utilized; for instance, melt electrospinning can be conducted in a way that the polymer with a high melting temperature is locally melted at the tip of the needle with a laser-heating device (e.g., CO<sub>2</sub> laser beam), without experiencing long-term heat exposure to high temperature [49,50]. Additionally, by adding additives in order to reduce the polymer melt viscosity, the fiber diameters can be reduced (**Figure 2-10**) [51]. The fiber diameters can be optimized also by tuning the electrospinning parameters, such as flow rate, applied voltage and spinneret-to-collector distance, and by modifying the melt temperature, the temperature of surrounding and using a moving collector. For example by heating the air around the jet, it cools down slower and thinner fibers up to 20 times can be obtained [52].

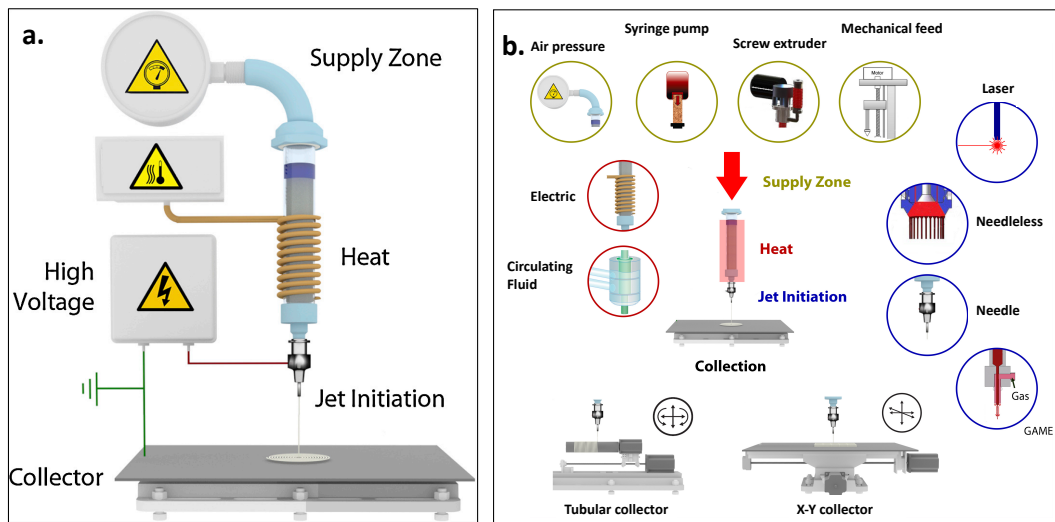


Figure 2-10 a. Melt-electrospinning setup; b. various process parameter in designing of the melt-electrospinning setups [ 56]

### Suspension and emulsion electrospinning

Suspensions are made of dispersion of solid particles in a liquid (mainly water). Polymer suspensions can be directly obtained by emulsion or mini-emulsion polymerizations or by dispersion of almost any water insoluble polymer in water. Accordingly, suspension electrospinning refers to the electrospinning of aqueous dispersions (latexes) of water insoluble polymers. Thus, suspension electrospinning when water is the continuous phase is an interesting approach that allows to reduce concerns regarding safety, toxicology, and environmental problems, in addition, it also overcomes the restrictions of too high polymer concentrations of polymer solutions. In general, for conducting a successful suspension electrospinning, a small quantity of an electrospinnable water soluble polymer (few wt.% with respect to latex part), acting as a template, is required and can be subsequently removed (**Figure 2-11**).

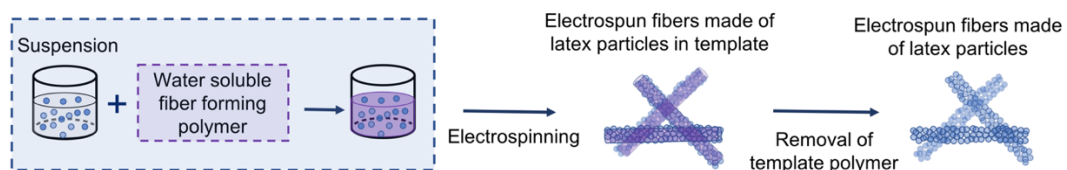


Figure 2-11 Schematic illustration of the suspension electrospinning

Emulsions are mixtures of two or more immiscible liquid: liquid droplets are distributed in a continuous liquid phase. Emulsion electrospinning is another interesting approach used for insoluble and non-melting polymers/compounds [53]. In contrast to suspension electrospinning, in emulsion electrospinning an immiscible liquid is dispersed as droplets into a polymer solution [54], which is the continuous phase. As shown in **Figure 2-12**, first the water/oil emulsion is formed, then a fiber forming polymer is dissolved in it, and finally the electrospinning of the

emulsion is conducted. The rheology and stability of the emulsion as well as its concentration and viscosity are the key factors in emulsion electrospinning. Depending on the materials employed, on the droplet size and on the process parameters, different morphologies of electrospun fibers can be obtained, such as bead-on-string, core-shell, or co-continuous two-phase structures. Emulsion electrospinning is a suitable approach to obtain polymer-based fibers with application in controlled drug release, encapsulation of different biologically active compounds, cell scaffolds, food packaging, enzyme immobilization and formation of nanotubes, and nano-fluidics [55].

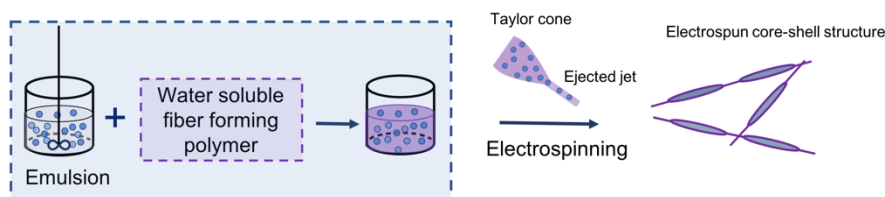


Figure 2-12 Schematic representation of emulsion electrospinning

### Oligomer electrospinning

Another interesting approach is the electrospinning of the monomers/oligomers and their *in-situ* polymerization/crosslinking as a jet flying toward the collector. Both thermally- and photo-induced reactions can be applied. For instance, He et al. [56] prepared electrospun fibers using PU precursors and low molecular weight polyethylene glycol chain extenders (PEG-400) subjected to melt electrospinning; upon jet extension the thermal radiation was applied leading to the PU polymerization and as a result PU fibers were fabricated. In another work, Shanmuganthan [57] coupled the electrospinning and *in-situ* photopolymerization of thiol-ene monomers. In this work a photo-curable formulation containing a multifunctional acrylate, a tetrafunctional thiol, and a photoinitiator was used for *in-situ* photopolymerization during electrospinning under ambient condition without using solvents or heat.

Indeed, the oligomer electrospinning becomes more appealing when the solvent is excluded from the process and the polymerization reaction is photo-initiated, which means a low-energy consumption and a process occurring at ambient temperature. [58,59]. The literature on the coupling of electrospinning and photo-induced reactions is reported in detail in Section 2.3.

### **2.1.5 Electrospinning setups**

Electrospinning can be conducted in both far-field mode and near-field mode. As explained above, polymer jet undergoes several stages (i.e. straight-line regime, stretching, whipping regime, ...) before deposition on the collector: the working distance determines at which regime fibers are collected. Typically, electrospinning is carried out in far-field mode with the working distance higher than 5 cm, consequently fibers are deposited as nonwoven mat after undergoing several

instability stages. Conversely, deposition in straight line regime can be called the near-field electrospinning. In this case, the working distance is reduced to the range 500  $\mu\text{m}$ -5 cm. In the near-field electrospinning the lower supply voltage and control over the fiber deposition location are advantageous. The precise location of deposition of nanofibers makes it a tool for direct-write processes. Expectedly, when fibers are not subjected to bending instabilities, the diameter of fibers are larger than those obtained with the far-field mode [60–62].

Electrospun membranes can be fabricated from multiple needle setups. Consequently, the throughput can be multiplied by the number of jets that are simultaneously generated. Although, the Coulombic repulsion and distribution of electric field greatly depend on needles configuration, spacing between them and number of needles. In order to obtain stable jets from all the needles, considerations should be taken into account, otherwise critical voltage may not be achieved for some needles to form the liquid jet [63].

Coaxial spinneret can be designed by inserting a thinner needle inside a large needle. Then two syringe pumps are used to provide the suitable flow rates for two separate liquids in the inner and outer needle. When the two liquids meet at the tip of the needle, the outer liquid wraps the inner liquid. At a certain voltage, the compound Taylor cone is formed, and the core-sheath structure is ejected from the needle. Coaxial electrospinning is a complicated setup and material selection as well as process parameters need careful adjustment and considerations [64–66]. In a successful coaxial electrospinning, the inner and outer fluids form a stable compound jet and stay together. Hence, sufficient viscosity and adequate miscibility are two important factors to achieve a continuous jet and a core-shell structure. Two miscible fluids cannot hold the core-shell structure due to their mixing. Coaxial electrospinning is a method to encapsulate unspinnable liquids as a core in a shell of an electrospinnable liquid [67], or vice versa [68].

In general, the electrospun fibers are deposited on a grounded solid collector that can be stationary or movable. A variety of stationary collectors with specific shape, structure and patterns for controlled deposition of fibers have been developed [69]. For instance, a collector can be designed in a way to exhibit heterogeneous conductivity by having both metal and insulator parts in the structure. Therefore, fibers tend to deposit on metal or conductive parts [70]; the insulator parts can act as a mask. For having aligned fibers, the collector can have an airgap between two conductive compartments [71].

The collector can be designed as a moving stage (in XY coordinates) for controlling the deposition of the fibers. Rotating collectors, in form of mandrel, wire, disc, drum, wheel, conveyor, and cone [72], offer a simple method for aligned fiber fabrications (**Figure 2-13**).

Another class of collectors is represented by liquid bath collectors, which can contain insulating or conductive liquids. The water vortex for preparing yarns made of electrospun fibers [73] or the flowing liquid for the fabrication of bundled nanofibers [74] can be named as different types.

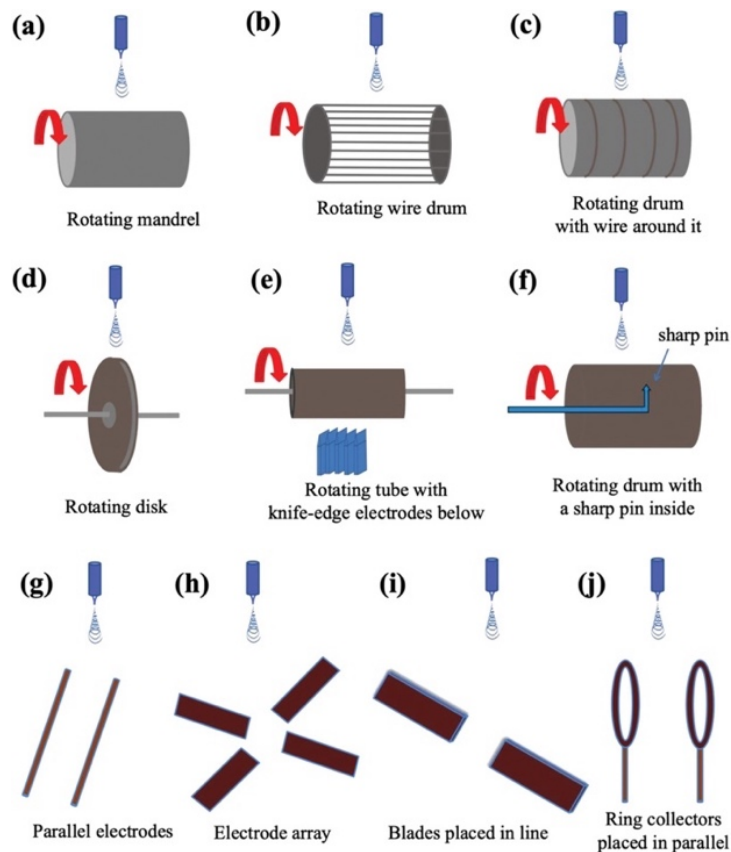


Figure 2-13 Schematic diagrams of rotating collectors for electrospinning. Blunt collectors: a) mandrel, b) wire drum, and c) drum with wire around it. Sharp edge collectors: d) disk, e) rotating tube collector with knife-edge electrodes (to induce more alignment on the tube collector) below, and f) rotating drum with a sharp pin (to fabricate arrayed fibers) inside it. Parallel collectors: g) parallel electrodes, h) electrode array, i) blades placed in line, and j) ring collectors placed in parallel (placed between the tip of the needle and the collector to control the surrounding electrical field in which the traveling jet pass through) [75].

### Electrospun fibers morphology

Depending on the electrospinning setup used, the fiber morphology can be tailored in the form of aligned, porous, core–shell, beaded, hollow structure, ribbon, rough, cactus-shape, decorated by nanoparticles or nanorod as shown in **Figure 2-14**, the selected electrospinning configuration can yield unique fibrous morphology, for example innovative spinnerets (e.g., simple needle versus coaxial spinneret, multiple needles or needleless electrospinning) or diverse types of collectors (e.g., rotating drum or disc, airgap [71], liquid bath collector, collectors equipped with a heating device particularly for porous structures) are utilized by several research groups to fabricate unique fiber structures [7,76].

Additionally, electrospun fibers can be further modified by post-modification. The fibrous membranes can be subjected to chemical or physical modifications (e.g., surface coating, thermal treatment, mechanical drawing, UV curing, vapor deposition, plasma treatment) in order to improve their properties or addition of other functionalities [76].

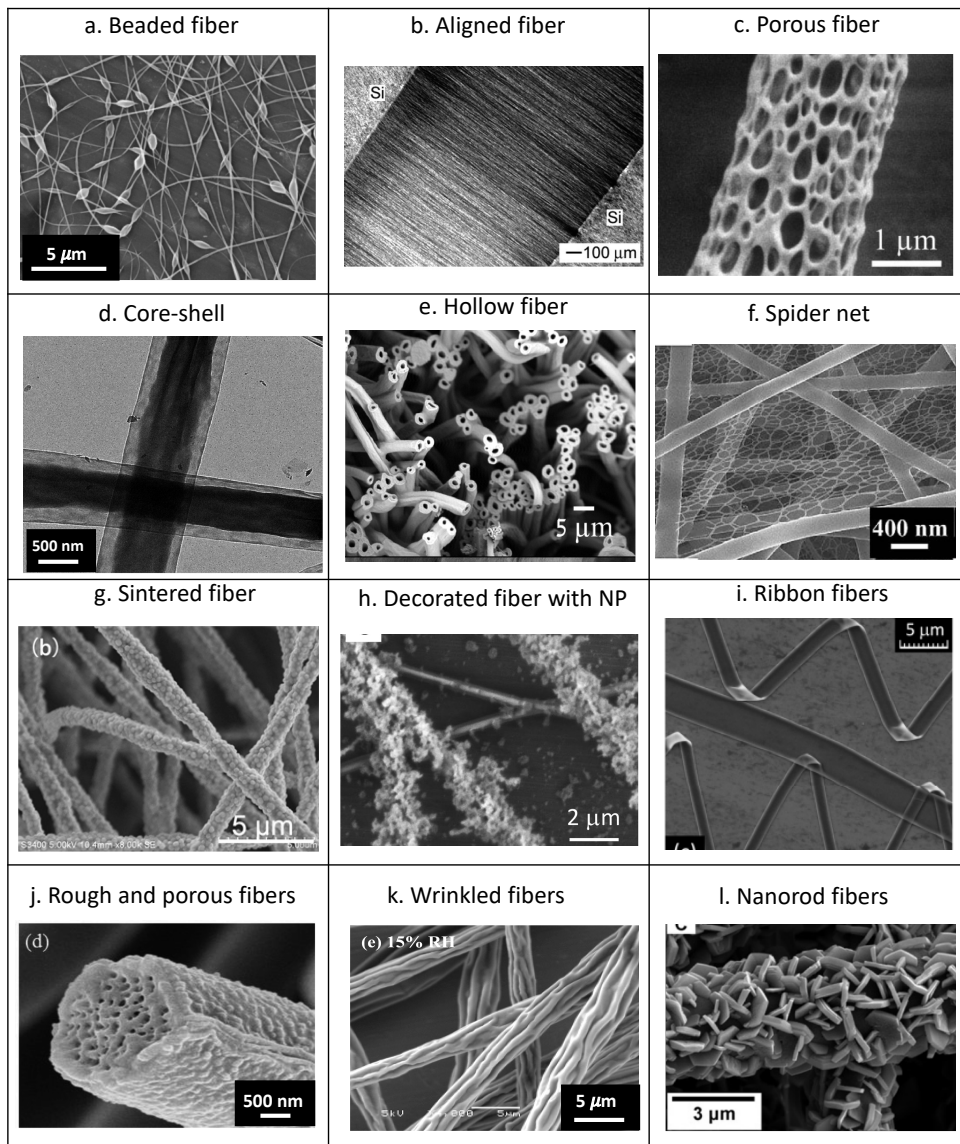


Figure 2-14 Microcopy images of: a. PEO beaded fibers [18], b. poly(vinyl pyrrolidone) (PVP) aligned nanofibers collected across an airgap between two silicon strips [71], c. PLA porous electrospun fibers obtained by binodal phase separation [77], d. co-axial electrospun fibers of PVDF and Teflon Amorphous Fluoropolymer in core and sheath, respectively [78], e. hollow fibers of PVDF-HFP and PVP, where PVP is deposited on the inner wall of the PVDF-HFP shell [79] f. spider-net in electrospun nylon 6 nanofiber mat containing NaCl [43], g. polytetrafluoroethylene (PTFE) electrospun fibers obtained by PTFE/PEO blend electrospinning and subsequent sintering [80], h. electrospun nanofibers of ionomer with catalyst nanoparticles (NP) separately electro-sprayed onto them [81], i. electrospun fibers of polyvinylpyrrolidone/ammonium metatungstate (PVP/AMT) with a ribbon shape [82], j. PVDF cactus-like fibers (rough and porous) [83], k. wrinkled fibers of PS obtained at relative humidity of 15% [45], l. electrospun fibers of ZnO/TiO<sub>2</sub> on TiO<sub>2</sub> fibers obtained by calcination and ZnO nanorods [84]

## 2.1.6 Materials subjected to electrospinning

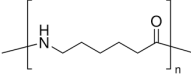
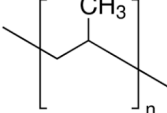
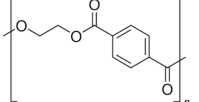
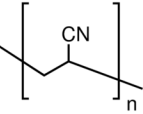
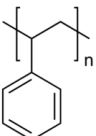
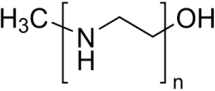
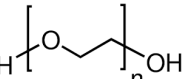
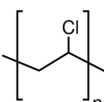
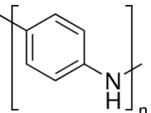
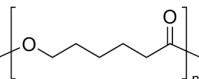
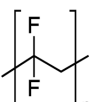
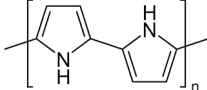
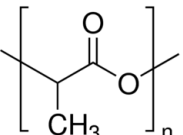
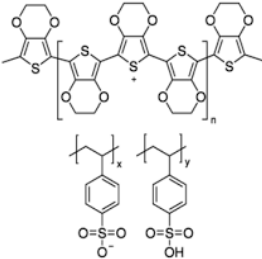
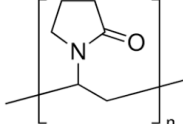
Electrospinning process can be applied to a number of different polymers, both synthetic and natural. The selection of the polymer for the electrospinning process is mainly based on the final application of the fibrous mat. The most frequent studies in electrospinning field are conducted on applications for tissue engineering scaffolds, biomaterials, cell adhesion and drug delivery systems: for these applications, polymers such as polycaprolactone (PCL), polylactic acid (PLA) or poly(lactic-co-glycolic acid) (PLGA) as well as natural polymers such as silk

fibroin, fibrinogens, collagen, gelatin, chitin, chitosan and also super-biomolecules such as DNA or peptides are used. The second most studied field in electrospinning is associated to filtration (water or air) and water/oil separation; electrospun materials generally used for these applications are polyacrylonitrile (PAN), polyvinylpyrrolidone (PVP), polystyrene (PS) and polyvinylidene fluoride (PVDF). Then applications in Li-ion batteries and energy storage devices can be seen, employing polymer materials such as PEO or PVDF.

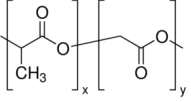
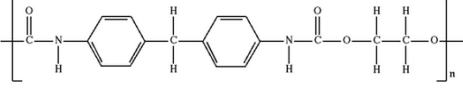
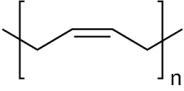
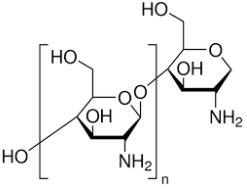
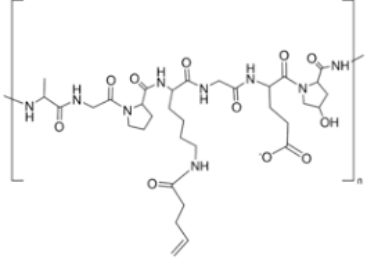
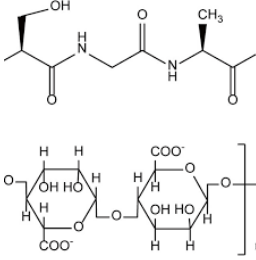
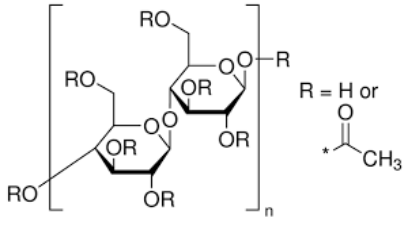
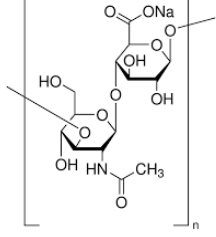
Interestingly, PCL and PS electrospun nanofibers are subjected to commercial applications. For instance, 3D Biotek (New Jersey, USA) produces biodegradable PCL nanofibers that has been used in various FDA approved devices such as implants, drug delivery devices, and suture.

A list of the most studied polymers for electrospinning is reported in **Table 2-2**.

Table 2-2 The most studied polymeric materials for electrospun fiber fabrication

<p><b>Polyamide 6 (Nylon-6)</b> [85]</p> 	<p><b>Polypropylene (PP)</b> [86]</p> 	<p><b>Polyethylene terephthalate (PET)</b> [87]</p> 
<p><b>Polyacrylonitrile (PAN)</b> [88]</p> 	<p><b>Polystyrene (PS)</b> [89]</p> 	<p><b>Polyethylenimine (PEI)</b> [90]</p> 
<p><b>Polyethylene oxide (PEO)</b> [91]</p> 	<p><b>Polyvinyl chloride (PVC)</b> [92]</p> 	<p><b>Polyaniline (PANi)</b> [93]</p> 
<p><b>Polycaprolactone (PCL)</b> [94]</p> 	<p><b>Polyvinylidene fluoride (PVDF)</b>[95]</p> 	<p><b>Polypyrrole (PPy)</b> [96]</p> 
<p><b>Poly(lactic acid) (PLA)</b> [97]</p> 	<p><b>poly(3,4-ethylenedioxythiophene) polystyrene sulfonate (PEDOT:PSS)</b> [98]</p> 	<p><b>Polyvinylpyrrolidone (PVP)</b> [99]</p> 



<p><b>Poly lactic-co-glycolic acid</b> <b>PLGA</b> [100]</p> 	<p><b>Polyurethane (PU)</b> [101]</p> 	<p><b>Polybutadiene (PB)</b> [102]</p> 
<p><b>Chitosan</b> [103]</p> 	<p><b>Gelatin</b> [104]</p> 	<p><b>Silk fibroin</b> [105]</p> 
<p><b>Collagen</b> [106]</p>	<p><b>Cellulose acetate</b> [107]</p> 	<p><b>Hyaluronic acid</b> [108]</p> 

In recent years, electrospinning has also been utilized to form fibrous structures beyond polymers, including novel carbon materials (by carbonization of polymeric nanofibers for preparing highly conductive carbon fibers), multi-metallic alloys (by using electrospun fibers as template and applying carbothermal shock) or inorganic particle-decorated fibers [109].

### Blends and multicomponent fibers

In addition to the choice of an appropriate setup configurations, tailoring the polymeric material used in electrospinning can also bring to new functionalities and properties. For instance, electrospinning blends of polymers can optimize the properties of the final product as well as facilitate the processability and versatility. One main requirement for blends is that the components have to be fully or partially miscible [110]. In many studies the blend electrospinning is conducted in order to produce electrospun fibers from non-electrospinnable or challenging material by help of an easily electrospinnable polymer such as PEO or PVA, for instance for electrospinning of chitosan or cellulose acetate this method has been reported [111,112].

Moreover, bicomponent fibers with a combination of properties of both components can also be fabricated by a side-by-side electrospinning setup, as designed by Gupta et al. [113], in which two polymer solutions (e.g., PVC and PVDF solutions) can be simultaneously and closely electrospun from a single

syringe divided into two compartments. Each polymer solution present in one of the syringe compartments receives the specific required voltage, the two polymers come in contact at the tip of the needle, and a single bicomponent jet or two separate jets can be formed depending on the working distance.

### Composite fibers

Thanks to the versatility of the electrospinning technique, preparing composite fibers particularly by adding sol-gel precursors or nanoscale compounds is feasible, and accordingly composite formulations have been extensively studied especially for solution electrospinning. Expectedly, for sol-gel precursors, the sol-gel reactions should be initiated during the jet flight time and not in the stock solution. The nature of sol-gel precursor, the type of carrier polymer, the electrical conductivity and the viscosity of the solution are important factors determining the outcome of the electrospinning [114]. In this regards, Li and Xia [114] prepared composite fibers of PVP and TiO<sub>2</sub> by using titanium tetraisopropoxide as titania precursor in electrospinning: the process was followed by calcination in air at 500 °C. This approach can also be used to produce ceramic nanofibers by solution electrospinning of a polymer carrier and ceramic precursors, followed by calcination phase in order to form the ceramic component and at the same time remove the organic phase. PVP, PVA and PEO are frequent carriers for such systems, for preparing ceramic nanofibers made of Al<sub>2</sub>O<sub>3</sub> [115], CeO<sub>2</sub> [116], Fe<sub>2</sub>O<sub>3</sub> [117], ZnO [118], ZnS [119], BaTiO<sub>3</sub> [120] and many more [121].

Moreover, composite fibers can be prepared by dispersing the nanoscale additives into the electrospinning formulation through extensive agitation or ultrasonication. The most studied nanofillers are nanoparticles such as Ag [122], Au [123], TiO<sub>2</sub> [124], SiO<sub>2</sub> [125], one dimensional structures such as nanorods or carbon nanotubes [126], and two-dimensional nanostructures such as graphene nanosheets [127].

### 2.1.7 Applications

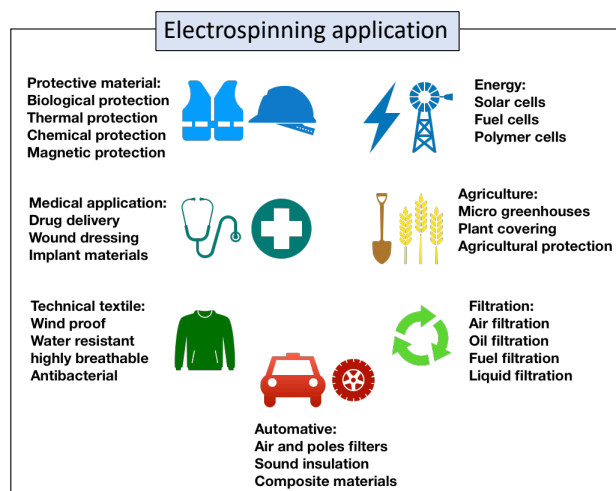


Figure 2-15 Potential applications of electrospun membranes

Thanks to the electrospinning versatility and the electrospun membrane properties, including large surface area to volume ratio, high porosity, presence of interconnected pores, high flexibility and lightweight, electrospinning is attractive for several applications (**Figure 2-15**), such as biomedical applications (including tissue regeneration applications, drug delivery systems, wound healing, cancer research) [128–134], filtration (e.g., water treatment, air purification) [135,136], energy (e.g., energy storage, rechargeable batteries, supercapacitors, dye-sensitized solar cells) [137–145], catalysis [77], textile (e.g., protective clothing, smart sport wear) [86,146], sensing (e.g., pH responsive, thermo responsive, electro-active, light sensitive membranes) [147–154], and many more [90–92].

### 2.1.8 Scaling up

One of the main drawbacks of the electrospinning process is its upscaling issue. The main throughput of conventional electrospinning setup for a long time was limited to the laboratory scale for research purposes. Electrospun fibers with particular material compositions, functionalities, tunable morphologies, peculiar shapes and very fine diameters were limited to the academic research scale, made feasible by using only milliliters of polymer solution with a very slow production rate (0.1-5 ml/h). However, exploring the leading potential of this technique for industrial application has now drawn great attention [72]. Nowadays, the upscaling of the electrospinning process is more and more subjected to commercial investigation and investments. The mass production of electrospun fibers is basically based on the increasing of the jet number, for which multiple needles setup, needleless electrospinning, centrifugal spinning and hybrid electrospinning display great potential. For instance, Bioinicia (Valencia, Spain) is the first company which dealt with large scale production of electrospun membranes, particularly for the pharmaceutical industry. Likewise, INOVENSO Technology (Istanbul, Turkey) developed an open surface industrial electrospinning machine for the fabrication of commercial fibrous products, especially for air-filtration and pharmaceutical applications, with significant higher throughput. For instance, INVENSO claimed a production rate of few meters per minute (i.e., TPU with flow rate of 1200 ml/h and production rate of 5.3 m/min), which can be revolutionary in the electrospinning process. Other well-known companies that offer a variety of technological solutions to large scale production of electrospun products, with main focus in pharmaceutical, filtration, wound dressing and biomedical applications, are Nanoflux (Singapore), NanoNC (Seoul, Korea), Progene Link Sdn Bhd (Selangor, Malaysia), SKE Research Equipment (Bollate, Italy), ANSTCO (Tehran, Iran) [158]. Correspondingly, in this particular era due to COVID19 pandemic that the face masks are turned into an essential part of our life, E-SPin NanoTech Pvt. Ltd. (Uttar Pradesh, India) produced N95/N99 technology face mask and surgical mask from electrospun nanofibers. Other examples of commercial products are surgical implants and wound treating products and patches by Biotronic (Berlin, Germany) or patches by Bioinicia (Valencia, Spain).

## 2.2 Photo-induced reactions

Inspired by nature which is powered by the energy in the form of light radiations from the sun, photochemistry is exploring the light as a driving force in organic chemistry and related fields. Photochemistry is based on the interactions of chromophore species with the photons produced by applying light: light absorption triggers the molecules to enter their excited states, which can then undergo a variety of processes to reach more energetically stable states (**Figure 2-16a**), consequently leading to changes in the molecule reactivity and properties. Briefly explaining the photo-induced reactions, initially the photon absorption by a photo-active agent induces an electron transfer from a ground state ( $S_0$ ) to its excited singlet state ( $S_1$ ). The excited singlet state can have two ends: either it can be deactivated to return to the ground state by emission of fluorescent light or by heat dissipation (in this case the photochemical process does not occur), or it undergoes intersystem crossing (ISC) to enter its triplet state ( $T_1$ ). Similarly,  $T_1$  either is deactivated to the ground state by phosphorescence emission or undergoes ISC leading to various photochemical reactions (**Figure 2-16b**). The primary photochemical reactions are isomerization, bond forming and bond breaking reactions (**Figure 2-16c**) [59,159,160].

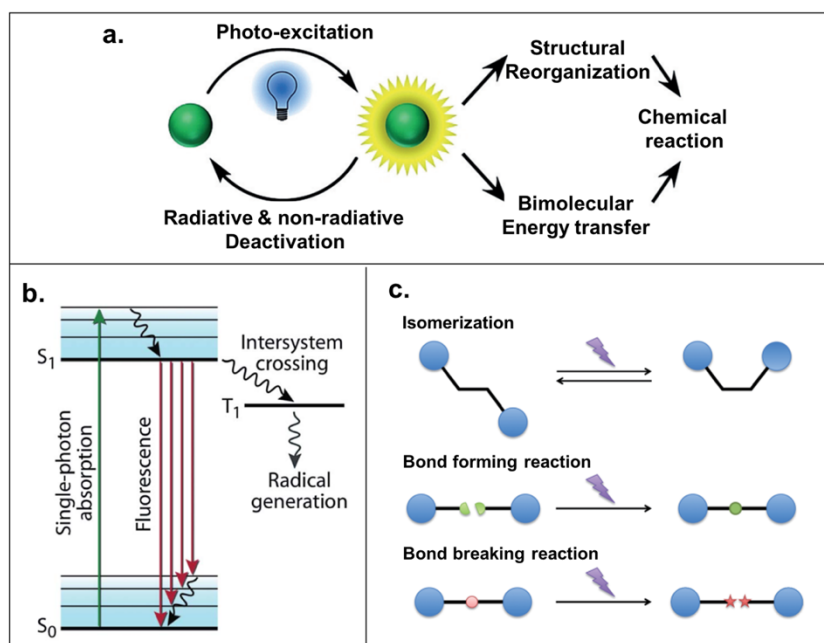


Figure 2-16 Schematic illustration of a. chromophores photophysical and photochemical reaction as a result of photoexcitation [59], b. the Jablonski diagram., showing that the singlet state  $S_1$  by intersystem crossing can enter the triplet state  $T_1$ , which can trigger photochemical reactions [160,161], c. the primary photochemical reactions including the isomerization, bond forming reaction and bond breaking reaction [59].

One of the common uses of light in photochemistry is the induction of polymerization reactions. Light as a driving force for polymerization has numerous advantages which are of high importance and privilege over analogous methods (e.g., thermal processes). Three principal characteristics, meaning initiation at ambient conditions, temporal control and spatial control, make light-triggered

polymerization reactions distinctive. Reactions that are not readily realized in a reasonable timescale at ambient condition due to the lack of sufficient energy overcoming the activation energy, can rapidly occur by using appropriate light sources. Then, the temporal control, which is simply possible by turning off and on the light, makes this approach more desirable for chemical reactions. In fact, most of photo-induced radical polymerization, isomerization and cyclization reactions are stopped immediately after removing the light source. Finally, the spatial control is possible by irradiating only selected areas (e.g., using masking or patterned illumination systems), making the light-induced reactions even more favorable. Moreover, photo-induced reactions are generally bulk processes, thus avoiding the use of solvents or toxic compounds: this make them environmentally friendly [162–165].

Photoinduced polymerization reactions consists of three main stages: production of the reactive species upon irradiation and initiation step, propagation, and termination. Basically, a photochemical reaction can occur only if light has been absorbed by the medium. Since most of the monomers are transparent to UV irradiation, the initiation of the polymerization reaction cannot be triggered without an initiating species [160,166]. Hence, the introduction of a photoinitiator to the formulation is a must in order to absorb the incident light and generate the initiating species, which can be free radicals or ions [167–172]. Photoinitiators in photo-induced polymerization play a very crucial role [173]; these molecules by absorbing photons can initiate the chain processes, and through their absorbance characteristics can influence the rate of initiation ( $r_i$ ) and also the depth of the reaction (e.g., depth of cure). The rate of initiation  $R_i$  depends on the incident light intensity ( $I_0$ ), the quantum yield of initiation ( $\Phi$ ) (i.e., the number of absorbed photons translated to the number of initiating species), the thickness of the sample ( $l$ ), the absorption coefficient ( $\varepsilon$ ) and the concentration of the photoinitiator ( $[PI]$ ):

$$R_i = \Phi_i I_0 [1 - \exp(-\varepsilon l [PI])] \quad \text{Eq7}$$

The polymerization rate ( $R_p$ ) can be obtained from the classic equation of polymerization rate as below:

$$R_p = \frac{k_p}{k_t^{0.5}} [M] \left(\frac{R_i}{2}\right)^{0.5} \quad \text{Eq8}$$

where  $[M]$  is the concentration of the monomer or functional groups, and  $k_p$  and  $k_t$  are propagation and termination rate coefficients, respectively. When the reaction is photoinitiated,  $R_p$  can be written as:

$$R_p = \frac{k_p}{k_t^{0.5}} [M] (\Phi I_a)^{0.5} \quad \text{Eq9}$$

where  $I_a$  is the absorbed light intensity ( $= I_0 [1 - \exp(-\varepsilon l [PI])$ ). According to the Beer-Lambert law, the absorbed light intensity is a function of initial incident light intensity, the extinction coefficient and the layer thickness.

The total polymerization rate can be approximately considered equal to the propagation rate.

The termination stage of the polymerization/crosslinking reaction can take place from different routes. During termination, a dead polymer chain which is no longer reactive can be formed by bimolecular combination, disproportionation or

chain transfer. The combination or disproportionation routes lead to the elimination of two reactive species and as a result the process is a second order mechanism with respect to the radicals concentration:

$$R_t = -\frac{d[\dot{P}]}{dt} = 2k_t[\dot{P}]^2 \quad \text{Eq10}$$

where  $R_t$  is the rate of termination,  $k_t$  is the termination rate coefficient (associated to both recombination and disproportionation) and  $[\dot{P}]$  is the radical concentration.

The free radical propagation reactions are often exothermic. As the reaction rate increases with temperature, due to the higher monomer mobility, studying the heat of reaction (i.e., the generated heat flow during the reaction) can reveal useful information regarding the reaction stages [174].

In general, the photoinduced excitation of a photoinitiator containing a chromophore group can lead to the generation of radical or cationic species initiating the polymerization reactions, which can follow a radical polymerization mechanism (e.g., acrylates and thiol-enes) or a ionic (generally cationic) polymerization mechanism (e.g., epoxides and vinyl ethers) [175]. In the following section, the main UV-curable systems are briefly explained encompassing unsaturated polyesters/styrene, thiol-ene and acrylate monomers as photoinitiated free radical polymerization systems and epoxides and vinyl ether as photoinitiated cationic polymerization systems [176].

## 2.2.1 Photoinitiated free radical polymerization

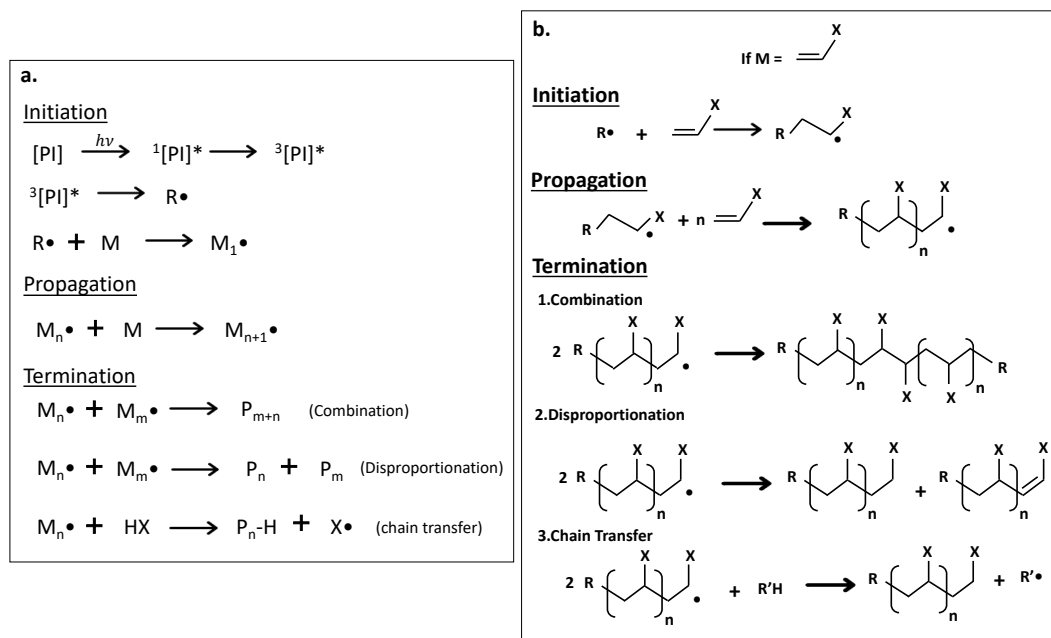


Figure 2-17 a. Schematic representation of free radical photopolymerization including three steps of initiation, propagation and termination, b. example of free radical polymerization of a monomer M containing a C=C double bond.

In general, a free radical photopolymerization reaction consists of three main steps, namely (i) the production of the reactive species upon irradiation and the initiation step of the chain radicals, (ii) the propagation step and (iii) the termination

stage in which the reactive species (primary radicals or secondary radicals) are removed (**Figure 2-17**). Accordingly, three well-known free radical polymerizing systems are unsaturated polyesters/styrene, thiol-ene and acrylate monomers.

### Photoinitiators

Two main types of free radical photoinitiators, are shown in **Figure 2-18**. Free radical photoinitiator systems, which are typically aromatic carbonyl compounds, are classified into two groups: Norrish type I and Norrish type II (**Figure 2-18**). Norrish type I radical photoinitiating systems undergo unimolecular homolytic bond photocleavage to generate benzoyl free radicals. Norrish type II systems instead undergo a bimolecular reaction in which the excited photoinitiator molecule in presence of a second molecule with H-donor characteristics can generate radicals, thus making an hydrogen abstraction [177–179]. A suitable photoinitiator exhibits high absorption in the light wavelength range received from the radiation source and generates a high number of initiating species with the highest possible quantum yields. A variety of radicals photoinitiators are developed, and their photolysis mechanisms are extensively studied [177].

Benzoylphosphine oxides are an important class of Norrish I photoinitiators undergoing a photocleavage from a very short-lived triplet state (< 1ns) resulting in the 2,4,5-trimethylbenzoyl (C-center) radical and diphenylphosphonyl (P-center) radical [180]. This class of photoinitiators have commercial applications for radical curing of resins (e.g., acrylates). For instance, 2,4,6-trimethylbenzoyl-diphenylphosphine oxide (TPO), as shown in **Figure 2-18** undergoes bimolecular cleavage forming benzoyl and phosphinoyl radicals upon UV irradiation (absorbance ~ 300-400 nm); both radicals are reactive and can initiate polymerization reactions. TPO was used in this work for the photoinduced crosslinking of polybutadienes (Chapter 5), as it has been proved to be the most efficient photoinitiator for butadiene systems, both in presence or absence of a crosslinker molecule [181].

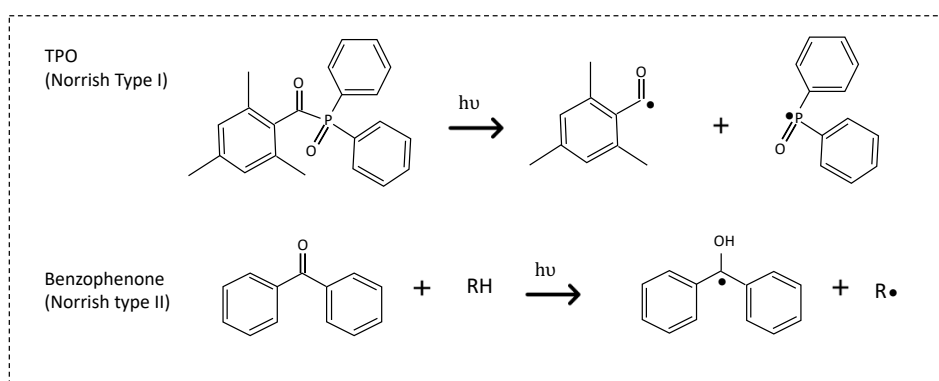


Figure 2-18 Norrish type I (direct photocleavage) and Norrish type II (hydrogen abstraction) radical photoinitiating system

One of the main Norrish type II photoinitiators is benzophenone (BP). BP photochemistry has been first introduced in 1974 [182], and it is particularly known as photoactivable reagent for remote C-H bonds in steroids. Three advantageous

properties of BP are its high stability, its high photosensitivity (also in ambient light) and more importantly its high reactivity with unreactive remote C-H bonds, even in presence of solvents such as water. Consequently, reactions inducing covalent modifications with site specificity become possible in the presence of BP.

Upon irradiation, the absorption of a photon (at  $\sim 350$  nm) by BP leads to the transfer of an electron from a nonbonding  $sp^2$  orbital of oxygen (in the BP chemical structure) to a  $\pi^*$ -orbital of the carbonyl group. Briefly, the mechanism of H-abstraction can be described by three consecutive steps: i) interaction of electron-deficient oxygen (which is electrophilic) by weak C-H  $\sigma$ -bond; ii) abstraction of hydrogen to fill the n-orbital; iii) recombination of the generated ketyl or alkyl radicals to form C-C bond. It is worth noting that also when amines or similar heteroatoms are in the vicinity of the excited carbonyl, an electron transfer step followed by proton-abstraction from an adjacent alkyl group can occur. In the photochemistry of BP, the geometrical accessibility of C-H bonds is one of the controlling factors. The lifetime of excited BP with two unpaired electrons is higher than the singlet one. Then, the lifetime of triplet state in absence of abstractable H is 80-120  $\mu s$ , while in presence of abstractable H can be 100 times shorter. The triplet state can readily return to ground state when well-oriented H-donor species are not present [183]. Interestingly, BP has been found the most effective photoinitiator for the photoinduced crosslinking of PEO polymer, which is the main focus of Chapter 3 and Chapter 4.

### Unsaturated polyesters/styrene systems

One of the first well-known photocurable resins with wide applications consisted of a mixture of styrene and an unsaturated polyester that can bear a fumaric or a maleic structure. Upon UV irradiation in presence of a suitable photoinitiator, a fast copolymerization reaction takes place leading to the formation of an insoluble crosslinked network (**Figure 2-19**).

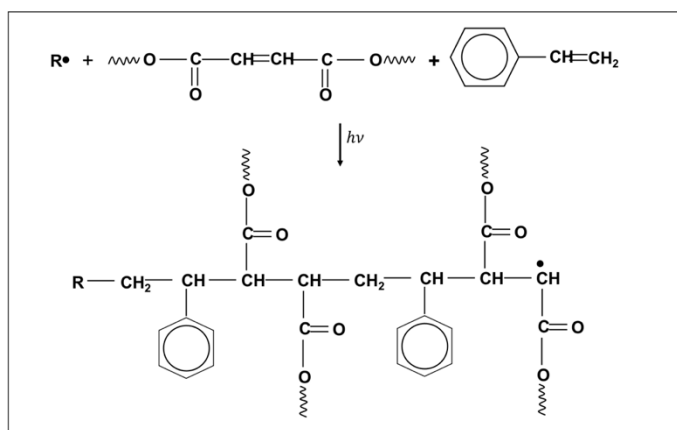


Figure 2-19 Unsaturated polyesters/styrene photoinduced polymerization and crosslinking [176]

### Acrylate monomers

Acrylates are known to be the most reactive monomers in free radical polymerization. The acrylate-based UV curable resins paved their way into many



commercial practices with significant chemical, optical and mechanical properties. The photopolymerization of acrylate-based systems has been extensively investigated [184–186]. An example of the photo-initiated polymerization and crosslinking of an acrylate monomer in presence of a Norrish type I photoinitiator is shown in **Figure 2-20**.

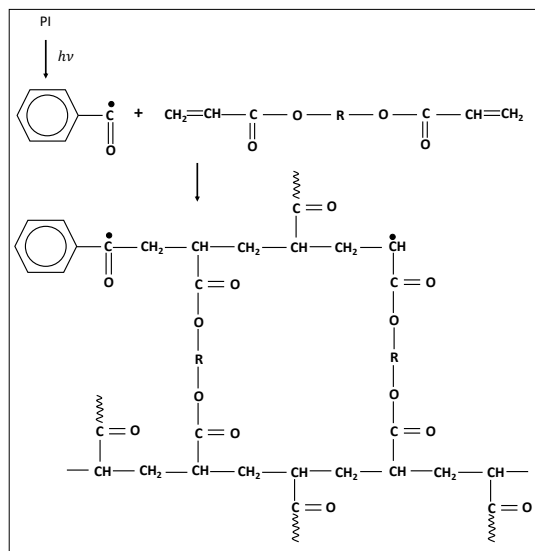


Figure 2-20 Simple example of photopolymerization of an acrylate monomer in presence of a Norrish type I photoinitiator during UV irradiation [176]

Typically, an acrylate formulation consists of a photoinitiator, a telechelic oligomer (i.e., having two reactive end-groups) and a monomer. The oligomer backbone (R) can contain polyurethanes, polyesters, polyether, polysiloxane, and other groups. Generally, the ultimate properties of a UV-cured acrylate-based polymer depend on the initial functionalized oligomer. Low modulus elastomers to glassy and brittle structures (as a result of highly crosslinked systems) can be obtained by tuning the aliphatic or aromatic structure of the oligomer and the crosslinking density. The high reactivity of the acrylic monomers together with the great variety of the functionalized oligomers make this system pioneer in UV-curing applications.

### Thiol-ene monomers

In 2001, click chemistry was first described by Sharpless and his co-workers [187]: inspired from nature's lead, they aimed at the developing and synthesizing of substances by joining small blocks using a heteroatom links (C-X-C). The click chemistry was then defined as a reaction that can be modular and stereospecific, with high yield generating byproducts that can be easily removed. These reactions are insensitive to oxygen and feasible in mild condition without using any solvent or by using benign solvents such as water [187].

Thiol-ene reactions thanks to the weak sulfur-hydrogen bonds and high reactivity towards ene functionality bears all requirements to be termed *click reactions*. Generally, photo-induced thiol-ene polymerization reaction works based on a free-radical chain mechanism in two main steps: first, addition of thiyl radical

(S•) to the carbon of the ene functional group (double bond), then abstraction of the hydrogen atom from a thiol group by a carbon-centered radical to generate a thiyl radical (back to the system). The termination stage takes place as a result of radical-radical coupling (**Figure 2-21**) [188].

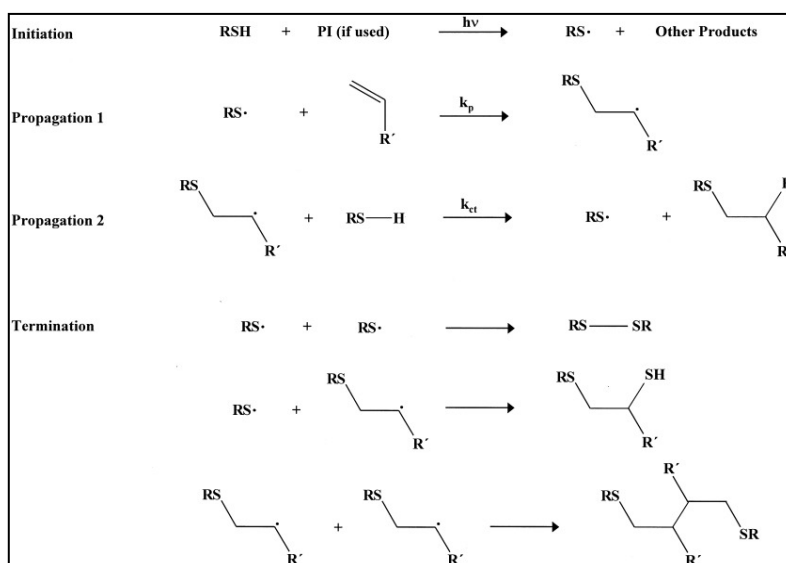


Figure 2-21 General thiol-ene photopolymerization process [188]

Thiyl radical can be generated in presence of both types of radical photoinitiators, as shown in **Figure 2-22**. For a thiol-ene crosslinking mechanism, the thiol and the compound containing the ene (double bonds) should have at least two reactive functionalities (e.g., diene and dithiol). Thiol-ene-type photopolymerization reactions, thanks to their step-growth mechanism, present significant advantages, such as delayed gelation, limited extractables, reduced shrinkage and shrinkage stress, and resistance to oxygen inhibition. The main disadvantages of thiol-ene systems are the unpleasant odor during the reaction and the lack of available materials [188]. Thiol-ene photopolymerization has numerous applications in protective coatings [189], adhesives [190] and photoresists [191].

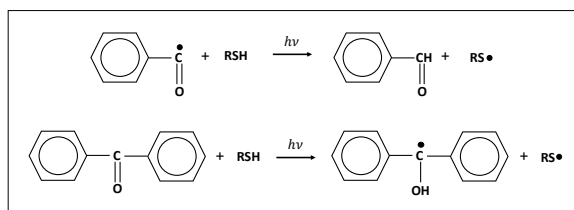


Figure 2-22 Both photoinitiator systems (Norrish type I and II) are used in thiol-ene chemistry

### Oxygen inhibition

Oxygen inhibition is one of the critical drawbacks in free radical photopolymerization systems: oxygen adversely affect the polymerization rate leading to low conversion, short polymer chain length formation and the so-called tacky (not dried) surfaces [192–196]. In fact, the reactive oxygen species (ROS), in particular, the peroxy ( $\text{ROO}\cdot$ ), hydroxyl ( $\text{OH}\cdot$ ), and superoxide ( $\text{O}_2\cdot$ ) radicals, and

the hydrogen peroxide ( $\text{H}_2\text{O}_2$ ) (**Figure 2-23**) have been known for long as degenerative species for DNA, proteins, fatty acids and cell organelles [197]. The influence of oxygen in photopolymerization has been studied for decades [196]. Oxygen as paramagnetic species has two unpaired electrons occupying separate  $\pi^*$  orbitals by parallel spins in the ground state (**Figure 2-23**), which is highly reactive toward triplet states. In presence of a triplet state or other atoms and molecules that participate in a single-electron transfer, the singlet state of oxygen can be quickly generated. Singlet oxygen has paired electron with opposite spins.

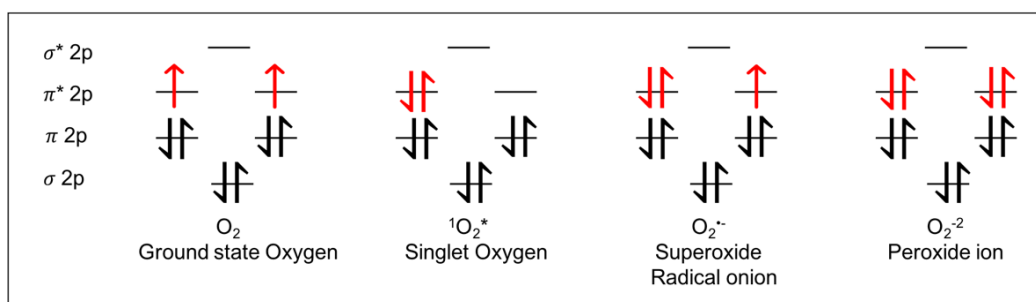


Figure 2-23 Molecular orbital diagram for ground state oxygen, singlet oxygen, superoxide radical anion and peroxide ion [198].

As shown in **Figure 2-24**, oxygen molecules can quench excited states as well as initiating and propagating species. Reaction of oxygen with initiating and propagating species yields highly stable peroxy radicals that are not participating further in polymerization reactions. As a consequence, the oxygen should be consumed before starting the polymerization. In order to overcome the inhibition effect of oxygen, different strategies have been applied, such as the use of high-intensity lamps (high dosage) [199], the protective layers, the application of inert atmosphere by using nitrogen, argon or  $\text{CO}_2$  [200] as purge gas or the addition of additives like thiols and amines [171].

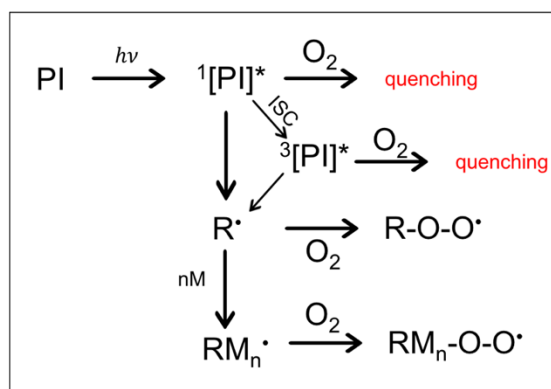


Figure 2-24 Oxygen inhibition on photoinitiation and polymerization reaction [171].

## 2.2.2 Photoinitiated cationic polymerization

Photoinitiated cationic polymerization has a more complicated nature compared to the free radical one. The cationic PI in presence of UV light (or visible light) exposure generates Brønsted ( $\text{H}^+$ ) or Lewis acids ( $\text{LA}^+$ ) reacting with a

monomer unit. The propagation phase advances as a reaction of macro-cation and monomer units. The propagation rate is generally lower than that of acrylate monomers [177]. The termination phase takes place with rather low rate in presence of nucleophilic species such as water or hydroxyl-containing compounds. These systems exhibit a living character, in which the termination rate is rather low and chain reaction can efficiently progress after removing the UV irradiation source (i.e., dark curing) [175]. The main advantages of cationic photopolymerization are the insensitivity to atmospheric oxygen, the low volatility, the very low toxicity and the good rheological properties of the photoactive formulations [171].

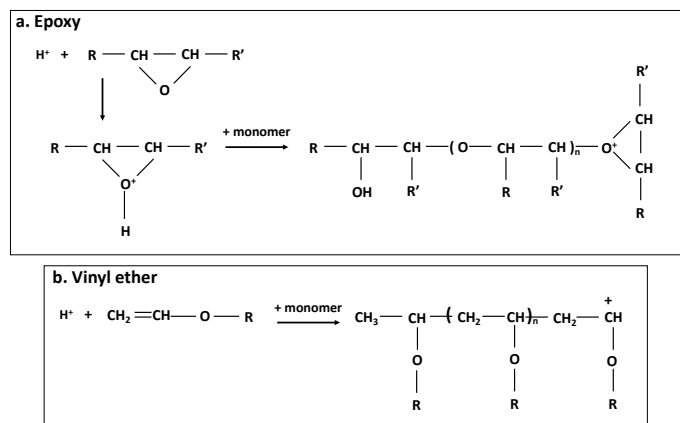


Figure 2-25 Examples of cationic photoinitiated reactions of a. epoxy monomer and b. vinyl ether monomer [176]

Epoxy- or vinyl ether-based monomers can undergo rapid cationic polymerization in presence of iodonium salts or aryl sulfonium salts, which in presence of hydrogen donor molecules can generate protonic acids during their photolysis. Epoxides undergo ring-opening polymerization and highly crosslinked polymers can be formed with difunctional epoxides, in which the chain reaction proceeds in three dimensions (**Figure 2-25a**).

Likewise, vinyl ethers in presence of protonic cations undergo fast cation polymerizations (**Figure 2-25b**). Vinyl ethers systems are advantageous thanks to the fast and complete polymerization leading to excellent solvent resistance and tailor-made properties strongly depending on the crosslinking agent properties.

### 2.2.3 Photo-induced crosslinking

Photo-crosslinking refers to the crosslinking reaction (i.e. formation of new covalent bonds among polymer chains) that is triggered and induced by light irradiation. When multifunctional monomers/polymers (i.e., molecules bearing at least two functional groups) are employed in photo-induced reactions, a 3D crosslinked polymer network is formed. The hardening of a monomeric, oligomeric or polymeric system by photo-crosslinking is also called photo-curing.

Similar to photo-polymerization reaction, the photo-induced crosslinking includes three main stages of initiation, propagation and termination. Accordingly, each stage can be defined by an associated kinetics. For free radical photo-crosslinking reaction, initially photoinitiators absorb light and reactive radicals are

generated; the rate of formation of free radicals is a function of incident light intensity, efficiency and concentration of the photoinitiator, quantum yield and number of reactive radicals per photolysis event (generally each photolysis event should yield two reactive species) [201,202]. Afterwards, the generated free radicals can react with functionalities on the polymer chain and as a result new covalent bonds and also secondary radicals as intermediate radicals are formed. The reaction can be continued with the new formed radicals reacting with other functional groups resulting in the propagation stage. The propagation is then followed by a termination stage through different routes, meaning radical coupling, disproportionation and transfer (i.e., radicals are transferred from the propagating chain through chain transfer events). During the photo-crosslinking reaction, volumetric shrinkage as a result of the new covalent bonds can take place. In fact, by newly formed covalent bond the distance between the two involving polymer chains decreases and as a result the reduction in free volume translates into an overall volume shrinkage. This phenomenon is more pronounced in acrylate-based systems; thiol-ene systems as expected are insensitive to oxygen and have lower degree of stress accumulation after crosslinking.

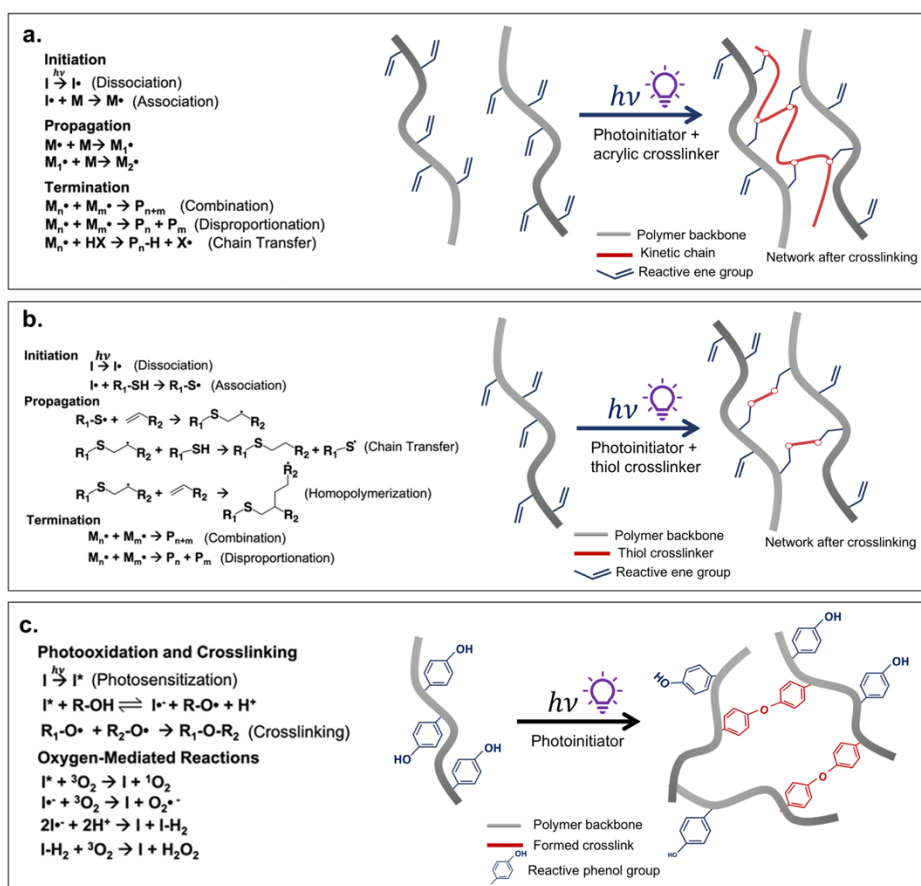


Figure 2-26 General mechanisms and schematic of free radical photo-crosslinking reactions: a. chain polymerization of polymers containing reactive double bonds, b. thiol-ene reaction between polymer chains with ene functionalities and a thiol crosslinker, c. photo-oxidation via benzoyl groups [201].

**Figure 2-26** demonstrates the three main mechanisms of free radical photo-crosslinking, namely through polymerization of multifunctional monomers bearing double bonds (e.g., acrylate, methacrylate), thiol-ene chemistry (e.g., reaction of

polymers containing ene functionalities with thiol crosslinkers) and oxygen-mediated reactions.

The photo-crosslinking through acrylate-based monomers has a long history. Generally, thermal and mechanical properties as well as solvent penetration and shrinkage of a crosslinked network can be tailored through the type of acrylate-based monomer and photoinitiator. Moreover, the thiol-ene photo-crosslinking thanks to its efficiency and mild processing conditions has been widely used in polymer science. Thiol-ene reactions are faster reactions compared to acrylate-based reactions and generally result in lower volume shrinkage. Photo-oxidation is another route that can induce crosslinking: oxygen reactive species take part in the propagation step and in the formation of covalent bonds between the polymer chains.

### **2.2.4 Applications**

In general, light-induced polymerization and crosslinking reactions can instantaneously transform a liquid monomer into a solid polymer in a selective manner in the illuminated areas. The photo-induced crosslinking, known as UV-curing, paved its way into a variety of applications thanks to its numerous advantages [175,203,204]. In past decades, UV-curing technology has introduced an increasing number of end-uses; for instance, one of the most advanced applications can be found in coating industries for almost all kind of materials, such as wood, metals, glass, paper, by applying fast-drying varnishes or inks [205]. Fabrication of electronic devices [206,207] and dental materials [208] are other important applications. As another well-known example, in photolithography the production of patterned devices with high resolution and precision is possible [209]. Finally, many emerging additive manufacturing technologies (e.g., stereolithography 3D printing) are based on photo-induced reactions [201].

Moreover, in addition to these applications, the control of polymerization or polymer degradation, the functionalization and surface modification of polymers [210,211] induced by light found their practice in many industries as a part of photochemistry [159].

As a potential application of UV-induced reactions, in this work photo-induced crosslinking techniques are coupled with electrospinning process in order to enhance the final properties of the electrospun nets. Bringing together the nanotechnology feature obtained by electrospinning and the advantages of photo-induced reactions can indeed lead to the fabrication of polymer membranes with fascinating properties.

## **2.3 Photo-induced reactions coupled with electrospinning**

The coupling of the photo-induced reactions and the electrospinning process is an interesting method that has been emerged to develop new and functional electrospun membranes. Photo-induced reactions including photo-crosslinking, photopolymerization or photo-induced grafting and functionalization can be named

as different approaches to modify the electrospun fibrous mat properties. They can be used for membranes for applications in which solvent resistance is required [91,212], antibacterial membranes [99,213], ultrafiltration membranes [214,215], stimuli responsive materials [216], and biomedical applications, such as drug delivery and tissue engineering [217].

The photo-induced reactions are particularly interesting and facile as an applicable technique in solid-state (solvent-free) on the deposited solid fibers. The initial electrospinning formulation can be tailored by using different photo-active agents, such as photoinitiators, crosslinkers, or photo-crosslinkable monomers and polymers. Then, the light irradiation can be performed *in-situ* during electrospinning [218] or on the preformed electrospun mat [218,219]; in this way, the fibrous structure with the desired properties can be obtained.

Additionally, it is also possible to prepare the electrospun fibrous membranes and subsequently to place them into a photoactive medium (i.e., by immersing in a solution containing photoactive agents [211]) prior to photo-curing.

Moreover, as already explained in Section 2.1.3, the coupling of monomer/oligomer electrospinning with *in-situ* photo-induced polymerization/crosslinking is another interesting approach. In this technique, during the electrospinning process, the flying jet is subjected to UV-irradiation and simultaneously the monomeric/oligomeric system (eventually in presence of a suitable crosslinker and/or a photoinitiator) undergoes photopolymerization and photo-crosslinking. As a result, electrospinning starts from small molecules in liquid state and finishes in solid polymer fibers, generally without using any solvent [220–222]. The initial electrospinning formulation has to be tuned to make the rate of photopolymerization/photo-crosslinking comparable to the jet flight time, in order to guarantee the sufficient solidification of the system before reaching the collector.

Herein some examples of different systems exploiting the coupling of electrospinning and photo-crosslinking are reported. In this regard, one of the main applications of combining the electrospinning process and the photo-induced reactions is to stabilize the electrospun fibers (i.e., the morphology and fiber structure) when in contact with water or another solvent by using different routes, including free radical photo-crosslinking in presence of photoinitiator with or without a crosslinker monomer (e.g., acrylic and thiol monomers), or photo-oxidation. For instance, in a work presented by Ignatova et al. [99], resistant electrospun fibers of chitosan derivative with quaternary ammonium groups (characterized by superior antibacterial properties) have been prepared by blend electrospinning in presence of poly(vinyl pyrrolidone) (PVP). The water resistance was achieved through the post-curing via UV-irradiation in presence of an acrylate monomer and a photoinitiator. The fabricated electrospun membrane exhibited solvent resistance as well as high antibacterial activity against both Gram-positive and Gram-negative bacteria. Similarly, hyaluronan (HA) grafted by functional groups such as anhydride groups and acrylic moieties was subjected to the electrospinning and subsequent photo-crosslinking to tackle the solubilization issue

for potential tissue engineering applications [223]. Also, poly(methyl methacrylate-co-2-hydroxyethyl acrylate) functionalized by cinnamate groups [224] was subjected to electrospinning and *in-situ* photo-crosslinking process in order to stabilize the fibers by forming a crosslinked network with high gel content. Moreover, Zeytuncu et al. [225] prepared electrospun membranes of modified PVA and polyethyleneimine PEI by glycidyl methacrylate. *In-situ* UV curing was applied during the electrospinning process in order to produce water-stable electrospun membranes. The membranes have been proposed as water microfilters for virus clearance. In fact, the microfilter properties have been tailored by having in the membrane both PVA, as biodegradable and hydrophilic constitute, and PEI, as a polycationic constitute, as well as by the enhanced structural properties obtained by electrospinning and *in-situ* curing.

Increasing the shape stability of electrospun mats by photo-induced reactions can be also applied in systems suffering from the shape instability issue over time due to the cold flow phenomenon. For example, polybutadiene rubbers (BR) with glass transition temperature below the room temperature can flow and thus present shape instability issues. In fact, the macromolecules of BR can move and rearrange their conformation to satisfy the increase of entropy in the course of time, even at room temperature. Hence, the electrospun fibers of BR show coagulation and collapsing, leading to the loss of the fibrous morphology of the membrane. Accordingly, Tian et al. [218] examined the electrospinning of BR systems and their *in-situ* UV irradiation in presence of a photoinitiator during the electrospinning. It has been demonstrated that the UV-cured BR fibers could resist the cold flow and exhibited prolonged shape stability [218].

The photo-induced crosslinking, in addition to stabilization of the fibrous structure, can also be applied to obtain particular membrane morphologies. For instance, Vitale et al. [226] used the photo-induced thiol-ene chemistry to control the morphology and also to modulate the overall porosity of electrospun membranes made of a styrene-butadiene rubber (SBR). Introducing a time interval between the electrospinning process and the UV-curing permitted the tailoring of the fibers shape and the porosity of the electrospun mats. Moreover, in this work off-stoichiometric ratio of thiol and ene groups allowed the easy functionalization of the electrospun membranes. Correspondingly, in another work presented by Lyoo et al. [219], poly(vinyl cinnamate)/poly(3-hydroxybutyrate-co-3-hydroxyvalerate) (PVCi/PHBV) blend was subjected to electrospinning process. Subsequently, the fabricated fibers were UV irradiated and PVCi underwent the crosslinking process. Afterwards, the PHBV was extracted from the blend fibers and as a result fibers showing a particular porosity were obtained.

As explained earlier one of the photo-crosslinking routes is through the photo-oxidation process (i.e., photo-mediated redox reactions induce the crosslinking). Bazbouz et al. [227] used this method to produce UV-cured vinylbenzylated gelatine-poly( $\epsilon$ -caprolactone) dimethacrylate electrospun membrane. UV-curing was performed as a post modification method. The stabilized gelatine-based electrospun fibrous structure was proposed for tissue engineering applications.



In the following chapters, different approaches to couple the electrospinning process with free radical photo-induced crosslinking reactions are investigated and studied. Applying these photo-induced reactions are aimed at enhancing the physico-chemical properties of the electrospun membranes.



# Chapter 3

## Chitosan-based photo-crosslinked electrospun membrane

### 3.1 Abstract

This study aims at the fabrication of nanofibers of chitosan (CS) through electrospinning and subsequent photo-crosslinking. Due to the stiffness and polycationic nature of chitosan, the processability of this natural polymer is indeed challenging, hence, the electrospinning was carried out by blending it with easily-spinnable poly(ethylene oxide) (PEO). Three composition ratios of CS/PEO were evaluated for the electrospinning process (namely 90/10, 70/30, 50/50). The optimum condition for electrospinning of CS/PEO blends was selected for subsequent photo-crosslinking reaction and further characterizations. The CS/PEO 70/30 composition was chosen as it allowed to fabricate defect free, uniform and smooth fibers. Subsequently, in order to improve the stability of the electrospun mat, it was subjected to chemical crosslinking by the fast and eco-friendly technique of photo-curing by UV-irradiation. The photo-crosslinking reaction was studied through the photo-DSC technique, and it was optimized to prepare CS/PEO fibers resistant to water for a wider application range, particularly in food industry and biomedical fields.

The study presented in this section, providing the optimization of a simple and fast process to fabricate CS-based photo-cured fibrous membranes with enhanced physico-chemical properties, has been partly published in [212].

### 3.2 Introduction

Chitosan (CS), the major derivative of chitin, is the second-most abundant natural polysaccharide after cellulose. This natural polymer is characterized by high biodegradability, nontoxicity and antimicrobial properties, arising from the protonated amide group [228–234]. CS can have a wide application range including active food packaging, tissue engineering, wound healing dressings, controlled released drug delivery systems, and water filtration [235–240]. In order to improve its physico-chemical properties, CS can be subjected to a crosslinking reaction, for instance by introducing specific crosslinker molecules that react with the amino

groups, such as glutaraldehyde [241,242], poly(ethylene glycol) dialdehyde diethyl acetal [243], formaldehyde [244], glyoxal [245], or genipin [246–248].

In many of the envisaged applications, CS can be used in the form of electrospun nanofibrous membranes, exploiting their high surface area to volume ratio, their high porosity and their flexibility [237]. However, CS is a challenging polymer in terms of processability by electrospinning due to its polycationic nature, together with its rigid structure and  $\beta(1,4)$ -linked D-glucosamine repeating units [249]. Expectedly, the cationic nature of the chitosan and accordingly the repulsive forces between ionic groups hinder the electrospinnability of chitosan leading to unstable jet and defects formation [250]. Moreover, CS due to its polycationic nature is only soluble in acidic solutions: acetic acid is the commonly used solvent for CS solution electrospinning process [251].

Among different methods for achieving electrospun nanofibers of CS, its blending with a second electrospinnable polymer is the easiest and feasible approach [237,249,252,253]. For instance, poly(ethylene oxide) (PEO) can facilitate the CS fiber fabrication by enhancing the overall chain entanglements [254,255]. Interestingly, CS and PEO are miscible thanks to the interactions between ether groups in PEO and hydroxyl/amine groups in CS. Accordingly, the entanglements among the chains of the two polymers lead to the decreasing of the blend crystallinity and the improving of the processability.

PEO is a semicrystalline polymer characterized by biocompatibility, hydrophilicity, and non-immunogenicity. As a result PEO, together with CS, is a potential candidate for biomedical and pharmaceutical applications and has been extensively studied in this fields [256]. Moreover, PEO is easily electrospinnable and thus PEO fibrous membranes have been largely studied for different applications. However, PEO is suffering from solubility issue: it is soluble in almost all used organic solvents and, when in the form of fibers, the nanostructured morphology and fiber shape is extremely unstable if the material is placed in contact with any solvent (even water). Different techniques have been proposed for PEO chemical crosslinking, which can improve its solvent resistance: for instance, low molecular weight PEO was crosslinked by reaction between end-groups [257] or by gamma radiation [258,259].

Photo-crosslinking, as a fast and ecofriendly technique, is a very interesting approach for PEO crosslinking and stabilization. It has been reported that PEO in solid state in the presence of an appropriate photoinitiator undergoes photo-crosslinking: UV irradiation leads to radicals formation (abstraction of hydrogens of the carbon chain (**Figure 3-1**)), and the combination of the generated polymeric radicals yields crosslinked networks [260]. PEO can therefore turn into a water insoluble material by photo-crosslinking [261,262]. Accordingly, crosslinked PEO allows to expand the application spectrum of the polymer [263].

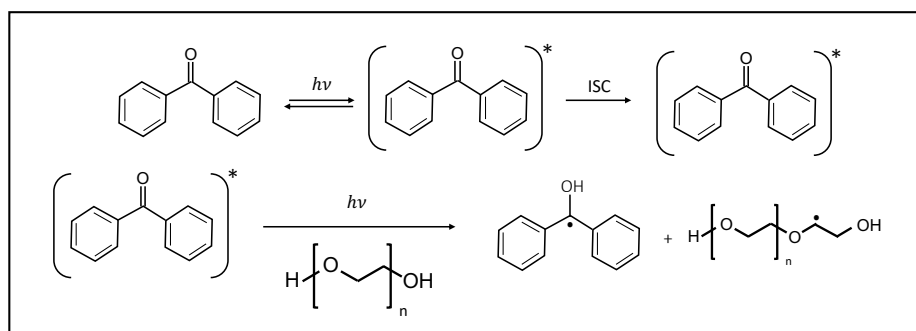


Figure 3-1 Generation of radical species on PEO chain in presence of a photoinitiator (i.e., benzophenone) upon UV irradiation

Herein, electrospun nanofibrous mats of CS/PEO are prepared from chitosan and PEO blend solutions with different composition ratio, with the addition of a photoinitiator (PI). The membranes are then irradiated to induce the photo-crosslinking reaction and improve their physico-chemical properties. It is shown that CS and PEO undergo the photo-crosslinking phenomena separately, and as a result, insoluble and stable chitosan-based nanofibrous membranes can be produced by an easy and environmentally friendly technique.

### 3.3 Materials and methods

#### 3.3.1 Materials

Medium molecular weight chitosan (molecular weight of 190,000–310,000 Da, deacetylation degree ~ 80%), poly(ethylene oxide) (average  $M_w$  ~ 1,000,000), benzophenone ( $\geq 99\%$ ) were purchased from Sigma-Aldrich, and acetic acid ( $\geq 99.8\%$ ) was purchased from lab-Honeywell, Germany (Figure 3-2).

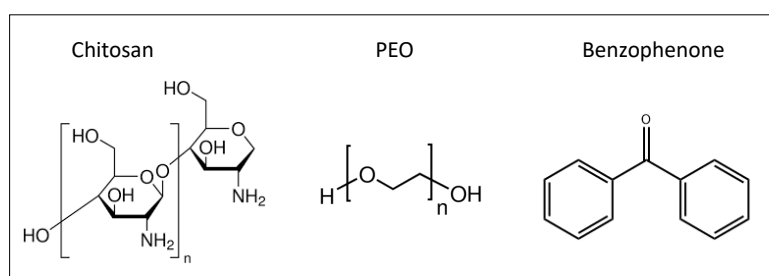


Figure 3-2 molecular structure of CS, PEO and benzophenone, used as photoinitiator

Electrospinning solutions of CS 4 wt.% and PEO 4 wt.% in aqueous acetic acid were prepared and stirred overnight. CS/PEO blend solutions with different composition ratio were formed from CS and PEO solutions and homogenized for a couple of hours. Extra acetic acid was added to the solutions with a higher chitosan content in order to maintain the proper viscosity. Prior to the electrospinning, the photoinitiator (benzophenone, 2 wt.% with respect to PEO content) was added to the blend solutions. The composition of the different blend solutions prepared is detailed in **Table 3-1**.

The CS/PEO blend solutions were used both for the electrospinning process and for preparing casted films.

Table 3-1 Composition of the solutions used for the electrospinning process.

CS/PEO mass fraction (% w/w)	PEO (wt.%)	CS (wt.%)	H <sub>2</sub> O (wt.%)	Acetic Acid (wt.%)
0/100	5	-	95	-
50/50	1.6	1.6	8	89
70/30	0.7	1.6	5.5	92.2
90/10	0.2	1.6	3.8	94.6
100/0	-	4	9.6	86.4

### 3.3.2 Electrospinning procedure

Electrospinning was carried out by an E-fiber electrospinning system SKE apparatus in horizontal setup, equipped with high voltage power supply, a programmable syringe pump and a stationary collector. Electrospinning was conducted at room temperature by applying a voltage of 15-30 kV, a flow rate of 0.5-1 ml/h, and a tip-to-collector distance of 15 cm. An aluminum foil was used as collector.

### 3.3.3 Photo-curing process

UV-curing was performed by two different intensities of 7 mW/cm<sup>2</sup> and 70 mW/cm<sup>2</sup> on the sample surface under constant flow of inert atmosphere (N<sub>2</sub>). The former irradiation with lower UV intensity was applied by means of a high-pressure mercury-xenon lamp (LIGHTNINGCURE Spotlight source LC8, Hamamatsu), using a UV dose (the product of the light intensity and the irradiating time) of ~2 J/cm<sup>2</sup>; this UV condition herein is defined as “low UV”. The latter irradiation condition with higher UV intensity was applied through a medium pressure mercury lamp (Dymax ECE UV-Curing flood lamp) delivering a UV dose of ~80 J/cm<sup>2</sup> on the sample surface; this UV condition herein is defined as “high UV”. The UV intensity of both light sources was measured by a UV Power Puck<sup>®</sup> II from EIT<sup>®</sup> Instrument Markets.

The photo-crosslinking reactions were studied by means of photo-differential scanning calorimetry (DSC1 STARE Mettler Toledo system equipped with a high-pressure mercury-xenon lamp). Prior to the experiment, 5 mg of samples were placed in an uncovered crucible and left in dark place at the laboratory condition for a couple of hours for complete solvent evaporation. Photo-DSC measurement was carried out under constant flow of N<sub>2</sub> as a purge gas at the constant flow of 60 ml/min and isothermal condition of 25 °C for 10 minutes. The heat released during UV-irradiation (for both intensities of 7 mW/cm<sup>2</sup> or 70 mW/cm<sup>2</sup>) was recorded, and a second run was carried out at the end of the photo-crosslinking reaction as a baseline, in order to remove the heat flow effect arising from the UV lamp.

### 3.3.4 Characterizations

The morphology of fabricated electrospun fibers was monitored by Field Emission Scanning Electron Microscopy (FE-SEM, ZEISS, Merlin). The samples were sputter coated with a thin layer of Cr film (~10 nm) by means of Quorum Q150T ES sputter coater. Size distribution of fibers diameter was obtained by approximately 100 measurements per sample by ImageJ software. Also, the solvent resistance of fiber morphology was evaluated by FE-SEM imaging; for this purpose, a drop of water was placed on the samples and left to get dried prior to the microscopy analysis.

Chemical bonds and composition of electrospun fibers prior and after UV-curing were evaluated by Attenuated Total Reflectance Fourier Transform Infrared (ATR FTIR) spectroscopy, using a Thermo Scientific Nicolet iS50 spectrometer with a diamond crystal. The quantification of peak bands and peak areas was performed by Omnic software.

Thermal properties of the electrospun samples were examined by thermogravimetric analysis (TGA) and also by differential scanning calorimetry (DSC). TGA was carried out using a Mettler Toledo TGA/SDTA 851°. Samples were heated up to 700 °C with a heating rate of 10 °C/min. The measurement was carried out under constant flow of N<sub>2</sub> to avoid thermo-oxidative process. The first derivative of the thermogram (DTGA) was calculated for defining the main decomposition peaks. The TGA was also studied for evaluating the real composition ratio of the fibers with respect to thermograms of pure CS and pure PEO. DSC measurements were performed by using a Mettler Toledo DSC1 STARE instrument. The analyses consisted in two cooling and heating cycles in the temperature range [-60 190] °C, with a heating and cooling rate of 20 °C/min. The crystallization degree was obtained by the area of the endothermic peak in the second heating cycle with respect to the enthalpy of 100% crystalline PEO.

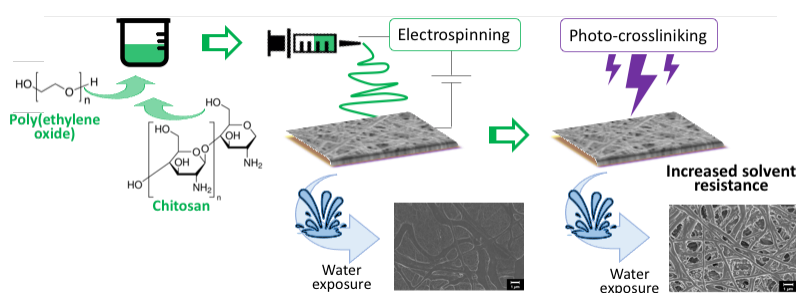


Figure 3-3 Schematic illustration of the electrospinning and photo-crosslinking procedure

## 3.4 Results and discussion

As indicated earlier, CS processability is troublesome due to the polycationic nature and its rigid structure. Particularly, CS electrospinning is challenging because of the inter and intra-molecular interaction and the presence of ionic groups and repulsive forces causing the jet instability, spraying the droplets and also

defects formation. In order to address this issue, a simple way is to blend CS with an easy electrospinnable polymer such as PEO. **Figure 3-3** shows the schematic of the electrospinning and the photo-crosslinking procedure.

### 3.4.1 Electrospinning of CS/PEO blend

As a preliminary study, the easily electrospinnability of PEO was confirmed: as expected, PEO electrospinning results in a uniform and defect-free fibrous membrane (**Figure 3-4**). Whereas, electrospinning of pure CS acidic solutions was unsuccessful, and CS fibers could not be obtained. Then, different solutions with diverse composition ratio of CS/PEO (**Table 3-1**) were used for electrospinning process. All the investigated solutions resulted to be processable by electrospinning and CS/PEO fibers were formed, although in some cases the membranes presented critical defects. The morphology of CS/PEO electrospun mats and their fiber size distribution was analyzed by FE-SEM images (**Figure 3-5**). The 50/50 and 70/30 CS/PEO blends yield very well-shaped and defect free fibers. While the higher content of CS in the blend (90/10 CS/PEO blend) causes jet instability and non-uniform fibers. Moreover, spraying of the solution during electrospinning process takes place for CS/PEO 90/10, and the presence of solvent on the collector can lead to a re-solubilization of the solid fibers previously deposited. As a result, it is demonstrated that the addition of PEO enhances the electrospinnability of CS to a great extent. In fact, PEO presence decreases the electrical conductivity of CS and also the chain entanglement increases by formation of H-bonds between PEO polyether oxygen and CS amino hydrogen; these two factors together makes possible the electrospinning of CS [264]. As seen in **Figure 3-5**, for all the blend compositions, nano-netting phenomena can be detected. In fact, when upon electrospinning process multiple jets of polymer solution are formed and interactions through H-bonds take place among them, very miniature jet of solution between the main polymer jets can be formed as a network accelerating toward the collector [265,266].

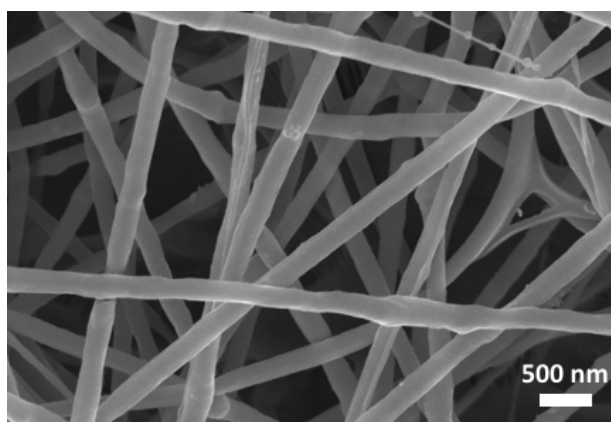


Figure 3-4 The FE-SEM image of electrospun PEO fibers prepared by 5 wt.% aqueous solution

The size distributions of fibers diameter are reported in **Figure 3-5**. As can be seen the content of CS clearly affects the fibers diameter: higher content of CS



resulted in lower fiber diameter. The change in CS content varies the fiber average diameter from 480 nm to 180 nm for CS/PEO 50/50 to 90/10, respectively. In fact, by increasing the CS content, the ionic conductivity of electrospinning solution increases and the viscosity of solution changes; as a result the fiber diameters decrease [267].

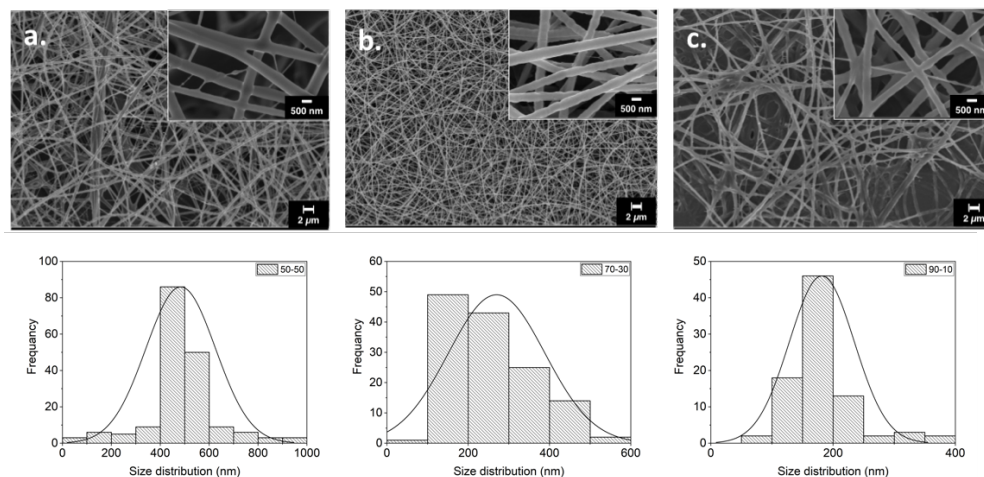


Figure 3-5 FE-SEM images and fiber size distribution of electrospun mats of CS/PEO blend solutions of a. 50/50, b.70/30 and c.90/10 composition ratio.

The thermal stability of electrospun fibers of CS/PEO with different composition (50/50, 70/30 and 90/10) was analyzed through TGA experiment. The TGA and first derivative DTGA of blend electrospun fibers as well as pure CS and pure PEO are reported in **Figure 3-6**. As can be seen, all blends exhibit small weight loss below 150 °C attributed to the residual solvent evaporation and drying phase. The mass loss in drying phase for 90/10 CS/PEO blend is more pronounced, which is due to higher content of acetic acid solvent. Interestingly, CS/PEO blend fibers exhibit two distinct weight losses attributed to CS and PEO decomposition. CS decomposes around 300 °C and PEO decomposes around 400 °C; CS/PEO blends show both decomposition stages, and clearly the composition of the blend determines the relative weight loss for each constitute.

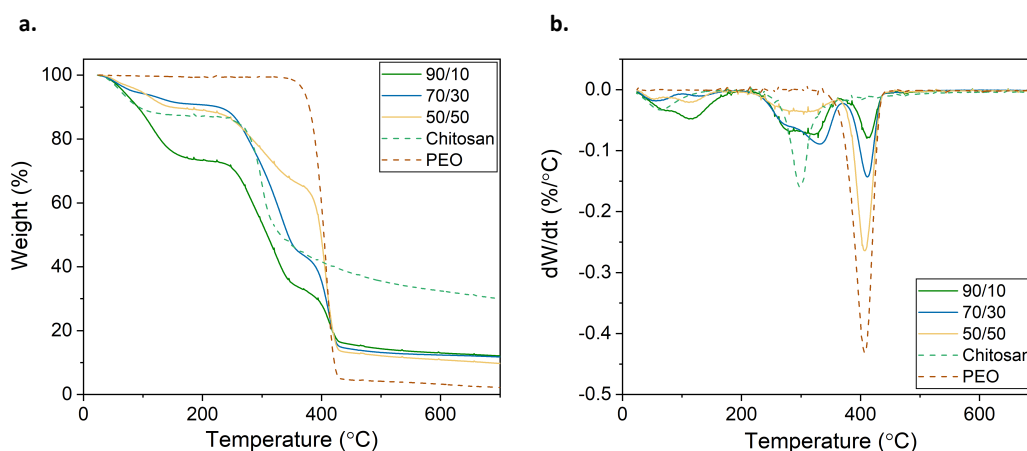


Figure 3-6 TGA (a) and first derivative DTGA (b) results of pure CS, pure PEO, and electrospun fibers with CS/PEO 50/50, 70/30 and 90/10 composition ratio.

By having the decomposition trend of pure CS and pure PEO, one can determine the real composition ratio of the fibers. **Table 3-2** summarizes the theoretical and the calculated composition of the fibers.

Table 3-2 Comparison of the composition of the investigated CS/PEO blends before (starting solution) and after (fiber mat) the electrospinning process, based on TGA data.

Sample	Residue (wt.%)	CS (wt.%)		PEO (wt.%)	
		starting solution	fiber mat	starting solution	fiber mat
CS	32.0				
PEO	4.8				
CS/PEO 50/50	9.7	50.0	34.1	50.0	65.9
CS/PEO 70/30	11.7	70.0	59.0	30.0	41.0
CS/PEO 90/10	12.1	90.0	72.2	10.0	27.8

Interestingly, a PEO enrichment of approximately 15 wt.% due to electrospinning can be seen for all CS/PEO blends and thus the fibers composition is different from the starting blend solution. The PEO enrichment in fibers can be due to the superior electrospinnability feature of PEO.

In order to have high CS content as well as suitable fiber formation feature, the CS/PEO 70/30 blend was chosen for further investigation and photo-crosslinking. In fact, although the CS/PEO 90/10 contains the highest content of CS in final product, the fiber morphology and challenging spinnability (i.e., beads/defect formation) made us to discard this sample. Henceforth, CS/PEO is referred to the sample with a starting spinning solution of CS/PEO 70/30, and a real blend composition of 59 wt.% and 41 wt.% for CS and PEO, respectively, in the fibers. This sample exhibits good electrospinnability with uniform fibers formation with an average diameter of  $270 \pm 10$  nm.

### 3.4.2 Photo-crosslinking of CS/PEO electrospun fibers

The electrospun mats of CS/PEO were subjected to UV irradiation with two different UV doses in order to improve the physico-chemical properties, particularly the solvent resistance, through the photo-induced crosslinking. As stated in the experimental section, a photo-initiator was introduced to the blends for efficient crosslinking initiation through hydrogen abstraction. The UV irradiation was applied by two different intensities:  $7 \text{ mW/cm}^2$  and  $70 \text{ mW/cm}^2$  called as low UV and high UV, respectively.

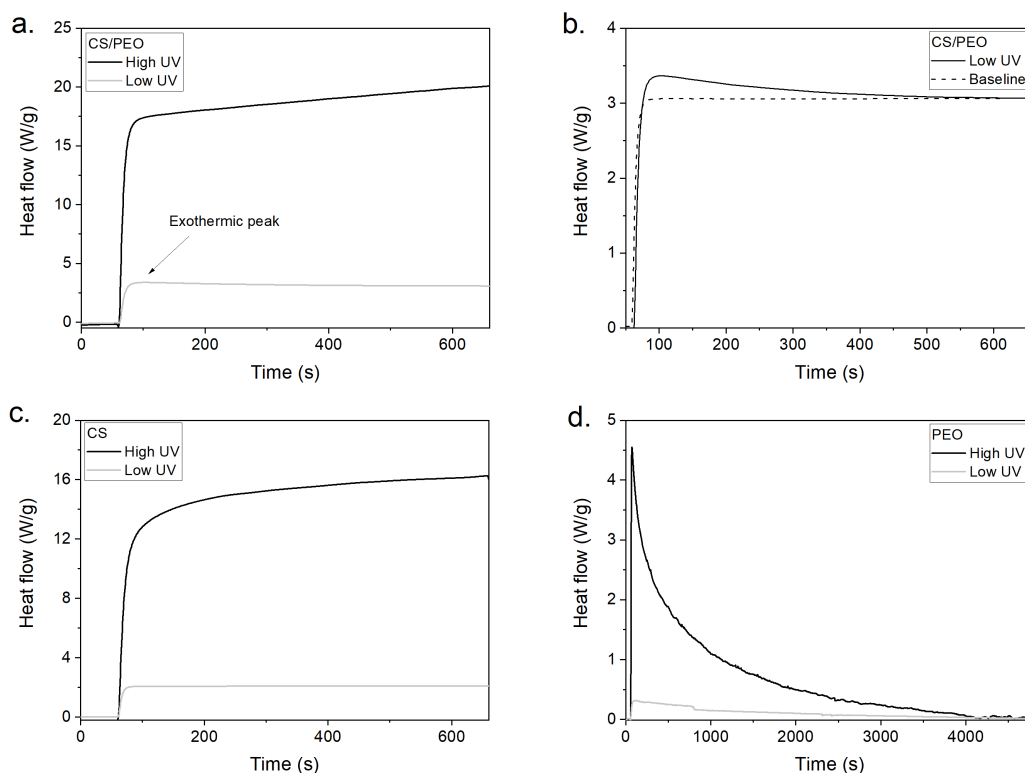


Figure 3-7 Photo-DSC thermograms of: a. CS/PEO blend irradiated by low UV and high UV ( $7 \text{ mW/cm}^2$  and  $70 \text{ mW/cm}^2$ , respectively) b. CS/PEO irradiated by low UV (the baseline is shown by dash line), c. CS irradiated by low UV and high UV and d. PEO irradiated by both UV intensities after baseline subtraction.

The kinetics of the photo-crosslinking was evaluated through photo-DSC measurements. In fact, by considering that the generated heat flow upon UV irradiation is proportional to the reaction rate, the kinetics of the reaction, which includes different stages of initiation, propagation and termination, can be monitored [268]. The heat flow evolution during the UV irradiation of the CS/PEO blend is depicted in **Figure 3-7**. When CS/PEO is subjected to the low UV, an exothermic peak indicating a photo-crosslinking phenomenon takes place. While for the high UV, the heat flow continuously increases. We assumed that for the higher intensity of UV, the crosslinking reaction is not the only progressing reaction and the generated heat flow is not exclusively because of crosslinking. For understanding the photo-DSC thermograms of CS/PEO, we performed photo-DSC on chitosan and PEO separately. The PEO thermograms for both UV intensities show the typical photo-crosslinking exothermic peak. The generated heat for high UV intensity was much higher as an indication for the formation of more crosslinking bonds. Instead, chitosan exhibited different behavior when it was subjected to UV irradiation. Seemingly, the low UV intensity does not provoke any reaction in CS, while the high UV causes the continuous increase of heat flow without reaching a stable plateau. It can be said that CS during the UV irradiation by higher intensity undergoes degradation. Thus, the thermogram of CS/PEO blend reflects these two competing phenomena: the photo-crosslinking of PEO and the photo-degradation of CS. As a result, the continuous growth of heat flow due to CS degradation surpasses the exothermic peak of PEO crosslinking.

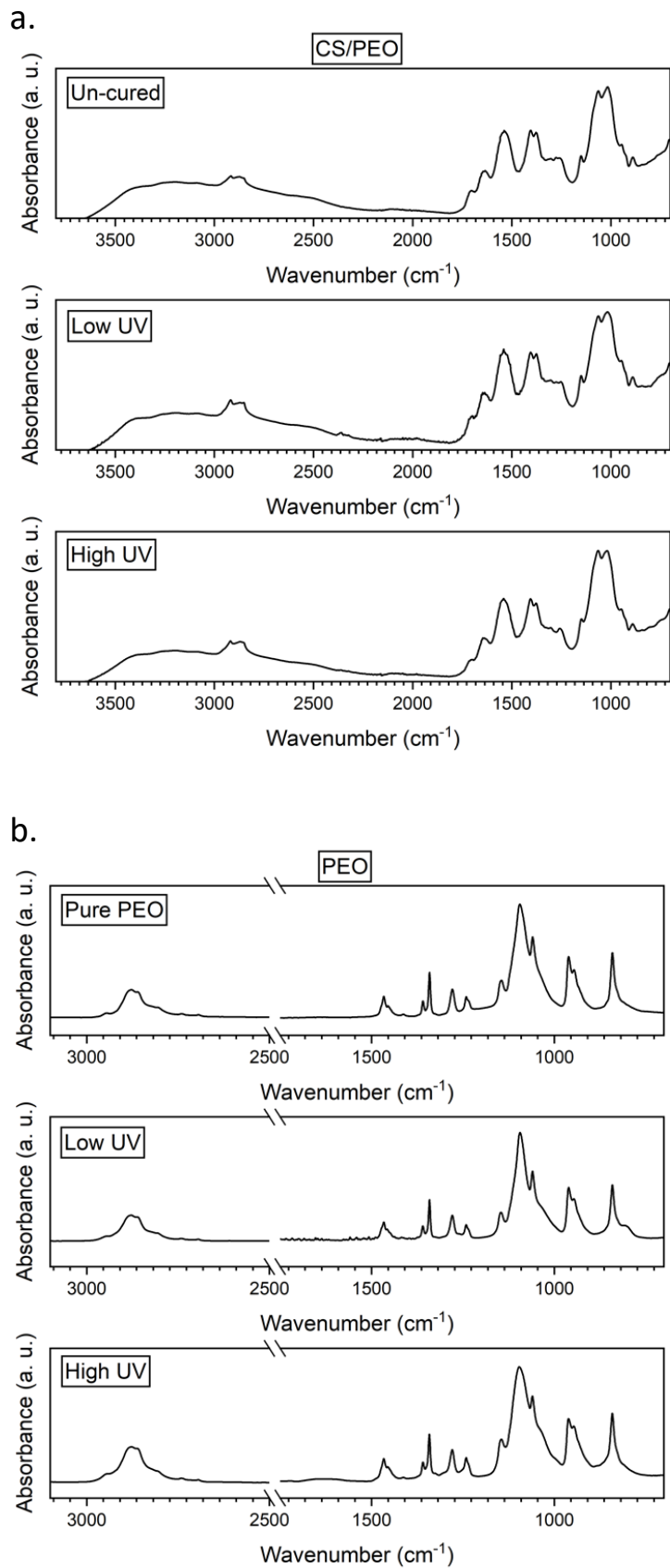


Figure 3-8 FTIR spectra of a. CS/PEO and b. PEO before UV irradiation and after UV with two intensities.

In order to evaluate the chemical structure, composition and changes caused by UV-irradiation, FTIR spectroscopy of CS/PEO electrospun mat prior and after UV-curing was performed. PEO and CS casted films were also studied by FTIR spectroscopy before and after UV-irradiation. The characteristics peaks of chitosan are found at  $3290\text{ cm}^{-1}$   $\nu(\text{OH})$ ,  $2867\text{ cm}^{-1}$   $\nu(\text{N-H})$ ,  $1645\text{ cm}^{-1}$   $\nu(\text{C=O})$  of the amide group and  $1540\text{ cm}^{-1}$   $\delta(\text{NH}_3)$ ,  $1372\text{ cm}^{-1}$   $\delta(\text{-CH}_3)$  in amide group, as well as the peaks at  $1150\text{ cm}^{-1}$  and  $1060\text{ cm}^{-1}$  associated to the glycosidic linkage [269]. The identified PEO peaks are  $2876\text{ cm}^{-1}$   $\nu(\text{C-H})$ ;  $1466\text{ cm}^{-1}$   $\delta(\text{CH}_2)$ ;  $1360\text{ cm}^{-1}$  and  $1341\text{ cm}^{-1}$   $\omega(\text{CH}_2)$ ;  $1279\text{ cm}^{-1}$  twisting of  $\tau(\text{CH}_2)$ ;  $1145\text{ cm}^{-1}$ ,  $1100\text{ cm}^{-1}$  and  $1060\text{ cm}^{-1}$  triplet peak due to C-O-C. The peak at  $1720\text{ cm}^{-1}$  which can be observed in some samples is due to carbonyl groups of the solvent residue.

The UV-irradiation effects on CS/PEO samples are evaluated by comparing the FTIR spectra obtained before and after UV-curing. Important changes that can be detected after the irradiation are the decreasing of the intensity of the bands at  $1150\text{ cm}^{-1}$  and  $1060\text{ cm}^{-1}$ , associated to glycosidic linkage (**Figure 3-8**). Although these peaks are present also in PEO FTIR spectrum, by performing FTIR spectroscopy on PEO alone and CS alone, one can conclude that such change in CS/PEO is associated to the chitosan component. In fact, the PEO spectrum after UV irradiation did not show any modifications in ether triple bonds.

According to the literature, UV light can affect chitosan in different ways: hydrogen abstraction, hydroxyl group abstraction,  $\text{NH}_2$  group abstraction, acetyl abstraction (the remaining acetyl group after deacetylation) and glycidyl bond scission between tetrahydropyran rings. The latter induces the main chain scission and accordingly shorter polymer chains can be obtained after UV-irradiation [270,271].

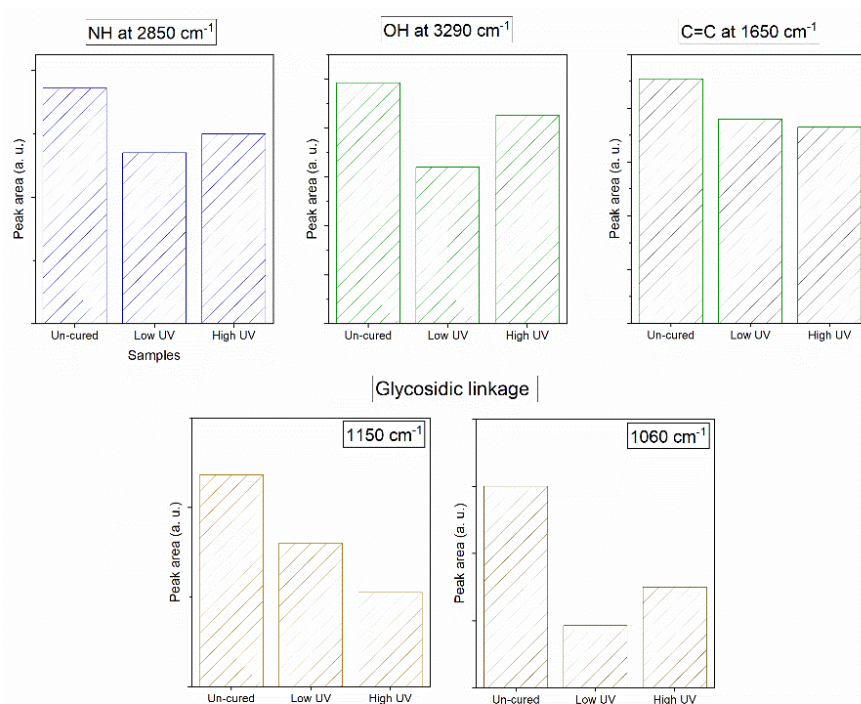


Figure 3-9 The area of characteristic peaks of CS/PEO obtained from FTIR spectroscopy before and after UV irradiation; the peak areas were normalized to peak  $845\text{ cm}^{-1}$  as the least affected peak during the UV irradiation.

However, even though the UV light may induce partial CS degradation, its biocompatibility and antimicrobial features should be sustained after curing [272]. In fact, the amide group is responsible for the aforementioned features of CS, and the FTIR spectrum of CS/PEO indicates the presence of both the OH and NH groups at  $3290\text{ cm}^{-1}$  and  $2850\text{ cm}^{-1}$  (although they show some extent of decline after UV-curing), as shown in **Figure 3-9**.

Moreover, changes in the band around  $1645\text{ cm}^{-1}$  can be detected after UV irradiation (**Figure 3-9**). This decrease in the peak absorbance can be due to the acetyl group abstraction. It is worth mentioning that the photo-oxidation of CS/PEO can be excluded as the UV-irradiation is conducted in an inert atmosphere by purging  $\text{N}_2$  gas into the UV-curing chamber.

### 3.4.3 Characterization of photo-crosslinked CS/PEO electrospun fibers

FE-SEM analysis was conducted to monitor the fibrous morphology of the membranes after UV irradiation by low UV and high UV. As can be seen in **Figure 3-10**, both UV doses do not affect the fiber morphology: trace of fiber fusion or shape deformation are not detected in UV-irradiated samples.

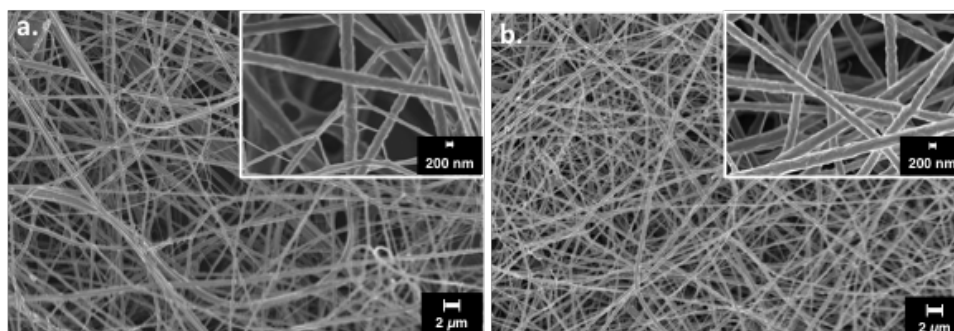


Figure 3-10 . FE-SEM images of CS/PEO electrospun fiber mats after photo-crosslinking with a. low UV dose and b. high UV dose.

The thermal stability and properties of the UV-cured samples were evaluated through TGA, ATR-FTIR and DSC.

TGA scans and DTGA of UV-cured CS/PEO samples show the presence of both chitosan and PEO components by distinct peaks, independently on UV-irradiation conditions (**Figure 3-11a and b**). The thermograms of PEO and CS did not show any modification of their decomposition peak after UV-irradiation. Although photo-DSC and FTIR results evidenced a CS degradation, changes in CS could not be detected by TGA.

In order to monitor the thermo- and photo-oxidation of CS/PEO samples, FTIR spectra were also collected for the un-cured, low UV-cured, and high UV-cured CS/PEO sample at  $25\text{ }^{\circ}\text{C}$ ,  $150\text{ }^{\circ}\text{C}$  and  $250\text{ }^{\circ}\text{C}$  (**Figure 3-11c**). Thermal treatment was conducted at temperatures lower than the main decomposition temperature of CS and also in air atmosphere, unlike the TGA which was conducted in inert atmosphere. The thermal treatment is intended to measure and compare the thermo-stability of the samples without receiving UV and samples cured with two UV

doses. In particular, through FTIR spectroscopy, the carbonyl groups (corresponding to the peak at  $1645\text{ cm}^{-1}$ ) as an indication for oxidized species were monitored during the measurement. Interestingly, the thermo-oxidative resistance of CS/PEO by irradiation increased: the un-cured CS/PEO exhibited the highest carbonyl intensity as a mark for thermo-oxidation at  $150\text{ }^{\circ}\text{C}$  and  $250\text{ }^{\circ}\text{C}$ , while the most resistant sample for thermo-oxidation is the CS/PEO receiving high-UV.

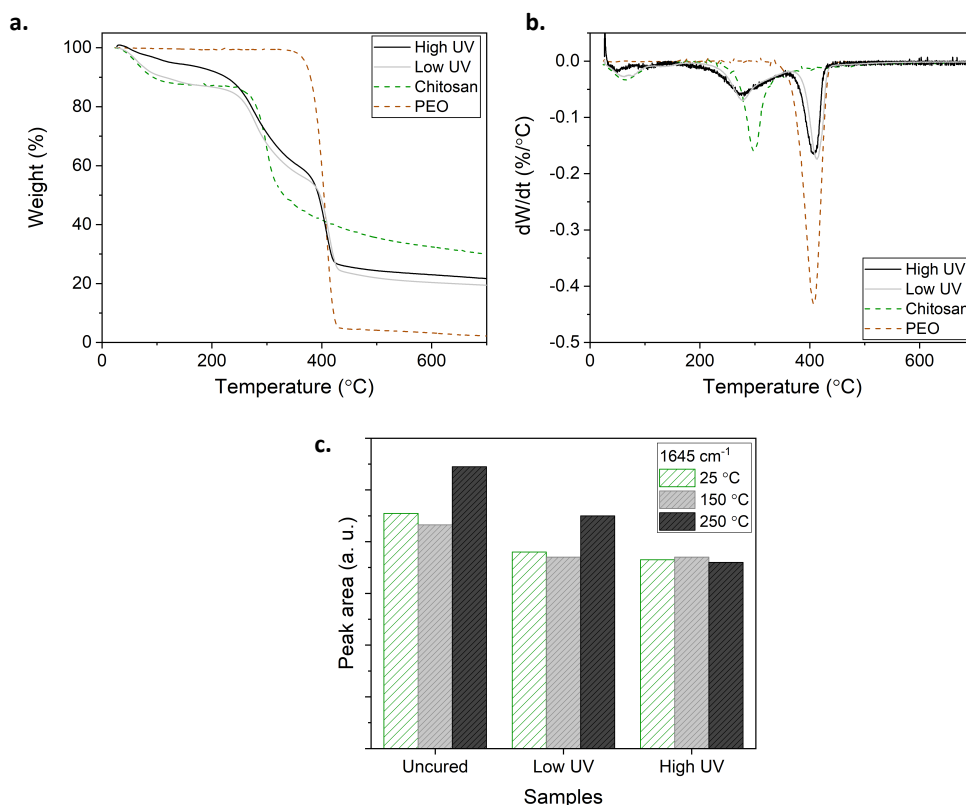


Figure 3-11 Thermal properties of the CS/PEO samples, a. TGA and first derivative b. DTGA results of pure CS, pure PEO, and the UV-cured CS/PEO with low UV and high UV, and c. carbonyl peak area obtained from FTIR experiments.

Table 3-3 Melting temperature and crystallization degree of CS/PEO electrospun fibers, based on DSC data.

Sample		$T_m$ ( $^{\circ}\text{C}$ )	Crystallization degree (%)
PEO powder	-	71.6	51.2
Electrospun PEO	Uncured	72.2	41.2
-----			
Electrospun	Uncured	65.7	13.3
CS/PEO 70/30	low UV	66.2	12.9
	high UV	68.6	12.6

The outcome of DSC scans is reported in **Table 3-3**. From the DSC thermograms the crystalline phase can be detected through the exothermic crystallization peak. The crystallinity is arising from the PEO component of the fibers and is approximately proportional to the PEO content. As it can be seen in **Table 3-3**, UV irradiation slightly changes and decreases the crystallinity of the

samples. While the UV irradiation increases the melting temperature of CS/PEO by few degrees. The glass transition of CS/PEO could not be detected through the performed DSC measurements and this is basically due to the low  $T_g$  of the PEO (around  $\sim -50$  °C) near the limit of the instrument.

Finally, the solvent resistance of fabricated CS/PEO electrospun mat was evaluated through FE-SEM imaging. When the uncured CS/PEO is in contact with a solvent (even water), the PEO component dissolves in it and the fibrous morphology is completely lost. While the fibrous morphology is partially or totally preserved after UV-curing, as shown in **Figure 3-12**. In particular, the CS/PEO electrospun mat irradiated with high UV exhibits better retention of morphology after contact with water. And expectedly, the sample with low UV dose demonstrates an enlargement of the fiber sizes and a partial fusion of fibers.

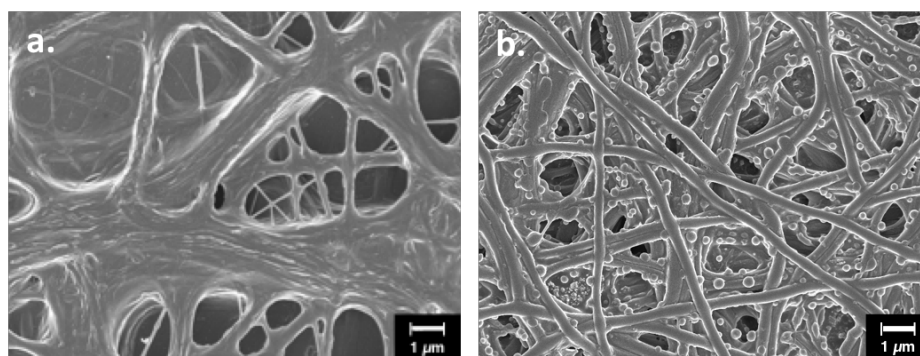


Figure 3-12 . FE-SEM images of CS/PEO fiber mats photo-crosslinked with low UV dose (a) and high UV dose (b), after water contact.

### 3.5 Conclusions

In the study reported in this section, the fabrication of CS nanofibers by electrospinning and subsequent photo-crosslinking was investigated. CS electrospinning was made successful by the employment of blends of CS and PEO. Three different CS/PEO blend compositions were used. The composition ratio with optimal fibrous morphology and processability was selected for the subsequent photo-crosslinking step, namely CS/PEO 70/30. Interestingly, a PEO enrichment in the electrospun fibers took place, as a result the sample with starting composition of CS/PEO 70/30 showed  $\sim 60$  wt.% of CS content. Uniform and defect free CS-based electrospun mats, formed by fibers with an average diameter of around 270 nm, were obtained. The photo-crosslinking of the electrospun mat was conducted in inert atmosphere with two different UV intensities, namely 7 (low UV) and 70  $\text{mW}/\text{cm}^2$  (high UV). The photo-crosslinking kinetics was studied through photo-DSC measurements: the lower UV intensity caused the photo-crosslinking typical heat flow pattern; while it has been shown that when higher UV intensity is used, in addition to crosslinking, another competing phenomenon (possibly partial CS degradation) occurs. Although all the FTIR characteristic peaks of CS and PEO were present after UV irradiation, the analysis showed some small traces of CS deterioration (i.e., the decrease of some CS absorption bands). The morphology of



the fibrous mats did not change after UV irradiation. The thermal properties of the photo-crosslinked samples slightly improved. Moreover, photo-cured CS/PEO fibrous mats showed enhanced solvent resistance and stability: their insolubility and their fiber morphology retention after contact with water was demonstrated, particularly in the case of applying the high UV intensity. The fabrication of stable photo-cured electrospun mat of CS/PEO is indeed promising for a wide range of applications, for example in the biomedical and packaging fields.



# Chapter 4

## Polyethylene oxide-based photo-crosslinked electrospun membranes

### 4.1 Abstract

In this study, shape stable and solvent resistant fibrous membranes of poly (ethylene oxide) (PEO) were fabricated through the versatile technique of electrospinning and subsequent photo-crosslinking process. PEO is an abundant polymer with outstanding characteristics such as biocompatibility, stability and inertness, also it is one of the most studied polymers for the electrospinning technique. However, this polymer suffers from shape instability as it is soluble in water and in most of the common organic solvents. As a result, when in contact with solvents, the fibrous morphology of the electrospun PEO membranes can be easily lost, hindering PEO applicability. For addressing this issue, here two different acrylic crosslinkers, namely polyethylene glycol diacrylate (PEGDA) and trimethylol propane triacrylate (TMPTA), were introduced to PEO electrospinning solution with different composition ratio. Fibrous mats of PEO/crosslinker were prepared by electrospinning and then were subjected to UV-irradiation. The kinetics of the photo-crosslinking reaction was studied by means of photo-DSC and FTIR spectroscopy. The crosslinking efficiency was evaluated by insoluble fraction measurements and FE-SEM imaging. Moreover, the effect of the crosslinker type and amount on the PEO electrospun membranes properties was studied through structural, thermal and mechanical characterizations.

The fibrous membrane composition and fabrication process were optimized in order to obtain efficiently photo-crosslinked PEO electrospun fibers exhibiting high stability and solvent resistance. The optimized PEO-based system was subjected to further thermal and mechanical characterizations in view of its application as a potential phase change material (PCM). PCMs are smart materials that can store and retrieve energy during their transition from one phase to another over a slight change of the temperature. Among organic PCMs, the polyethylene glycol family (including PEO) has been extensively investigated due to high latent enthalpy, biocompatibility and inertness. The developed PEO-based electrospun mat was subjected to several thermal cycles over its melting point, and the melting enthalpy, the crystallinity and the shape retention properties were particularly characterized. Furthermore, the mechanical and thermo-mechanical properties of the modified

PEO fibrous membranes were examined. The results showed a promising solid-solid form-stable PEO fibrous structure to be applied as PCM.

The work presented in this section has been partly published in [91,273] confirming the importance and the request for an in-depth study on the preparation of solvent resistant and shape-stable PEO-based fibrous membranes, as well as the relevance of these innovative systems in advanced applications (such as PCMs).

## 4.2 Introduction

PEO is an abundant semi-crystalline and thermoplastic synthetic polymer with general formula of  $(-O-CH_2-CH_2-)_n$ . It is commercially available in a wide range of molecular weights from tens of repeating units (in this case the polymer is called polyethylene glycol, PEG) to higher than a million [274]. This polymer is colorless, odorless, stable against heat and hydrolysis, and inert to many chemical reagents. The biocompatibility, non-immunogenicity, alongside physicochemical properties of PEO, make this polymer an excellent candidate for biomedical fields, particularly as scaffolds in tissue engineering [275,276], biocompatible coatings [277–279] and pharmaceutical applications [280]. Additionally, PEO has been applied in other application fields, such as filtration for CO<sub>2</sub> separations [281–283] and energy storage applications particularly as separator in lithium ion batteries [284,285]. However, as already explained in the previous chapter, PEO is soluble in water as well as in almost all organic solvents limiting its domains of applicability [275]. Accordingly, crosslinked form of PEO has enlarged its possibility of use in aforementioned fields. such as wound dressings [286,287], drug delivery systems [288], filtration, membranes with controlled permeability and many others [263].

Crosslinking of PEO can be categorized in the three subgroups: i) crosslinking by gamma irradiation [258], for which Paul A. King in 1961 patented induction of PEO crosslinks in degassed dilute aqueous solution [259,289]; ii) chemical crosslinking [257] by the introduction of functional end-groups in the structure or by addition of a low molecular weight crosslinker [290]; iii) crosslinking by UV irradiation [261,291], which is an eco-friendly technique applicable to PEO in solid state or in solution [262]. It has been shown that PEO can be crosslinked by UV-irradiation with or without photo-initiator. Upon UV irradiation, in fact, hydrogens can be abstracted from the PEO carbon chain and radicals are generated, the combination of these radicals yields a crosslinked network (**Figure 4-1**). Doytcheva et al. [292], in their work examined the effects of different photo-initiators (namely benzophenone (BP), acetophenone (AP), benzoin methyl ether (BME), benzoin (Bn), Darocur<sup>®</sup> 1173, Darocur<sup>®</sup> 1116, Darocur<sup>®</sup> 953 and Darocur<sup>®</sup> 1664) on crosslinking efficiency of PEO. It was demonstrated that benzophenone with concentration of 0.4 wt.% to 4 wt.% resulted in the system with the highest insoluble fraction. The crosslinking homogeneity along the thickness was also examined by irradiating the samples on one side and on both sides: as expected, the samples that received the UV light only on one side showed a non-homogeneous crosslinking distribution [290,292]. It is worth noting that PEO can also undergo

chain scission upon UV irradiation leading to breaking of the C–O bonds and generating a pair of free radicals. In general, in bulk the chain scission predominates over crosslinking [262,274,291]. The competition between the chain scission reaction and crosslinking reaction during the UV irradiation greatly depends on irradiation time, photo-initiator concentration and oxygen presence. Accordingly, the addition of a crosslinking agent can accelerate the photo-induced reaction limiting the degradation of PEO due to chain scission [262,288,293].

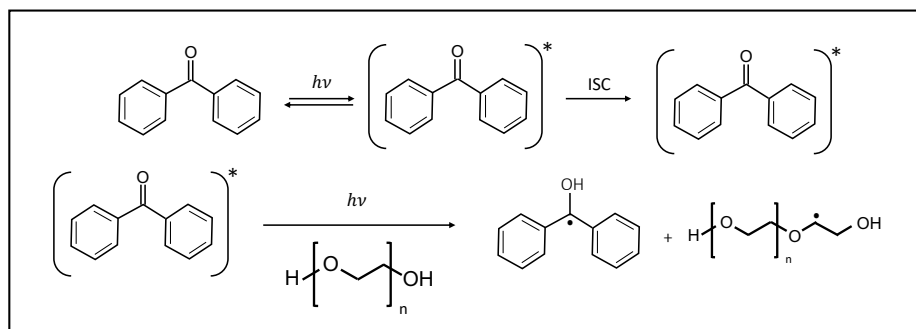


Figure 4-1 radical generation upon UV irradiation of PEO in the presence of a photo-initiator (e.g., benzophenone)

Regarding the electrospinning of PEO, in the literature this polymer is mainly used as a carrier/template for non-electrospinnable or hardly electrospinnable polymers, such as chitosan [294,295], alginate [296,297], collagen [298], hyaluronic acid [108], keratin [299], and PTFE [300]. In many of these works, PEO is then extracted from the electrospun structure through washing or calcination [108,296].

The photo-crosslinking of PEO electrospun membranes as its own by using an acrylic crosslinker (i.e., pentaerythritol triacrylate) has been studied in few works [301,302], however the crosslinking efficiency and the fibrous morphology retention of the fibers were not assessed. For instance, Şimşek et al. [303] proposed PEO-based electrospun membranes as a coating for metallic implants; although the fibrous coating was crosslinked, after immersion in distilled water its morphology was lost. Therefore, the optimization of a crosslinking process that allows the enhancement of the solvent resistance of PEO electrospun membranes and the retention of their fibrous morphology when in contact with solvents is indeed of great interest as well as very challenging.

A potential application for crosslinked PEO electrospun systems can be found in phase change materials (PCMs). PCMs are functional materials that can absorb and retrieve a large amount of latent heat during their changing phase (i.e., liquid-gas, liquid-solid, solid-solid) over a narrow temperature change in response to the environment temperature variations. The crucial properties of an ideal PCM are a suitable transition temperature, large phase change enthalpy, proper thermal conductivity, cyclic durability, shape stability during phase transition, as well as availability and low costs [304–308]. This class of materials has been applied in smart buildings[309], food and pharmaceutical packaging [310], heat management in electronic devices [311], temperature regulating textiles [312–314], biomedical field [315] and also in solar energy storage [316]. Among the organic PCMs,

polyethylene glycol (PEG) family (thus including higher molecular weight PEO) has been one of the most diffused polymer due to its high latent enthalpy, tunable transition temperature thanks to the wide range of molecular weight (especially in the low-mid temperature range, meaning 0-100 °C), chemical stability, biocompatibility, inertness, non-toxicity and competitive price [316–318]. However, PEG- and PEO-based PCMs suffer from shape instability in the melted state as well as low thermal conductivity, which hinder their commercial applications. Consequently several approaches have been proposed in order to develop shape-stable PEG- and PEO-based PCMs, such as embedding PEG in a polymer matrix with higher melting temperature over the range of the specific application, macro, micro or nano-encapsulation in polymeric or inorganic shells [309,319] [320], preparing composites and blends [321,322], shell, and using chemical methods such as grafting [323], crosslinking [324,325] and copolymerization [326].

Accordingly, electrospinning can be used to incorporate PCMs into fibrous structures [327]. As a result, electrospun phase change fibers characterized by high flexibility, controllable morphology, specific high surface area and lightness can be obtained, introducing new domains of applicability of such materials. Electrospun fibrous PCMs are particularly interesting for the temperature regulating properties with application in smart fabrics [328–330], packaging [331], biomedical applications [332], heat storage/retrieval system [333–335]. Relevantly, shape stabilization in electrospun systems has been realized through the polymer blending, copolymerization, or by core-shell systems [329], in all of the examples a second polymer phase is required. A simple way to fabricate shape-stabilized electrospun PEG- or PEO-based PCMs that uses a single polymer system is thus envisaged.

Therefore, in this work, in the first part, photo-crosslinking of PEO electrospun nanofibrous mats containing an acrylic crosslinker was investigated. Two multifunctional acrylic monomers, namely polyethylene glycol diacrylate (PEGDA) and trimethylol propane triacrylate (TMPTA), were introduced in different contents as crosslinking agents in PEO electrospinning aqueous solutions, together with benzophenone as photoinitiator. The electrospun mats were then irradiated with UV light, and the photo-crosslinking reaction kinetics and its efficiency were studied through photo-differential scanning calorimetry (photo-DSC), Fourier transform Infrared (FTIR) spectroscopy and insoluble fraction measurements. Photo-crosslinking reaction was used to enhance the properties (e.g., chemical, thermal and mechanical properties) of the nanofibrous membranes, in particular their solvent resistance, and thus enlarge their applicability domain. A comprehensive characterization encompassing morphological analysis, thermal and mechanical properties, permeability and water resistance, of the photo-crosslinked membranes was conducted.

Then, in the second part of the work, the optimized PEO-based electrospun photo-crosslinked system is subjected to further mechanical and thermal characterization to assess its suitability as a potential shape-stable nanofibrous PCM.

## 4.3 Materials and methods

### 4.3.1 Materials

High molecular weight polyethylene oxide ( $M_w$  1,000,000 g/mol), benzophenone ( $\geq 99\%$ ) as a photoinitiator, polyethylene glycol diacrylate ( $M_w$  575 g/mol, viscosity 57 cP) and trimethylolpropane triacrylate ( $M_w$  296 g/mol, viscosity 70-12 cP) as acrylic crosslinkers were purchased from Sigma-Aldrich. The molecular structures of the materials are shown in **Figure 4-2**.

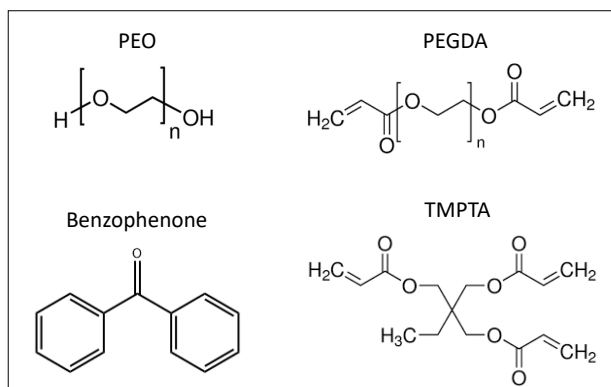


Figure 4-2 Molecular structure of PEO polymer, PEGDA and TMPTA acrylic crosslinkers, and benzophenone photo-initiator.

### 4.3.2 Sample preparations

PEO 5 wt.% aqueous solution was prepared and homogenized through magnet-stirring overnight. Multifunctional acrylic crosslinker PEGDA or TMPTA was added to the PEO aqueous solution. Prior to the electrospinning process, benzophenone as a photo-initiator (2 wt.%) was also added to the PEO/crosslinker solutions.

PEO/PEGDA and PEO/TMPTA solutions were prepared with different composition ratios (as detailed in Table 1), in a way to have similar ratio of double bonds over ethylene oxide groups ( $C=C/EO$ , mol/mol). Three composition ratios for  $C=C/EO$  were used: 1)  $C=C/EO = 0.065$ , which refers to the lowest crosslinker content and samples with this composition ratio are called L-PEGDA and L-TMPTA; 2)  $C=C/EO = 0.15$  corresponds to the medium crosslinker content and samples are called M-PEGDA and M-TMPTA; and 3)  $C=C/EO = 0.35$  composition ratio, associated to the samples containing the highest crosslinker content which are called H-PEGDA and H-TMPTA. The PEO/PEGDA samples have weight ratio of 70/30, 50/50 and 30/70 for L-PEGDA, M-PEGDA and H-PEGDA respectively; while PEO/TMPTA samples have weight ratio of 87.5/12.5, 75/25 and 55/45 for L-TMPTA, M-TMPTA and H-TMPTA, respectively. **Table 4-1** summarizes the composition of the 6 PEO/crosslinker samples.

Table 4-1 Composition details of the investigated samples.

Sample name	C=C/EO ratio (mol/mol)	Crosslinker	Composition	
			PEO (wt.%)	Crosslinker (wt.%)
L-PEGDA	0.065	PEGDA	70	30
M-PEGDA	0.15	PEGDA	50	50
H-PEGDA	0.35	PEGDA	30	70
L-TMPTA	0.065	TMPTA	87.5	12.5
M-TMPTA	0.15	TMPTA	75	25
H-TMPTA	0.35	TMPTA	55	45

### 4.3.3 Electrospinning procedure

Electrospinning was carried out by an E-fiber electrospinning system SKE apparatus in horizontal setup, equipped with high voltage power supply, a programmable syringe pump and a stationary collector. The fibers were deposited on an aluminum foil. Electrospinning was conducted at room temperature by applying a voltage of 8-14 kV (14 kV for pure PEO and lower voltage for PEO/PEGDA and PEO/TMPTA), a flow rate of 0.1-0.2 ml/h, and a tip-to-collector distance of 15 cm. Fibrous mats with thickness of 10–100  $\mu\text{m}$  were fabricated. The thickness of the electrospun mat was measured by digital micrometer.

### 4.3.4 Film Casting

Some PEO/crosslinker solutions were also employed to obtain flat continuous films by solution casting. The solutions were cast onto a glass Petri dish and water was left to evaporate for 48 h before testing.

### 4.3.5 Photo-curing process

UV-curing was performed by a medium pressure mercury lamp (Dymax ECE UV-Curing flood lamp) delivering a UV intensity of 70  $\text{mW}/\text{cm}^2$  on the sample surface. During the UV-irradiation,  $\text{N}_2$  gas was purged into the curing chamber in order to prevent photo-oxidation and oxygen quenching phenomena. The UV intensity was measured by a UV Power Puck<sup>®</sup> II from EIT<sup>®</sup> Instrument Markets.

### 4.3.6 Characterization

The photo-crosslinking reactions were analyzed by means of photo-DSC using a DSC1 STARe Mettler Toledo system equipped with a high-pressure mercury-xenon lamp (LIGHTNINGCURE Spotlight source LC8, Hamamatsu). Prior to the experiment, 5-10 mg of sample were placed in an uncovered crucible and left at dark for a couple of hours for complete solvent evaporation. Photo-DSC measurement was performed in two steps: first, isothermal condition at 25  $^{\circ}\text{C}$  at



constant flow of N<sub>2</sub> at 60 ml/min without UV irradiation for one minute was applied, then a UV light with an intensity of 200 mW/cm<sup>2</sup> was irradiated on the sample surface under same isothermal conditions and N<sub>2</sub> flow. For all samples a second photo-DSC run was performed as a baseline.

During the measurement, the heat flow evolution versus time during the photo-crosslinking reaction was monitored and recorded. Photo-DSC was also carried out on pure PEO, pure PEGDA and pure TMPTA. The heat evolution of pure PEGDA and pure TMPTA was used to calculate the conversion of acrylic groups upon the UV irradiation, by knowing the required energy for converting 1 mol of vinyl groups (which is equal to 86 kJ/mol [336]).

The fiber morphology was monitored by Field Emission Scanning Electron Microscopy (FE-SEM), using a Merlin FE-SEM, ZEISS. Samples were sputter-coated with a thin Cr film (~10 nm thick) prior the imaging using a Quorum Q150T ES sputter coater. The size distribution of fiber diameters was obtained by ImageJ software analyzing the FE-SEM images, approximately ~100 measurements were performed for each sample. The fiber morphology and solvent resistance of the fibers were examined by placing a drop of water on a sample surface and allowing it to get dried before FE-SEM imaging. The full width at half maximum (FWHM) of the size distribution curve was calculated using ImageJ software and DiameterJ plugin [337].

Chemical bonds and structure of the fibers prior and after UV-curing were assessed by FTIR spectroscopy in Attenuated Total Reflectance (ATR) mode, using a Thermo Scientific Nicolet iS50 spectrometer with a diamond crystal. All spectra were collected with an accumulation of 32 scans at the resolution of 4 cm<sup>-1</sup>. The peak bands and areas were quantified through the Omnic software. The normalization was performed with respect to the peak at ~845 cm<sup>-1</sup>, characterized as the least affected band during the UV-curing [338,339].

Conversion of functional groups of acrylic monomers was obtained by calculating the area *A* of absorption band of the reactive group (C=C of the acrylate group at around 1640 cm<sup>-1</sup>) in FTIR spectrum with respect to the area *A* of a constant signal (C=O carbonyl peak at around 1720 cm<sup>-1</sup>). Percent C=C conversion is calculated by Eq1:

$$Conversion \% = \left( 1 - \frac{|A_{C=C/A_{C=O}}|_t}{|A_{C=C/A_{C=O}}|_{t=0}} \right) \times 100 \quad Eq1$$

The insoluble fraction of photo-cured electrospun mats was measured by immersing the electrospun samples wrapped in a metallic mesh in distilled water (i.e., the solvent for the un-crosslinked constitutes) for 24 h, drying the samples at room temperature for 48 h, and gravimetrically calculating the mass loss of the fibers.

The structural properties of the electrospun mats were examined using a Triton Technology instrument. The DMTA was carried out in tensile configuration, in the temperature range of -100 °C to 80 °C with a heating rate of 3 °C/min at a frequency of 1 Hz. The glass transition temperature (*T<sub>g</sub>*) values of the electrospun samples were obtained from the maxima of tan δ curve.

The classic rubbery theory is applied to estimate the crosslinking density  $\nu$  by Eq2:

$$G' = \nu RT \quad \text{Eq2}$$

where  $G'$  is the shear modulus,  $\nu$  is the crosslinking density (mmol/cm<sup>3</sup>),  $R$  and  $T$  are the gas constant (J/(K.mol)) and absolute temperature (K), respectively. The crosslinking density  $\nu$  was calculated at the temperature of 40 °C, in which all samples have reached their rubbery plateau after their glass transition temperature.  $G'$  can also be written as Eq3 by having  $E'$  from DMTA measurement:

$$G' = \frac{E'}{2(1+\nu_p)} \quad \text{Eq3}$$

By considering the Poisson ratio of rubbery materials as  $\sim 0.5$ , Eq4 is obtained:

$$G' = \frac{E'}{3} \quad \text{Eq4}$$

Additionally, for the samples proposed for PCM application, DMTA was carried out using a TA DMA Q800 (TA Instruments) equipped with 16 N load cell. Scans were performed in the temperature range from -80 °C to 100 °C, at a rate of 3 °C/min with a strain amplitude of 0.005% and a frequency of 1 Hz. For evaluating if the differences between different formulations are significant and meaningful, the single-factor analysis of variance (ANOVA) was performed. For this, formulations three replicates for each sample were measured.

In order to analyze the photo-crosslinking effects on melting temperature ( $T_m$ ),  $T_g$  and degree of crystallinity ( $X_c$ ), differential scanning calorimetry (DSC) was performed using a DSC1 STARe Mettler Toledo instrument. Experiments were conducted in the temperature range of -60 °C to 190 °C with a heating rate of 20 °C/min in 6 steps: 5 minutes isothermal step at -60 °C, heating from -60 °C to 120 °C, 5 minutes isothermal step at 190 °C, cooling from 190 °C to -60 °C, 5 minutes of isothermal step at -60 °C and heating up to 190 °C.  $T_m$  was measured by the maximum of the endothermic peaks,  $T_g$  was obtained from the midpoint of the heat increment in the second heating cycle, and  $X_c$  was measured by calculating the enthalpy of fusion in the second heating cycle ( $\Delta H_m$ ) with respect to the enthalpy of fusion for a 100% crystalline PEO sample ( $\Delta H_m^0$ ), which is 196 J/g [340], at the equilibrium melting point ( $T_m^0$ ), by Eq5:

$$X_c = \frac{\Delta H_m(T_m)}{\Delta H_m^0(T_m^0)} \quad \text{Eq5}$$

Moreover, in order to understand the durability and long-term stability of the PEO-based electrospun mats, cyclic DSC with 50 heating-cooling cycles in the temperature range of 0 °C to 100 °C was performed. Also in this case, melting and crystallization enthalpies were calculated as the area of the melting and crystallization peak, respectively.

Thermal stabilities of the fabricated electrospun fibers were evaluated by thermogravimetric analysis (TGA). TGA was performed using a Mettler Toledo TGA/SDTA 851<sup>e</sup> apparatus. Samples were heated up from 25 °C to 700 °C with a heating rate of 10 °C/min under constant flow of N<sub>2</sub> as a purge gas at flow of 60 ml/min in order to prevent the thermo-oxidative process. The first derivative of the TGA profile was calculated to identify the decomposition temperature of the fibers constitutes.

In order to evaluate the morphology retention and shape-stability of the crosslinked PEO-based electrospun fibers, thermal cycling was also conducted on the membranes using a climatic chamber DiscoveryMy DM340 C (Angelantoni Test Technologies Srl). Specimens with 1 cm<sup>2</sup> surface area were subjected to 80 thermal cycles in the temperature range from 0 °C to 100 °C at 3 °C/min. Samples were analyzed by FE-SEM imaging after 1, 20 and 80 thermal cycles to evaluate their shape-stability.

The tensile strength of the samples and their elongation at break were examined using an INSTRON 3366 electromechanical universal testing machine (ITW Test and Measurement Italia S.r.l., Instron CEAST Division) equipped with 10 kN load cell. After peeling off the fibrous mats from the aluminum substrate, membranes were cut to obtain samples with dimensions of 30 mm in length, 8 mm in width and thickness of 10–40 µm, which were then placed between the clamps. Measurements were performed in ambient conditions by applying a constant stretching speed (5 mm/min), at least three replicates were tested for each sample. During the tensile testing, the stress (through machine-recorded force) and strain (the displacement based on initial cross-section area and gauge length) were measured and the Young's modulus  $E$  was calculated based on the initial linear elasticity regime of the stress-strain curves.

For the samples proposed for PCM applications, the mechanical characterizations were conducted using a TA DMA Q800 (TA Instruments) equipped with 16 N load cell. The specimens were subjected to a pre-load of 0.005 N and displacement rate of 500 µm/min. The elastic modulus ( $E$ ) was calculated as the slope in the initial linear regime of stress-strain curve.

The permeability of the electrospun mats was evaluated by ASTM E96/E96M-16 standard [341]: an open mouth vessel containing distilled water was used to seal the electrospun mat on the top with an air space of  $19 \pm 6$  mm from the water surface. The test assembly was kept in a controlled atmosphere (relative humidity (RH) = 45% and temperature = 25 °C), and by periodic gravimetric method the water loss was obtained. The water vapor transmission (WVT) was calculated by Eq6:

$$WVT = \frac{W}{tA} \quad Eq6.$$

in which  $W$ ,  $t$  and  $A$  are the weight change (g), time (h), and the test area (vessel mouth area) (m<sup>2</sup>) respectively.

## 4.4 Results and discussion

### 4.4.1 Study and optimization of the PEO-based fibrous membranes

In this work, as represented in **Figure 4-3** fibrous mats were produced by electrospinning of PEO added of two different acrylic crosslinkers (i.e., PEGDA and TMPTA) and then irradiated to promote the radical curing of the material. It is worth noting that both acrylic crosslinkers are non-toxic, and provoke minimal immune system response, with application in biomedical, pharmaceutical and

environmental fields [342–344]. Moreover, distilled water has been used as the only solvent, which makes the fabrication process green.

PEO/PEGDA and PEO/TMPTA blend solutions were used with different composition ratios (Table 1), and the effect of the functionality and amount of crosslinker on the photo-crosslinking reaction and on the fibrous membrane properties was evaluated.

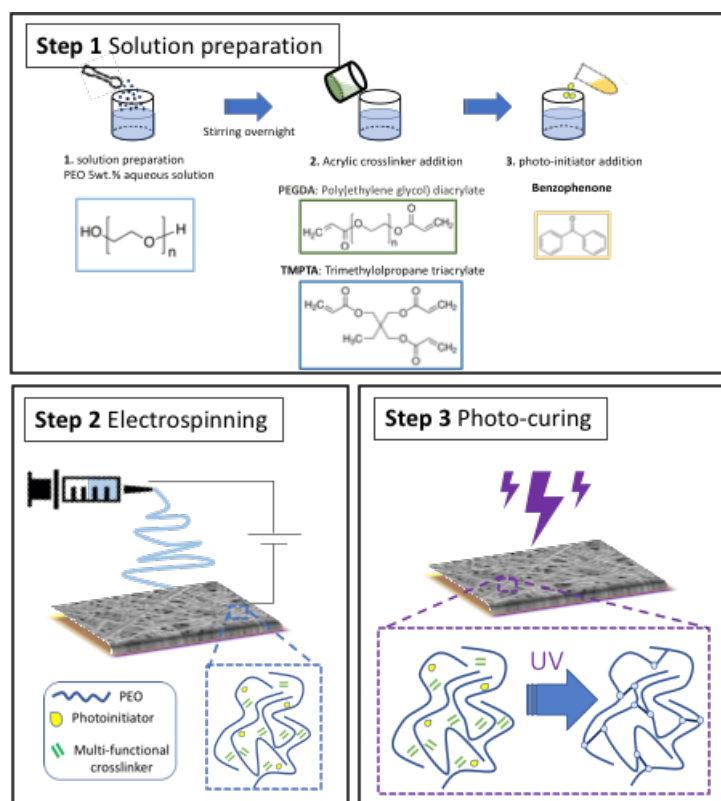


Figure 4-3 Schematic illustration of the electrospinning solution preparation, the electrospinning process and the photo-curing process

### Electrospun mat morphology

The fibrous morphology of the fabricated PEO/PEGDA and PEO/TMPTA electrospun mats (after UV irradiation) was analyzed by FE-SEM. As can be seen in **Figure 4-4a**, the crosslinker addition did not interfere with fiber fabrication during electrospinning process, and fine fibers were acquired from all the formulations with low to high content of multifunctional crosslinker (**Figure 4-4a**). However, the PEO/PEGDA systems show fibers with inhomogeneities and irregular shapes, compared with PEO/TMPTA fibers that have a uniform and regular morphology.

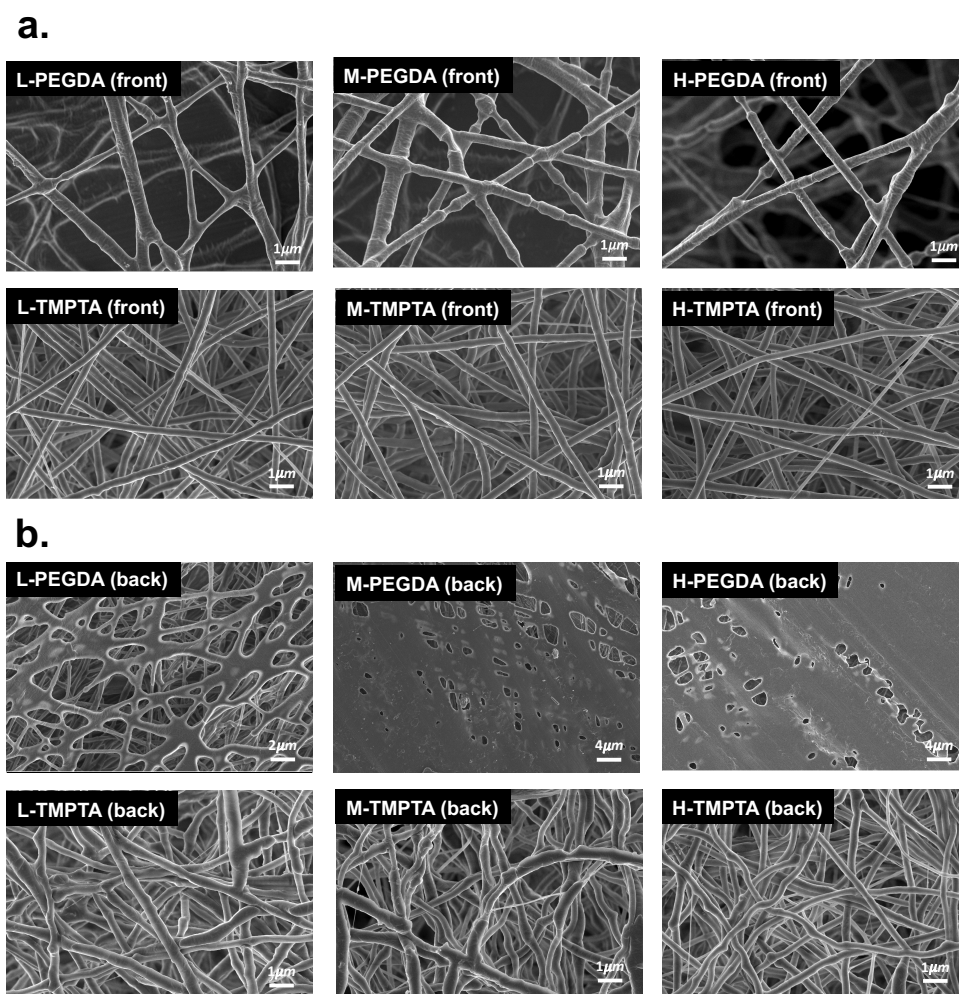


Figure 4-4 Morphology of the PEO-based photo-cured electrospun fibrous mats with different type of crosslinker and different composition ratio of PEO/crosslinker (L-PEGDA, M-PEGDA, H-PEGDA and L-TMPTA, M-TMPTA, H-TMPTA). (a) FE-SEM images of the front side (top surface) of the membranes. (b) FE-SEM images of the back side (bottom surface) of the membranes.

In order to evaluate the uniformity of the electrospun mats alongside their thickness, the membranes were analyzed by FE-SEM also on their backside. To do so samples were carefully peeled off from the aluminum substrate and flip over prior to the FE-SEM imaging (**Figure 4-4b**) (the FE-SEM images of the cross-section of two samples of H-PEGDA and H-TMPTA are shown in Appendix A). The PEO/PEGDA samples exhibit a completely different morphology on the two sides. By increasing the PEGDA content, the back side tends to be like a semi-film, and in particular the back side of M-PEGDA and H-PEGDA is in the form of a semi-film and the fiber morphology is completely lost. In fact, 50 and 70 wt.% of liquid crosslinker in the formulation is too much to obtain solid fibers upon electrospinning: the liquid crosslinker tends to flow as soon as it reaches the collector, leading to the collapse of the fiber shape. Whereas, for the PEO/TMPTA electrospun mats, the fiber morphology can be detected also on the back side: the fibers are well-shaped and uniform even on the first layers deposited on the collector. This is due to the fact that TMPTA monomer has higher viscosity than PEGDA, and also that TMPTA content in the formulations varies in the range of 12.5 wt.% to 45 wt.%, which is lower compared to PEO/PEGDA systems.

The size distribution of the fibers (on the top surface) is reported in **Figure 4-5a**. The PEO/TMPTA fibers exhibit a narrower size distribution and a smaller average diameter ( $320 \pm 3$  nm,  $357 \pm 3$  nm,  $324 \pm 4$  for L-TMPTA, M-TMPTA and H-TMPTA, respectively); instead, the PEO/PEGDA samples show larger fibers ( $366 \pm 12$  nm,  $483 \pm 11$  nm,  $499 \pm 12$  nm for L-PEGDA, M-PEGDA and H-PEGDA, respectively) and a wider diameter distribution.

The surface porosity of the electrospun membranes was also analyzed by FE-SEM images on both sides (**Figure 4-5b**). For PEO/PEGDA mats the top surface shows a much higher porosity compared to the back side: due to the formation of fibers on the front side and of a semi-film on the back side, a gradient of porosity can be noticed. Moreover, on the back side, the porosity further decreases with the increase of the liquid crosslinker content. As expected, the PEO/TMPTA electrospun mats do not show significant differences between the two sides: the surface porosity is  $\sim 30\%$  for all samples and sides and is independent of the crosslinker content.

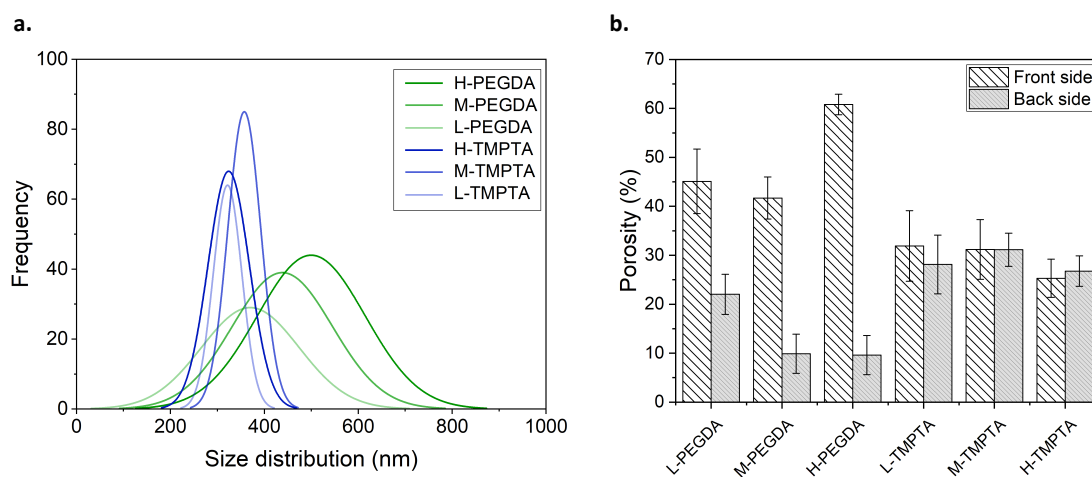


Figure 4-5 (a) Fiber diameters distribution of the top surface of the electrospun mats. (b) Surface porosity of both sides of the fibrous membranes.

### Photo-curing of fibrous mats

Photo-crosslinking of the fibrous membranes was used to enhance their physico-chemical properties (in particular their solvent resistance and morphology stability). After electrospinning, the mats were irradiated to promote radical curing of the material, exploiting both the high reactivity of the acrylic groups of the multifunctional crosslinker and the photo-induced hydrogen abstraction reaction from PEO. The kinetics and efficiency of the photo-curing reaction were studied through photo-DSC, FTIR spectroscopy and the insoluble fraction measurements.

The kinetics of photo-crosslinking can be investigated by photo-DSC by considering that the generated heat during the reaction is proportional to the reaction kinetics. As explained in the experimental section, the photo-DSC was performed at isothermal condition by constant flow of  $N_2$ . Accordingly, the exothermic heat of the photo-induced reaction was measured and recorded over time for all the PEO/PEGDA and PEO/TMPTA formulations, as well as for pure

PEO, PEGDA and TMPTA (all the systems contained the photo-initiator). As can be seen in **Figure 4-6**, all samples showed the typical curve trend of photo-crosslinking (i.e., an asymmetric exothermic peak followed by a stable plateau), including initiation or activation of the reactant species, propagation or reaction of the excited species and termination phase.

Neat PEGDA and neat TMPTA exhibit a fast photo-crosslinking reaction, reaching the plateau in a range of few minutes of UV irradiation (**Figure 4-6a** and **b**, dash lines). The exothermic peak is more pronounced for PEGDA than for TMPTA, meaning higher generated heat in neat PEGDA system. The pristine PEO also shows the occurrence of the photo-crosslinking reaction by an exothermic peak; however, the reaction rate is much lower, and the reaction needs more than an hour to reach a plateau. As explained in the introduction, PEO in solid state in presence of a proper photo-initiator can undergo photo-crosslinking upon UV-irradiation. The photo-DSC curve demonstrates this photo-crosslinking reaction: the initiation of the reaction (i.e., the formations of radicals along the PEO chain), followed by the propagation and a long and slow termination phase, corresponding to the long tail in the curve before the reaching of the plateau.

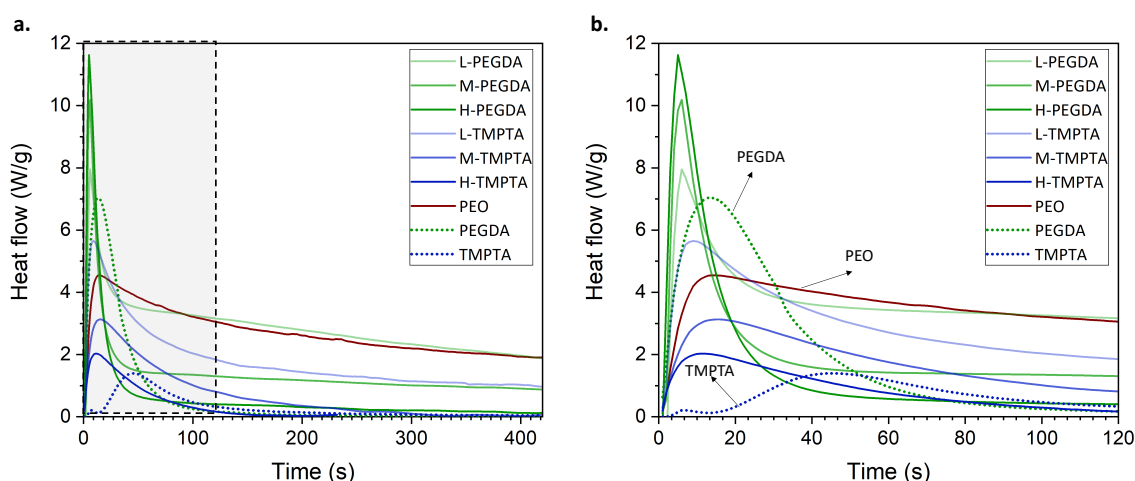


Figure 4-6 a. Photo-DSC of PEO/PEGDA and PEO/TMPTA blends as well as pure PEO, pure PEGDA and pure TMPTA, in presence of photoinitiator, at isothermal condition of 25°C under inert atmosphere of N<sub>2</sub> and irradiation with light intensity of 200 mW/cm<sup>2</sup>. b. reports the photo-DSC curves for the first 120 seconds of irradiation

For the PEO/PEGDA samples, an accelerated reaction rate, compared with the pristine PEO, can be clearly observed in **Figure 4-6**. The curve trend varies depending on the formulation: higher the PEGDA content, sharper the heat flow peak, with smaller reaction tail; similarly, higher the PEO content, wider the exothermic peak and longer the curve tail. As expected, considering that TMPTA initially reacts slower than both PEGDA and PEO, in PEO/TMPTA samples the reaction is not as fast as in PEO/PEGDA systems, and in general the effect of the amount of crosslinker on the reaction kinetics is the opposite than for PEO/PEGDA samples. In fact, lower the amount of TMPTA in the formulation, sharper the exothermic peak. Thus, when the TMPTA content in the formulation is higher, the photo-DSC curve is more similar to that of neat TMPTA, and vice versa for PEO.

In order to quantitatively evaluate the photo-crosslinking reaction, the enthalpy of reaction after subtraction of the baseline was calculated for all samples by photo-DSC curves. The slow reaction of PEO after 80 minutes of irradiation produces ~3000 J/g, while PEGDA and TMPTA produce ~244 J/g and ~110 J/g after 200 and 300 seconds of irradiation, respectively. For the PEO/crosslinker systems, the reaction is more complex, and the generated heat can be due to different reactions between crosslinker and PEO, PEO-PEO chains or crosslinker-crosslinker molecules.

The photo-DSC analysis was performed not only to study the kinetics of photo-crosslinking, but also to determine the required UV dose (i.e., the product of irradiation time and UV intensity) for having a sufficient photo-crosslinking reaction without degrading the material (as demonstrated in the previous chapter for chitosan/PEO systems, the photo-degradation could be detected by photo-DSC measurements). As a result, a UV dose of 84 J/cm<sup>2</sup> was selected, corresponding to 7 minutes of irradiation with a UV intensity of 200 mW/cm<sup>2</sup>. This UV dose was used to irradiate the electrospun mats of PEO/crosslinker.

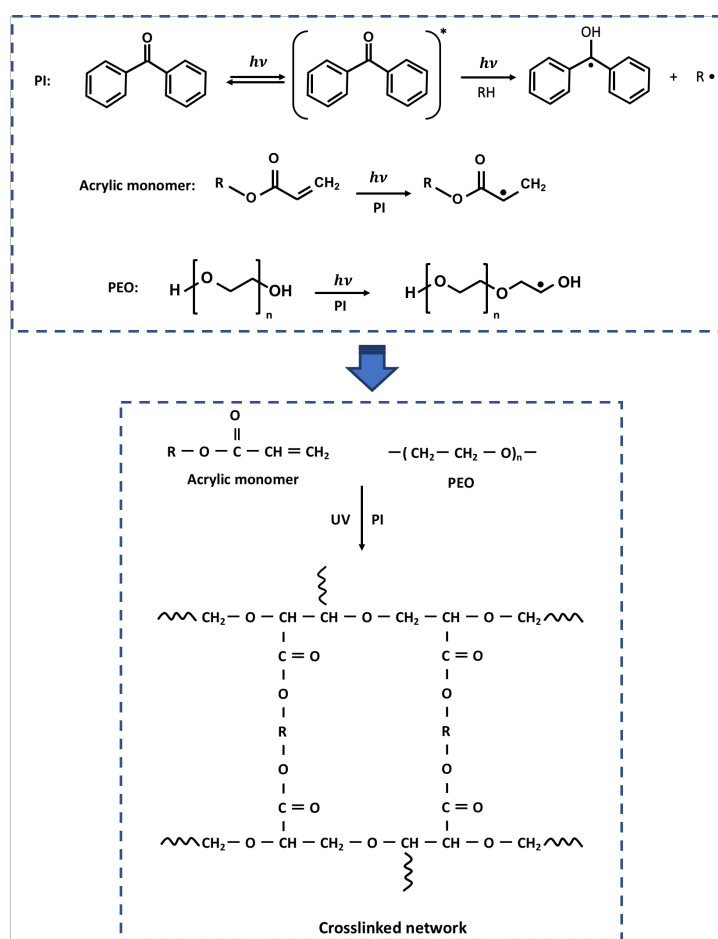


Figure 4-7 Scheme of free-radical photo-crosslinking in presence of an acrylic monomer

The Scheme of photo-induced crosslinking reaction in presence of an acrylic monomer is proposed in **Figure 4-7**. In order to evaluate the chemical structure of the fabricated electrospun membranes and follow the effect of UV-curing, FTIR-ATR was performed prior and after UV-irradiation on the fibrous samples (**Figure 4-8**). **Figure 4-8a** shows the FTIR spectrum of pure PEO as reference and of M-



PEGDA and M-TMPTA samples prior and after UV irradiation (low and high content of crosslinker exhibit similar spectra). In the spectra of the PEO/crosslinker electrospun mats, the presence of PEO is identified by characteristic peaks at 2876  $\text{cm}^{-1}$  (C-H stretching), 1466  $\text{cm}^{-1}$  (C-H bending); 1360  $\text{cm}^{-1}$  and 1341  $\text{cm}^{-1}$  ( $\text{CH}_2$  wagging), 1279  $\text{cm}^{-1}$  ( $\text{CH}_2$  twisting); 1145  $\text{cm}^{-1}$ , 1100  $\text{cm}^{-1}$  and 1060  $\text{cm}^{-1}$  (triplet peak due to C–O–C absorption complex). The identification peaks of PEGDA are found at 1638  $\text{cm}^{-1}$  (double peak due to the stretching of vinyl groups), 910  $\text{cm}^{-1}$  and 1720  $\text{cm}^{-1}$  (C=O absorption band). Similarly, TMPTA spectrum shows peak bands at 1638  $\text{cm}^{-1}$  (vinyl groups) and 1720  $\text{cm}^{-1}$  (intense carbonyl peak).

The FTIR spectra of the photo-cured electrospun mats show a slight shift of the peaks by few wavenumbers for all the samples. For PEO/PEGDA and PEO/TMPTA membranes, the decrease of the peak at 1638  $\text{cm}^{-1}$  associated to the C=C bond of the acrylic functional groups is clearly visible after UV irradiation (**Figure 4-8b**). As reported in **Table 4-2**, the C=C conversion was calculated (by considering the C=O band at 1720  $\text{cm}^{-1}$  as reference peak): as can be seen in **Figure 4-8c** the PEO/PEGDA systems shows higher C=C conversion (~70-80%) than the PEO/TMPTA systems (~40-45%). The particular fibrous mat morphology alongside the branched structure of TMPTA (i.e., higher functionality) can be the possible reasons for the lower conversion rate, leading to the remaining of unreacted functional C=C bonds in the structure. Therefore, some of the TMPTA double bonds do not react during UV-irradiation due to their position in the polymer structure or in the fiber, while a sufficient amount of them takes part to the curing reaction forming a crosslinked network. The FTIR spectra of all samples of PEO/PEGDA and PEO/TMPTA prior and after photo-curing are brought in Appendix A, additionally the C=C conversion of PEO/PEGDA samples in form of cast film was monitored through the real-time FTIR and the results are shown in Appendix A.

The gel content measurement was carried out by gravimetric method through the immersion of the UV-cured electrospun mats of PEO/PEGDA and PEO/TMPTA in distilled water, as it is a good solvent for un-crosslinked PEO and also for TMPTA and PEGDA monomers. **Table 4-2** reports the insoluble fraction results. The weight loss varies from 8% up to 33%, depending on the system. For both PEO/PEGDA and PEO/TMPTA samples, by increasing the crosslinker content in the initial formulation, the insoluble fraction increases. The PEO/PEGDA electrospun samples show comparable insoluble fraction values for medium and high content of crosslinker, and a slightly lower value for the lowest content of PEGDA. Instead for the PEO/TMPTA samples, the difference among samples is more pronounced: the lowest and highest content of TMPTA result in ~68% and ~92% of insoluble fraction, respectively. This can be due to the different concentration of crosslinker in the formulation; in fact, L-PEGDA contains 30 wt.% of crosslinker, while L-TMPTA only 12.5 wt.%.

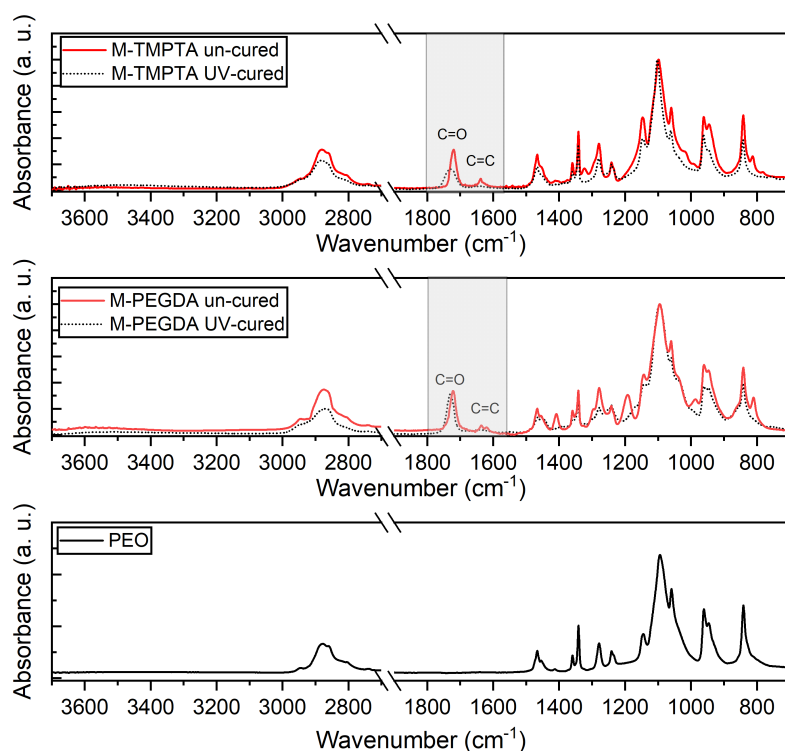


Figure 4-8 ATR-FTIR spectroscopic analyses Spectra of pure PEO, and of M-PEGDA and M-TMPTA electrospun fibrous membranes prior (uncured) and after (UV-cured) UV irradiation.

Table 4-2 C=C conversion and insoluble fraction of PEO/PEGDA and PEO/TMPTA photo-cured fibrous membranes.

Sample	C=C conversion (%)	Insoluble fraction (%)
L-PEGDA	71 % ± 10.5%	76.4% ± 1.8%
M-PEGDA	79 % ± 7.5%	87.4% ± 2.8%
H-PEGDA	76 % ± 2.1%	88.3% ± 2.6%
L-TMPTA	40.5% ± 0.7%	67.7% ± 0.5%
M-TMPTA	44.6% ± 3.9%	76.0% ± 3.3%
H-TMPTA	42.6% ± 3.3%	92.0% ± 2.0%

DMTA experiments were carried out in order to evaluate the crosslinking density  $\nu$  of the UV-cured membranes. For this purpose, we considered the electrospun mats as plain films and by applying the classic rubbery theory the crosslinking density was calculated. However, it should be noted that the electrospun structures are porous and compressible and thus the calculation was used only as rough estimation. **Table 4-3** reports the calculated values of the crosslinking density at the quasi-plateau regime after the glass transition. For all samples the crosslinking density was obtained in the range of  $10^{-3}$  to  $10^{-2}$  mol/cm<sup>3</sup> confirming the formation of an adequately crosslinked network. The one-way ANOVA performed: samples showed that variation within each group (formulation) is comparable with the variation between different groups, (P-value  $\sim 0.2$ ). As a result, these values all belong to the same group of data and cannot be interpreted based on the crosslinker type and the amount of bifunctional or

trifunctional acrylic monomer (the ratio of double bonds to ethoxy group C=C/EO) in the formulation.

Table 4-3 Crosslinking density  $\nu$  of PEO/PEGDA and PEO/TMPTA photo-cured fibrous membranes by considering the membranes as plain films.

Sample	$\nu$ at 40 °C ( $10^{-3}$ mol/cm <sup>3</sup> )
L-PEGDA	3.9
M-PEGDA	9.4
H-PEGDA	4.4
L-TMPTA	6.5
M-TMPTA	11.0
H-TMPTA	4.1

### Characterization of the photo-cured fibrous mats

The electrospun samples were characterized thermally through DMTA, DSC and TGA. **Table 4-4** summarizes the thermal properties of PEO, PEO/PEGDA and PEO/TMPTA fibrous membranes.

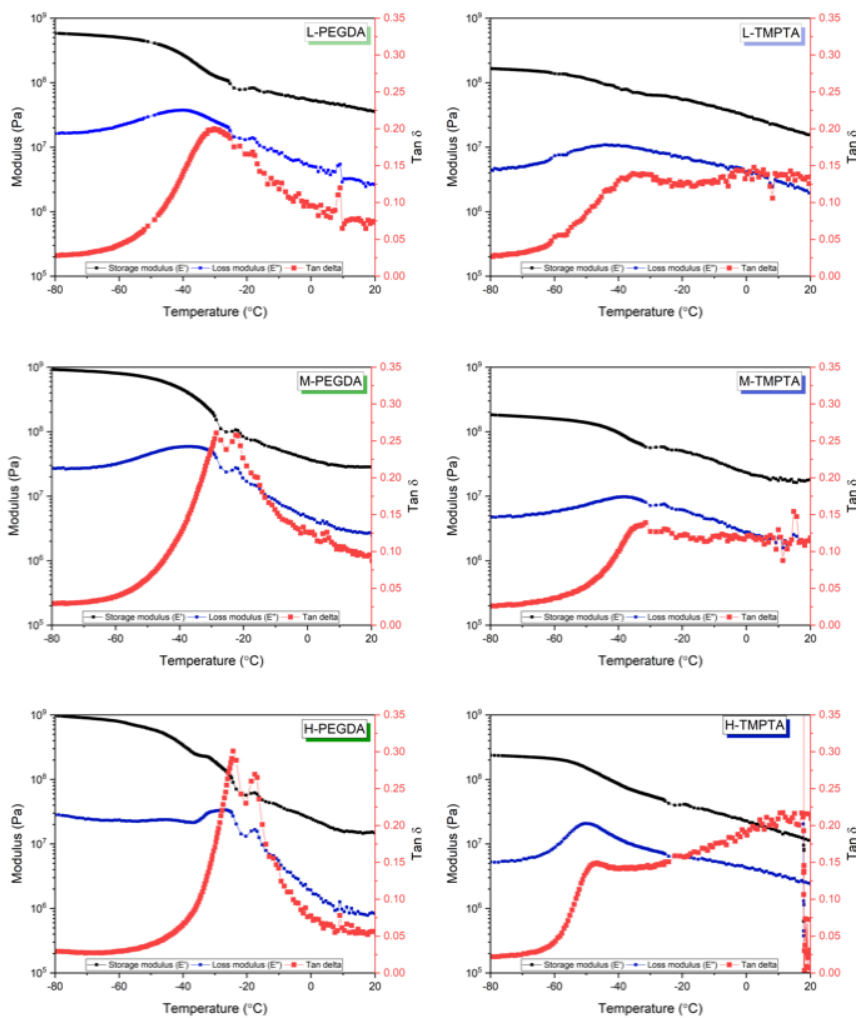


Figure 4-9 DMTA curves of PEO/PEGDA and PEO/TMPTA samples.

The  $T_g$  values of the investigated systems were obtained by DMTA (**Figure 4-9**). The  $T_g$  of pure PEO was found at  $-53$  °C. For PEO/PEGDA systems, in general by increasing PEGDA in the initial formulation the  $T_g$  increases. It is worth mentioning that M-PEGDA and H-PEGDA exhibit a dual  $T_g$  transition (Table 4), which can be due to their particular morphology. In fact, the flowing of the liquid crosslinker on the collector leads to the formation of a semi-film at the bottom of the sample that is most likely mainly made of polymerized PEGDA monomer; thus, the separation of PEO and PEGDA constitutes in the sample can be concluded. Due to their crosslinked network structure, the PEO/TMPTA samples also have higher  $T_g$  compared to the uncured PEO sample (**Table 4-4**). Instead, they present an opposite trend of the effect of the crosslinker amount compared to PEO/PEGDA samples: higher is the TMPTA content, lower is the  $T_g$ .

Table 4-4 Thermal properties of PEO/PEGDA and PEO/TMPTA photo-cured fibrous membranes, as well as pure PEO, obtained by DMTA, DSC and TGA analyses.

Sample	$T_g$ (°C) by DMTA	$T_m$ (°C) by DSC		Theoretical $\chi^1$ (%)	$\chi$ (%) by DSC	$T_d$ (°C) by TGA	$T_{10}$ (°C) by TGA
PEO	-53	64		-	62.9	399	380
L-PEGDA	-30.2	61.7	55.3	44.0	39.74	408	368
M-PEGDA	-27 -21.7	62	55.5	31.4	23.99	401	345
H-PEGDA	-24.7 -19	62.7	56.3	18.9	22.63	400	351
L-TMPTA	-34.4	63.48		55.0	61.19	408	358
M-TMPTA	-35.4	61.1	50	47.2	55.34	418	364
H-TMPTA	-47.6	56.15	48.58	34.6	33.22	408	356

<sup>1</sup> Degree of crystallinity

DSC analyses allowed to measure the melting temperature of the PEO/crosslinker electrospun samples (**Figure 4-10**). As reported in **Table 4-4**, almost all samples show a double endothermic peak in the second heating cycles (L-TMPTA peak only exhibits a shoulder): one peak is near PEO melting temperature while the second one is found at lower temperature. This second maximum can be explained by the different microstructure rising from the formation of crosslinks in the sample.

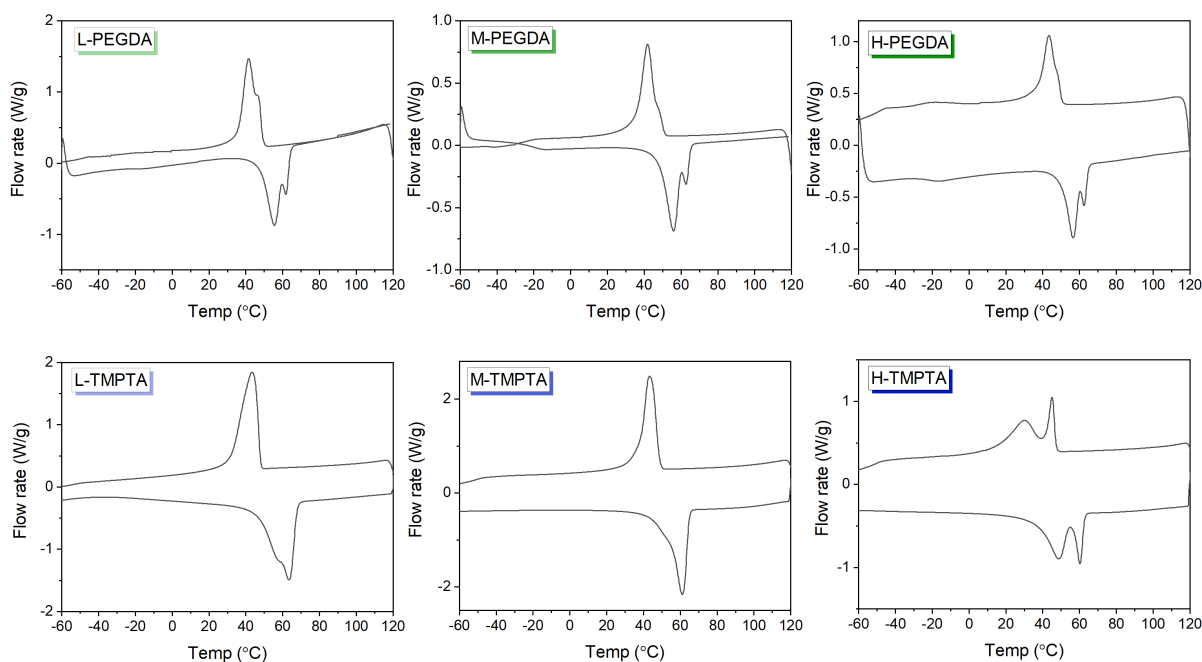


Figure 4-10 DSC scans of PEO/PEGDA and PEO/TMPTA samples

DSC was also used to determine the degree of crystallinity (**Table 4-4**) and assess the effect of the crosslinker and the photo-curing reaction on the morphological structure of PEO/crosslinker electrospun samples. Pure PEO shows  $\sim 63\%$  of crystallinity; as expected, the PEO/crosslinker samples exhibit lower crystallinity degree, considering that only PEO has a semi-crystalline structure while both PEGDA and TMPTA are amorphous. Interestingly, the crystallinity of photo-cured PEO/crosslinker samples is proportional to the PEO content (as evaluated by comparison with the theoretical crystallinity values calculated considering the PEO content in the initial electrospinning formulation), and nor the electrospinning process neither the photo-curing reaction meaningfully affected the PEO crystallinity.

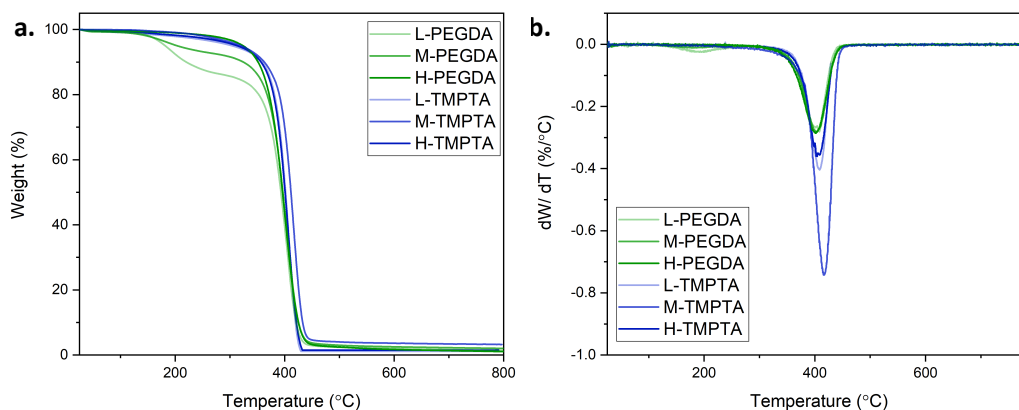


Figure 4-11 TGA thermograms of the PEO/PEGDA and PEO/TMPTA systems

In order to evaluate the thermal resistance of the photo-cured electrospun samples, TGA was carried out. The thermograms are shown in **Figure 4-11** and the

main results are reported in **Table 4-4**. All samples show very high resistance, with a similar decomposition temperatures  $T_d$  (i.e., the temperature 400 °C according to the first derivative): as reported in Table 4, the crosslinked fibrous membranes have a  $T_d$  near 400-418 °C. However,  $T_{10}$  (the temperature at which the material loses 10 % of its initial weight) is shifted to lower temperatures by addition of the crosslinker (**Table 4-4**). Accordingly, this lower temperature of degradation onset can be due to the presence of a crosslinker residue in the system that remains unreacted.

The mechanical properties of the photo-cured PEO-based electrospun samples were investigated through the tensile test. The Young's modulus  $E$  was calculated from the initial linear regime of the stress-strain curve (**Figure 4-12**). As the electrospun samples are porous and compressible, evaluating their thickness is challenging. For this, the specimens thickness was measured in different spots of the samples by a digital micrometer; moreover, the cross section of a sample was analyzed by FE-SEM for checking its thickness and confirming the measurements by micrometer (Appendix A). **Table 4-5** reports the modulus and the elongation at the breaking point for the PEO/crosslinker membranes. All electrospun samples exhibit an elastic deformation, without plastic deformation before their failure. The modulus  $E$  is found in the range of 5 to 40 MPa, thus in agreement with the literature values for electrospun mats of PEO [301,303]. The two systems PEO/PEGDA and PEO/TMPTA show different behaviour in terms of the effect of the amount of crosslinker on the mechanical properties. In PEO/PEGDA system, L-PEGDA presents the highest elongation at the breaking point with the lowest modulus  $E$  (comparable with that of PEO sample), instead M-PEGDA and H-PEGDA show very similar behavior for both tensile strength and strain value at the failure point, having very low extensibility with modulus up to one order of magnitude higher than L-PEGDA.

Table 4-5 Mechanical properties of the electrospun fibrous membranes

Sample	Young's Modulus (MPa)	Elongation at the breaking point (%)
L-PEGDA	6.1 ± 0.9	36.2 ± 6.4
M-PEGDA	36.3 ± 4.6	9.6 ± 3.0
H-PEGDA	34.3 ± 3.4	9.7 ± 1.4
L-TMPTA	33.1 ± 4.5	9.3 ± 1.1
M-TMPTA	14.5 ± 1.1	14.5 ± 2.5
H-TMPTA	11.5 ± 0.3	26.9 ± 1.0

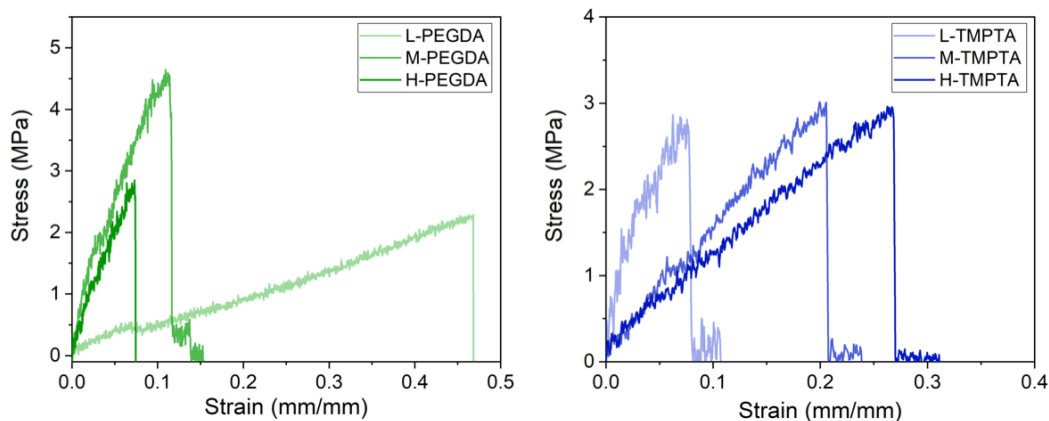


Figure 4-12 Mechanical tensile characterization of photo-cured fibrous mats of PEO/PEGDA and PEO/TMPTA: stress vs. strain curves; one curve for each sample is reported as an example.

The permeability of the photo-cured PEO/crosslinker fibrous mats was assessed through the periodic gravimetric method according to the ASTM E96/E96M-16 standard. The water vapor transmission (WVT) based on the weight of test assembly was monitored for two weeks. As demonstrated in **Figure 4-13**, the PEO/PEGDA membranes exhibit higher WVT and generally by increasing the PEGDA content the WVT value is higher. Interestingly, the packed surface of the bottom layer in M-PEGDA and H-PEGDA (i.e., the semi-film) did not affect the vapor transmission of the membranes and the highest value of WVT is found for the H-PEGDA sample. The PEO/TMPTA samples show lower WVT (compared to PEO/PEGDA system) and very similar values for all three formulations have been obtained. In general, the obtained permeability values are found in the range of 900-1030  $\text{g}\cdot\text{day}^{-1}\cdot\text{m}^{-2}$ . It is worthy to mention that these PEO-based electrospun membranes are porous, and highly permeable and breathable.

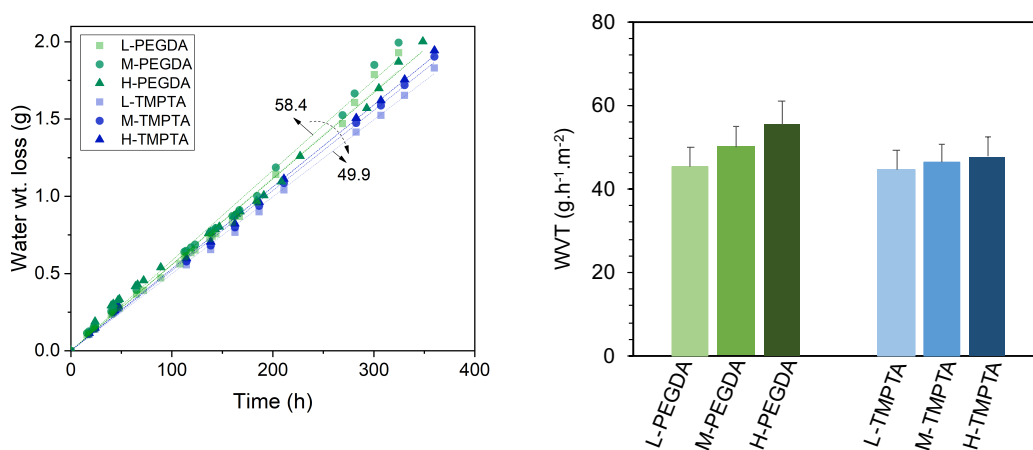


Figure 4-13 Water permeability of the photo-cured electrospun membranes of PEO/PEGDA and PEO/TMPTA. (a) Water weight loss as a function of time. (b) Average measurement of the water vapor transmission WVT after two weeks.

Finally, in order to control the solvent resistance of the photo-cured electrospun fibrous membranes, they were immersed in distilled water and then subjected to FE-SEM imaging once dried. As explained in the introduction part, when PEO

electrospun fibers are placed in contact with a solvent, first the membrane fibrous morphology is lost and then the polymer starts to solubilize in its solvent.

**Figure 4-14** shows the investigated membrane morphology after contact with water. All PEO/PEGDA samples retain the fiber morphology. While for PEO/TMPTA samples, the L-TMPTA membrane clearly loses its fibrous morphology, as could be also predicted from the insoluble fraction results. In fact, although a sufficient number of functional groups are present in the formulation, the crosslinking is not efficient to preserve the fibrous morphology. Whereas M-TMPTA and H-TMPTA electrospun membranes maintain their morphology even after water treatment, without change in fiber diameter sizes.

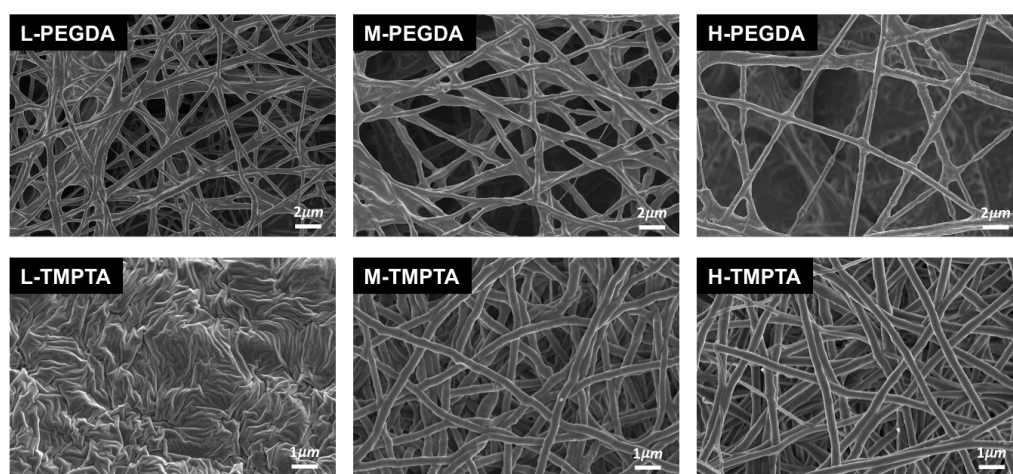


Figure 4-14 FE-SEM images of the photo-cured electrospun fibrous membranes of PEO/PEGDA and PEO/TMPTA after water treatment.

In conclusion, it has been shown that these two systems of PEO/acrylic crosslinker (PEO/PEGDA and PEO/TMPTA) can yield shape-stable fibrous membranes with high water resistance, obtained by electrospinning and subsequent photo-curing, thus allowing to envision wider applications for PEO-based electrospun membranes.

#### 4.4.2 Optimized PEO-based fibrous membranes as PCMs

In the first part of the work, it has been demonstrated that the M-TMPTA formulation can be easily processed by electrospinning obtaining uniform and defect-free membranes formed by fine fibers with an average diameter of  $357 \pm 3$  nm. The photo-crosslinking reaction is efficient and allows to enhance the solvent resistance of the material and obtain completely stable fibrous membranes showing good thermal and mechanical properties. Herein, M-TMPTA photo-cured electrospun membranes are thus selected for further characterization and are proposed as innovative PEO-based shape-stable PCMs.

The electrospun M-TMPTA fibrous membrane is compared with its counterpart in the form of cast film (M-TMPTA-C), and with an electrospun fibrous mat of PEO added only with benzophenone as photoinitiator, i.e., without the crosslinker, (PEO-PI). After electrospinning or casting, the three samples (meaning M-TMPTA,



M-TMPTA-C and PEO-PI) were UV-irradiated with the conditions detailed in Materials and Method section. **Table 4-6** describes the preparation conditions of these three samples.

Table 4-6 List of prepared samples with nominal composition, processing and obtained form.

Sample	Composition	Processing	Form
PEO-PI	PEO; PI	ES + UV-irradiation	Fibrous mat
M-TMPTA	PEO; PI; TMPTA	ES + UV-irradiation	Fibrous mat
M-TMPTA-C	PEO; PI; TMPTA	Film casting + UV-irradiation	Continuous film

### Control of the crosslinking efficiency and mat morphology

In order to assess the effects of the sample composition (i.e., addition of crosslinker) and form (i.e., fibrous membrane vs. continuous film) on the photocuring reaction, the chemical structure of the samples (PEO-PI, M-TMPTA and M-TMPTA-C) was analyzed by ATR-FTIR spectroscopy prior and after UV-irradiation (**Figure 4-15**). As explained above, when PEO is subjected to UV-irradiation, it can undergo chain scission, photo-oxidation and photo-crosslinking. Being irradiated under inert atmosphere, the photo-oxidation can be excluded. Also, in the FTIR spectrum (**Figure 4-15**), the UV-cured PEO-PI sample did not show any degradation feature in terms of disappearance of its characteristic peaks. Instead, a slightly lower intensity of the ether triple peaks at 1000-1180  $\text{cm}^{-1}$ , which can be due to photo-crosslinking phenomena [339], can be detected.

In both systems containing crosslinker, meaning M-TMPTA and M-TMPTA-C, all the characteristic peaks of PEO and TMPTA are present in both spectra, and traces of photo-degradation could not be detected after UV-irradiation. For those two samples, the crosslinking reaction can be followed by the decrease in the intensity of the peak at 1638  $\text{cm}^{-1}$  associated to C=C acrylic functional groups with UV-irradiation. The C=C conversion for M-TMPTA as well as for M-TMPTA-C is quite low (**Table 4-7**): it is found ~45% and ~38% for the fibrous mat and the cast film sample, respectively. As explained above, these values are due to the branched structure of TMPTA crosslinker, leading to inaccessible and remote functional groups.

Table 4-7 Results of C=C conversion (calculated by Eq 1) and gel content measurement

Samples	C=C conversion (%)	Insoluble fraction (%)
M-TMPTA	44.6 ± 4	76.0 ± 3
M-TMPTA-C	38.3 ± 5	95.8 ± 1

The FTIR spectrum of M-TMPTA-C, in addition to the decrease of intensity of the C=C reactive groups band, exhibits a wider triple peak of ether bonds with lower intensity, also indicating crosslinking phenomena [339]. Moreover, the double peak at 1360  $\text{cm}^{-1}$  and 1340  $\text{cm}^{-1}$ , as a crystallinity marker in PEO FTIR spectrum, show lower intensity [339]. The UV-irradiation thus decreases the crystallinity of M-

TMPTA-C, as will be also proved by DSC measurements below. All these changes could not be detected in the case of M-TMPTA; it can then be suggested that the crosslinking efficiency in the cast film M-TMPTA-C is higher than in the homologue electrospun mat M-TMPTA, probably due to the different micro- and nanostructure of the samples.

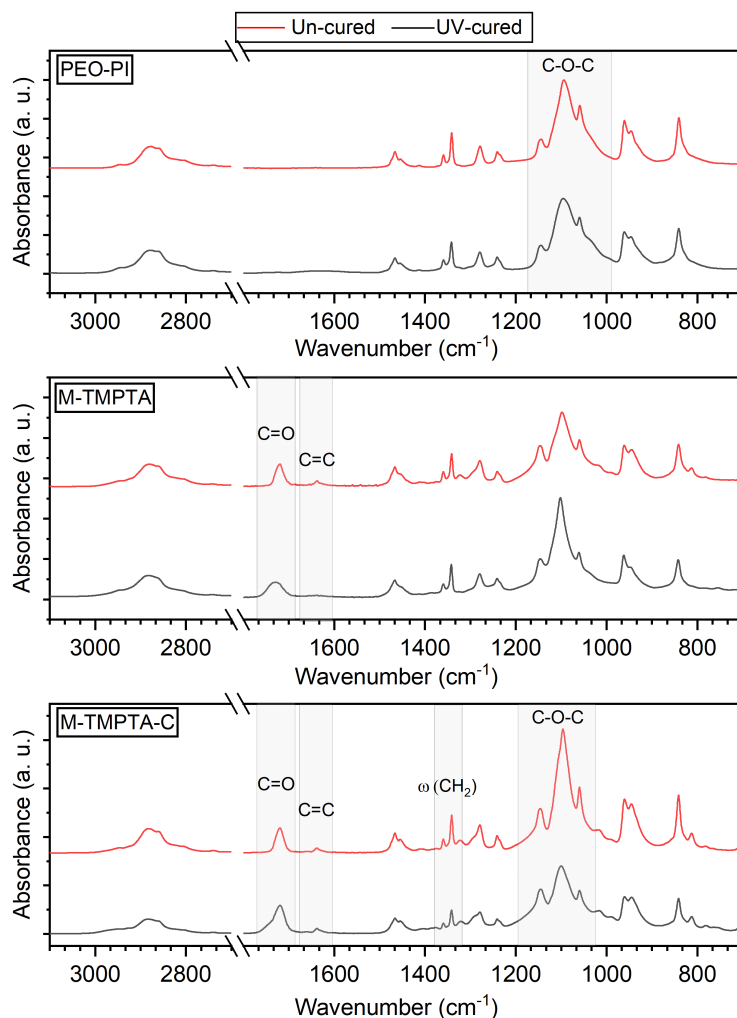


Figure 4-15 FTIR spectra of the PEO-PI, M-TMPTA and M-TMPTA-C

For both M-TMPTA and M-TMPTA-C, despite the low acrylic conversion (**Table 4-7**), the crosslinking reaction is sufficient to yield a cured and solvent resistant sample, as confirmed by the values of gel content, which is found 76% and 96% for M-TMPTA and M-TMPTA-C, respectively. The lower crosslinking in the fibrous structure compared with the cast film was also shown by FTIR results. This effect can lay in the particular fibrous morphology and in the presence of pores that can further reduce the accessibility of the crosslinker molecules in the proximity of each other.

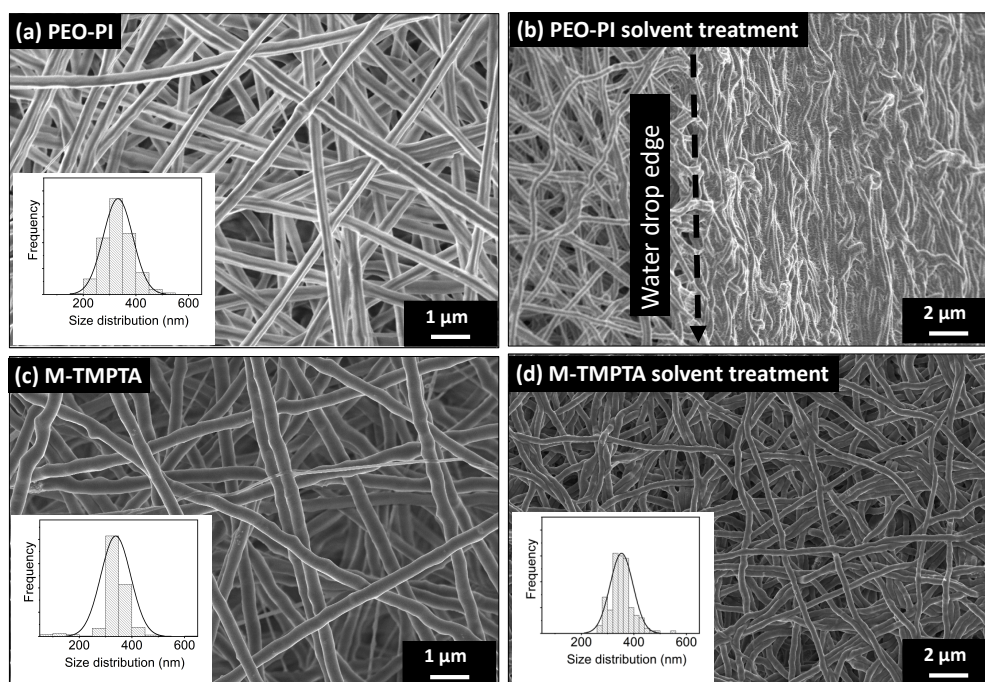


Figure 4-16 FE-SEM images of the PEO-PI (a,b) and M-TMPTA (c,d) fibers after UV-irradiation and after water treatment, the insets are the size distribution of the fibers.

As already explained before, one of the main objectives of photo-induced chemical crosslinking of PEO electrospun mats is to make them insoluble in water as well as other solvents. **Figure 4-16** demonstrates how the morphology of the investigated electrospun samples changes after contact with a drop of water. The fibrous morphology of PEO-PI sample is lost after contact with water (**Figure 4-16a**): the fibers, which have a diameter in range of  $312 \pm 40$  nm, are completely deformed and collapse as soon as they touch the solvent. Whereas, **Figure 4-16b** shows that crosslinked M-TMPTA fibrous system can resist the water treatment, preserving its fibrous morphology. The average fiber diameter is not changed by the contact with water, being  $357 \pm 3$  nm and  $353 \pm 3$  prior and after water treatment, respectively. These results demonstrate that the photo-initiator alone cannot yield an efficient crosslinked network to retain the fibrous morphology. Whereas the addition of a sufficient amount of crosslinker (together with the photo-initiator) leads to shape-stable PEO-based fibrous structures that can be interesting candidates for PCM applications.

### Mechanical and dynamic-mechanical analysis

Mechanical and thermo-mechanical properties are fundamental for the application of PCMs. In this regard, the three samples PEO-PI, M-TMPTA and M-TMPTA-C were subjected to tensile test measurements (**Figure 4-17a**). For the M-TMPTA sample, during the test the stress increases with the strain until the sample failure; interestingly, at the beginning of the measurement the slope is lower and then it increases with higher strains (as can be clearly seen in the inset of **Figure 4-17a**). This can be due to the gradual alignment of the fibers parallel to the direction of stress application and the presence of crosslinks in the structure. The

M-TMPTA-C sample shows a stress increase until failure, with a much higher modulus compared with both PEO-PI and M-TMPTA. Both M-TMPTA and M-TMPTA-C samples undergo a catastrophic failure immediately after the maximum stress, while for PEO-PI the behaviour is dissimilar: the stress grows till a maximum and then slowly decreases until sample rupture by tearing.

The mechanical properties, meaning the elastic modulus ( $E$ ), the ultimate tensile strength (UTS) and the strain at the breaking point ( $\epsilon_b$ ), are reported in **Figure 4-17b**. For M-TMPTA, there are two values for  $E$ : an initial value and a second higher value. The M-TMPTA-C sample exhibits the highest elastic modulus ( $268 \pm 44$  MPa) and UTS ( $8.8 \pm 1.5$  MPa) compared with the two fibrous structures, due to the compactness and absence of porosity of the cast film. Comparing the two electrospun fibrous samples (PEO-PI and M-TMPTA), it is evident that the presence of the crosslinker enhanced the failure properties, meaning UTS (from 0.15 MPa of PEO-PI to 0.74 MPa of M-TMPTA) and strain at the breaking point (from 2.5% of PEO-PI to 12.2% of M-TMPTA), due to an efficient crosslinking reactions.

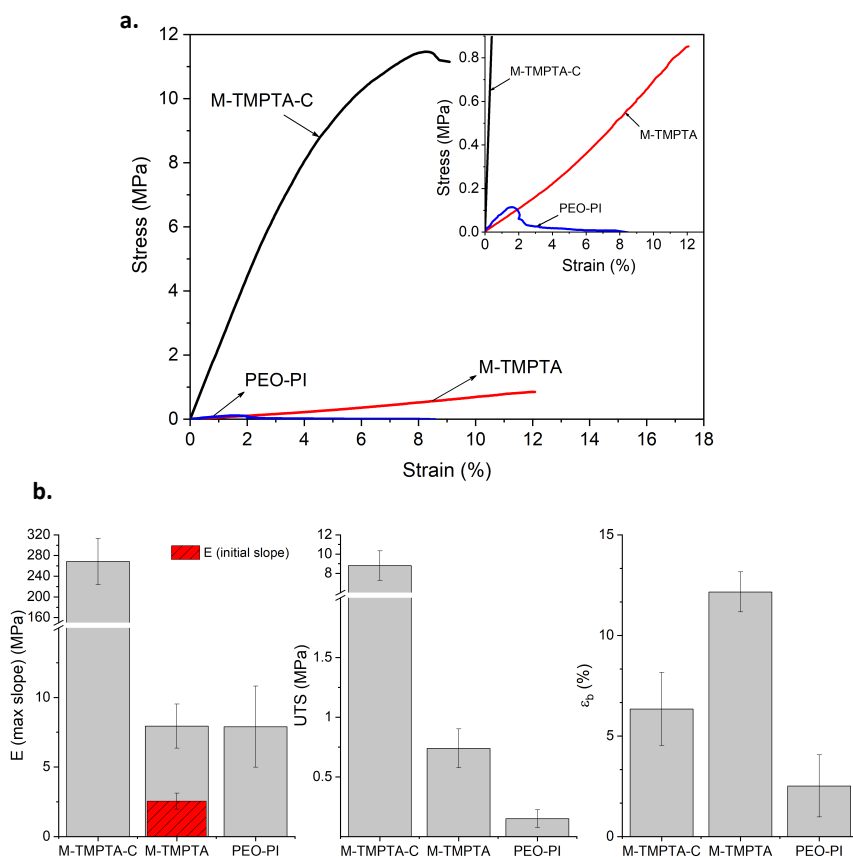


Figure 4-17 a. strain vs. stress curve and b. Young's modulus, ultimate tensile strength (UTS) and elongation at the breaking point obtained from tensile tests of PEO-PI, M-TMPTA and M-MPTA-C samples.

In order to study the thermomechanical properties of the samples, DMTA was carried out. The outcomes of such analysis (storage modulus ( $E'$ ), loss modulus ( $E''$ ) and loss factor ( $\tan\delta$ )) are depicted in the **Figure 4-18**. Temperature scan was performed in the range of  $-80$  °C to  $100$  °C (above the PEO melting point) in order

to monitor the glass transition temperature ( $T_g$ ) changes as well as the viscoelastic behaviour of the samples. It can be seen from **Figure 4-18** that the M-TMPTA-C sample presents one order of magnitude higher values for  $E'$  and  $E''$  compared with the fibrous structures of PEO-PI and M-TMPTA.

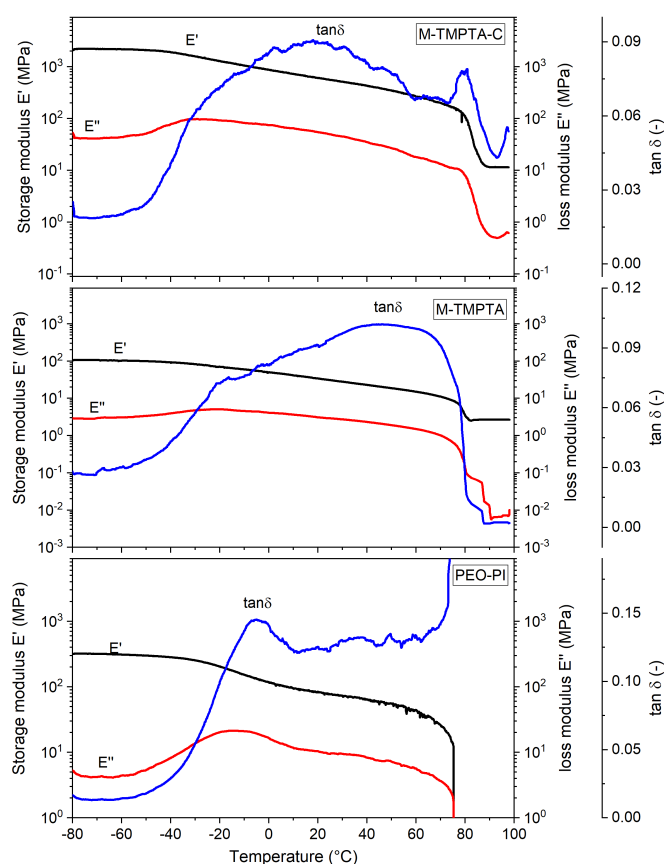


Figure 4-18 Results of DMTA tests. Storage modulus ( $E'$ ), loss modulus ( $E''$ ) and  $\tan\delta$  as a function of temperature.  $E''$  and  $\tan\delta$  have been smoothed.

During the measurement, PEO-PI sample broke into two pieces after the melting temperature of PEO (around  $60^\circ\text{C}$ ) and the measurement could not be continued and was stopped. Whereas the two samples containing the crosslinker, meaning M-TMPTA and M-TMPTA-C, could retain the integrity without rupture until the end of the measurement. However, it is important to notice that the crosslinking treatment does not suppress completely the melting transition of PEO, as the melting signal is observable in both UV-crosslinked samples as a step in  $E'$  and  $E''$  and, for M-TMPTA-C, also as a small peak in  $\tan\delta$ . This signal is evident between  $75^\circ\text{C}$  and  $80^\circ\text{C}$  for M-TMPTA and at a slightly higher temperature (between  $80^\circ\text{C}$  and  $85^\circ\text{C}$ ) for M-TMPTA-C. This can evidence that the presence of TMPTA, leading to efficient crosslinking, in addition to solvent resistance can result in shape-stabilization in the molten state. The potential of M-TMPTA system as shape-stabilized fibrous phase change material is thus confirmed. The glass transition temperature values of the samples, measured by DMTA, are reported in

**Table 4-8**. As can be seen, the  $T_g$  is increased for all samples in comparison with uncured-PEO sample (PEO without any additive was solvent casted and subjected to DMTA). To better understand the effect of morphology, a UV-

irradiated cast film of PEO containing PI was also tested (PEO-PI-C). It can be concluded that the fibrous morphology also can affect the  $T_g$  value: electrospun samples exhibit higher  $T_g$  compared with their cast film counterpart.

Table 4-8 Glass transition temperature for different samples

Sample	$T_g$ (°C)
PEO-PI	$-17 \pm 4$
PEO-PI-C	$-22 \pm 2$
M-TMPTA	$-20 \pm 1$
M-TMPTA-C	$-28 \pm 2$

### Heat storage and long-term stability

Thermal energy storage properties and durability of the samples have been studied through DSC measurement and thermal characterization in a climatic chamber. The results of DSC measurement are reported in **Figure 4-19** and **Table 4-9**.

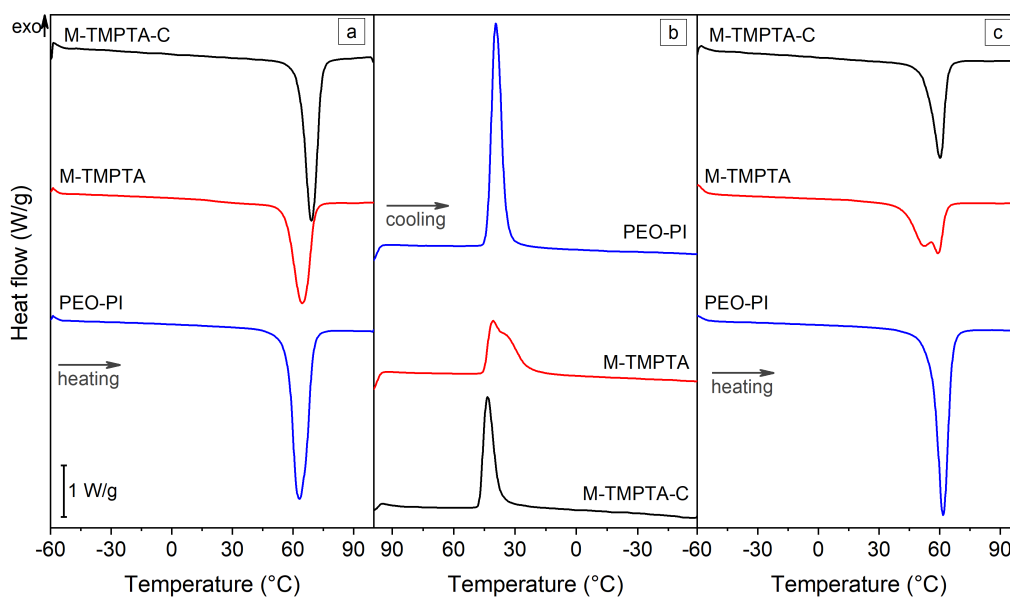


Figure 4-19 Results of DSC tests on the prepared samples: (a) first heating scan; (b) cooling scan; (c) second heating scan.

Table 4-9 Main results of DSC tests on the prepared samples.

Sample	$T_{m1}$ (°C)	$\Delta H_{m1}$ (J/g)	$T_c$ (°C)	$\Delta H_c$ (J/g)	$T_{m2}$ (°C)	$\Delta H_{m2}$ (J/g)
PEO-PI	62.2	186.2	40.8	160.9	60.6	169.7
M-TMPTA	63.8	161.2	41.1	102.5	50.8, 58.8	112.3
M-TMPTA-C	68.6	179.6	43.9	105.1	60.0	115.9

All three samples (PEO-PI, M-TMPTA and M-TMPTA-C) show a single narrow melting peak in the first heating scan, paralleled by a crystallization peak in the cooling scan and a second melting peak in the second heating scan (as already discussed, M-TMPTA display a double peak), which is at slightly lower temperature compared with that of the first cycle. PEO melting and crystallization temperatures are not affected by the addition of the crosslinker, the photo-crosslinking reaction, nor the sample morphology. As for M-TMPTA and M-TMPTA-C only the PEO chains can crystallize, the  $\Delta H_m$  and  $\Delta H_c$  values obtained from DSC measurements were normalized over the PEO weight only (i.e., 75 wt.% of the total weight of the sample). Expectedly, PEO-PI shows a higher melting enthalpy of the second heating scan ( $\Delta H_{m_2}$ ) than the other two samples containing the crosslinker (Table 4-9). In fact, the addition of the crosslinker and the photo-crosslinking process decrease the PEO melting enthalpy by hindering the crystallization, due to the presence of crosslinks in the network. The lower melting enthalpy of M-TMPTA and M-TMPTA-C can translate into a lower thermal energy storage capacity.

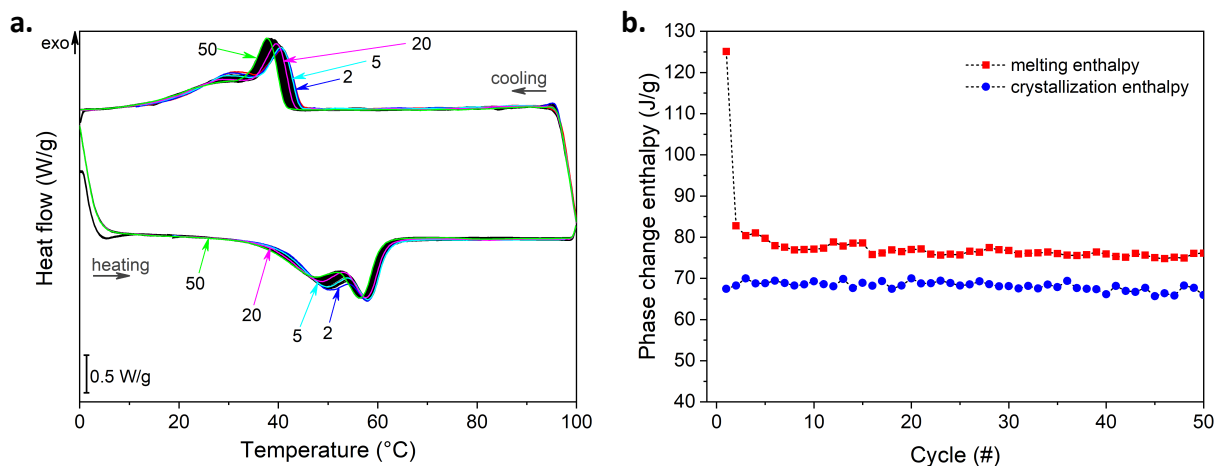


Figure 4-20 Results of 50-cycles DSC tests on the sample M-TMPTA. a. thermograms of cycles #1, #2, #5, #20 and #50 are colored and indicated with an arrow, while all the other cycles are black. B. values of melting and crystallization enthalpy for all cycles.

In order to evaluate the heat storage/release properties of the fibrous M-TMPTA sample a cyclic DSC measurement for 50 cycles was performed: results are reported in **Figure 4-20**. **Figure 4-20a** shows all 50 heating-cooling thermograms, which are stable and with the same curve trend, confirming that the thermal storage properties of the fibrous membrane do not change over many subsequent cycles. The values of crystallization and melting enthalpy measured in each cycle are shown in **Figure 4-20b**, confirming the enthalpy stability in both heating and cooling cycles.

To further check the long-term stability of the M-TMPTA thermal properties, the cyclic DSC tested sample was checked after 15 days (preserved in laboratory condition at  $T = 23^\circ\text{C}$  and  $\text{RH} = 40\%$ ). A melting enthalpy of  $\sim 100.9$  J/g was obtained, which is very similar to the values recorded during the cyclic DSC measurements, suggesting the prolonged stability of such system.

The thermal energy management of the sample was also examined through the thermal cycling in a climatic chamber on a bigger sample scale as described in experimental section. Prior to this test, PEO-PI and M-TMPTA samples were heated up to 100 °C on a laboratory hot plate (simulating a single thermal cycle);

**Figure 4-21** shows the samples prior and after heating. As expected, the most affected sample by temperature is PEO-PI, which is distorted and loses its macroscopic shape, as well as its fibrous morphology (as demonstrated by FE-SEM imaging). Instead, M-TMPTA not only retain its macroscopic shape after heating and cooling again, but also its nanostructured fibrous morphology is not affected by the thermal treatment.

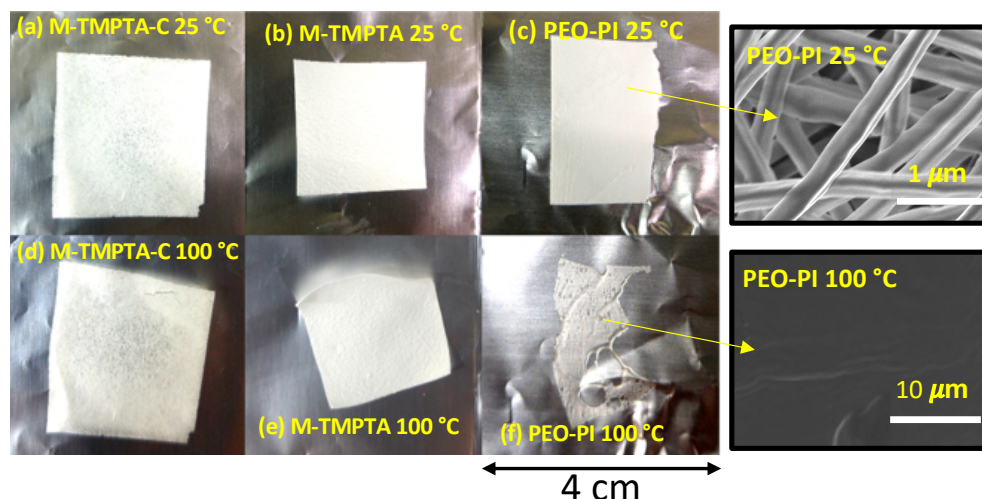


Figure 4-21 Macroscopic view of the (a) M-TMPTA-C, (b) M-TMPTA and (c) PEO-PI electrospun samples at 25 °C (as prepared) and (d) M-TMPTA-C, (e) M-TMPTA and (f) PEO-PI after thermal treatment at 100 °C for 2 min, and FE-SEM images of PEO-PI electrospun sample at 25 °C and 100 °C

After it demonstrated to resist to one cycle, the sample M-TMPTA was also characterized in a climatic chamber for 80 thermal cycles above the melting point of PEO. The samples were collected after the first, the twentieth and the eightieth cycle and analyzed by FE-SEM imaging. In **Figure 4-22** the FE-SEM micrographs, the size distribution of fibers as well as the average fiber diameters, the FWHM and the surface porosity of the electrospun photo-crosslinked membranes are shown. Interestingly, the fibrous morphology retention can be observed even after 80 thermal cycles. Although, the fibers after many thermal cycles are not uniform and well-shaped as before, they are not fused together due to the PEO melting. Therefore, the crosslinks in the M-TMPTA electrospun system are demonstrated to hinder the melt flowing and make shape-stable the fibrous membranes.

As shown in **Figure 4-22e**, the M-TMPTA sample which has not been subjected to the cyclic thermal experiment, displays a narrow size distribution range [265 nm – 425 nm], while after thermal cyclic experiment the size distribution range increases which has been shown with FWHM values (**Figure 4-22f**) meaning that the fibers are distorted, and the overall morphology has been changed. Despite the morphology distortion after heating-cooling cycles, the electrospun membranes are still porous with the similar average fiber diameter value after 0, 1, 20 and 80



heating-cooling cycles. Regarding the porosity of the membrane, it can be observed that the porosity has not been significantly changed.

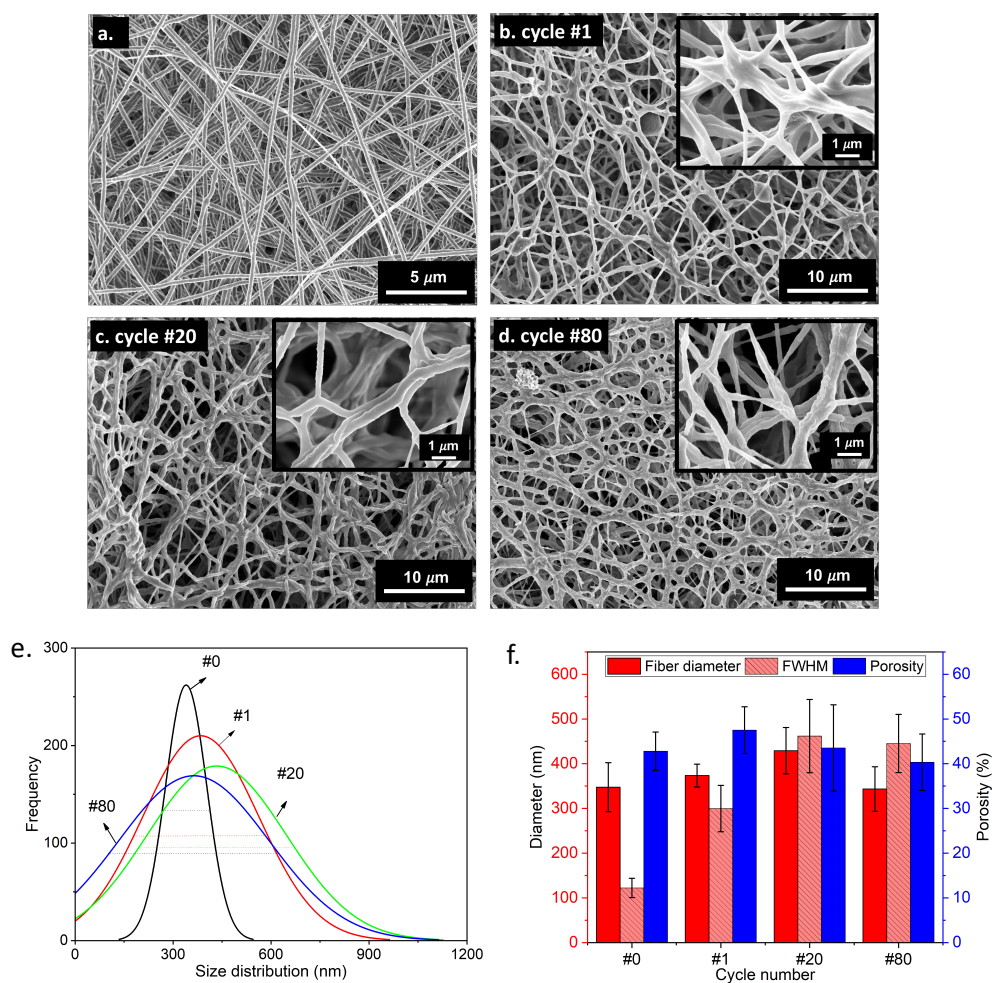


Figure 4-22 FE-SEM micrograph of M-TMPTA sample as prepared (a) and after 1 (b), 20 (c), and 80 (d) thermal cycles in the climatic chamber; the insets are FE-SEM images in greater magnification. e. size distribution of fibers before (#0) and after (#1, #20, and #80) thermal cycles. f. fiber diameters, FWHM and surface porosity of the electrospun mats, obtained by DiamaterJ, after thermal cycling

## 4.6 Conclusions

In this work PEO-based photo-crosslinked electrospun fiber mats with excellent solvent resistance and enhanced properties were fabricated. The fibrous mats were prepared by electrospinning of PEO solutions containing a multifunctional crosslinker and subsequent UV irradiation. Two different multifunctional crosslinkers were used, namely PEGDA and TMPTA, and different acrylic groups/PEO ratios were examined. The morphology of the electrospun membranes were analyzed by FE-SEM: for PEO/PEGDA systems, the upper surface was made of fibers and the bottom side (on the collector side) was a semi-continuous film, while in PEO/TMPTA systems both sides had a fibrous structure with similar surface porosity. The kinetics of photo-crosslinking was studied through photo-DSC experiments. The crosslinking efficiency was evaluated by FTIR spectroscopy and gel content, which both confirmed the successful crosslinking of the network. Then, the effect of the crosslinker (type and amount)

was studied through thermal, mechanical and structural characterizations. Particularly, it was demonstrated that the fibrous morphology of the photo-crosslinked membranes can be retained after contact with water, addressing the main obstacle of PEO-based system (meaning the solubility). Thus, the domain of applicability of this type of membranes can be extremely widened.

The most performing PEO-based investigated system (i.e., M-TMPTA) was then selected for further characterization and in view of its application as form-stable fibrous PCM. In particular, mechanical and thermal properties of the sample were investigated in detail. Photo-crosslinking was proven to effectively enhance the mechanical properties (i.e., tensile strength and strain at break) of the electrospun fibrous mats. DMTA showed that unlike uncured-PEO electrospun mat, the crosslinked system kept its integrity also above its melting temperature, with measurable values of storage and loss moduli. DSC experiments demonstrated that the crosslinked electrospun PEO samples have decent heat retrieve/storage capacity, and remarkable stability in term of melting/crystallinity phase change enthalpy over 50 heating/cooling cycles. Interestingly, the photo cured fibrous PEO samples showed great resistance to heat, even above the PEO melting temperature, and thermal shape stability: they retained their macroscopic shape, as well as their nanofibrous morphology, after thermal treatments and over 80 heating/cooling cycles.

Therefore, the developed crosslinked electrospun PEO membranes, thanks to their thermal and heat storage properties, in combination with their superior shape stability when subjected to solvents or heat, are promising as potential candidates for solid-solid form stable PCMs in heat storage/management applications. Future work will be focused on further enhancing the membranes properties, particularly the thermal conductivity and the heat storage/retrieve capacity.



# Chapter 5

## Polybutadiene-based photo-crosslinked electrospun membranes

### 5.1 Abstract

This chapter focuses on the development of two environmentally friendly electrospinning processes of polybutadiene-based polymers and their photo-induced thiol-ene crosslinking to fabricate stable rubber fibrous membranes.

The first process consists in the electrospinning of low molecular weight liquid polybutadienes and polybutadienes grafted with maleic anhydride without using any solvent or heat and their *in-situ* photo-crosslinking at ambient conditions, which is performed to control the fibrous morphology and enhance the performance of the mats. Liquid polybutadiene-*graft*-maleic anhydride polymers demonstrated a faster rate of reaction, compared to pure polybutadienes, due to the concomitant oxygen mediated photo-crosslinking reaction of the polybutadiene chains and the photo-induced esterification of the maleic anhydride ring. In order to further speed up the crosslinking reaction, enhancing its efficiency and assuring the fiber solidification during electrospinning and the fibrous morphology retention, a thiol-based crosslinker and a photoinitiator were introduced into the formulations. Moreover, a polar additive was used to control the electrospinning process by lowering the viscosity and increasing the electrical conductivity. The proposed single-step sustainable electrospinning method allowed to rapidly fabricate photo-cured polybutadiene-based electrospun membranes with an excellent morphology stability, high insolubility, good thermal properties and a pronounced hydrophobic and oleophilic character.

The second process consists in the electrospinning of styrene-butadiene rubber (SBR) latexes using polyethylene oxide (PEO) as a template and water as the only solvent, the subsequent photo-crosslinking of the electrospun membrane at ambient conditions, and a final water treatment step to remove the unreacted monomers and PEO from the structure. In order to accelerate the photo-crosslinking reaction, a multifunctional thiol crosslinker and an appropriate photo-initiator system were used. The crosslinker amount was varied to tune the photo-induced curing kinetics and efficiency, and the properties of the electrospun fibrous membranes. It was demonstrated that the electrospun fibers were formed by distinct rubber nanoparticles partially fused together. The photo-cured rubber electrospun mats

showed excellent stability and insolubility degree, high thermal resistance, good mechanical properties, and high hydrophobicity and oleophilicity. Finally, these fibrous membranes were proved to be promising for water/oil separation applications.

The results obtained from this work, demonstrating the efficiency of the proposed approaches in fabricating stable polybutadiene-based fibrous membranes with interesting and tunable properties by coupling electrospinning and photo-crosslinking, are part of a manuscript under review (Appendix B) and of a manuscript in preparation.

## 5.2 Introduction

Polybutadiene-based polymers are characterized by high elasticity and extensibility, low hysteresis loss, excellent resilience, and high abrasion resistance. Rubber micro- and nanofibers and nonwoven fibrous membranes are important for applications in need of flexibility, good mechanical resistance, large deformation and elasticity, such as stretchable or wearable electronics [345], flexible sensors and actuators [346,347], selectively permeable membranes and filters [348,349] as well as in lithium ion batteries with insulating properties [350]. Therefore, the electrospun elastic rubber fibers characterized by the lightweight, high flexibility and stretchability, high porosity and breathability can play an important role in the development of high-performance devices. However, electrospinning of polybutadienes has not been extensively studied, and there are only few works in the literature focusing on fiber fabrication of these rubbery materials [351–354]. In fact, such electrospinning process can be challenging (i.e., poor spinning ability and unsteady process) due to their high viscoelasticity and high molecular weight. Moreover, these polymers struggle with a very well-known drawback in the processing and storage that is the tendency to cold flow over time [355,356]. Having the  $T_g$  below the room temperature, the macromolecules of the polybutadiene rubbers are free to move, consequently they constantly change their structure in order to satisfy the increase of entropy and as a result they are not shape stable. In the case of fibrous structures, the fibers gradually increase their diameter over time after the electrospinning and eventually collapse together [357]. In order to tackle this issue, chemical crosslinking can be applied to confine the polymer macromolecules from moving and to prevent the overall flowing of the material.

Being rich in C=C double bonds, polybutadienes are potential candidate for photo-induced reactions. Upon UV irradiation, the allylic hydrogen atoms in the  $\alpha$  position of the double bonds in polybutadienes can be abstracted [358,359]: subsequently, the generated radicals can trigger the photo-induced reaction. The photo-crosslinking process of polybutadienes can be made more efficient and substantially accelerated by the addition of multifunctional thiol monomers that copolymerize with C=C double bonds, such as the easily accessible pendant vinyl groups of butadiene polymers and copolymers [181]. Generally, thiol-ene polymerization works based on a free-radical step-growth addition mechanism

(**Figure 5-1a**) in which the propagation and chain-transfer reactions continually cycle [360,361]. A polymer network is then formed if a diene or a polyene reacts with a multifunctional thiol (**Figure 5-1b** shows the formation of the crosslinks in presence of the trifunctional thiol monomer). Accordingly, photoinitiated thiol-ene polymerization is a highly efficient way to crosslink polybutadiene-based rubbers in a fast manner [361].

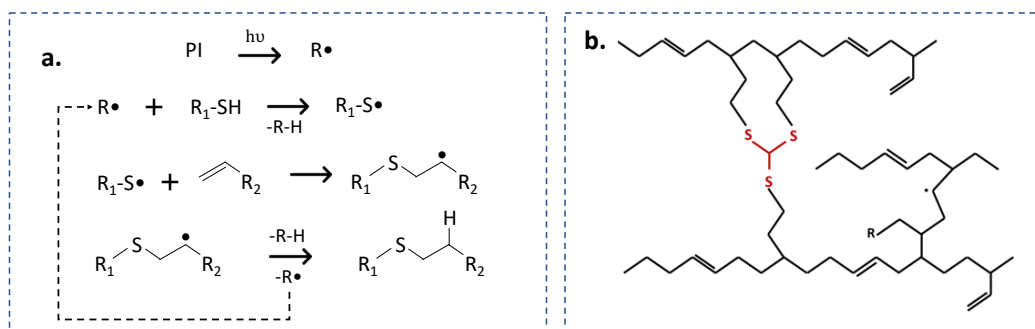


Figure 5-1 a. Thiol-ene reaction in presence of free radicals, b. schematic representation of the crosslinked polybutadiene based network in presence of trifunctional thiol monomer [159,362]

It has been previously demonstrated by our group that the coupling of electrospinning and thiol-ene photo-crosslinking of butadiene-based polymers allows fine-tuning the morphology of the nanofibrous mats, in terms of the fiber diameter up to the nanometer range and of the membrane porosity [357]. However, polybutadienes are soluble only in harsh solvents, such as aliphatic and aromatic hydrocarbons. Generally, tetrahydrofuran (THF), dichloromethane and toluene are used for solution electrospinning of such polymers, as well as dimethylformamide (DMF) to improve the stability of the electrospinning jet [348], but these solvents are highly toxic and raise concerns about environmental and safety issues [351]. Therefore, the development of greener electrospinning processes of polybutadiene-based polymers whose properties are similar to those obtained by solution electrospinning is envisaged. With this aim, in this work, two environmentally friendly electrospinning processes of polybutadiene-based systems were investigated, meaning the electrospinning of low molecular weight liquid polybutadienes and the electrospinning of styrene-butadiene rubber latexes. In both cases, photo-induced thiol-ene crosslinking at ambient conditions was used in order to prepare stable electrospun membranes. Indeed, tailoring the polybutadiene formulation containing a multifunctional thiol crosslinker and a suitable photoinitiator system is of high importance to ensure the occurrence of a sufficient crosslinking degree for complete shape-stabilization of the electrospun structure.

In the first part of the work, low molecular weight liquid pure polybutadienes and polybutadienes grafted with maleic anhydride were subjected to electrospinning (without using any solvent), and *in-situ* UV irradiation during fiber formation. As explained in Chapter 2, the electrospinning of monomers and oligomers at the liquid state and their *in-situ* photo-polymerization and/or photo-crosslinking [57,58,222,363,364] is an interesting approach. It is well known that liquid polybutadienes can be crosslinked by an oxidatively process by heating at 160–200 °C, eventually adding metallic catalysts [365,366], moreover when they

are modified by maleic anhydride, the curing reaction can take place using appropriate amine crosslinkers and reactive polyols [367,368]. However, thermal curing processes are slow, while photo-induced reactions are advantageous due to their very short conversion time. This fast reaction rate is suitable for electrospinning process in which the flying jet speed is very high (in the range of 1-5 m/s) and in a matter of seconds the flying jet undergoes the different electrospinning stages and deposits as a fiber on the collector [11,59]. Thus, with the aim of producing rubber fibrous membranes, electrospinning of low molecular weight polybutadiene polymers at the liquid state and their counterparts grafted with maleic anhydride was coupled with a photo-induced *in-situ* thiol-ene curing reaction, using a multifunctional thiol crosslinker and a photoinitiator. The liquid polybutadienes formulation was optimized for electrospinning, especially in terms of reaction rate, viscosity and conductivity. Then, the fibrous morphology, the thermal, mechanical, and surface properties of the photo-crosslinked electrospun mats were characterized.

The fabricated rubber electrospun fibers exhibited an excellent morphology stability, high insolubility, good thermal properties and pronounced hydrophobic and oleophilic character. It has been also shown that crosslinked polybutadiene-based fibers fabricated through liquid polymer electrospinning and *in-situ* photocuring process exhibit comparable properties of fibers obtained by solution electrospinning of high molecular weight polybutadienes [348,351,353,354,357,369,370].

In the second part of this chapter, suspension electrospinning of styrene-butadiene rubber (SBR) latexes and the subsequent photo-crosslinking reactions have been studied for stable rubber fiber fabrication. To avoid using harsh solvents such as toluene, THF and DMF, green electrospinning using water as the process medium is proposed. As butadiene-based polymers are not soluble in water, latexes (i.e., stable dispersions of polymer particles in water) are a suitable alternative to fabricate butadiene-based nanofibers by electrospinning without using any toxic solvent or surfactant [371]. One easy way to produce electrospun fibers by latexes is using a small amount of an electrospinnable template polymer [372]. In this regard, PEO can be employed, and ultimately it can be easily extracted from the nanofibers by a simple water treatment procedure.

Herein, in order to stabilize the butadiene-based nanofiber mats obtained by latex electrospinning in the presence of PEO, thiol-ene photo-crosslinking by introducing a multifunctional thiol monomer and appropriate photo-initiators was applied. It is worth noting that water has been used as the only medium for electrospinning, and photo-crosslinking has been carried out in ambient condition. After electrospinning and UV irradiation, a water treatment step was applied to remove PEO from the fibrous mats. The kinetics and the efficiency of the photo-crosslinking together with the morphological, thermal, mechanical and surface properties of the fabricated membranes were studied. It was demonstrated that the optimized process conditions lead to the easy production of stable and insoluble fiber mats containing styrene-butadiene rubber. The simple water treatment step

allowed to extract the unreacted monomers and PEO from the fibrous structure. The fabricated rubber electrospun membranes exhibited an interesting morphology, being the fibers formed by the assembly of rubber nanoparticles. In addition to good thermal and mechanical properties, the fibrous mats showed high hydrophobicity and oleophilicity.

## 5.3 Materials and method

### 5.3.1 Materials

Lithene ultra® liquid polybutadiene N4-5000 and PM4, and liquid polybutadienes grafted with maleic anhydride N4-5000-10MA (grafted maleic anhydride = 10wt.%), N4-5000-15MA (grafted maleic anhydride = 15 wt.%) and PM4-7.5MA (grafted maleic anhydride = 7.5%) were kindly provided by Synthomer. **Table 5-1** summarizes the main characteristics of the liquid polybutadienes used in this study. To simplify the samples' name, PB, PB-10MA, PB-15MA, PB-2, PB-7.5MA were used for N4-5000, N4-5000-10MA, N4-5000-15MA, PM4 and PM4-7.5MA respectively.

Table 5-1 Properties of the liquid polybutadienes, provided by the supplier

Name	Mn (g/mol)	Grafted MA (wt.%)	Vinyl 1,2 content (%)	f <sup>r</sup> (functional groups/chain)	T <sub>g</sub> by DSC (°C)	Viscosity (dPa.s)
<b>PB (N4-5000)</b>	5000	0	10-20	-	-92.5	30-50
<b>PB-10MA (N4-5000-10MA)</b>	5200	10	10-20	5.1	-84.4	250-600
<b>PB-15MA (N4-5000-15MA)</b>	5750	15	10-20	7.7	-79.1	1200-2200
<b>PB-2 (PM4)</b>	1500	0	15-25	-	-90.2	7-9.5
<b>PB-7.5MA (PM4-7.5MA)</b>	1600	7.5	15-25	1.1	-83.6	20-60

A styrene-butadiene rubber (SBR) latex, an aqueous dispersion of a 50 wt.% of styrene-butadiene copolymer in water (Elastolan S19, 100–200 nm particle size, T<sub>g</sub> = 6 °C and viscosity of 300 cPa s at 25°C) was provided by Rescom S.r.l (Italy). Polyethylene oxide (PEO) of Sigma-Aldrich (USA) (M<sub>w</sub>=1,000,000) was used as a water-soluble electrospinning template polymer. Trimethylolpropane tris(3-mercaptopropionate) (TRIS) of Bruno Bock Thiochemicals (Germany) was used as a thiol-ene photo-crosslinker. Diphenyl (2,4,6-trimethylbenzoyl) phosphine oxide (TPO) and 2-Hydroxy-2-methyl-1-phenyl-1-propanone (Darocur 1173) of Ciba Speciality Chemicals Corp. were used as photoinitiators. Oleic acid (OA) from Sigma-Aldrich was used as polar electrospinning additive. The chemical structures of materials used in this chapter are shown in **Figure 5-2**.



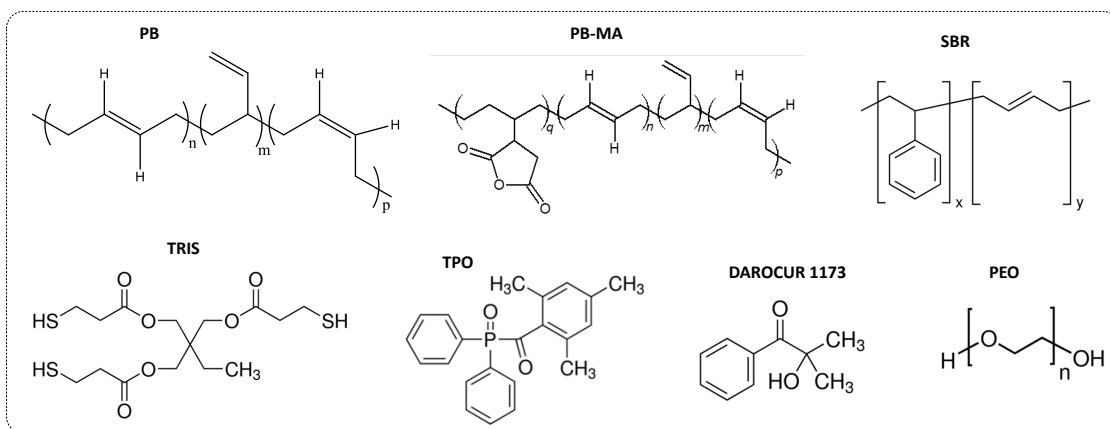


Figure 5-2 Scheme of chemical structure of materials used in this study including polybutadiene (PB), maleinized polybutadiene (PB-MA), SBR, PEO, TRIS thiol crosslinker, TPO and Darocur 1173 photoinitiators.

### 5.3.2 Sample preparation

The liquid polybutadienes formulations were subjected to the electrospinning and *in-situ* photo-curing without using any solvent. To accelerate the photo-crosslinking process, 3 wt.% TRIS trifunctional thiol monomer and 1 wt.% TPO photoinitiator were added to the formulation. To improve the electrospinnability of the formulation, oleic acid as a polar additive was added with different contents of 3, 5 and 9 wt.% with respect to the liquid polybutadiene. Electrospinning was conducted by an E-fiber electrospinning system SKE apparatus in horizontal setup, equipped with a high voltage power supply, a programmable syringe pump and a grounded collector covered by aluminum foil as substrate. Electrospinning was performed by applying a voltage of 14-16 kV, a flow rate of 0.1-0.4 ml/h, and a working distance of 6 cm. *In-situ* curing was carried out by means of a high-pressure mercury-xenon lamp equipped with an optical fiber LIGHTNINGCURE™ Spotlight source LC8, Hamamatsu, applying a UV intensity of 280 mW/cm<sup>2</sup> on the collector. The UV light intensity was measured by a UV Power Puck® II from EIT® Instrument Markets.

In order to better study the polymer curing reaction, plain films with a thickness of 12 μm were prepared by coating a glass substrate with the liquid polybutadienes, using a wire-wound applicator. The curing process was performed by means of the same UV light source, with an intensity of 280 mW/cm<sup>2</sup>. The polymer films were irradiated for different exposure times until solidification.

For the work on SBR latexes, the electrospinning solutions were prepared using the SBR aqueous dispersion and PEO aqueous solution. Initially, PEO 5 wt.% aqueous solution was prepared through magnet-stirring overnight, then the SBR latex was added to PEO solution with composition ratio SBR:PEO 10:3 (wt:wt) and the solution was homogenized by magnet-stirring for 2 hours. Afterward, 1 wt.% photoinitiator system (TPO:Darocur 1173 1:1 wt:wt) with respect to the SBR part was added to the blend solution. Ultimately the TRIS crosslinker was added to the formulation with a content of 3 wt.%, 10 wt.% or 50 wt.% with respect to SBR.

Electrospinning was performed by an E-fiber electrospinning system SKE apparatus in horizontal setup, using an aluminum foil as substrate. The feed rate

was set at 0.2-0.3 ml/h, with the working distance of 15 cm and applied voltage of 13-17 kV. Throughout the electrospinning process, the environment condition including temperature and relative humidity of were 25 °C and 45%, respectively. Immediately after electrospinning, the samples were photo-cured by UV light using a high-pressure mercury-xenon lamp equipped with an optical fiber LIGHTNINGCURE Spotlight source LC8, Hamamatsu. The electrospun mats were irradiated in air condition with the light intensity of 32 mW/cm<sup>2</sup> for 5 min (UV dose ~ 9.6 J/cm<sup>2</sup>). The intensity of light source was measured using a UV Power Puck<sup>®</sup> II from EIT<sup>®</sup> Instrument Markets.

For comparison, SBR and PEO cast films were also produced. The SBR latex and the PEO water solution were poured on a glass slide and let dry for 48 h at room temperature.

### 5.3.3 Characterizations

The chemical structures of the samples prior and after UV-irradiation were analyzed by Fourier Transform Infrared (FTIR) spectroscopy using a Thermo Fisher Scientific Nicolet<sup>™</sup> iS50 spectrometer in the spectral range of 4000 – 400 cm<sup>-1</sup>. The spectra were collected in transmission mode and also in attenuated total reflectance (ATR) mode with an accumulation of 32 scans at the resolution of 4 cm<sup>-1</sup>. Moreover, real-time FTIR analyses were carried out using a liquid nitrogen cooled mercury–cadmium–telluride (MCT) detector. The spectra were collected with 1 spectra/scan in transmission mode at the resolution of 4 cm<sup>-1</sup> during UV irradiation. UV irradiation was applied using a high-pressure mercury-xenon lamp equipped with an optical fiber LIGHTNINGCURE Spotlight source LC8 (Hamamatsu). Silicon wafer was used as a transparent substrate to IR wavelengths and measurements were performed in ambient condition. Upon UV irradiation, the conversion of the C=C double bonds (vinyl and trans) of the styrene-butadiene rubber and of the S-H thiol groups of the crosslinker were monitored by calculating the area  $A_r$  of the absorption band of the reactive groups at different irradiation time  $t$  with respect to the time  $t=0$  [181]. Percent functional groups conversion was calculated by Eq1:

$$\text{Conversion \%} = \left(1 - \frac{(A_r)_t}{(A_r)_0}\right) \times 100 \quad \text{Eq1}$$

The peak intensity and peak area were quantified through the Omnic software.

The insoluble fraction of the photo-cured electrospun mats was measured by gravimetrically calculating the mass loss after 24 h extraction from solvent by using chloroform, toluene or water, and 3 h drying at 60 °C.

The tack-free time of 12 μm thick flat films irradiated for different time lengths was assessed by pressing the thumb on the specimen surface, then, while the forefinger supporting the specimen, the thumb moved upward. When there was no mark left by thumb on the specimen surface or no trace of sticky surface on the thumb, the film was considered tack free.

The morphology of fibrous mats was controlled using an Olympus BX53M Microscope and also a Merlin Field Emission Scanning Electron Microscopy

(Merlin FE-SEM), ZEISS. Prior to FE-SEM imaging, samples were sputter coated with ~10 nm Cr film using a Quorum Q150T ES sputter coater. The size distribution of fiber diameters was obtained by ImageJ software analyzing the FE-SEM images: approximately 100 measurements were performed for each sample.

Thermal stability and resistance were characterized by thermogravimetric analysis (TGA) using a Mettler Toledo TGA/SDTA 851<sup>e</sup> apparatus. TGA was carried out in a temperature range of 25 °C to 800 °C with a heating rate of 10 °C/min and a constant nitrogen flux of 60 ml/min in order to avoid the thermo-oxidative process.

Thermal properties including the glass transition temperature ( $T_g$ ), the enthalpy of crystallization ( $\Delta H_m$ ) and the melting point ( $T_m$ ) were measured through Differential Scanning Calorimetry (DSC) experiment using a DSC1 STAR<sup>e</sup> Mettler Toledo instrument. DSC was carried out in a heating-cooling-heating cycle in a temperature range of -60 °C to 180 °C with heating rate of 20 °C/min and a constant nitrogen flux of 60 ml/min.  $T_g$  was obtained from the midpoint of the heat increment in the second heating cycle, and  $T_m$  was obtained from the maximum of the endothermic peak in the second heating cycle. For PEO-containing samples  $X_c$  was measured by calculating the enthalpy of fusion in the second heating cycle ( $\Delta H_m$ ) with respect to the enthalpy of fusion for a 100% crystalline PEO sample (196 J/g [340]) at the equilibrium melting point ( $T_m^0$ ).

The viscoelastic properties of the electrospun samples were analyzed through Dynamic Mechanical Thermal Analysis (DMTA) using a Triton Technology instrument, in tensile configuration with heating rate of 3 °C/min at a frequency of 1 Hz in the temperature range of -100 °C to 100 °C. Samples were cut into rectangular shape with dimensions of 20 mm \* 10 mm and thickness of 30  $\mu$ m to 50  $\mu$ m measured with digital micrometer. The glass transition temperature was calculated based on the maximum in Tan  $\delta$  curve.

The tensile strength was examined using an INSTRON 3366 electromechanical universal testing machine (ITW Test and Measurement Italia S.r.l., Instron CEAST Division) equipped with 500 N load cell. After peeling off the fibrous mats from the aluminum substrate, membranes were cut to obtain samples with dimensions of 30 mm in length, 8 mm in width and thickness of 10–40  $\mu$ m, which were then placed between the clamps. Measurements were performed in ambient conditions by applying a constant stretching speed (5 mm/min). During the tensile testing, the stress (through machine-recorded force) and strain (the displacement based on initial cross-section area and gauge length) were measured and the Young's modulus  $E$  was calculated based on the initial linear elasticity regime of the stress-strain curves.

The surface wettability of the fibrous membranes was evaluated by means of a FTA 1000C instrument, at room temperature with the sessile drop technique. Five replicates were performed for each sample in different spots of the sample surface: the mean value and the error were determined. Water and hexadecane, with surface tensions of 72.1 mN/m and 28.1 mN/m, respectively, were used as the probe liquids.

In order to assess the oil-water separation performance of the SBR membranes, a filtering setup composed of a filtering flask, a fritted glass support base, a glass funnel, a spring clamp and a silicon stopper, a vacuum tubing and a vacuum pump was used. The electrospun membrane was fixed between the glass funnel and the base. The separation was driven using a vacuum pump and the filtrate was collected in the flask. For this purpose, hexadecane and distilled water with a red colorant were used to examine the separation efficiency of the SBR electrospun membrane.

## 5.4 Results and discussion

### 5.4.1 Electrospinning of liquid polybutadienes and their *in-situ* photo-curing

Liquid polybutadienes were subjected to the electrospinning process and *in-situ* UV curing at ambient condition without the use of any solvent. The schematic representation of the process is depicted in **Figure 5-3a**.

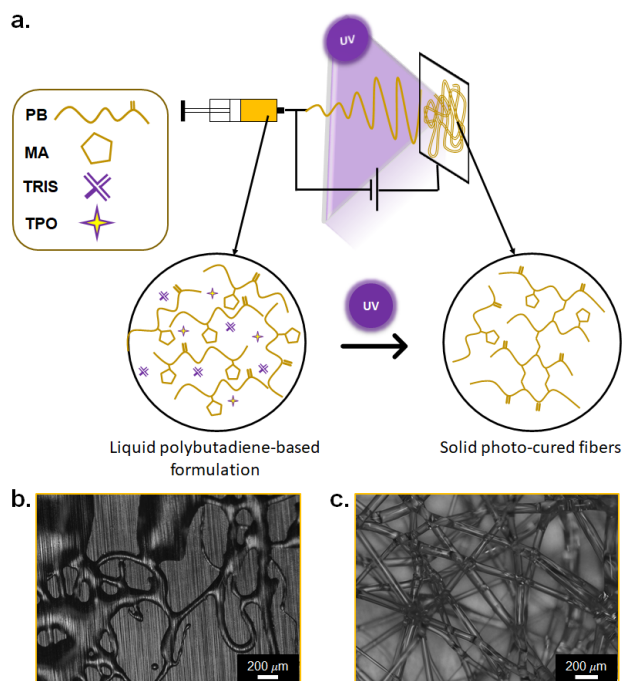


Figure 5-3 a. Scheme of the electrospinning process with *in-situ* photocuring of liquid polybutadienes. b. Optical microscope image of PB-MA after electrospinning and *in-situ* photocuring. c. Optical microscope image of PB-MA-2%TPO-3%TRIS fibers obtained by electrospinning and *in-situ* photocuring.

Both pristine liquid polybutadiene and liquid polybutadiene grafted by maleic anhydride samples, meaning PB, PB-2, PB-7.5MA, PB-10MA and PB-15MA were processed (electrospinning and *in-situ* UV-curing). It is expected that the grafting of the maleic anhydride moiety increases the conductivity and also the viscosity of the liquid polybutadiene. Thus, the electrospinnability is foreseen to be facilitated by having maleic anhydride groups in the polymer structure. Among the three examined polybutadienes, the sample PB-15MA (Mn of 5750 g/mol and maleic anhydride content of 15 wt.%) was the only one with successful formation of a

continuous polymer jet reaching the collector during electrospinning. For the other samples, dripping of the liquid polymer or forming a discontinuous jet of polymer was obtained, which can be due to the lower viscosity and lower grafted maleic anhydride content. Although, PB-15MA was the only sample forming a continuous jet of polymer during the electrospinning process, the deposited fibers on the collector were deformed and collapsed together (**Figure 5-3b**): thus, the photo-crosslinking was not efficient enough to allow the retaining of the fiber morphology and to guarantee the shape stability of the fibers.

#### Study of the polybutadienes photo-curing process

Accordingly, the photo-induced crosslinking process was studied in detail. For that the solidification speed of PB and maleinized PBs by means of tack free time was examined in two curing conditions, meaning in air and in nitrogen atmosphere. For this aim, a very thin film of liquid polymer on a glass slide was prepared and subjected to the UV irradiation by different time intervals: the results are reported in **Table 5-2**. The samples were solidified in the range of few minutes, and the photo-curing was faster in air atmosphere than in inert atmosphere, which demonstrates the effect of oxygen molecules in the photo-curing process. Interestingly, a higher maleic anhydride graft amount leads to a higher photo-curing reaction rate and a faster solidification. As a result, the sample with the highest amount of maleic anhydride, meaning PB-15MA, in presence of oxygen has the fastest solidification process.

Table 5-2 Tack free time of PB and maleinized PB in two curing atmospheres (air and nitrogen)

Sample	Curing atmosphere	
	Air	Nitrogen
PB	8 min	12 min
PB-10MA	5 min	7 min
PB-15MA	3 min	5 min
PB-2	7 min	10 min
PB-7.5MA	5 min	8 min

To better understand and follow the photo-crosslinking reaction, the structural changes of the polybutadiene and polybutadienes grafted by maleic anhydride upon UV irradiation in air were studied through FTIR-ATR spectroscopy. FTIR spectra were collected from thin films of PB and maleinized PB at different time intervals during the UV irradiation and as a result the evolution of absorption changes was monitored. The FTIR spectra of all liquid polybutadienes (Table 1) are reported in Appendix A in which the evolution and disappearing of peaks are clearly shown.

As shown in **Figure 5-4a**, polybutadiene shows some changes in absorbance at peak band at  $1090\text{ cm}^{-1}$  associated to the ether bond, at  $1730\text{ cm}^{-1}$  related to the carbonyl groups and the broad peak at  $3400\text{ cm}^{-1}$  of hydroxyl groups. According to

the literature, this suggests that PB under UV irradiation in presence of oxygen undergoes the three reactions of photo-crosslinking, photo-oxidation and chain scission [358,373].

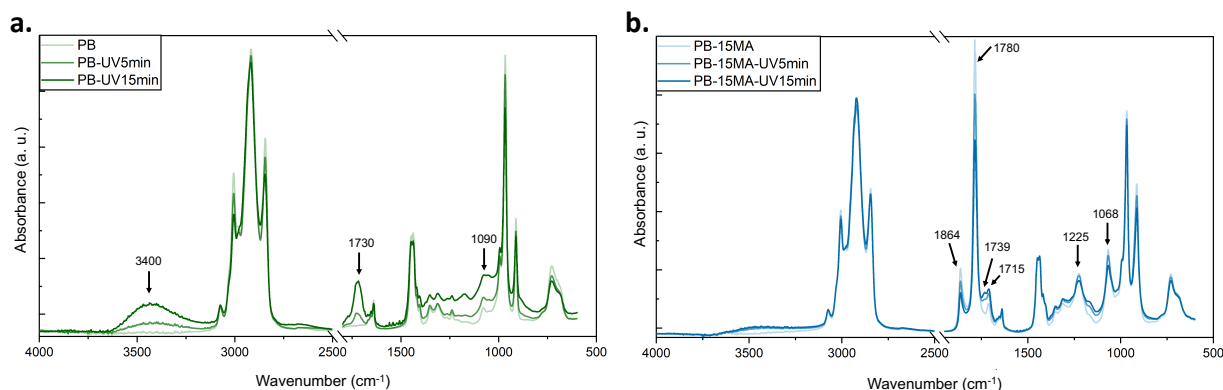


Figure 5-4 FTIR spectra of PB (a) and PB-15MA (b) prior (irradiation time = 0 min), during (irradiation time = 5 min) and after (irradiation time = 15 min) UV irradiation

During the UV irradiation in air atmosphere, oxygen molecules actively participate in the curing reaction. Oxygen molecules by absorbing UV light get excited and as a result, oxygen reactive species are generated. These species can form carbonyl or hydroxyl groups (with peak bands at  $1730\text{ cm}^{-1}$  and  $3400\text{ cm}^{-1}$ , respectively) on the polybutadiene chains. In fact, singlet oxygen leads to the shift of the double bond (from cis to trans configuration) and to the formation of allylic hydroperoxides [374]. The absorption at  $3400\text{ cm}^{-1}$  can thus arise from -OOH or -OH groups [375,376], indicating the oxidation reaction. Therefore, singlet oxygen is a photo-oxidative agent that enhances the curing process by free radical oxidation [377]. On the other hand, the reactive oxygen species can attack the  $\alpha$ -carbons of the polybutadiene chain as well as the alkene groups, and then hydroperoxide ( $\text{ROO}\cdot$ ) and hydroxyl radicals ( $\text{RO}\cdot$ ) are formed. Thus, ether linkages (with peak band at  $1090\text{ cm}^{-1}$ ) between the reactive chains are generated during the UV irradiation. Longer curing time results in more crosslinks between the macroradicals and consequently the formation of a three dimensional network. The scheme of the photo-induced crosslinking reaction in the presence of oxygen is proposed in **Figure 5-5a**. The FTIR spectra also show the decrease in some peaks during UV irradiation, namely out-of-plane deformation of cis and trans  $-\text{CH}=\text{CH}-$  with peak band at  $720\text{ cm}^{-1}$  and  $960\text{ cm}^{-1}$  respectively, out-of-plane wagging of  $-\text{CH}=\text{CH}_2$  found at  $910\text{ cm}^{-1}$  and stretching of double bonds in alkene associated to band at  $1650\text{ cm}^{-1}$ . The decrease of such peaks indicates the double bonds consumption of the polybutadiene chains. UV irradiation can also degrade the polybutadiene by forming ketones and alcohols by chain scission, however the solidification and high gel content confirmed that photo-crosslinking is the dominant progressing reaction.

The FTIR spectra of maleinized PB compared to pristine PB have two extra intense peaks at  $1864\text{ cm}^{-1}$  and  $1780\text{ cm}^{-1}$ , associated to the pendant carbonyl peaks of maleic anhydride. Upon the UV irradiation, the intensity of these two carbonyl

peaks decreases and instead the carbonyl peak at  $1715\text{ cm}^{-1}$ , assigned to the C=O bonds of carboxylic acids (due to partial hydrolysis of the maleic ring), increases and a new carbonyl peak at  $1739\text{ cm}^{-1}$ , attributed to C=O in the ester group, is formed. The increase of these two carbonyl peaks confirms the ring opening of the maleic anhydride leading to the esterification and the crosslinking of the polybutadiene chains [367,368]. In **Figure 5-5b** the crosslinking of the maleinized polybutadiene in presence of oxygen (in air atmosphere) as a result of esterification is proposed. Moreover, as indicated in **Figure 5-4b**, the consumption of C=C double bonds can be detected in FTIR spectra of maleinized PB (decrease in peak bands at  $720\text{ cm}^{-1}$ ,  $910\text{ cm}^{-1}$ ,  $960\text{ cm}^{-1}$  and  $1650\text{ cm}^{-1}$ ). Finally, the peaks at  $1225\text{ cm}^{-1}$  and  $1068\text{ cm}^{-1}$ , which are attributed to the symmetric and asymmetric stretching of the ring, change during UV irradiation. Thanks to the coincidence of photo-induced oxidation and esterification during UV irradiation of maleinized polybutadienes, solidification is accelerated, compared to pure PB (as indicated by the tack-free time in **Table 5-2**).

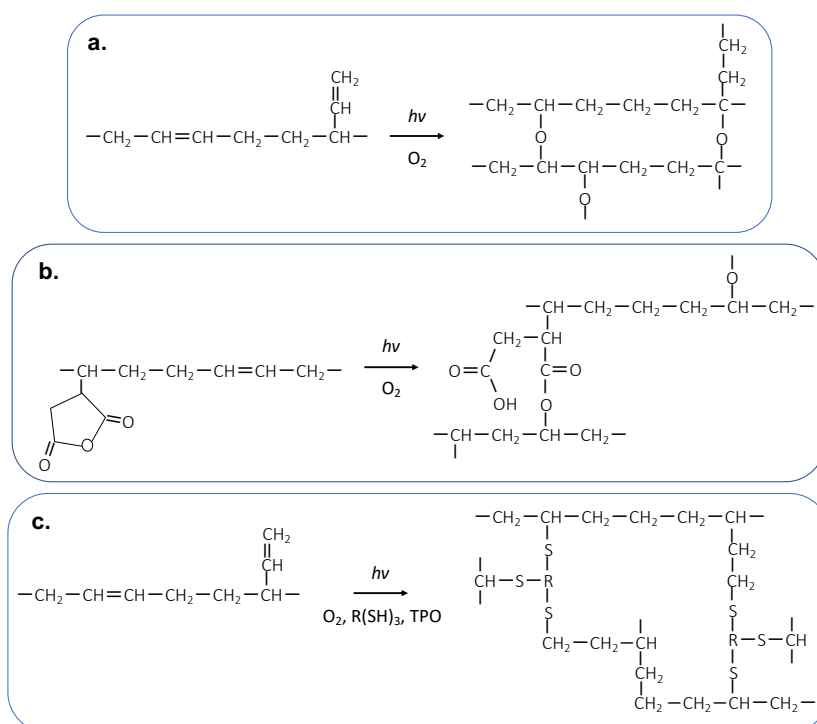


Figure 5-5 Scheme of the photo-induced crosslinking reactions of PB (a) and maleinized PB (b), and of polybutadienes in the presence of the trifunctional thiol crosslinker TRIS ( $\text{R(SH)}_3$ ) and the photoinitiator TPO (c), occurring during UV irradiation in air.

Although PB-15MA exhibited the fastest photo-induced crosslinking reaction, the reaction rate was not high enough to assure a sufficient crosslinking degree during the polymer jet flying time in the electrospinning process. Therefore, the electrospun fibers immediately after reaching the collector tended to deform and collapse (**Figure 5-5b**). In order to accelerate the photo-crosslinking reaction, the thiol-ene chemistry by addition of a multifunctional thiol monomer and a radical-type photoinitiator was examined. For this purpose, TPO and TRIS were used as photo-initiator and multifunctional thiol crosslinker. **Figure 5-5b** proposes the

photo-crosslinking reaction of polybutadiene chains occurring during the UV-irradiation in presence of a multifunctional thiol monomer and a photoinitiator, which proceeds with a free radical step-growth mechanism by thiyl radicals (RS•) in ambient conditions.

To examine the effect of the TPO photoinitiator (1 or 2 wt.%) and the TRIS thiol crosslinker (1.5 or 3 wt.%) on the solidification of the PB and PB-15MA, tack free time measurements were conducted: Table 5-3 summarizes the required UV irradiation time to solidify (tack-free time) the examined formulations. Addition of the photo-initiator and the crosslinker greatly reduces the solidification time. The PB and PB-15MA formulations containing 2 wt.% of TPO and 3wt.% of TRIS (henceforth indicated as PB-2TPO-3TRIS and PB-15MA-2TPO-3TRIS) showed the fastest reaction and the solidification occurred in a matter of seconds.

Table 5-3 Effect of TPO photoinitiator and TRIS crosslinker on the tack-free time of thin films of PB and PB-15MA due to UV irradiation in air.

Sample	Tack-free time
PB-1%TPO	480 s
PB-2%TPO	360 s
PB-2%TPO-1.5%TRIS	60 s
PB-2%TPO-3%TRIS	5 s
PB-15MA-1%TPO	90-150 s
PB-15MA-2%TPO	45-90 s
PB-15MA-2%TPO-1.5%TRIS	25 s
PB-15MA-2%TPO-3%TRIS	< 5 s

The photo-crosslinking reaction of PB-2TPO-3TRIS and PB-15MA-2TPO-3TRIS was studied through FTIR spectroscopy of the samples prior and after UV-irradiation (**Figure 5-6a** and **b**). As indicated earlier, after almost 5 seconds of irradiation the solidification took place for both systems, hence only the spectra after solidification (and not during UV irradiation) were analyzed. The characteristic peak of a thiol monomer is at  $2556\text{ cm}^{-1}$ , however in the FTIR spectra of the investigated samples containing only 3 wt.% TRIS, this peak was not detectable due to its very low intensity. Therefore, the consumption of thiol groups with the crosslinking reaction has not been studied.



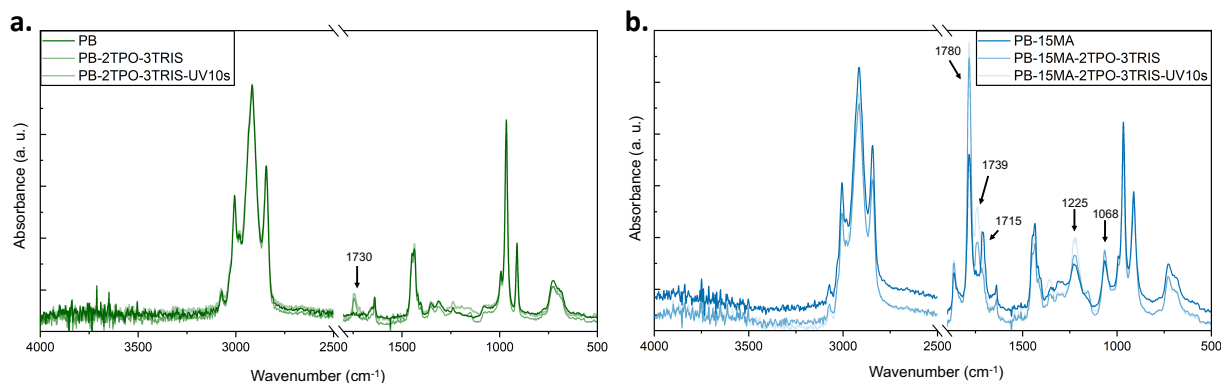


Figure 5-6 FTIR spectra of 12  $\mu\text{m}$  thick film of a. PB and b. PB-15MA containing 2 wt.% photoinitiator and 3 wt.% crosslinker (PB-2TPO-3TRIS and PB-15MA-2TPO-3TRIS, respectively) prior (irradiation time = 0 s) and after UV irradiation (irradiation time = 10 s) in air.

The FTIR spectra of the PB-based samples exhibit the appearance of a peak band at  $1730\text{ cm}^{-1}$ , assigned to C=O carbonyl bond, immediately after addition of the crosslinker and the photo-initiator. The evolution of the broad peak at  $3400\text{ cm}^{-1}$  as a signal for oxidation reactions cannot be observed: it can be concluded that the photo-crosslinking is the main reaction over the other reactions such as photo-oxidation or chain scission of PB when added of the photoinitiator and the crosslinker. Upon irradiation of PB-15MA-2TPO-3TRIS a new band at  $1739\text{ cm}^{-1}$  appeared; as explained above, this peak is a remark for a photo-induced esterification reaction of the anhydride. Therefore, the photo-induced crosslinking in the presence of oxygen of PB-15MA-2TPO-3TRIS is supposed to be a multivalent and complex reaction, which concurrently involves the oxidation, the esterification, and the crosslinker links (**Figure 5-5**).

Showing the highest photo-crosslinking reaction rate (i.e., shorter solidification time), samples PB-2TPO-3TRIS and PB-15MA-2TPO-3TRIS were subjected to electrospinning and *in-situ* UV curing. Although the addition of the photoinitiator and the thiol crosslinker led to much faster crosslinking reaction, these additives decreased the viscosity of the formulations. Consequently, electrospinning was not successful for PB-2TPO-3TRIS. Whereas fibers with an average diameter of  $61\text{ }\mu\text{m}$  and a stable morphology were obtained with PB-15MA-2TPO-3TRIS (**Figure 5-3c**). This sample (i.e., PB-15MA-2TPO-3TRIS) was thus selected for further investigation and characterization.

### Optimization of electrospinning process and characterization of the photo-cured electrospun mats

A polar additive was then used to tune the electrospinning process. In fact, polar additives can improve the electrical conductivity of the polymer jet by increasing the charge mobility thanks to the presence of extra ions or charge carriers. Moreover, by having a polar additive, the viscoelastic forces in the polymer jet are reduced and during electrospinning the jet can undergo higher stretching. Therefore, a polar additive in the formulation causes higher repulsive forces and accordingly greater stretching and more stable electrospinning process [378–380].

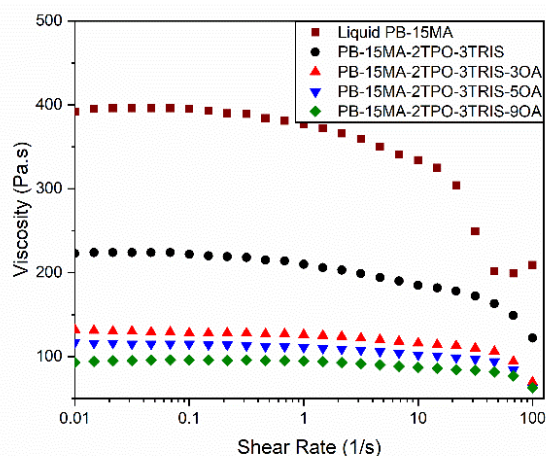


Figure 5-7 Viscosity vs. shear rate of PB-15MA and of the PB-15MA–2TPO–3TRIS formulations used in electrospinning with 0, 3, 5 and 9 wt.% OA.

In this study, oleic acid (OA) was used as polar additive. In order to assess the effect on the rheological properties of OA as well as of the photoinitiator and the thiol crosslinker in the formulation, the viscosity of PB-15MA and of the formulations containing 2 wt.% TPO and 3 wt.% TRIS with 0 wt.%, 3 wt.%, 5 wt.% and 9 wt.% of OA was monitored. As demonstrated in **Figure 5-7**, addition of TRIS and TPO decreases the viscosity of the liquid PB-15MA from ~400 Pa s to ~230 Pa s (at shear rate  $0.01 \text{ s}^{-1}$ ). Addition of OA further decreases the viscosity of the formulation to values even lower than 100 Pa s.

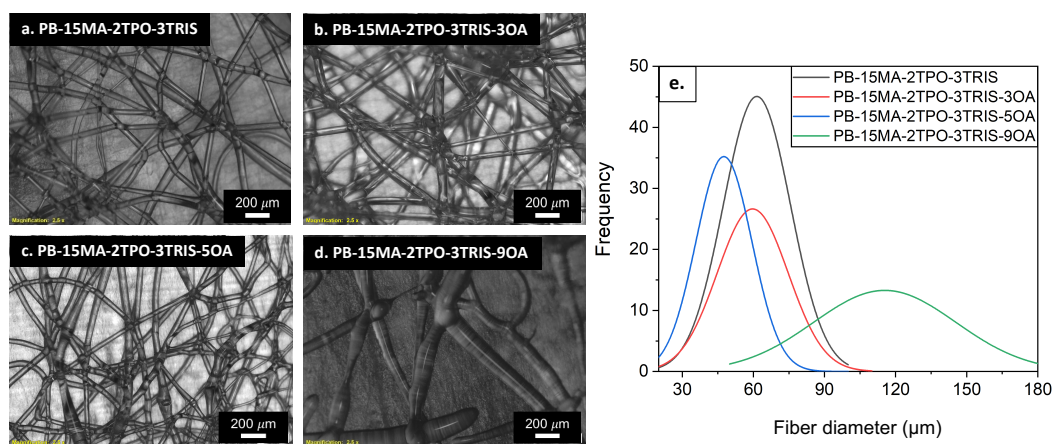


Figure 5-8 Fiber morphology by optical microscope images of PB-MA–2TPO–3TRIS formulations with 0 (a), 3 (b), 5 (c) and 9 (d) wt.% OA and (e) their size distribution.

The electrospinning and *in-situ* curing (**Figure 5-3**) were performed on PB-15MA-2TPO-3TRIS formulations containing OA at 3, 5 and 9 wt.%. **Figure 5-8** shows the electrospun fiber morphology (and their size distribution) obtained. The optical microscope images demonstrate the stability of the overall morphology. In fact, not only the stability is realized along a single fiber but also at the contact points of different fibers. In general, addition of OA as a polar additive decreases the average fiber diameter. The formulation containing 5 wt.% OA shows the lowest average fiber diameter, whereas 9 wt.% of polar additive yields unstable jet of polymer with large fibers and a wide size distribution.

The crosslinking efficiency leading to solid rubber fibers was also confirmed by gel content experiments: as indicated in **Figure 5-9** for all formulation the insoluble fraction is found higher than 80%. The polar additive is not participating in the photo-crosslinking reaction and remains soluble part after irradiation; as a result the OA addition decreases the insoluble fraction based on its content in the formulation.

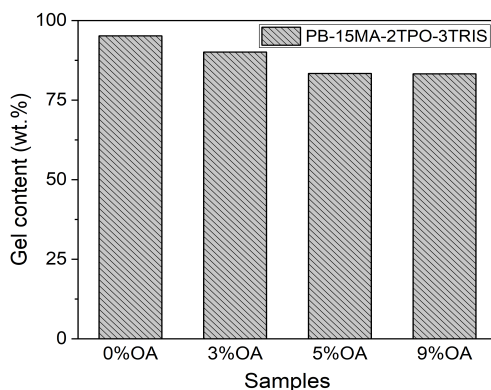


Figure 5-9 Insoluble fraction of photo-cured electrospun PB-15MA-2TPO-3TRIS samples with 0, 3, 5 and 9 wt.% OA

The thermal resistance of the electrospun mats was assessed by TGA. As shown in **Figure 5-10a**, all samples exhibit an excellent thermal stability: major degradation takes place after 350 °C. The thermal resistance of the liquid PB-15MA is higher than that of the photo-cured samples. In fact, the addition of the photoinitiator and the thiol crosslinker leads to a decomposition onset at lower temperature. Moreover, the addition of OA further decreases the thermal resistance of the fibrous membranes, and the formulations containing 5 and 9 wt.% of oleic acid show the lowest resistance to thermal degradation. In order to evaluate the shape stability of the photo-crosslinked electrospun mats, one sample meaning PB-15MA-2TPO-3TRIS-3OA was heated up (to 80 °C and 100 °C) and its morphology was monitored by optical microscopy. Interestingly, the fibers exhibit excellent stability, and as shown in **Figure 5-10b**, the morphology is retained with a slight increase in the average fiber diameter. Considering the fact that the  $T_g$  of these polybutadiene-based samples is very low ( $\sim -80$  °C for the liquid polymers, as reported by the supplier, and  $\sim -60$  °C for the photo-cured electrospun samples, as acquired by DMTA shown in **Figure 5-10**) the shape stability at 100 °C highlights the efficiency of the photo-crosslinking.

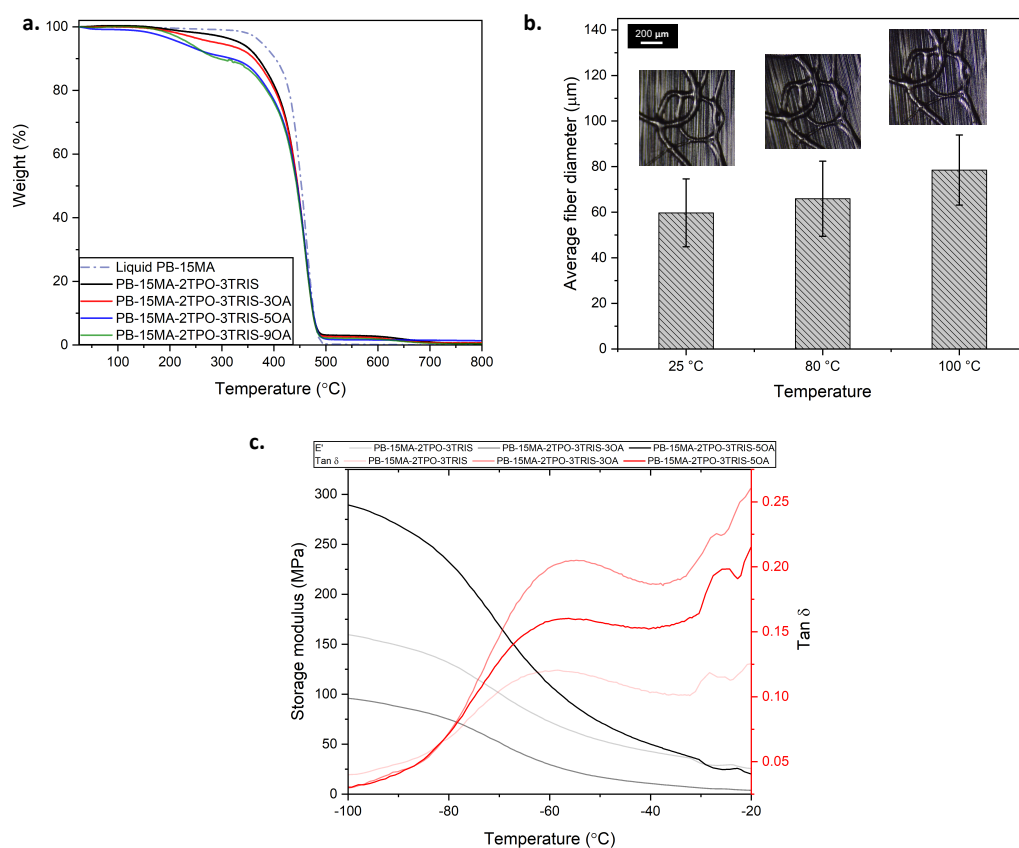


Figure 5-10 a. TGA thermograms of liquid PB-15MA and crosslinked electrospun PB-MA-2TPO-3TRIS systems containing 0, 3, 5 and 9 wt.% OA. b. Average fiber diameter of photocured electrospun PB-MA-2TPO-3TRIS with 3 wt.% OA after a thermal treatment. The insets show the fiber morphology by optical microscope images. c. DMTA results on photo-cured electrospun mats of PB-MA-2TPO-3TRIS without (0OA), with 3 wt.% (3OA) and 5 wt.% (5OA) of oleic acid as polar additive.

Due to the high surface area of the electrospun membranes, their surface properties are of primary importance. The wettability of the rubber fibrous mats was characterized by contact angle measurements. As shown in **Figure 5-11**, the fibrous mats of all examined formulations, except the PB-15MA-2TPO-3TRIS-9OA, exhibit a very high hydrophobicity. As it is expected, having 9 wt.% of oleic acid salt in the structure decreases the water contact angle values. The contact angle with hexadecane of the photo-cured rubber mats was also examined and the values for all samples were close to 0 °.

These results showing concomitant hydrophobicity and oleophilicity, together with the high thermal stability, are particularly promising for the use of the photocured polybutadiene-based electrospun mats as membranes for water/oil separation.

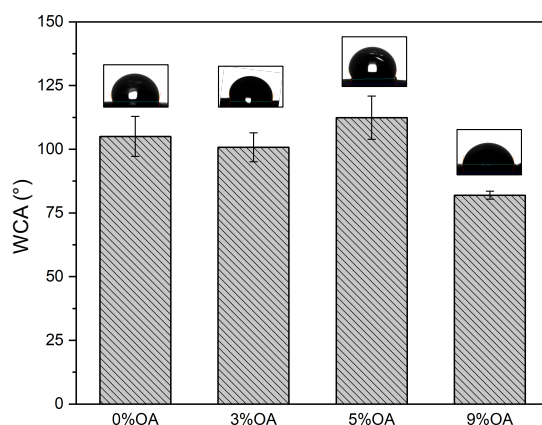


Figure 5-11 Contact angle with water (WCA) of the photocured electrospun mats of PB-15MA-2TPO-3TRIS with 0, 3, 5 and 9 wt.% OA.

### 5.4.2 Styrene-butadiene-based materials fiber fabrication

In the second part of the work, styrene-butadiene rubber (SBR) latexes were subjected to electrospinning and subsequent photo-crosslinking. Styrene-butadiene-based materials can undergo the photo-induced crosslinking reaction upon UV irradiation, even without photo-active agents meaning a photoinitiator and a crosslinker (in this case the crosslinking reaction rate is low) [381]. Addition of a suitable photoinitiator and a multifunctional thiol monomer speeds up the photo-crosslinking reaction rate [181]. Accordingly, TPO has been found as the most efficient photoinitiator for the styrene-butadiene based rubbers [362]. Here, a mixture of TPO and Darocur 1173 1:1 (wt./wt.) was used as photoinitiating system, together with TRIS as multifunctional thiol crosslinker. Three different concentrations of TRIS were investigated: 3 wt.%, 10 wt.% and 50 wt.% with respect to SBR content.

The SBR latex was found to be not electrospinnable by its own (i.e., a stable jet could not be formed), therefore the use of a small amount of an electrospinnable template polymer was needed. PEO was employed as template, with a weight composition ratio SBR:PEO of 10:3.

The details of the four studied formulations are reported in Table 5-4.

Table 5-4 Composition of the latex-based formulations used for electrospinning

Sample name	SBR:PEO(wt./wt.)	TRIS(wt.%)	Photoinitiator(wt.%)
SBR/PEO	10:3	0	0
SBR/PEO/3%TRIS	10:3	3	1
SBR/PEO/10%TRIS	10:3	10	1
SBR/PEO/50%TRIS	10:3	50	1

## SBR/PEO fiber production by electrospinning

The water-based formulations were electrospun, and the obtained fibrous membranes were subsequently irradiated. The schematic representation of the process is depicted in **Figure 5-12**.

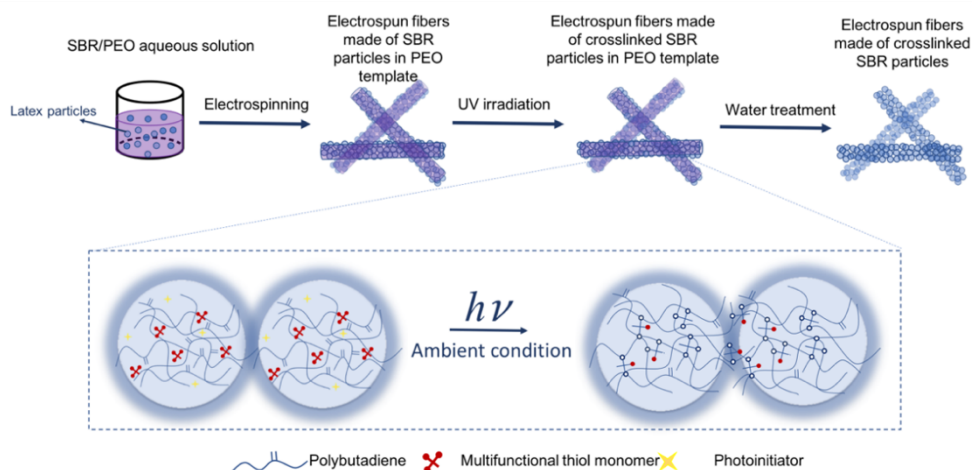


Figure 5-12 Schematic illustration of SBR/PEO fibers and their photo-crosslinking: SBR particles are dispersed in PEO template upon electrospinning and subjected to thiol-ene crosslinking by UV irradiation; then a water treatment is applied to remove the uncured PEO, leaving crosslinked rubber fibers formed by SBR nanoparticles

As preliminary work, the electrospinning of SBR/PEO blend (without any irradiation) was investigated: it resulted in successful fabrication of continuous fibers. As shown in **Figure 5-13a**, uniform fibers with the diameter size distribution in the range of 670 to 1000 nm, and an average diameter of  $\sim 820$  nm were obtained. It is important to notice that the SBR/PEO fibers do not display any trace of latex particles in their structure, being completely smooth, thus demonstrating that the rubber particles completely coalesce during and/or after the electrospinning.

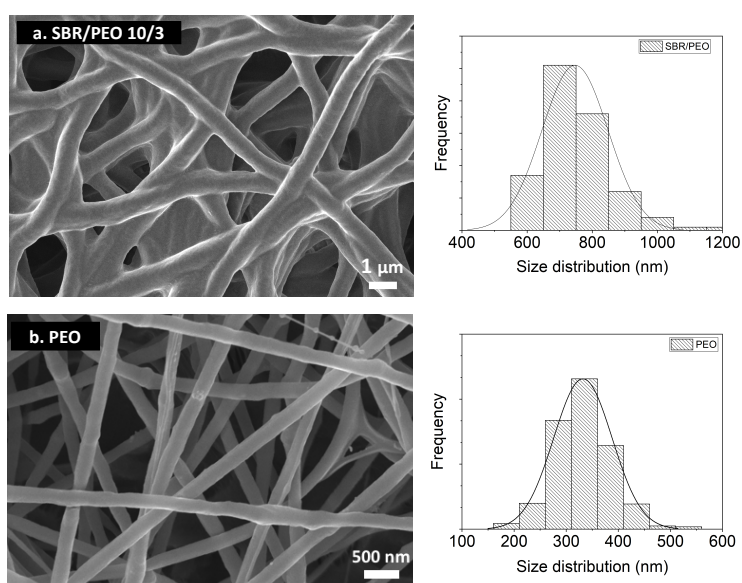


Figure 5-13 FE-SEM images of electrospun membrane of (a) SBR/PEO, with the diameter distribution in the range of 670 to 1000 nm, and of (b) PEO, with the diameter distribution in the range of 160 to 540 nm.

A FE-SEM image of PEO electrospun fibers obtained from electrospinning of a PEO aqueous solution is also shown in **Figure 5-13b** for comparison. The difference between PEO fibers and SBR/PEO fibers can be clearly seen. The PEO membrane exhibits distinct and separate fibers with well-defined borders along each single fiber, without any coagulation, while the SBR/PEO membrane shows diverse morphology in which the fibers tend to coagulate together, particularly the beneath fibers (i.e., the first fibers deposited on the collector) have more contact points and some of them are collapsed together.

In order to assess the chemical structure of SBR/PEO fibers and to ensure that the blend electrospinning process was successful forming fibers composed of both PEO and SBR, FTIR spectroscopy was performed (spectra are shown in **Figure 5-14**). The characteristic peaks of SBR are: CH groups in the aromatic ring (styrene) at  $699\text{cm}^{-1}$ , out-of-plane vibrations of the CH groups near the double bond of the butadiene vinyl group at  $910\text{ cm}^{-1}$ , out-of-plane (wagging) vibrations of the CH groups near the double bond in trans-butadiene units at  $962\text{ cm}^{-1}$ , stretching vibrations in cis-butadiene units  $\nu(\text{C-C})$  at  $1029\text{ cm}^{-1}$ , vinyl-butadiene  $\delta(\text{CH})$  in  $\text{CH}_2=\text{CH}-$  at  $1451\text{ cm}^{-1}$ , stretching vibrations of the carbons in the aromatic ring  $1601\text{ cm}^{-1}$ . The characteristic groups of PEO are:  $-\text{CH}_2-\text{CO}$  rocking/stretching group at  $843\text{ cm}^{-1}$  and  $\text{C-O-C}$  group at  $1104\text{ cm}^{-1}$ . In the FTIR spectrum of the electrospun SBR/PEO fibers (**Figure 5-14**), the identification peaks at  $699\text{ cm}^{-1}$ ,  $843\text{ cm}^{-1}$  and  $1104\text{ cm}^{-1}$  (associated to aromatic ring in SBR,  $-\text{CH}_2-\text{CO}$  rocking and  $-\text{C-O-C}-$  in PEO, respectively) were clearly detected, confirming the presence of both SBR and PEO constitutes in the fibrous membranes.

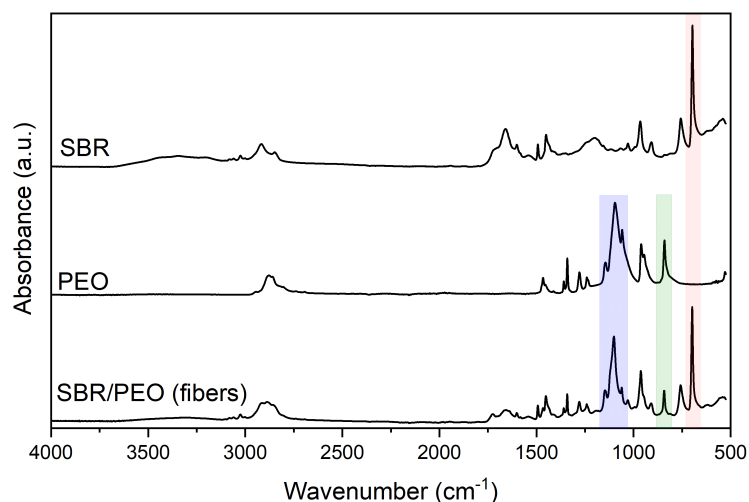


Figure 5-14 ATR FTIR spectra of SBR cast film, PEO film and SBR/PEO electrospun fibers. The triple peak associated to ether bond in PEO, the  $-\text{CH}_2-\text{CO}$  rocking of PEO backbone at  $\sim 840\text{ cm}^{-1}$  and the peak at  $699\text{ cm}^{-1}$  related to aromatic ring in SBR are shown with blue, green and red frames, respectively.

### Photo-crosslinking of SBR/PEO electrospun fibers

In view of optimizing the photo-crosslinking reaction of the rubber fibers, a trifunctional thiol crosslinker (TRIS) in different concentration and a photoinitiator system (TPO:Darocur 1173 1:1) were added to the SBR/PEO blend (**Table 5-4**) prior to electrospinning. Then, the formulations containing 3, 10 and 50 wt.% of

TRIS and 1 wt.% of the photoinitiator system were subjected to the electrospinning process and subsequent UV irradiation (**Figure 5-12**). In order to study the kinetics of the photo-induced reactions, real-time transmission FTIR spectroscopy was conducted on the electrospun fibers deposited on a silicon wafer: the spectra were acquired during the *in-situ* UV irradiation. As shown in **Figure 5-15a**, a polybutadiene chain generally contains three double bond isometric units, meaning vinyl-1,2, cis-1,4 and trans-1,4. In general, the pendant vinyl group is the most reactive toward thiyl radicals (RS•) and the conversion of vinyl is expected to be higher than that of trans groups. Moreover, in the course of the crosslinking reaction, cis-1,4 structure can undergo an internal rotation to generate trans-1,4 configuration [382]. Therefore, the FTIR peaks associated to the vinyl groups (at  $910\text{ cm}^{-1}$ ) and trans group ( $962\text{ cm}^{-1}$ ) of the polybutadiene system, and also the peak associated to the S-H groups (S-H stretching at  $2573\text{ cm}^{-1}$ ) of the thiol crosslinker were tracked during 10 minutes of UV-irradiation.

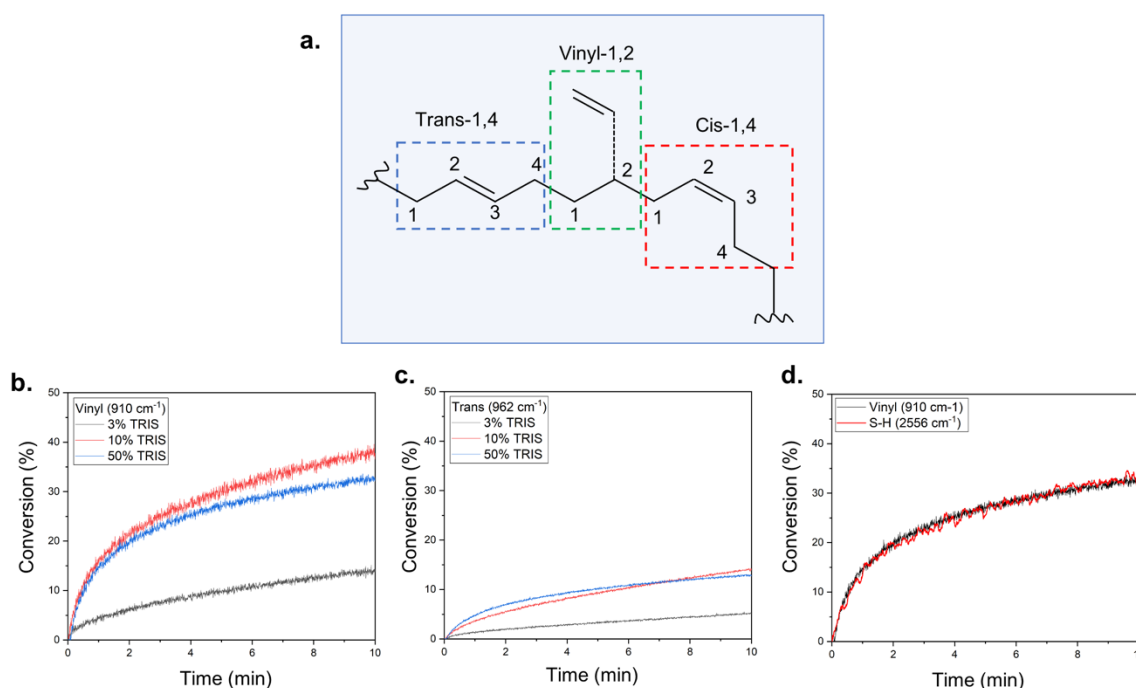


Figure 5-15 a. Schematic of three double bond isomers of trans-1,4, vinyl-1,2 and cis-1,4 in polybutadiene b. vinyl and c. trans conversion for SBR/PEO fibers containing three different contents of TRIS upon UV irradiation and c. S-H and vinyl conversion for the sample SBR/PEO/50%TRIS upon UV irradiation. The conversion data were obtained by real time FTIR spectroscopy.

Comparing **Figure 5-15b** and **c**, it is evident that the vinyl conversion for all three formulations is higher than the trans conversion, which was found to be lower than 15 % after 10 minutes of irradiation. These results confirmed the higher reactivity of pendant vinyl groups. Considering both the vinyl and trans C=C groups, the systems containing 10 and 50 wt.% of TRIS crosslinker displayed a similar conversion curve, while the system with 3 wt.% of TRIS showed a much lower conversion. The S-H thiol group has a weak signal in FTIR spectra and as a result the consumption of such group during the irradiation could not be tracked for the two systems with a TRIS content of 3 and 10 wt.%. Instead, the S-H



consumption could be recorded for the formulation containing a higher amount of TRIS, meaning SBR/PEO/50%TRIS, and interestingly it is found identical to the vinyl conversion (~ 32 % after 10 minutes of irradiation) for the same formulation (**Figure 5-15c**). Although the TRIS functionality at 2556 cm<sup>-1</sup> could not be tracked due to its very low signal intensity in the samples containing 3 and 10 wt.% of TRIS, its participation in the photo-crosslinking reaction can be expected based on the kinetics study on the sample containing 50 wt.% of TRIS.

In order to assess the photo-crosslinking efficiency, insoluble fraction measurements were performed. Water was used as solvent to evaluate the water-soluble fraction of the electrospun fibers, related to uncured PEO and to the unreacted portion of the thiol crosslinker. As reported in Table 5-5, the results confirm that the quantity of PEO in the fibers (as the water-soluble portion) is approximately equal to that of the initial formulation. As a result, electrospun SBR/PEO fibers have the same composition ratio as the initial blend, and unlike the study in Chapter 3 on electrospinning of chitosan/PEO systems, a PEO enrichment has not occurred. Moreover, the fact that PEO chains remain soluble in water after UV irradiation suggests that the photo-crosslinking thiol-ene reaction of SBR and TRIS is much favored (and faster) with respect to the crosslinking of PEO.

For the SBR/PEO/50%TRIS sample, the water-soluble fraction of the fibers was higher than the amount of PEO in the electrospinning formulation (Table 5-5). This is probably due to an excess of thiol crosslinker: a portion of TRIS do not react with the polybutadiene-based polymer and can thus be solubilized in water even after irradiation. Insoluble fraction measurements were also conducted with chloroform as a solvent. The results reported in Table 5-5 confirm the high insoluble fraction of the photo-cured systems: higher than 60 % of the initial weight of the photo-cured electrospun samples (SBR/PEO/3%TRIS, SBR/PEO/10%TRIS and SBR/PEO/50%TRIS) is insoluble. It is important to note that these samples contain ~19 % of PEO and unreacted crosslinker, therefore the normalized soluble fraction after irradiation is <21% for all the formulations. These results are also supported by literature data demonstrating that insolubilization of styrene-butadiene-block copolymers due to their photo-crosslinking takes place at very low content of thiol monomer and photoinitiator (i.e., ≤ 1 wt.% and ≤0.1wt.%, respectively) [383].

Table 5-5 Theoretical amount of PEO in the electrospun fibers, the soluble fraction of the photo-cured electrospun fibers after water treatment and their insoluble fraction after chloroform treatment

Sample	Theoretical content (%) <sup>1</sup>	PEO	Water treatment	Chloroform treatment
			Soluble fraction (% weight loss)	Insoluble fraction (%)
SBR/PEO	23.08		19.08	-
SBR/PEO/3%TRIS	22.61		19.38	60.28
SBR/PEO/10% TRIS	21.21		18.69	67.44
SBR/PEO/50 % TRIS	16.83		19.46	64.17

<sup>1</sup>%PEO in theory is obtained based on initial formulations for electrospinning.

### Characterization of the photo-crosslinked SBR/PEO electrospun membranes

The fibrous morphology of the photo-cured electrospun membranes containing 3 wt.% and 10 wt.% of the TRIS crosslinker and the photoinitiator was analyzed by FE-SEM (images are shown in **Figure 5-16**).

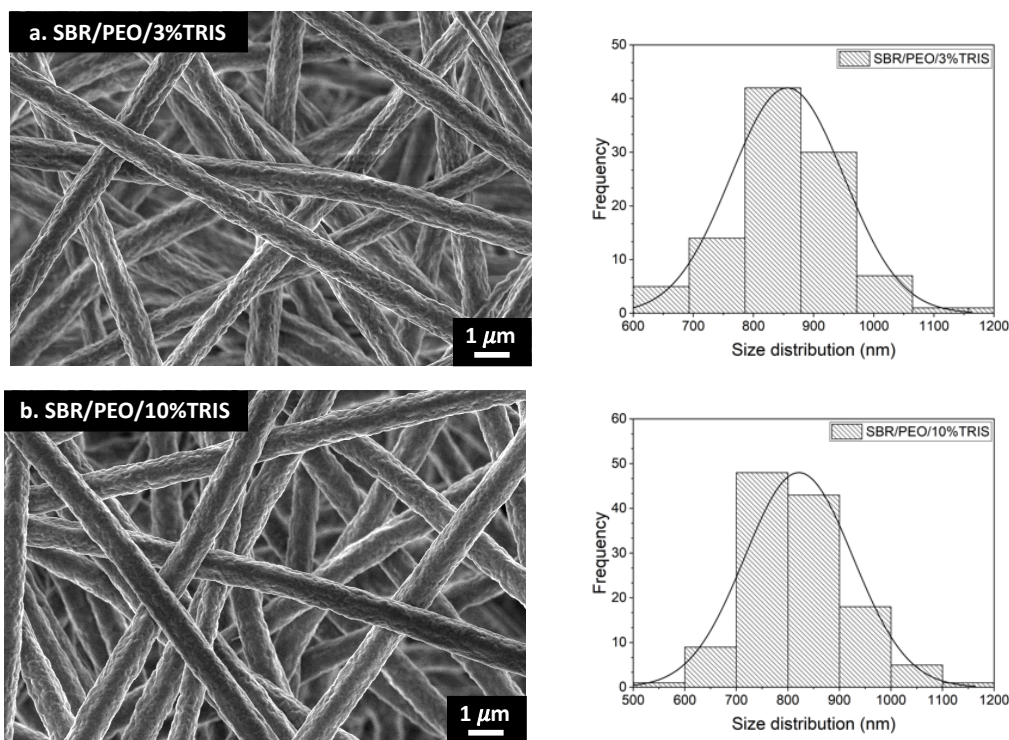


Figure 5-16 FE-SEM images of the photo-cured electrospun membranes made of PEO/SBR with a. 3 wt.% and b.10 wt.% of the thiol crosslinker and 1 wt.% of TPO:Darocur 1173 1:1 photoinitiator system, and their fiber diameters distribution.

As indicated earlier, the un-cured electrospun fibers of SBR/PEO have a smooth surface and some points where the fibers are fused together (see **Figure 5-13a**). Whereas photo-cured electrospun fibers display a coarse surface possibly due to the presence of crosslinked rubber particles embedded in the PEO template. Interestingly, the photo-cured membranes do not exhibit the collapsing points among fibers, and the fibers have defined borders along the length. Moreover, also the fibers deposited primarily in the beneath layers are intact and exhibit well-defined uniform cylindrical shape. The photo-crosslinking reaction is thus demonstrated to make the rubber fibers shape-stable, as the SBR flowing, which is responsible for the fiber collapsing, is inhibited, and the fibrous morphology remains unchanged over time. The size distribution of the fibers diameter is reported in the histograms in **Figure 5-16**. Both investigated systems show narrow size distribution with an average fiber diameter of  $850 \pm 10$  nm and  $820 \pm 10$  nm for SBR/PEO/3%TRIS and SBR/PEO/10%TRIS, respectively. The morphology of the electrospun photo-cured SBR/PEO/50%TRIS system was not investigated, but similar results to those reported in **Figure 5-16** can be expected.

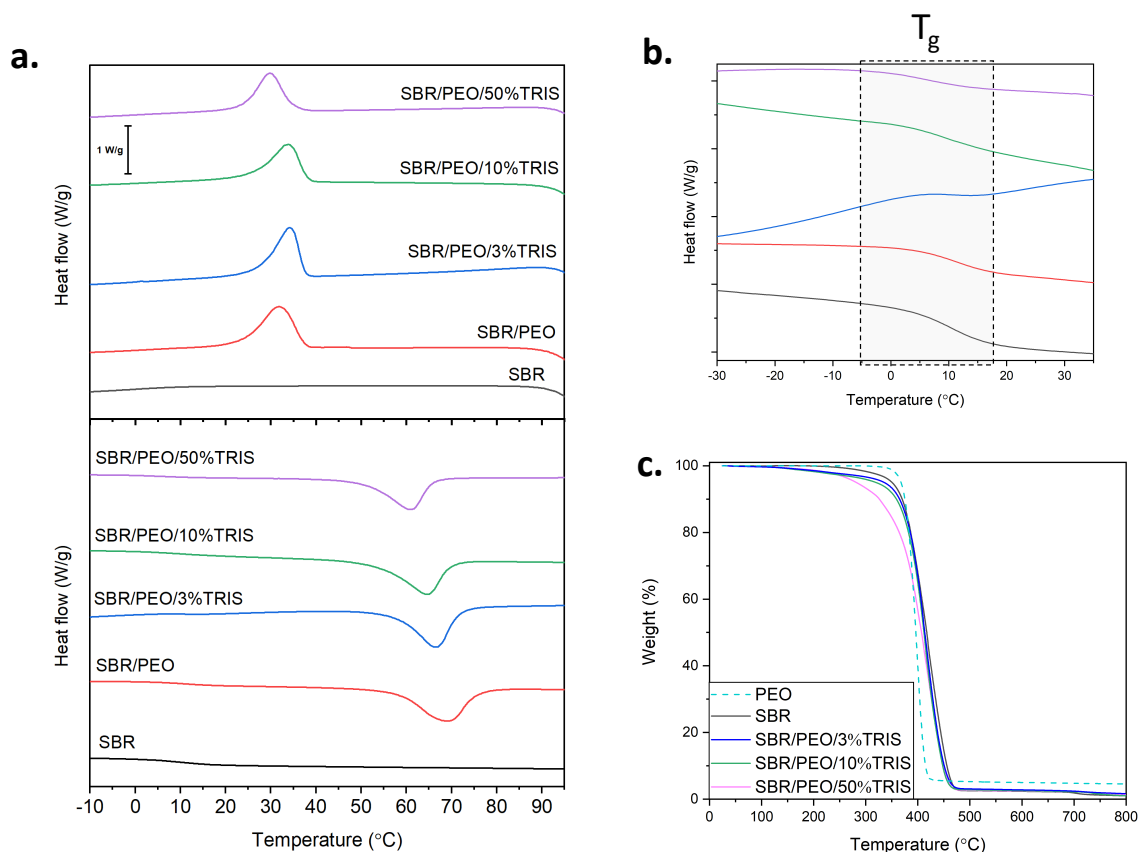


Figure 5-17 a. DSC scans (cooling and second heating) of the prepared electrospun samples and pristine SBR, b. zoom of the DSC scans to better show the  $T_g$  of the SBR/PEO samples, c. TGA thermograms of the SBR/PEO photo-cured fibers as well as of pristine PEO and SBR

The thermal properties of all the electrospun photo-cured samples were studied through DSC and TGA measurements (**Figure 5-17**). From the DSC scans (**Figure 5-17a and b**), the enthalpy of fusion ( $\Delta H_m$ ), the melting temperature ( $T_m$ ) and the glass transition temperature ( $T_g$ ) were obtained: results are reported in **Table 5-6**. As shown in **Figure 5-17a**, the DSC scan of pristine SBR cast film did not display any melting and crystallization peaks, while the  $T_g$  could be obtained at 8 °C from the second heating cycle. Therefore, the peaks appearing in the cooling cycle and in the second heating cycle in the DSC scans of SBR/PEO photo-cured fibers are associated to the PEO constitute. Calculating the enthalpy of fusion from the second heating cycle, one can estimate the real PEO content in the electrospun structure, which is found to be the same as in the initial formulations (**Table 5-6**). These results are comparable with those of the water-soluble fraction measurement reported before and confirm that the electrospinning process does not change the SBR/PEO ratio of the samples. Analyzing the DSC scans of the photo-cured SBR/PEO electrospun fibers (**Figure 5-17b**), a  $T_g$  in the second heating cycle in the range of 7 °C to 12 °C, associated to the SBR component, could be detected. As indicated in the previous chapters, PEO has a  $T_g$  at around -50 °C (which increases to around -20°C in the case of crosslinked systems). Considering that in the present work DSC measurements were conducted starting from -50 °C (due to instrument limitations), as expected, the  $T_g$  of the PEO component could not be detected. In general, the  $T_g$  value of the SBR/PEO electrospun photo-cured samples has not

shown a significant change with the photo-crosslinking. The increment of the crosslinker amount slightly decreases the melting point and the glass transition of the samples (**Table 5-6**).

The thermal resistance of the SBR/PEO electrospun photo-crosslinked fibers was evaluated by TGA experiment (**Figure 5-17c**). All samples exhibited excellent resistance until 400 °C except the formulation containing 50 wt.% TRIS (SBR/PEO/50%TRIS) undergoing its major weight loss from 300 °C. This is probably due to the degradation of the residual unreacted thiol crosslinker. Because of its inferior thermal properties, this sample (SBR/PEO/50%TRIS) was not subjected to further characterizations (described in the following sections).

Table 5-6 Theoretical and calculated PEO concentration, melting enthalpy ( $\Delta H_m$ ), melting temperature ( $T_m$ ) and glass transition temperature ( $T_g$ ) of the SBR/PEO photo-cured fibers, and of pristine SBR and PEO films, from DSC measurements

Samples	Theoretical PEO content (%) <sup>1</sup>	Calculated PEO content (%) <sup>2</sup>	$\Delta H_m$ (J/g)	$T_m$ (°C)	$T_g$ (°C)	$T_d$ (°C) <sup>3</sup>	$T_{10}$ (°C) <sup>4</sup>
SBR	-	-	-	-	11	425.37	369.02
PEO	100.00	100.00	124.07	72	-	399.03	375.18
SBR/PEO/3%TRIS	22.61	22.39	23.18	65	12	319.75	364.78
SBR/PEO/10%TRIS	21.21	21.28	21.75	65.5	11	420.64	358.91
SBR/PEO/50%TRIS	16.83	16.57	19.76	61	7	421.02	326.18

<sup>1</sup>%PEO *in theory* is obtained based on initial formulations for electrospinning; <sup>2</sup>calculated %PEO is obtained based on crystallinity of the formulation depending only on PEO content; <sup>3</sup>decomposition temperature obtained from maxima of the first derivative of TGA thermograms; <sup>4</sup>temperature at which 10% of the initial weight is lost.

### Characterization of the photo-crosslinked SBR electrospun membranes after PEO removal

As explained earlier, PEO was used as a template to produce SBR fibers through the emulsion electrospinning. With the aim of removing PEO to allow the characterization of photo-cured fully rubber fibers (i.e., fabricated with 3 wt.% and 10 wt.% TRIS), the fibrous membranes were subjected to a water treatment (WT), namely immersion in distilled water for 24 h and drying in oven at 60 °C for 3 h.

In order to evaluate the fibers chemical structure, FTIR spectra of photo-cured electrospun membranes prior and after PEO removal were collected and compared. As shown in **Figure 5-18**, after WT, the PEO peaks (843  $\text{cm}^{-1}$  and 1090  $\text{cm}^{-1}$ ) were still present, even though with a much lower intensity. Therefore, although most of PEO component is removed by the water treatment (solubility results of Table 5-5), some traces are still present in the fibers. In fact, it is possible that some PEO chains remain trapped in the crosslinked rubber network, and that a partial PEO photo-

crosslinking reaction in presence of the photoinitiator system takes place during the UV irradiation.

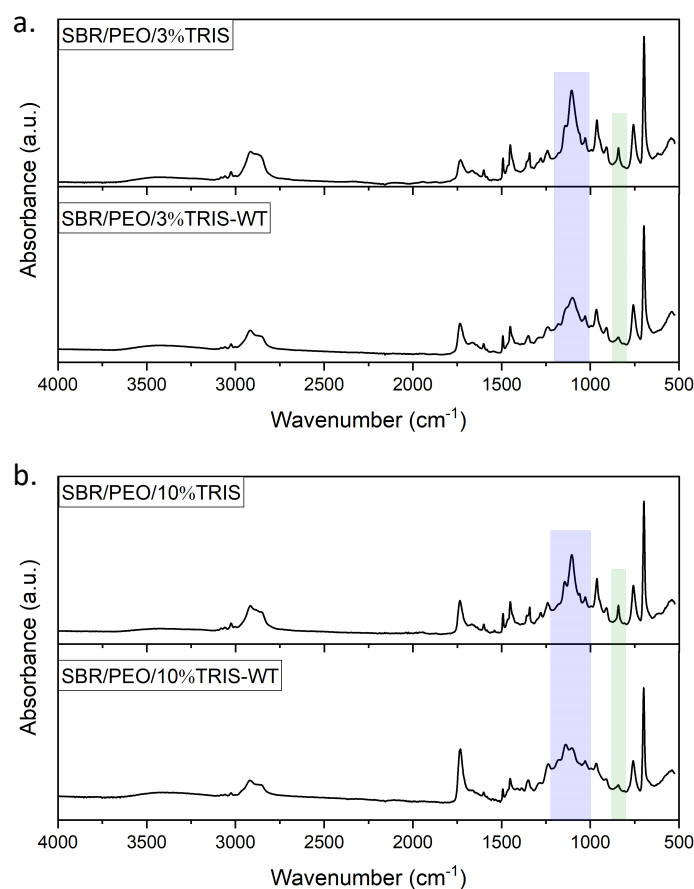


Figure 5-18 FTIR spectra of SBR-based photo-cured electrospun samples (a. SBR/PEO/3%TRIS and b. SBR/PEO/10%TRIS) before and after water treatment for PEO removal.

The morphology of the SBR/PEO/3%TRIS and SBR/PEO/10%TRIS fibrous mats after PEO removal (i.e., WT) is analyzed by FE-SEM imaging, as shown in **Figure 5-19**. Whilst the fibers morphology prior to PEO removal was smooth and the SBR particles could not be detected (**Figure 5-16**), the PEO removal step results in a fiber morphology with higher roughness. In fact, after water treatment, a particular surface structure of the fibers composed of distinct rubber particles partially fused together with high available surface area can be clearly observed. Therefore, the removal of the PEO template makes visible the photo-cured SBR particles, and it is demonstrated that such particles are able to maintain their shape for a long time thanks to the photo-crosslinking process.

The average diameter of the fibers after water rinsing slightly decreases (**Figure 5-19**): it is  $760 \pm 9$  nm for SBR/PEO/10%TRIS-WT (with respect to the  $820 \pm 10$  nm prior to the washing process) and  $800 \pm 8$  nm for SBR/PEO/3%TRIS-WT (with respect to the  $850 \pm 10$  nm prior to the washing process). This is clearly due to the PEO removal from the electrospun fibers. The rubber particle size was also measured (**Figure 5-19**) and a similar diameter ( $105 \pm 4$  nm) was obtained for the two investigated samples. The measured value is also comparable to the size of the

SBR particles in the latex, demonstrating that both crosslinker contents (3wt.% and 10 wt.%) efficiently induced the photo-crosslinking of the rubber particles, stabilizing their shape.

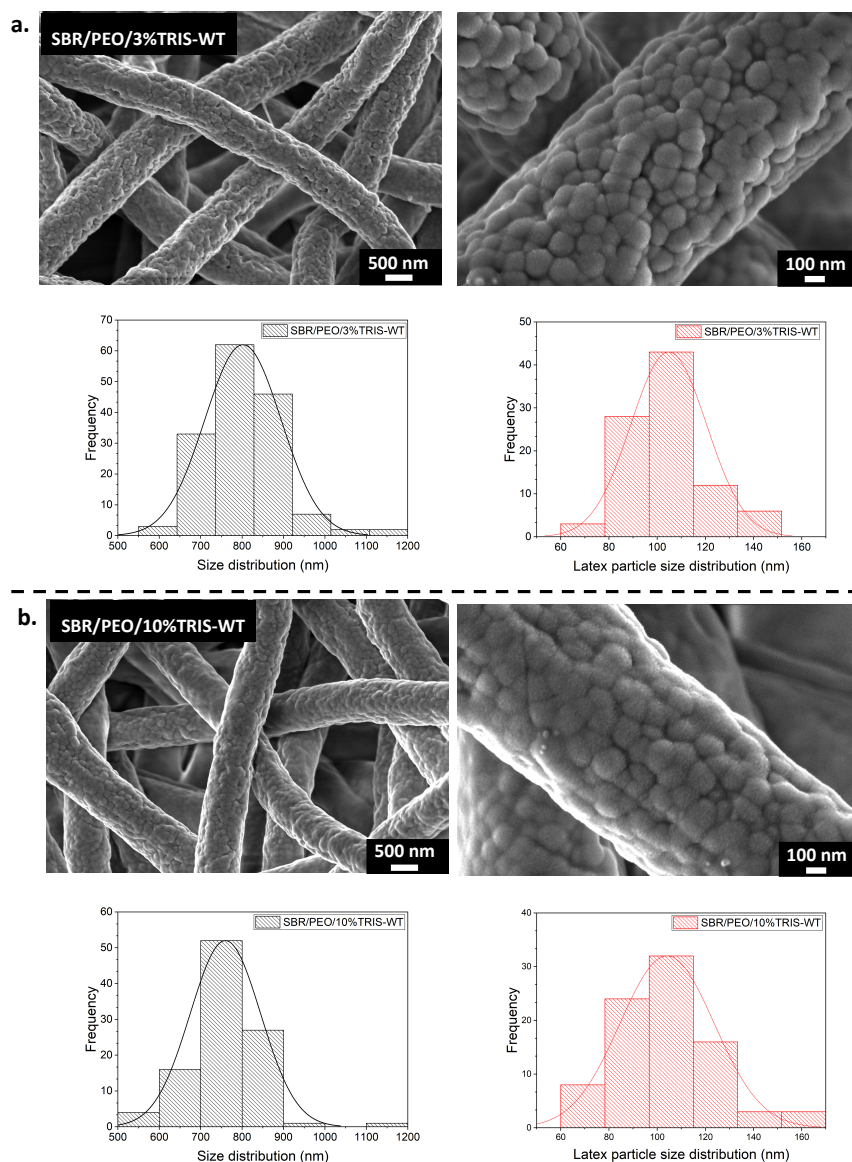


Figure 5-19 FE-SEM images of SBR-based photo-cured electrospun fibers with a. 3 wt.% TRIS and b. 10 wt.% TRIS after water treatment, their fiber diameters distribution, and the distributions of the rubber particles that form the fibers.

The viscoelastic properties of the photo-cured electrospun membranes were examined through DMTA experiment. **Figure 5-20a** and **b** show the storage modulus and  $\tan \delta$  of the fibrous mats prior and after PEO removal. SBR/PEO fibers (before WT) show a severe drop of storage modulus around the melting point of PEO ( $\sim 60^\circ\text{C}$ ). Whilst, after PEO removal, the fibrous samples exhibit the typical trend of a crosslinked network: the storage modulus reaches a plateau in the rubbery regime. These results confirm that the photo-curing reaction allows to form an adequately crosslinked network within the fibers, and that the PEO component is efficiently removed by the water treatment. From DMTA data, the glass transition temperature of the samples was measured as the temperature corresponding to the

maximum of  $\text{Tan } \delta$ ; a  $T_g$  of  $\sim 20^\circ\text{C}$  and of  $\sim 30^\circ\text{C}$  was obtained for the membranes before and after PEO removal, respectively.

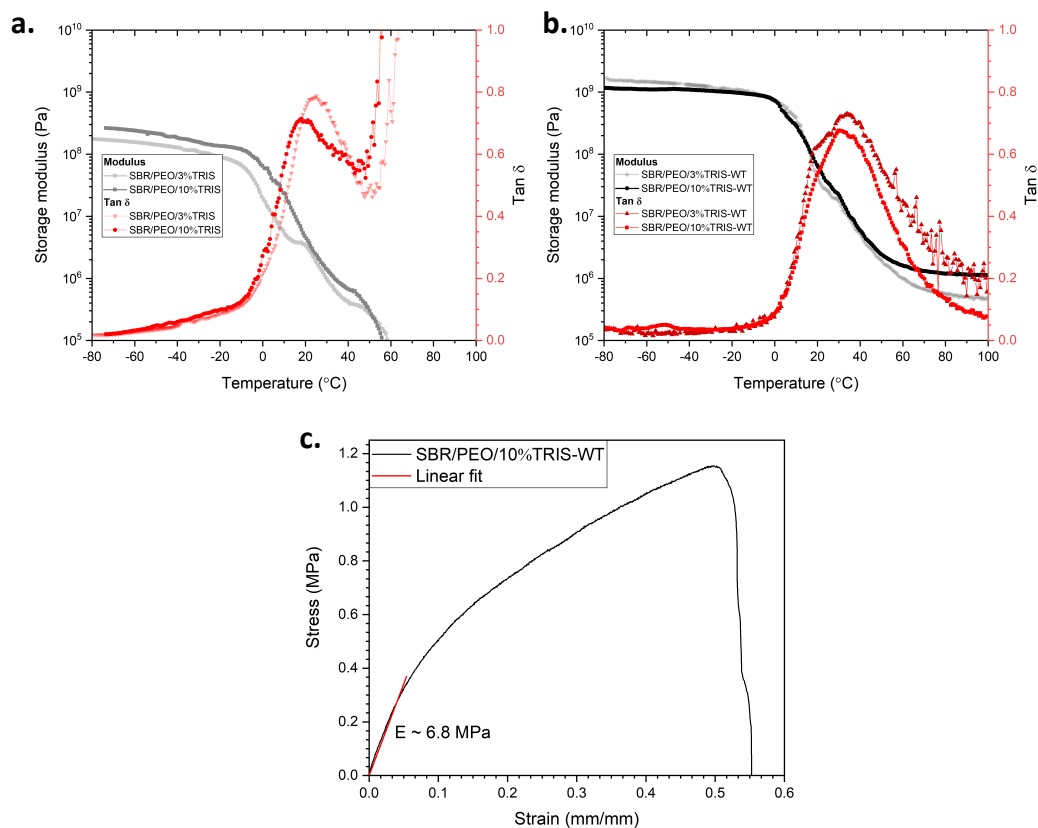


Figure 5-20 DMTA results on photo-cured SBR/PEO electrospun mats containing 3 and 10 wt.% TRIS a. prior and b. after water treatment, c. example of a tensile test measurement on SBR/PEO/10%TRIS photo-cured fibrous membrane after water treatment

Considering that the final SBR fibers obtained from latex electrospinning (and PEO removal) are composed of rubber particles, some concerns on their mechanical properties, especially in comparison to SBR electrospun fibers obtained by solution electrospinning, can be raised. For addressing this issue, tensile tests were performed on SBR/PEO/10%TRIS mats after PEO removal. **Figure 5-20c** shows an example of a stress-strain curve acquired from the tensile test: an elastic modulus  $E$  of  $\sim 6.8 \text{ MPa}$  and an elongation at break of  $\sim 50\%$  were obtained. Indeed, as the investigated fibers are made of nanoparticles, their behavior under tension can be different from that of fibers with a homogenous structure made of crosslinked SBR obtained by solution electrospinning. However, interestingly, the fibrous SBR membrane from latex electrospinning exhibits comparable mechanical strength to the membranes obtained by solution electrospinning [357], while the extensibility is lower. It is thus demonstrated that the photo-induced crosslinks in the SBR fibers from latex electrospinning are formed not only within each spherical rubber particle but also among different adjacent particles.

The thermal resistance of the rubber fibrous membranes after PEO removal was monitored through TGA measurements (**Figure 5-21**). After the WT the electrospun fibers have comparable thermal resistance with respect to their homologue samples before the rinsing process, but the major thermal degradation

starts at even higher temperature ( $T_{10}$ : 372 °C and 373 °C and  $T_d$ : 435.8 °C and 434.9 °C for SBR/PEO/3%TRIS and SBR/PEO/10%TRIS, respectively). This is probably due the removal of residual unreacted monomer during the water treatment.

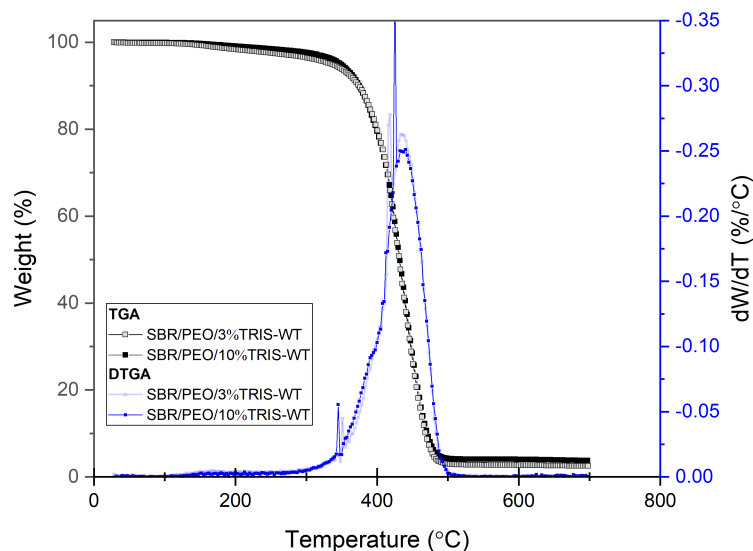


Figure 5-21 TGA thermograms and first derivative of the TGA of electrospun fibers of SBR/PEO/3%TRIS and SBR/PEO/10%TRIS after water treatment

The surface wettability of the electrospun rubber samples after water treatment was assessed by contact angle measurements using water (WCA) and hexadecane (HCA) as test liquids (results are in **Table 5-7**). Cast films of SBR, tested as reference, shows WCA of  $\sim 48^\circ$ . Interestingly, SBR/PEO electrospun membranes exhibit higher WCA ( $67^\circ$ ), probably due to their nanofibrous surface structure. After PEO removal, the photo-cured SBR electrospun samples containing 3 wt.% TRIS and 10 wt.% TRIS exhibit high hydrophobicity with WCA  $\sim 107^\circ$  and  $\sim 105^\circ$ , respectively. In fact, thanks to the peculiar hierarchical structure of the mats, which consist of fibers with  $\sim 780$  nm diameters, made of  $\sim 105$  nm nanoparticle and removal of the hydrophilic component (i.e., PEO), the water wettability of the samples is highly decreased.

As shown in Table 5-7 all the investigated samples are highly oleophilic, having hexadecane contact angle (HCA) values of  $\leq 20^\circ$ .

The fabricated electrospun rubber membranes with high thermal resistance, high hydrophobicity and high oleophilicity can be a potential system for water/oil separation applications. As a demonstrator, the membrane SBR/PEO/10%TRIS after water treatment **Figure 5-22a** was used in a filtration experiment performed with a simple set-up, as shown in **Figure 5-22b**. The membrane was put on top of the porous plate of a funnel, it was wetted by hexadecane, the water/oil mixture (water was colored by a red dye) was poured, and the vacuum was applied to speed up the separation. As demonstrated in **Figure 5-22c**, hexadecane quickly passed through the membrane, while water remained in the glass funnel, because of the highly hydrophobic/superoleophilic characteristics of the rubber fibrous membrane.



Table 5-7 Static water and hexadecane contact angle values of the photo-cured electrospun mats after PEO removal, and of SBR and PEO films

Sample	WCA	HCA
SBR (flat film)	$48^{\circ} \pm 6^{\circ}$	$6^{\circ} \pm 2^{\circ}$
SBR/PEO	$67^{\circ} \pm 3^{\circ}$	$10^{\circ} \pm 2^{\circ}$
SBR/PEO/3%TRIS-WT	$107^{\circ} \pm 6^{\circ}$	$5^{\circ} \pm 1^{\circ}$
SBR/PEO/10%TRIS-WT	$105^{\circ} \pm 7^{\circ}$	$7^{\circ} \pm 1^{\circ}$

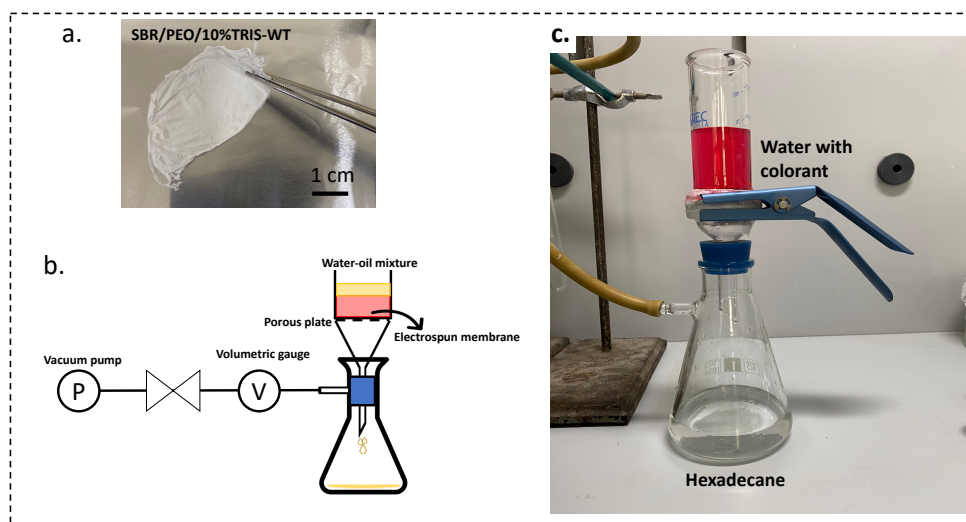


Figure 5-22 a. photograph of the electrospun membrane of SBR/PEO/10wt.%TRIS after water treatment, b. schematic representation of the filtration setup for water/oil separation experiment, c. the experimental setup for the water/oil filtration.

However, it was observed that the performance of the membrane was not stable and after few minutes also water could pass through the membrane, resulting in a scarcely efficient separation. In order to assess the stability of the surface wettability of the membranes, in particular their hydrophobicity durability, the evolution of the static WCA over a period of 20 minutes was assessed. **Figure 5-23** shows the WCA vs. time measurement results for the photo-cured electrospun rubber membranes after water treatment: it can be clearly observed that WCA is not stable over time, and the membranes after almost 5 minutes of contact with water become hydrophilic with  $WCA < 70^{\circ}$ . This instability can be due to the surface rearrangements of the polymeric chains when in contact with a polar solvent. In fact, the residual hydrophilic PEO chains (which are photo-crosslinked and thus are not removed by the WT) could migrate to the surface in contact with water driven by thermodynamic forces, in order to minimize the total energy of the system. This spontaneous rearrangement of the polymeric network is also facilitated by the low  $T_g$  of the system. Indeed, further studies need to be conducted in order to stabilize the wettability properties of the photo-cured rubber fibrous membranes and thus improve their performance in water/oil separation applications.

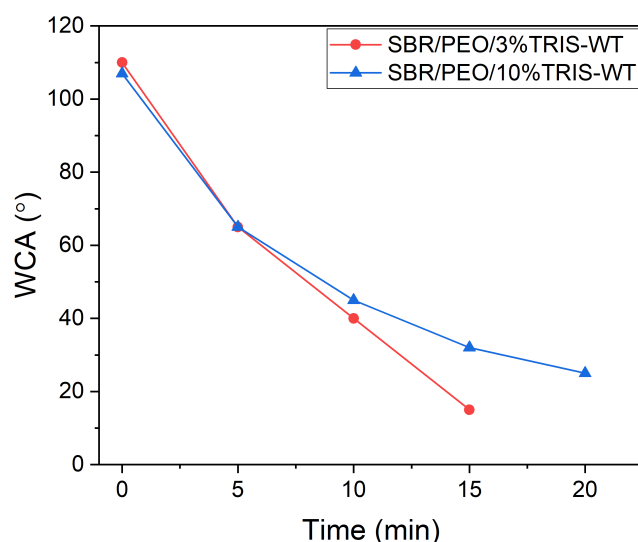


Figure 5-23 Water contact angle versus time for SBR/PEO/3%TRIS-WT and SBR/PEO/10%TRIS-WT

## 5.5 Conclusions

This work described two green methods to fabricate ultrafine rubber fibers and fibrous membranes: the electrospinning of low molecular weight liquid polybutadienes and the electrospinning of styrene-butadiene rubber latexes. For both processes, a photo-induced thiol-ene crosslinking reaction was applied to stabilize the electrospun membranes.

In the first part of this study, liquid polybutadienes were subjected to electrospinning (without using any solvent or heat) and *in-situ* photo-curing, during the spinning process. Both liquid pure polybutadienes and polybutadienes grafted with maleic anhydride were examined. Liquid PB-MA exhibited a faster photo-induced solidification compared to pure PB thanks to two concomitant curing processes: the esterification of the maleic anhydride ring and the oxygen mediated photo-crosslinking reaction of the polybutadiene chains. In addition, PB-MA system showed a better electrospinning processability by forming a more stable jet of polymer during the process. In order to further accelerate the photo-curing reaction, a thiol-based crosslinker and a photo-initiator were introduced to the polybutadiene-*graft*-maleic anhydride system. Additionally, for enhancing the electrospinning process yield and tuning the fiber morphology, a polar additive was added to the formulation to decrease the viscosity and increase the conductivity of the polymer. Rubber fibers with an average diameter of  $\sim 50 \mu\text{m}$  and with excellent shape-stability features were thus fabricated by a green single-step approach applied to liquid polybutadiene. Besides, the crosslinking efficiency, viscoelastic and thermal properties, as well as structural and surface properties were characterized. In addition to a remarkably stable morphology, the electrospun photo-cured fibrous membranes showed high insolubility, good thermal properties and a pronounced hydrophobic and oleophilic character. We believe that our proposed approach offers a simple single-step and sustainable method for preparing

rubber-based fibrous membranes suited for a wide range of applications, especially in the water treatment and water/oil separation areas.

The second part of the work proposed a green approach to prepare ultrafine photo-cured rubber electrospun fibers based on the electrospinning of a SBR latex by using PEO as a template polymer, the subsequent thiol-ene photo-crosslinking in ambient conditions, and the final water treatment step to remove the unreacted monomers and PEO from the structure. Water was used as the only solvent during the whole process. A multifunctional thiol monomer in different amounts and appropriate photo-initiators were added to the electrospinning dispersion to accelerate the photo-crosslinking reaction. The photo-induced curing kinetics and efficiency were evaluated and optimized, leading to the production of stable and insoluble fiber mats containing styrene-butadiene rubber. The fibrous membranes showed a particular morphology characterized by high surface roughness: fibers with a diameter of  $\sim 780$  nm were formed by distinct rubber nanoparticles (diameter of  $\sim 105$  nm) partially fused together. The photo-cured rubber electrospun mats exhibited high thermal resistance, good mechanical properties, and high hydrophobicity ( $WCA > 105^\circ$ ) and oleophilicity. These fibrous membranes with high available surface area thanks to the crosslinked SBR nanoparticles and interesting surface properties are promising for a wide range of applications. Herein, the photo-cured electrospun rubber membranes were tested for water/oil separation, demonstrating to be effective, but only for a short period of time. In fact, the separation efficiency of the membrane decreased with time, due to the instability of the surface water wettability (i.e., the membrane become hydrophilic after almost 5 minutes of contact with water). Future work will be focused on enhancing the membranes performance in water/oil separation applications by stabilizing their wettability properties.



# Chapter 6

## General conclusions and future perspectives

The main goal of this research work was to prepare polymeric fibrous membranes through the versatile technique of electrospinning and to enhance their properties by applying photo-induced crosslinking reactions, in particular addressing the shape instability issues of fibers. This approach was successfully applied to different polymeric systems, namely chitosan (CS)-based, polyethylene oxide (PEO)-based and polybutadiene (PB)-based materials. Accordingly, depending on the polymer structure, the chemistry of the systems were tailored in order to optimize the electrospinning process and to induce an efficient crosslinking degree for retaining the fibrous morphology when the membranes are placed in contact with a solvent, or at elevated temperature (above the melting point of the polymer), or over storage time. As a result, stable photo-cured electrospun membranes were fabricated with potential application in a variety of areas, such as food packaging, phase change materials for energy management and water/oil separation.

In the first part of the doctoral work (Chapter 3), the fabrication of CS nanofibers by electrospinning was successfully conducted with the aid of an easily electrospinnable polymer, namely PEO, in the presence of a photoinitiator. Three different CS/PEO blend compositions were studied and the composition leading to the optimal fibrous morphology and the easiest processability (i.e., CS/PEO 70/30 wt./wt.) was selected for the subsequent photo-crosslinking step. Upon electrospinning process, a PEO enrichment occurred causing a reduced CS content (~60 wt.%) in the electrospun fibers compared to the initial formulation. Uniform and defect free CS-based electrospun mats, formed by fibers with an average diameter of around 270 nm, were produced. The electrospun membranes were irradiated to trigger radical crosslinking in inert atmosphere with two different UV intensities, namely 7 and 70 mW/cm<sup>2</sup>. Although a partial degradation of CS was detected by photo-DSC and FTIR spectroscopy, the photo-cured CS-based electrospun samples showed enhanced morphology retention in contact with water, especially when the higher UV intensity was used, in addition to improved thermal stability. Therefore, the CS/PEO membranes are proposed for potential application in food packaging. For the real application, a confirmation of their antibacterial properties, as well as a characterization of their permeability towards different small molecules (e.g., gases, aromas, additives) are in progress. Moreover, as a

perspective the assembling of the CS-based electrospun membranes with other polymeric films to form multi-layer packaging systems can be tried. Evidently, the biomedical application can also be explored.

In the following chapter (Chapter 4), the investigation of the electrospinning and photo-induced crosslinking reaction of PEO-based systems is described for assessing their suitability as potential candidates for solid-solid shape-stable phase change materials (PCMs) in heat storage/management applications. The fibrous mats were prepared by electrospinning of PEO solutions containing a multifunctional acrylic monomer and a photoinitiator. The formed fibrous membranes were subsequently UV irradiated to initiate the photo-curing reaction. The effect of the reactive group, average functionality and amount of the chosen crosslinker on the morphology of the PEO-based fibrous membranes was assessed and membranes formed by fibers in a range of ~300-500 nm were obtained. The kinetics of the photo-crosslinking process was followed through photo-DSC analyses, and FTIR spectroscopy and insoluble fraction experiments confirmed the successful crosslinking of all the studied systems. Then, a comprehensive characterization of the photo-cured electrospun membranes was conducted. Particularly, it was demonstrated that the fibrous morphology of the photo-crosslinked PEO-based electrospun membranes could be retained after contact with water, thus addressing the main issue of PEO systems. Accordingly, the most efficient PEO-based electrospun membrane in terms of morphology uniformity and retention over solvent exposure was selected for further characterization of the mechanical and thermal properties. The photo-crosslinked PEO-based membranes showed enhanced mechanical properties compared to un-cured samples (i.e., ultimate tensile strength and strain at the breaking point). Cyclic thermal measurements were especially designed to study the heat storage ability and structural stability of the fabricated electrospun systems. As a result, the membranes showed remarkable stability in terms of melting/crystallinity phase change enthalpy and high thermal resistance (even above the melting point of PEO) over multiple cycles. Thus, the developed PEO electrospun membranes, being resistant to both solvent and heat, and showing good thermal and heat storage properties, were demonstrated to have a wider domain of applicability: besides the well-known biomedical applications, they are suitable for heat management as solid-solid shape-stable fibrous PCM. The ongoing work on the developed PEO-based electrospun system is focused on further enhancing the membranes properties, particularly their thermal conductivity and their heat storage/retrieve capacity. The production of composite fibrous membranes containing conductive nanofillers (e.g., graphene oxide, silver nanoparticles) is under investigation.

Finally, electrospinning processes and photo-induced crosslinking of PB-based materials were investigated (Chapter 5) with a special attention to sustainability. Two different systems, meaning liquid polybutadienes and styrene-butadiene rubber (SBR) latexes, were studied. In the first part of this work on PB systems, different low molecular weight polybutadienes (at the liquid state), among which some were grafted with maleic anhydride, were subjected to electrospinning at room temperature and without using any solvent, solidifying the fibers by *in-situ*

photo-curing (i.e., by irradiating the ejected polymer fiber before reaching the collector and forming the mat). The electrospinning process and the photo-induced crosslinking reaction were tailored to yield stable solid PB-based rubber fibers. Interestingly, the polybutadiene grafted with the highest amount of maleic anhydride (15 wt.%) successfully yielded electrospun fibers and also exhibited the fastest solidification reaction by UV-irradiation in air. In fact, FTIR spectroscopy studies demonstrated concomitant reactions of the polybutadiene chains, i.e. oxygen mediated photo-crosslinking and photo-induced esterification of the maleic anhydride ring, with an overall enhancement of the crosslinking reaction rate. For having reaction rates comparable to the flying jet time during electrospinning, the thiol-ene chemistry was chosen for the curing reaction (i.e., a multifunctional thiol crosslinker and a photoinitiator were added to the formulations). As a result, rubber fibers with excellent shape stability feature were fabricated while using a green single-step approach. The rubber fibers with an average diameter as low as  $\sim 50 \mu\text{m}$  were obtained with the aid of polar additive. The rubber fibrous membranes showed high insolubility, good thermal properties and a pronounced hydrophobic and oleophilic character, thus being promising for instance for water/oil separation applications.

In the second part of the work on PB systems, the suspension electrospinning of aqueous SBR latexes was studied. In this case, rubber electrospun fibers were obtained by using PEO as a fiber forming template; a multifunctional thiol monomer in different concentration and a photoinitiating system were added to the latex to assure crosslinking via thio-ene reactions when the fabricated mats were subjected to irradiation. Finally, a simple water treatment step was performed in order to remove the unreacted monomers and PEO. Thus, water was used as the only solvent for the whole process. As a result, stable SBR fibers with a diameter of  $\sim 780 \text{ nm}$  were formed; a peculiar fiber morphology made of distinct spherical rubber nanoparticles (diameter of  $\sim 105 \text{ nm}$ ) partially fused together was obtained. This particular surface topography led to a high hydrophobicity (water contact angle  $> 105^\circ$ ) of the electrospun membranes. Moreover, the photo-cured SBR mats showed high thermal resistance and good mechanical properties comparable with those of SBR membranes obtained from conventional solution electrospinning using toxic solvents. The photo-crosslinked SBR membranes were tested for water/oil separation, demonstrating to be effective. However, this system needs further optimization to make it suitable for real applications: a better control of the surface wettability properties and their evolution over time has to be achieved. In this regard, the interesting strategy currently explored to enhance the hydrophobicity and make it stable for long term application is to functionalize the rubber fibrous membranes, exploiting the unreacted thiol or ene groups on their surface to chemically bond suitable monomers/polymers (e.g., siloxane and fluorinated systems). It is worth mentioning that the primary attempts showed a successful functionalization of the photo-cured SBR fibrous membranes, exhibiting more stable surface properties for water/oil separation.

In conclusions, the processes developed in this thesis work, which are based on the coupling of electrospinning and photo-crosslinkg, have been demonstrated to be successfully applied to different polymeric systems, enhancing their properties and enlarging the applicability domain of the electrospun membranes. It is worth noting that the method proposed in this thesis is highly versatile as different chemistry can be used for crosslinking the fibrous membranes, thus it is potentially applicable to any polymeric system. Moreover, the chosen approach fullfils the criteria of sustainability: the process developed in this research employs green chemistries, in particular does not require heating, takes place at room temperature, without solvent or with aqueous systems, thus limiting energy consumption and the use of toxic and harmful substances, and overall raising the least possible environmental and health concerns.





# References

1. Reneker, D.H.; Chun, I. Nanometre diameter fibres of polymer, produced by electrospinning. *Nanotechnology* **1996**, *7*, 216.
2. Huang, Z.M.; Zhang, Y.Z.; Kotaki, M.; Ramakrishna, S. A review on polymer nanofibers by electrospinning and their applications in nanocomposites. *Compos. Sci. Technol.* **2003**, *63*, 2223–2253, doi:10.1016/S0266-3538(03)00178-7.
3. Bhardwaj, N.; Kundu, S.C. Electrospinning: A fascinating fiber fabrication technique. *Biotechnol. Adv.* **2010**, *28*, 325–347, doi:10.1016/j.biotechadv.2010.01.004.
4. Teo, W.E.; Ramakrishna, S. A review on electrospinning design and nanofibre assemblies. *Nanotechnology* **2006**, *17*, R89.
5. Reneker, D.H.; Yarin, A.L.; Fong, H.; Koombhongse, S. Bending instability of electrically charged liquid jets of polymer solutions in electrospinning. *J. Appl. Phys.* **2000**, *87*, 4531–4547.
6. Boys, C.V. On the production, properties, and some suggested uses of the finest threads. *Proc. Phys. Soc. London* **1887**, *9*, 8.
7. Xue, J.; Wu, T.; Dai, Y.; Xia, Y. Electrospinning and electrospun nanofibers: Methods, materials, and applications. *Chem. Rev.* **2019**, *119*, 5298–5415, doi:10.1021/acs.chemrev.8b00593.
8. Taylor, G.I. Electrically driven jets. *Proc. R. Soc. London. A. Math. Phys. Sci.* **1969**, *313*, 453–475.
9. Xue, J.; Wu, T.; Dai, Y.; Xia, Y. Electrospinning and electrospun nanofibers: methods, materials, and applications. *Chem. Rev.* **2019**, *119*, 5298–5415.
10. Spivak, A.F.; Dzenis, Y.A.; Reneker, D.H. Model of steady state jet in the electrospinning process. *Mech. Res. Commun.* **2000**, *27*, 37–42.
11. Reneker, D.H.; Yarin, A.L. Electrospinning jets and polymer nanofibers. *Polymer (Guildf).* **2008**, *49*, 2387–2425.
12. Fridrikh, S. V; Jian, H.Y.; Brenner, M.P.; Rutledge, G.C. Controlling the fiber diameter during electrospinning. *Phys. Rev. Lett.* **2003**, *90*, 144502.
13. Cloupeau, M.; Prunet-Foch, B. Electrostatic spraying of liquids in cone-jet mode. *J. Electrostat.* **1989**, *22*, 135–159.
14. Xue, J.; Xie, J.; Liu, W.; Xia, Y. Electrospun nanofibers: new concepts, materials, and applications. *Acc. Chem. Res.* **2017**, *50*, 1976–1987.
15. Feng, J.J. The stretching of an electrified non-Newtonian jet: A model for electrospinning. *Phys. Fluids* **2002**, *14*, 3912–3926, doi:10.1063/1.1510664.
16. Gañán-Calvo, A.M. Cone-jet analytical extension of Taylor’s electrostatic solution and the asymptotic universal scaling laws in electrospinning. *Phys. Rev. Lett.* **1997**, *79*, 217.
17. He, J.-H.; Wu, Y.; Zuo, W.-W. Critical length of straight jet in electrospinning. *Polymer (Guildf).* **2005**, *46*, 12637–12640.
18. Fong, H.; Chun, I.; Reneker, D.H. Beaded nanofibers formed during electrospinning.

- Polymer (Guildf)*. **1999**, *40*, 4585–4592.
19. Munir, M.M.; Suryamas, A.B.; Iskandar, F.; Okuyama, K. Scaling law on particle-to-fiber formation during electrospinning. *Polymer (Guildf)*. **2009**, *50*, 4935–4943.
  20. Shin, Y.M.; Hohman, M.M.; Brenner, M.P.; Rutledge, G.C. Experimental characterization of electrospinning: The electrically forced jet and instabilities. *Polymer (Guildf)*. **2001**, *42*, 09955–09967, doi:10.1016/s0032-3861(01)00540-7.
  21. Kirichenko, V.; Filatov, Y.; Budyka, A. Electrospinning of micro-and nanofibers: fundamentals in separation and filtration processes. *Danbury, CT Begell House* **2007**.
  22. Bhardwaj, N.; Kundu, S.C. Electrospinning: a fascinating fiber fabrication technique. *Biotechnol. Adv.* **2010**, *28*, 325–347.
  23. Subbiah, T.; Bhat, G.S.; Tock, R.W.; Parameswaran, S.; Ramkumar, S.S. Electrospinning of nanofibers. *J. Appl. Polym. Sci.* **2005**, *96*, 557–569.
  24. Taylor, G.I. Disintegration of water drops in an electric field. *Proc. R. Soc. London. Ser. A. Math. Phys. Sci.* **1964**, *280*, 383–397.
  25. Yarin, A.L.; Koombhongse, S.; Reneker, D.H. Taylor cone and jetting from liquid droplets in electrospinning of nanofibers. *J. Appl. Phys.* **2001**, *90*, 4836–4846.
  26. Kowalewski, T.A.; Błoński, S.; Barral, S. Experiments and modelling of electrospinning process. *Bull. polish Acad. Sci. Tech. Sci.* **2005**, 385–394.
  27. Eggers, J.; Villermaux, E. Physics of liquid jets. *Reports Prog. Phys.* **2008**, *71*, 36601.
  28. Spivak, A.F.; Dzenis, Y.A. Asymptotic decay of radius of a weakly conductive viscous jet in an external electric field. *Appl. Phys. Lett.* **1998**, *73*, 3067–3069.
  29. Deitzel, J.M.; Kleinmeyer, J.; Harris, D.E.A.; Tan, N.C.B. The effect of processing variables on the morphology of electrospun nanofibers and textiles. *Polymer (Guildf)*. **2001**, *42*, 261–272.
  30. Deitzel, J.M.; Kosik, W.; McKnight, S.H.; Beck Tan, N.C.; DeSimone, J.M.; Crette, S. Electrospinning of polymer nanofibers with specific surface chemistry. *Polymer (Guildf)*. **2001**, *43*, 1025–1029, doi:10.1016/S0032-3861(01)00594-8.
  31. Hohman, M.M.; Shin, M.; Rutledge, G.; Brenner, M.P. Electrospinning and electrically forced jets. II. Applications. *Phys. fluids* **2001**, *13*, 2221–2236.
  32. Hohman, M.M.; Shin, M.; Rutledge, G.; Brenner, M.P. Electrospinning and electrically forced jets. I. Stability theory. *Phys. fluids* **2001**, *13*, 2201–2220.
  33. Wan, Y.Q.; Guo, Q.; Pan, N. Thermo-electro-hydrodynamic model for electrospinning process. *Int. J. Nonlinear Sci. Numer. Simul.* **2004**, *5*, 5–8, doi:10.1515/IJNSNS.2004.5.1.5.
  34. Yarin, A.L.; Koombhongse, S.; Reneker, D.H. Bending instability in electrospinning of nanofibers. *J. Appl. Phys.* **2001**, *89*, 3018–3026.
  35. Zuo, W.; Zhu, M.; Yang, W.; Yu, H.; Chen, Y.; Zhang, Y. Experimental study on relationship between jet instability and formation of beaded fibers during electrospinning. *Polym. Eng. Sci.* **2005**, *45*, 704–709.
  36. Thompson, C.J.; Chase, G.G.; Yarin, A.L.; Reneker, D.H. Effects of parameters on nanofiber diameter determined from electrospinning model. *Polymer (Guildf)*. **2007**, *48*, 6913–6922, doi:10.1016/j.polymer.2007.09.017.
  37. Reneker, D.H.; Fong, H. Polymeric nanofibers: introduction. In; ACS Publications, 2006 ISBN 1947-5918.
  38. Theron, S.A.; Zussman, E.; Yarin, A.L. Experimental investigation of the governing parameters in the electrospinning of polymer solutions. *Polymer (Guildf)*. **2004**, *45*, 2017–2030, doi:10.1016/j.polymer.2004.01.024.

39. Theron, S.A.; Zussman, E.; Yarin, A.L. Experimental investigation of the governing parameters in the electrospinning of polymer solutions. *Polymer (Guildf)*. **2004**, *45*, 2017–2030.
40. Haider, A.; Haider, S.; Kang, I.K. A comprehensive review summarizing the effect of electrospinning parameters and potential applications of nanofibers in biomedical and biotechnology. *Arab. J. Chem.* **2018**, *11*, 1165–1188, doi:10.1016/j.arabjc.2015.11.015.
41. Shenoy, S.L.; Bates, W.D.; Frisch, H.L.; Wnek, G.E. Role of chain entanglements on fiber formation during electrospinning of polymer solutions: good solvent, non-specific polymer–polymer interaction limit. *Polymer (Guildf)*. **2005**, *46*, 3372–3384.
42. Hu, J.; Wang, X.; Ding, B.; Lin, J.; Yu, J.; Sun, G. One-step Electro-spinning/netting Technique for Controllably Preparing Polyurethane Nano-fiber/net. *Macromol. Rapid Commun.* **2011**, *32*, 1729–1734.
43. Barakat, N.A.M.; Kanjwal, M.A.; Sheikh, F.A.; Kim, H.Y. Spider-net within the N6, PVA and PU electrospun nanofiber mats using salt addition: Novel strategy in the electrospinning process. *Polymer (Guildf)*. **2009**, *50*, 4389–4396, doi:10.1016/j.polymer.2009.07.005.
44. Tripatanasuwan, S.; Zhong, Z.; Reneker, D.H. Effect of evaporation and solidification of the charged jet in electrospinning of poly (ethylene oxide) aqueous solution. *Polymer (Guildf)*. **2007**, *48*, 5742–5746.
45. Pai, C.-L.; Boyce, M.C.; Rutledge, G.C. Morphology of porous and wrinkled fibers of polystyrene electrospun from dimethylformamide. *Macromolecules* **2009**, *42*, 2102–2114.
46. Larrondo, L.; St. John Manley, R. Electrostatic fiber spinning from polymer melts. I. Experimental observations on fiber formation and properties. *J. Polym. Sci. Polym. Phys. Ed.* **1981**, *19*, 909–920.
47. Lyons, J.; Li, C.; Ko, F. Melt-electrospinning part I: processing parameters and geometric properties. *Polymer (Guildf)*. **2004**, *45*, 7597–7603.
48. Brown, T.D.; Dalton, P.D.; Hutmacher, D.W. Melt electrospinning today: An opportune time for an emerging polymer process. *Prog. Polym. Sci.* **2016**, *56*, 116–166.
49. Ogata, N.; Yamaguchi, S.; Shimada, N.; Lu, G.; Iwata, T.; Nakane, K.; Ogihara, T. Poly (lactide) nanofibers produced by a melt-electrospinning system with a laser melting device. *J. Appl. Polym. Sci.* **2007**, *104*, 1640–1645.
50. Shimada, N.; Tsutsumi, H.; Nakane, K.; Ogihara, T.; Ogata, N. Poly (ethylene-co-vinyl alcohol) and Nylon 6/12 nanofibers produced by melt electrospinning system equipped with a line-like laser beam melting device. *J. Appl. Polym. Sci.* **2010**, *116*, 2998–3004.
51. Hutmacher, D.W.; Dalton, P.D. Melt electrospinning. *Chem. Asian J.* **2011**, *6*, 44–56.
52. Zhmayev, E.; Cho, D.; Joo, Y.L. Nanofibers from gas-assisted polymer melt electrospinning. *Polymer (Guildf)*. **2010**, *51*, 4140–4144.
53. Zhang, C.; Feng, F.; Zhang, H. Emulsion electrospinning: Fundamentals, food applications and prospects. *Trends Food Sci. Technol.* **2018**, *80*, 175–186.
54. Angeles, M.; Cheng, H.; Velankar, S.S. Emulsion electrospinning: composite fibers from drop breakup during electrospinning. *Polym. Adv. Technol.* **2008**, *19*, 728–733.
55. Yarin, A.L. Coaxial electrospinning and emulsion electrospinning of core–shell fibers. *Polym. Adv. Technol.* **2011**, *22*, 310–317.
56. He, H.-W.; Zhang, B.; Yan, X.; Dong, R.-H.; Jia, X.-S.; Yu, G.-F.; Ning, X.; Xia, L.-H.; Long, Y.-Z. Solvent-free thermocuring electrospinning to fabricate ultrathin polyurethane fibers with high conductivity by in situ polymerization of polyaniline. *RSC Adv.* **2016**, *6*, 106945–106950.

57. Shanmuganathan, K.; Sankhagowit, R.K.; Iyer, P.; Ellison, C.J. Thiol–ene chemistry: a greener approach to making chemically and thermally stable fibers. *Chem. Mater.* **2011**, *23*, 4726–4732.
58. Lv, D.; Zhu, M.; Jiang, Z.; Jiang, S.; Zhang, Q.; Xiong, R.; Huang, C. Green electrospun nanofibers and their application in air filtration. *Macromol. Mater. Eng.* **2018**, *303*, 1800336.
59. Corrigan, N.; Yeow, J.; Judzewitsch, P.; Xu, J.; Boyer, C. Seeing the light: advancing materials chemistry through photopolymerization. *Angew. Chemie Int. Ed.* **2019**, *58*, 5170–5189.
60. Sun, D.; Chang, C.; Li, S.; Lin, L. Near-field electrospinning. *Nano Lett.* **2006**, *6*, 839–842.
61. Wang, X.; Zheng, G.; Xu, L.; Cheng, W.; Xu, B.; Huang, Y.; Sun, D. Fabrication of nanochannels via near-field electrospinning. *Appl. Phys. A* **2012**, *108*, 825–828.
62. Chang, J.; Liu, Y.; Heo, K.; Lee, B.Y.; Lee, S.; Lin, L. Direct-Write Complementary Graphene Field Effect Transistors and Junctions via Near-Field Electrospinning. *Small* **2014**, *10*, 1920–1925.
63. Liu, Y.; Zhang, L.; Sun, X.-F.; Liu, J.; Fan, J.; Huang, D.-W. Multi-jet electrospinning via auxiliary electrode. *Mater. Lett.* **2015**, *141*, 153–156.
64. Lee, B.-S.; Jeon, S.-Y.; Park, H.; Lee, G.; Yang, H.-S.; Yu, W.-R. New electrospinning nozzle to reduce jet instability and its application to manufacture of multi-layered nanofibers. *Sci. Rep.* **2014**, *4*, 1–9.
65. Moghe, A.K.; Gupta, B.S. Co-axial electrospinning for nanofiber structures: preparation and applications. *Polym. Rev.* **2008**, *48*, 353–377.
66. Lee, G.H.; Song, J.-C.; Yoon, K.-B. Controlled wall thickness and porosity of polymeric hollow nanofibers by coaxial electrospinning. *Macromol. Res.* **2010**, *18*, 571–576.
67. Wang, M.; Yu, J.H.; Kaplan, D.L.; Rutledge, G.C. Production of submicron diameter silk fibers under benign processing conditions by two-fluid electrospinning. *Macromolecules* **2006**, *39*, 1102–1107.
68. Reddy, C.S.; Arinstein, A.; Avrahami, R.; Zussman, E. Fabrication of thermoset polymer nanofibers by co-electrospinning of uniform core-shell structures. *J. Mater. Chem.* **2009**, *19*, 7198–7201.
69. Zhao, S.; Zhou, Q.; Long, Y.-Z.; Sun, G.-H.; Zhang, Y. Nanofibrous patterns by direct electrospinning of nanofibers onto topographically structured non-conductive substrates. *Nanoscale* **2013**, *5*, 4993–5000.
70. Garcia Garcia, A.; Hebraud, A.; Duval, J.-L.; Wittmer, C.R.; Gaut, L.; Duprez, D.; Egles, C.; Bedoui, F.; Schlatter, G.; Legallais, C. Poly ( $\epsilon$ -caprolactone)/hydroxyapatite 3D honeycomb scaffolds for a cellular microenvironment adapted to maxillofacial bone reconstruction. *ACS Biomater. Sci. Eng.* **2018**, *4*, 3317–3326.
71. Li, D.; Wang, Y.; Xia, Y. Electrospinning of polymeric and ceramic nanofibers as uniaxially aligned arrays. *Nano Lett.* **2003**, *3*, 1167–1171, doi:10.1021/nl0344256.
72. Persano, L.; Camposeo, A.; Tekmen, C.; Pisignano, D. Industrial upscaling of electrospinning and applications of polymer nanofibers: a review. *Macromol. Mater. Eng.* **2013**, *298*, 504–520.
73. Teo, W.-E.; Gopal, R.; Ramaseshan, R.; Fujihara, K.; Ramakrishna, S. A dynamic liquid support system for continuous electrospun yarn fabrication. *Polymer (Guildf)*. **2007**, *48*, 3400–3405.
74. Liu, J.; Chen, G.; Gao, H.; Zhang, L.; Ma, S.; Liang, J.; Fong, H. Structure and thermo-

- chemical properties of continuous bundles of aligned and stretched electrospun polyacrylonitrile precursor nanofibers collected in a flowing water bath. *Carbon N. Y.* **2012**, *50*, 1262–1270.
75. Li, Y.; Zhu, J.; Cheng, H.; Li, G.; Cho, H.; Jiang, M.; Gao, Q.; Zhang, X. Developments of Advanced Electrospinning Techniques: A Critical Review. *Adv. Mater. Technol.* **2021**, 2100410.
  76. Li, D.; Xia, Y. Electrospinning of nanofibers: reinventing the wheel? *Adv. Mater.* **2004**, *16*, 1151–1170.
  77. Dersch, R.; Steinhart, M.; Boudriot, U.; Greiner, A.; Wendorff, J.H. Nanoprocessing of polymers: applications in medicine, sensors, catalysis, photonics. *Polym. Adv. Technol.* **2005**, *16*, 276–282.
  78. Muthiah, P.; Hsu, S.H.; Sigmund, W. Coaxially electrospun PVDF-teflon AF and teflon AF-PVDF core-sheath nanofiber mats with superhydrophobic properties. *Langmuir* **2010**, *26*, 12483–12487, doi:10.1021/la100748g.
  79. Haloui, R.; Moldavsky, A.; Cohen, Y.; Semiat, R.; Zussman, E. Development of micro-scale hollow fiber ultrafiltration membranes. *J. Memb. Sci.* **2011**, *379*, 370–377.
  80. Zhao, P.; Soin, N.; Prashanthi, K.; Chen, J.; Dong, S.; Zhou, E.; Zhu, Z.; Narasimulu, A.A.; Montemagno, C.D.; Yu, L.; et al. Emulsion Electrospinning of Polytetrafluoroethylene (PTFE) Nanofibrous Membranes for High-Performance Triboelectric Nanogenerators. *ACS Appl. Mater. Interfaces* **2018**, *10*, 5880–5891, doi:10.1021/acsami.7b18442.
  81. Yoshino, S.; Shinohara, A.; Kodama, K.; Morimoto, Y. Fabrication of catalyst layer with ionomer nanofiber scaffolding for polymer electrolyte fuel cells. *J. Power Sources* **2020**, *476*, 228584, doi:10.1016/j.jpowsour.2020.228584.
  82. Stanishevsky, A.; Wetuski, J.; Walock, M.; Stanishevskaya, I.; Yockell-Lelièvre, H.; Košťáková, E.; Lukáš, D. Ribbon-like and spontaneously folded structures of tungsten oxide nanofibers fabricated via electrospinning. *RSC Adv.* **2015**, *5*, 69534–69542.
  83. Zaarour, B.; Zhu, L.; Huang, C.; Jin, X. Fabrication of a polyvinylidene fluoride cactus-like nanofiber through one-step electrospinning. *RSC Adv.* **2018**, *8*, 42353–42360.
  84. Wang, N.; Sun, C.; Zhao, Y.; Zhou, S.; Chen, P.; Jiang, L. Fabrication of three-dimensional ZnO/TiO<sub>2</sub> heteroarchitectures via a solution process. *J. Mater. Chem.* **2008**, *18*, 3909–3911.
  85. Fong, H.; Liu, W.; Wang, C.-S.; Vaia, R.A. Generation of electrospun fibers of nylon 6 and nylon 6-montmorillonite nanocomposite. *Polymer (Guildf)*. **2002**, *43*, 775–780.
  86. Lee, S.; Kay Obendorf, S. Developing protective textile materials as barriers to liquid penetration using melt-electrospinning. *J. Appl. Polym. Sci.* **2006**, *102*, 3430–3437.
  87. Ma, Z.; Kotaki, M.; Yong, T.; He, W.; Ramakrishna, S. Surface engineering of electrospun polyethylene terephthalate (PET) nanofibers towards development of a new material for blood vessel engineering. *Biomaterials* **2005**, *26*, 2527–2536.
  88. Yoon, K.; Kim, K.; Wang, X.; Fang, D.; Hsiao, B.S.; Chu, B. High flux ultrafiltration membranes based on electrospun nanofibrous PAN scaffolds and chitosan coating. *Polymer (Guildf)*. **2006**, *47*, 2434–2441.
  89. Lee, M.W.; An, S.; Latthe, S.S.; Lee, C.; Hong, S.; Yoon, S.S. Electrospun polystyrene nanofiber membrane with superhydrophobicity and superoleophilicity for selective separation of water and low viscous oil. *ACS Appl. Mater. Interfaces* **2013**, *5*, 10597–10604.
  90. Wang, X.; Ding, B.; Sun, M.; Yu, J.; Sun, G. Nanofibrous polyethyleneimine membranes as sensitive coatings for quartz crystal microbalance-based formaldehyde sensors. *Sensors*

- Actuators B Chem.* **2010**, *144*, 11–17.
91. Kianfar, P.; Vitale, A.; Dalle Vacche, S.; Bongiovanni, R. Enhancing properties and water resistance of PEO-based electrospun nanofibrous membranes by photo-crosslinking. *J. Mater. Sci.* **2020**, *56*, 1879–1896.
  92. Lee, K.H.; Kim, H.Y.; La, Y.M.; Lee, D.R.; Sung, N.H. Influence of a mixing solvent with tetrahydrofuran and N, N-dimethylformamide on electrospun poly (vinyl chloride) nonwoven mats. *J. Polym. Sci. part B Polym. Phys.* **2002**, *40*, 2259–2268.
  93. Miao, Y.-E.; Fan, W.; Chen, D.; Liu, T. High-performance supercapacitors based on hollow polyaniline nanofibers by electrospinning. *ACS Appl. Mater. Interfaces* **2013**, *5*, 4423–4428.
  94. Yoshimoto, H.; Shin, Y.M.; Terai, H.; Vacanti, J.P. A biodegradable nanofiber scaffold by electrospinning and its potential for bone tissue engineering. *Biomaterials* **2003**, *24*, 2077–2082.
  95. Liao, Y.; Wang, R.; Tian, M.; Qiu, C.; Fane, A.G. Fabrication of polyvinylidene fluoride (PVDF) nanofiber membranes by electro-spinning for direct contact membrane distillation. *J. Memb. Sci.* **2013**, *425–426*, 30–39, doi:10.1016/j.memsci.2012.09.023.
  96. Chronakis, I.S.; Grapenson, S.; Jakob, A. Conductive polypyrrole nanofibers via electrospinning: electrical and morphological properties. *Polymer (Guildf)*. **2006**, *47*, 1597–1603.
  97. Kenawy, E.-R.; Bowlin, G.L.; Mansfield, K.; Layman, J.; Simpson, D.G.; Sanders, E.H.; Wnek, G.E. Release of tetracycline hydrochloride from electrospun poly (ethylene-co-vinylacetate), poly (lactic acid), and a blend. *J. Control. release* **2002**, *81*, 57–64.
  98. Sun, B.; Long, Y.-Z.; Liu, S.-L.; Huang, Y.-Y.; Ma, J.; Zhang, H.-D.; Shen, G.; Xu, S. Fabrication of curled conducting polymer microfibrillar arrays via a novel electrospinning method for stretchable strain sensors. *Nanoscale* **2013**, *5*, 7041–7045.
  99. Ignatova, M.; Manolova, N.; Rashkov, I. Novel antibacterial fibers of quaternized chitosan and poly (vinyl pyrrolidone) prepared by electrospinning. *Eur. Polym. J.* **2007**, *43*, 1112–1122.
  100. Gentile, P.; Chiono, V.; Carmagnola, I.; Hatton, P. V An overview of poly (lactic-co-glycolic) acid (PLGA)-based biomaterials for bone tissue engineering. *Int. J. Mol. Sci.* **2014**, *15*, 3640–3659.
  101. Yao, C.; Li, X.; Neoh, K.G.; Shi, Z.; Kang, E.T. Surface modification and antibacterial activity of electrospun polyurethane fibrous membranes with quaternary ammonium moieties. *J. Memb. Sci.* **2008**, *320*, 259–267.
  102. Choi, S.S.; Hong, J.P.; Seo, Y.S.; Chung, S.M.; Nah, C. Fabrication and characterization of electrospun polybutadiene fibers crosslinked by UV irradiation. *J. Appl. Polym. Sci.* **2006**, *101*, 2333–2337, doi:10.1002/app.23764.
  103. Jayakumar, R.; Prabakaran, M.; Nair, S. V; Tamura, H. Novel chitin and chitosan nanofibers in biomedical applications. *Biotechnol. Adv.* **2010**, *28*, 142–150.
  104. Campiglio, C.E.; Contessi Negrini, N.; Farè, S.; Draghi, L. Cross-linking strategies for electrospun gelatin scaffolds. *Materials (Basel)*. **2019**, *12*, 2476.
  105. Min, B.-M.; Lee, G.; Kim, S.H.; Nam, Y.S.; Lee, T.S.; Park, W.H. Electrospinning of silk fibroin nanofibers and its effect on the adhesion and spreading of normal human keratinocytes and fibroblasts in vitro. *Biomaterials* **2004**, *25*, 1289–1297.
  106. Matthews, J.A.; Wnek, G.E.; Simpson, D.G.; Bowlin, G.L. Electrospinning of collagen nanofibers. *Biomacromolecules* **2002**, *3*, 232–238.

107. Liu, H.; Hsieh, Y. Ultrafine fibrous cellulose membranes from electrospinning of cellulose acetate. *J. Polym. Sci. Part B Polym. Phys.* **2002**, *40*, 2119–2129.
108. Ji, Y.; Ghosh, K.; Shu, X.Z.; Li, B.; Sokolov, J.C.; Prestwich, G.D.; Clark, R.A.F.; Rafailovich, M.H. Electrospun three-dimensional hyaluronic acid nanofibrous scaffolds. *Biomaterials* **2006**, *27*, 3782–3792, doi:<https://doi.org/10.1016/j.biomaterials.2006.02.037>.
109. Tebyetekerwa, M.; Ramakrishna, S. What is next for electrospinning? *Matter* **2020**, *2*, 279–283.
110. Ameduri, B. From vinylidene fluoride (VDF) to the applications of VDF-Containing polymers and copolymers: Recent developments and future trends. *Chem. Rev.* **2009**, *109*, 6632–6686, doi:10.1021/cr800187m.
111. Ohkawa, K.; Cha, D.; Kim, H.; Nishida, A.; Yamamoto, H. Electrospinning of chitosan. *Macromol. Rapid Commun.* **2004**, *25*, 1600–1605.
112. Ding, B.; Kimura, E.; Sato, T.; Fujita, S.; Shiratori, S. Fabrication of blend biodegradable nanofibrous nonwoven mats via multi-jet electrospinning. *Polymer (Guildf)*. **2004**, *45*, 1895–1902.
113. Gupta, P.; Wilkes, G.L. Some investigations on the fiber formation by utilizing a side-by-side bicomponent electrospinning approach. *Polymer (Guildf)*. **2003**, *44*, 6353–6359.
114. Li, D.; Xia, Y. Fabrication of titania nanofibers by electrospinning. *Nano Lett.* **2003**, *3*, 555–560.
115. Azad, A.-M. Fabrication of transparent alumina (Al<sub>2</sub>O<sub>3</sub>) nanofibers by electrospinning. *Mater. Sci. Eng. A* **2006**, *435*, 468–473.
116. Yang, X.; Shao, C.; Liu, Y.; Mu, R.; Guan, H. Nanofibers of CeO<sub>2</sub> via an electrospinning technique. *Thin Solid Films* **2005**, *478*, 228–231.
117. Zheng, W.; Li, Z.; Zhang, H.; Wang, W.; Wang, Y.; Wang, C. Electrospinning route for  $\alpha$ -Fe<sub>2</sub>O<sub>3</sub> ceramic nanofibers and their gas sensing properties. *Mater. Res. Bull.* **2009**, *44*, 1432–1436.
118. Ren, H.; Ding, Y.; Jiang, Y.; Xu, F.; Long, Z.; Zhang, P. Synthesis and properties of ZnO nanofibers prepared by electrospinning. *J. sol-gel Sci. Technol.* **2009**, *52*, 287–290.
119. Lin, D.; Wu, H.; Zhang, R.; Pan, W. Preparation of ZnS nanofibers via electrospinning. *J. Am. Ceram. Soc.* **2007**, *90*, 3664–3666.
120. Sahoo, B.; Panda, P.K. Preparation and characterization of barium titanate nanofibers by electrospinning. *Ceram. Int.* **2012**, *38*, 5189–5193.
121. Dai, Y.; Liu, W.; Formo, E.; Sun, Y.; Xia, Y. Ceramic nanofibers fabricated by electrospinning and their applications in catalysis, environmental science, and energy technology. *Polym. Adv. Technol.* **2011**, *22*, 326–338.
122. Yang, Q.B.; Li, D.M.; Hong, Y.L.; Li, Z.Y.; Wang, C.; Qiu, S.L.; Wei, Y. Preparation and characterization of a PAN nanofibre containing Ag nanoparticles via electrospinning. In Proceedings of the ICSM 2002: Proceedings of the 2002 International Conference on Science and Technology of Synthetic Metals; Elsevier SA, 2003; pp. 973–974.
123. Wang, Y.; Li, Y.; Sun, G.; Zhang, G.; Liu, H.; Du, J.; Yang, S.; Bai, J.; Yang, Q. Fabrication of Au/PVP nanofiber composites by electrospinning. *J. Appl. Polym. Sci.* **2007**, *105*, 3618–3622.
124. Zhang, Y.; Park, M.; Kim, H.-Y.; El-Newehy, M.; Rhee, K.Y.; Park, S.-J. Effect of TiO<sub>2</sub> on photocatalytic activity of polyvinylpyrrolidone fabricated via electrospinning. *Compos. Part B Eng.* **2015**, *80*, 355–360.
125. Song, B.; Wu, C.; Chang, J. Dual drug release from electrospun poly (lactic-co-glycolic



- acid)/mesoporous silica nanoparticles composite mats with distinct release profiles. *Acta Biomater.* **2012**, *8*, 1901–1907.
126. Dror, Y.; Salalha, W.; Khalfin, R.L.; Cohen, Y.; Yarin, A.L.; Zussman, E. Carbon nanotubes embedded in oriented polymer nanofibers by electrospinning. *Langmuir* **2003**, *19*, 7012–7020.
  127. Wang, C.; Li, Y.; Ding, G.; Xie, X.; Jiang, M. Preparation and characterization of graphene oxide/poly (vinyl alcohol) composite nanofibers via electrospinning. *J. Appl. Polym. Sci.* **2013**, *127*, 3026–3032.
  128. Sun, Y.; Cheng, S.; Lu, W.; Wang, Y.; Zhang, P.; Yao, Q. Electrospun fibers and their application in drug controlled release, biological dressings, tissue repair, and enzyme immobilization. *RSC Adv.* **2019**, *9*, 25712–25729.
  129. Hussey, G.S.; Dziki, J.L.; Badylak, S.F. Extracellular matrix-based materials for regenerative medicine. *Nat. Rev. Mater.* **2018**, *3*, 159–173.
  130. Wang, X.; Ding, B.; Li, B. Biomimetic electrospun nanofibrous structures for tissue engineering. *Mater. today* **2013**, *16*, 229–241.
  131. Cheng, J.; Jun, Y.; Qin, J.; Lee, S.-H. Electrospinning versus microfluidic spinning of functional fibers for biomedical applications. *Biomaterials* **2017**, *114*, 121–143.
  132. Chen, Z.; Chen, Z.; Zhang, A.; Hu, J.; Wang, X.; Yang, Z. Electrospun nanofibers for cancer diagnosis and therapy. *Biomater. Sci.* **2016**, *4*, 922–932.
  133. Paul, K.B.; Singh, V.; Vanjari, S.R.K.; Singh, S.G. One step biofunctionalized electrospun multiwalled carbon nanotubes embedded zinc oxide nanowire interface for highly sensitive detection of carcinoma antigen-125. *Biosens. Bioelectron.* **2017**, *88*, 144–152.
  134. Chen, S.; Boda, S.K.; Batra, S.K.; Li, X.; Xie, J. Emerging roles of electrospun nanofibers in cancer research. *Adv. Healthc. Mater.* **2018**, *7*, 1701024.
  135. Qin, X.; Wang, S. Filtration properties of electrospinning nanofibers. *J. Appl. Polym. Sci.* **2006**, *102*, 1285–1290.
  136. Manesh, K.M.; Santhosh, P.; Gopalan, A.; Lee, K.P.Y.; Choi, S.-S.W.; Lee, Y.S.; Joo, C.W.; Lee, S.W.S.G.; Park, J.K.; Han, K.-S.; et al. Electrospun nanofibrous filtration membrane. *Polymer (Guildf)*. **2006**, *50*, 6353–6359, doi:10.1016/j.polymer.2006.11.036.
  137. Liu, Q.; Zhu, J.; Zhang, L.; Qiu, Y. Recent advances in energy materials by electrospinning. *Renew. Sustain. Energy Rev.* **2018**, *81*, 1825–1858.
  138. Bandara, T.M.W.J.; Weerasinghe, A.M.J.S.; Dissanayake, M.A.K.L.; Senadeera, G.K.R.; Furlani, M.; Albinsson, I.; Mellander, B.E. Characterization of poly (vinylidene fluoride-co-hexafluoropropylene) (PVdF-HFP) nanofiber membrane based quasi solid electrolytes and their application in a dye sensitized solar cell. *Electrochim. Acta* **2018**, *266*, 276–283, doi:10.1016/j.electacta.2018.02.025.
  139. Ren, Y.; Sun, D.; Cao, Y.; Tsao, H.N.; Yuan, Y.; Zakeeruddin, S.M.; Wang, P.; Grätzel, M. A stable blue photosensitizer for color palette of dye-sensitized solar cells reaching 12.6% efficiency. *J. Am. Chem. Soc.* **2018**, *140*, 2405–2408.
  140. Wang, G.; Xiao, W.; Yu, J. High-efficiency dye-sensitized solar cells based on electrospun TiO<sub>2</sub> multi-layered composite film photoanodes. *Energy* **2015**, *86*, 196–203.
  141. Hwang, T.H.; Lee, Y.M.; Kong, B.-S.; Seo, J.-S.; Choi, J.W. Electrospun core-shell fibers for robust silicon nanoparticle-based lithium ion battery anodes. *Nano Lett.* **2012**, *12*, 802–807.
  142. Dunn, B.; Kamath, H.; Tarascon, J.-M. Electrical energy storage for the grid: a battery of choices. *Science (80-. )*. **2011**, *334*, 928–935.

143. Costa, C.M.; Lizundia, E.; Lanceros-méndez, S. Polymers for advanced lithium-ion batteries : State of the art and future needs on polymers for the different battery components. **2020**, *79*, doi:10.1016/j.pecs.2020.100846.
144. Lee, H.; Yanilmaz, M.; Toprakci, O.; Fu, K.; Zhang, X. A review of recent developments in membrane separators for rechargeable lithium-ion batteries. *Energy Environ. Sci.* **2014**, *7*, 3857–3886.
145. Zhao, H.; Liu, L.; Vellacheri, R.; Lei, Y. Recent advances in designing and fabricating self-supported nanoelectrodes for supercapacitors. *Adv. Sci.* **2017**, *4*, 1700188.
146. Mirjalili, M.; Zohoori, S. Review for application of electrospinning and electrospun nanofibers technology in textile industry. *J. Nanostructure Chem.* **2016**, *6*, 207–213.
147. Chen, K.; Chou, W.; Liu, L.; Cui, Y.; Xue, P.; Jia, M. Electrochemical sensors fabricated by electrospinning technology: an overview. *sensors* **2019**, *19*, 3676.
148. Apsite, I.; Stoychev, G.; Zhang, W.; Jehnichen, D.; Xie, J.; Ionov, L. Porous stimuli-responsive self-folding electrospun mats for 4D biofabrication. *Biomacromolecules* **2017**, *18*, 3178–3184.
149. Ramanan, V. V.; Hribar, K.C.; Katz, J.S.; Burdick, J.A. Nanofiber–nanorod composites exhibiting light-induced reversible lower critical solution temperature transitions. *Nanotechnology* **2011**, *22*, 494009.
150. Demirci, S.; Celebioglu, A.; Aytac, Z.; Uyar, T. pH-responsive nanofibers with controlled drug release properties. *Polym. Chem.* **2014**, *5*, 2050–2056.
151. Chunder, A.; Sarkar, S.; Yu, Y.; Zhai, L. Fabrication of ultrathin polyelectrolyte fibers and their controlled release properties. *Colloids Surfaces B Biointerfaces* **2007**, *58*, 172–179.
152. Garain, S.; Jana, S.; Sinha, T.K.; Mandal, D. Design of in Situ Poled Ce<sup>3+</sup>-Doped Electrospun PVDF/Graphene Composite Nanofibers for Fabrication of Nanopressure Sensor and Ultrasensitive Acoustic Nanogenerator. *ACS Appl. Mater. Interfaces* **2016**, *8*, 4532–4540, doi:10.1021/acsami.5b11356.
153. Lou, Z.; Chen, S.; Wang, L.; Jiang, K.; Shen, G. An ultra-sensitive and rapid response speed graphene pressure sensors for electronic skin and health monitoring. *Nano Energy* **2016**, *23*, 7–14, doi:10.1016/j.nanoen.2016.02.053.
154. Chen, M.; Besenbacher, F. Light-driven wettability changes on a photoresponsive electrospun mat. *ACS Nano* **2011**, *5*, 1549–1555.
155. Liu, H.; Gough, C.R.; Deng, Q.; Gu, Z.; Wang, F.; Hu, X. Recent Advances in Electrospun Sustainable Composites for Biomedical, Environmental, Energy, and Packaging Applications. *Int. J. Mol. Sci.* **2020**, *21*, 4019.
156. Mele, E. Electrospinning of natural polymers for advanced wound care: towards responsive and adaptive dressings. *J. Mater. Chem. B* **2016**, *4*, 4801–4812.
157. Chen, R.; Wan, Y.; Wu, W.; Yang, C.; He, J.-H.; Cheng, J.; Jetter, R.; Ko, F.K.; Chen, Y. A lotus effect-inspired flexible and breathable membrane with hierarchical electrospinning micro/nanofibers and ZnO nanowires. *Mater. Des.* **2019**, *162*, 246–248, doi:https://doi.org/10.1016/j.matdes.2018.11.041.
158. Omer, S.; Forgách, L.; Zelkó, R.; Sebe, I. Scale-up of Electrospinning: Market Overview of Products and Devices for Pharmaceutical and Biomedical Purposes. *Pharmaceutics* **2021**, *13*, 286.
159. Dadashi-Silab, S.; Doran, S.; Yagci, Y. Photoinduced electron transfer reactions for macromolecular syntheses. *Chem. Rev.* **2016**, *116*, 10212–10275.
160. Chatani, S.; Kloxin, C.J.; Bowman, C.N. The power of light in polymer science:

- photochemical processes to manipulate polymer formation, structure, and properties. *Polym. Chem.* **2014**, *5*, 2187–2201.
161. Scott, T.F.; Kloxin, C.J.; Forman, D.L.; McLeod, R.R.; Bowman, C.N. Principles of voxel refinement in optical direct write lithography. *J. Mater. Chem.* **2011**, *21*, 14150–14155.
  162. Brieke, C.; Rohrbach, F.; Gottschalk, A.; Mayer, G.; Heckel, A. Light-controlled tools. *Angew. Chemie Int. Ed.* **2012**, *51*, 8446–8476.
  163. Orski, S. V; Poloukhine, A.A.; Arumugam, S.; Mao, L.; Popik, V. V; Locklin, J. High density orthogonal surface immobilization via photoactivated copper-free click chemistry. *J. Am. Chem. Soc.* **2010**, *132*, 11024–11026.
  164. Noirbent, G.; Dumur, F. Photoinitiators of polymerization with reduced environmental impact: Nature as an unlimited and renewable source of dyes. *Eur. Polym. J.* **2020**, 110109.
  165. Voet, V.S.D.; Guit, J.; Loos, K. Sustainable photopolymers in 3d printing: A review on biobased, biodegradable, and recyclable alternatives. *Macromol. Rapid Commun.* **2021**, *42*, 2000475.
  166. Xiao, P.; Zhang, J.; Dumur, F.; Tehfe, M.A.; Morlet-Savary, F.; Graff, B.; Gigmès, D.; Fouassier, J.P.; Lalevee, J. Visible light sensitive photoinitiating systems: Recent progress in cationic and radical photopolymerization reactions under soft conditions. *Prog. Polym. Sci.* **2015**, *41*, 32–66.
  167. Kaur, M.; Srivastava, A.K. Photopolymerization: A review. *J. Macromol. Sci. Part C Polym. Rev.* **2002**, *42*, 481–512.
  168. Karasu, F.; Croutxé-Barghorn, C.; Allonas, X.; Van Der Ven, L.G.J. Free radical photopolymerization initiated by UV and LED: Towards UV stabilized, tack free coatings. *J. Polym. Sci. Part A Polym. Chem.* **2014**, *52*, 3597–3607.
  169. Bowman, C.N.; Kloxin, C.J. Toward an enhanced understanding and implementation of photopolymerization reactions. *AIChE J.* **2008**, *54*, 2775–2795.
  170. Fouassier, J.P.; Allonas, X.; Burget, D. Photopolymerization reactions under visible lights: principle, mechanisms and examples of applications. *Prog. Org. coatings* **2003**, *47*, 16–36.
  171. Yagci, Y.; Jockusch, S.; Turro, N.J. Photoinitiated polymerization: advances, challenges, and opportunities. *Macromolecules* **2010**, *43*, 6245–6260.
  172. Shao, J.; Huang, Y.; Fan, Q. Visible light initiating systems for photopolymerization: status, development and challenges. *Polym. Chem.* **2014**, *5*, 4195–4210.
  173. Monroe, B.M.; Weed, G.C. Photoinitiators for free-radical-initiated photoimaging systems. *Chem. Rev.* **1993**, *93*, 435–448.
  174. Ravve, A. *Principles of polymer chemistry*; Springer Science & Business Media, 2013; ISBN 1489912835.
  175. Decker, C. The use of UV irradiation in polymerization. *Polym. Int.* **1998**, *45*, 133–141.
  176. Decker, C. Photoinitiated crosslinking polymerisation. *Prog. Polym. Sci.* **1996**, *21*, 593–650.
  177. Fouassier, J.-P.; Lalevée, J. *Photoinitiators for polymer synthesis: scope, reactivity, and efficiency*; John Wiley & Sons, 2012; ISBN 3527332103.
  178. Gruber, H.F. Photoinitiators for free radical polymerization. *Prog. Polym. Sci.* **1992**, *17*, 953–1044.
  179. Hageman, H.J. Photoinitiators for free radical polymerization. *Prog. Org. coatings* **1985**, *13*, 123–150.
  180. Sluggett, G.W.; Turro, C.; George, M.W.; Koptuyug, I. V; Turro, N.J. (2, 4, 6-Trimethylbenzoyl) diphenylphosphine oxide photochemistry. A direct time-resolved

- spectroscopic study of both radical fragments. *J. Am. Chem. Soc.* **1995**, *117*, 5148–5153.
181. Decker, C.; Viet, T.N.T. Photocrosslinking of functionalized rubbers, 8. The thiol-polybutadiene system. *Macromol. Chem. Phys.* **1999**, *200*, 1965–1974.
  182. Galarzy, R.E.; Craig, L.C.; Jamieson, J.D.; Printz, M.P. Photoaffinity labeling of peptide hormone binding sites. *J. Biol. Chem.* **1974**, *249*, 3510–3518.
  183. Dorman, G.; Prestwich, G.D. Benzophenone photophores in biochemistry. *Biochemistry* **1994**, *33*, 5661–5673.
  184. Ballard, N.; Asua, J.M. Radical polymerization of acrylic monomers: An overview. *Prog. Polym. Sci.* **2018**, *79*, 40–60.
  185. Scherzer, T.; Decker, U. Kinetic investigations on the UV-induced photopolymerization of a diacrylate by time-resolved FTIR spectroscopy: the influence of photoinitiator concentration, light intensity and temperature. *Radiat. Phys. Chem.* **1999**, *55*, 615–619.
  186. Block, H.; Ledwith, A.; Taylor, A.R. Polymerization of methyl methacrylate photosensitized by benzophenones. *Polymer (Guildf)*. **1971**, *12*, 271–288.
  187. Kolb, H.C.; Finn, M.G.; Sharpless, K.B. Click chemistry: diverse chemical function from a few good reactions. *Angew. Chemie Int. Ed.* **2001**, *40*, 2004–2021.
  188. Hoyle, C.E.; Lee, T.Y.; Roper, T. Thiol–enes: Chemistry of the past with promise for the future. *J. Polym. Sci. Part A Polym. Chem.* **2004**, *42*, 5301–5338.
  189. Black, M.; Rawlins, J.W. Thiol–ene UV-curable coatings using vegetable oil macromonomers. *Eur. Polym. J.* **2009**, *45*, 1433–1441.
  190. Granskog, V.; García-Gallego, S.; von Kieseritzky, J.; Rosendahl, J.; Stenlund, P.; Zhang, Y.; Petronis, S.; Lyvén, B.; Arner, M.; Håkansson, J. High-performance thiol–ene composites unveil a new era of adhesives suited for bone repair. *Adv. Funct. Mater.* **2018**, *28*, 1800372.
  191. Zieger, M.M.; Müller, P.; Blasco, E.; Petit, C.; Hahn, V.; Michalek, L.; Mutlu, H.; Wegener, M.; Barner-Kowollik, C. A Subtractive Photoresist Platform for Micro-and Macroscopic 3D Printed Structures. *Adv. Funct. Mater.* **2018**, *28*, 1801405.
  192. Maillard, B.; Ingold, K.U.; Scaiano, J.C. Rate constants for the reactions of free radicals with oxygen in solution. *J. Am. Chem. Soc.* **1983**, *105*, 5095–5099.
  193. O’Brien, A.K.; Bowman, C.N. Impact of oxygen on photopolymerization kinetics and polymer structure. *Macromolecules* **2006**, *39*, 2501–2506.
  194. Belon, C.; Allonas, X.; Crouxé-Barghorn, C.; Lalevée, J. Overcoming the oxygen inhibition in the photopolymerization of acrylates: A study of the beneficial effect of triphenylphosphine. *J. Polym. Sci. Part A Polym. Chem.* **2010**, *48*, 2462–2469.
  195. Decker, C. A novel method for consuming oxygen instantaneously in photopolymerizable films. *Die Makromol. Chemie Macromol. Chem. Phys.* **1979**, *180*, 2027–2030.
  196. Lee, T.Y.; Guymon, C.A.; Jönsson, E.S.; Hoyle, C.E. The effect of monomer structure on oxygen inhibition of (meth) acrylates photopolymerization. *Polymer (Guildf)*. **2004**, *45*, 6155–6162.
  197. Auten, R.L.; Davis, J.M. Oxygen Toxicity and Reactive Oxygen Species: The Devil Is in the Details. *Pediatr. Res.* **2009**, *66*, 121–127, doi:10.1203/PDR.0b013e3181a9eafb.
  198. Krumova, K.; Cosa, G. Overview of reactive oxygen species. **2016**.
  199. Decker, C.; Jenkins, A.D. Kinetic approach of oxygen inhibition in ultraviolet-and laser-induced polymerizations. *Macromolecules* **1985**, *18*, 1241–1244.
  200. Studer, K.; Decker, C.; Beck, E.; Schwalm, R. Overcoming oxygen inhibition in UV-curing of acrylate coatings by carbon dioxide inerting, Part I. *Prog. Org. Coatings* **2003**, *48*, 92–

- 100.
201. Lim, K.S.; Galarraga, J.H.; Cui, X.; Lindberg, G.C.J.; Burdick, J.A.; Woodfield, T.B.F. Fundamentals and applications of photo-cross-linking in bioprinting. *Chem. Rev.* **2020**, *120*, 10662–10694.
  202. Xie, H.; Yang, K.-K.; Wang, Y.-Z. Photo-cross-linking: a powerful and versatile strategy to develop shape-memory polymers. *Prog. Polym. Sci.* **2019**, *95*, 32–64.
  203. Felipe-Mendes, C.; Ruiz-Rubio, L.; Vilas-Vilela, J.L. Biomaterials obtained by photopolymerization: from UV to two photon. *Emergent Mater.* **2020**, 1–16.
  204. Ibrahim, A.; Stefano, L. Di; Tarzi, O.; Tar, H.; Ley, C.; Allonas, X. High-Performance Photoinitiating Systems for Free Radical Photopolymerization. Application to Holographic Recording. *Photochem. Photobiol.* **2013**, *89*, 1283–1290.
  205. Roper, T.M.; Kwee, T.; Lee, T.Y.; Guymon, C.A.; Hoyle, C.E. Photopolymerization of pigmented thiol-ene systems. *Polymer (Guildf)*. **2004**, *45*, 2921–2929, doi:10.1016/j.polymer.2004.02.038.
  206. Zarek, M.; Layani, M.; Cooperstein, I.; Sachyani, E.; Cohn, D.; Magdassi, S. 3D printing of shape memory polymers for flexible electronic devices. *Adv. Mater.* **2016**, *28*, 4449–4454.
  207. Kloosterboer, J.G. Network formation by chain crosslinking photopolymerization and its applications in electronics. *Electron. Appl.* **1988**, 1–61.
  208. Van Landuyt, K.L.; Snauwaert, J.; De Munck, J.; Peumans, M.; Yoshida, Y.; Poitevin, A.; Coutinho, E.; Suzuki, K.; Lambrechts, P.; Van Meerbeek, B. Systematic review of the chemical composition of contemporary dental adhesives. *Biomaterials* **2007**, *28*, 3757–3785, doi:https://doi.org/10.1016/j.biomaterials.2007.04.044.
  209. Bagheri, A.; Jin, J. Photopolymerization in 3D printing. *ACS Appl. Polym. Mater.* **2019**, *1*, 593–611.
  210. Dyer, D.J. Photoinitiated synthesis of grafted polymers. *Surface-Initiated Polym. I* **2006**, 47–65.
  211. Seidi, F.; Zhao, W.; Xiao, H.; Jin, Y.; Saeb, M.R.; Zhao, C. Radical polymerization as a versatile tool for surface grafting of thin hydrogel films. *Polym. Chem.* **2020**, *11*, 4355–4381.
  212. Kianfar, P.; Vitale, A.; Dalle Vacche, S.; Bongiovanni, R. Photo-crosslinking of chitosan/poly (ethylene oxide) electrospun nanofibers. *Carbohydr. Polym.* **2019**, *217*, 144–151.
  213. Maciejewska, B.M.; Wychowaniec, J.K.; Woźniak-Budych, M.; Popenda, Ł.; Warowicka, A.; Golba, K.; Litowczenko, J.; Fojud, Z.; Wereszczyńska, B.; Jurga, S. UV cross-linked polyvinylpyrrolidone electrospun fibres as antibacterial surfaces. *Sci. Technol. Adv. Mater.* **2019**, *20*, 979–991.
  214. Zahran, S.M.E.; Abdel-Halim, A.H.; Nassar, K.; Nada, A.A. Fabrication of nanofiltration membrane based on non-biofouling PVP/lecithin nanofibers reinforced with microcrystalline cellulose via needle and needle-less electrospinning techniques. *Int. J. Biol. Macromol.* **2020**, *157*, 530–543.
  215. Tang, Z.; Wei, J.; Yung, L.; Ji, B.; Ma, H.; Qiu, C.; Yoon, K.; Wan, F.; Fang, D.; Hsiao, B.S. UV-cured poly (vinyl alcohol) ultrafiltration nanofibrous membrane based on electrospun nanofiber scaffolds. *J. Memb. Sci.* **2009**, *328*, 1–5.
  216. Yang, H.; Zhang, Q.; Lin, B.; Fu, G.; Zhang, X.; Guo, L. Thermo-sensitive electrospun fibers prepared by a sequential thiol-ene click chemistry approach. *J. Polym. Sci. Part A*

- Polym. Chem.* **2012**, *50*, 4182–4190.
217. Zare, M.; Parvin, N.; Prabhakaran, M.P.; Mohandesi, J.A.; Ramakrishna, S. Highly porous 3D sponge-like shape memory polymer for tissue engineering application with remote actuation potential. *Compos. Sci. Technol.* **2019**, *184*, 107874.
  218. Tian, M.; Hu, Q.; Wu, H.; Zhang, L.; Fong, H.; Zhang, L. Formation and morphological stability of polybutadiene rubber fibers prepared through combination of electrospinning and in-situ photo-crosslinking. *Mater. Lett.* **2011**, *65*, 3076–3079.
  219. Lyoo, W.S.; Youk, J.H.; Lee, S.W.; Park, W.H. Preparation of porous ultra-fine poly (vinyl cinnamate) fibers. *Mater. Lett.* **2005**, *59*, 3558–3562.
  220. Niu, Q.; Zeng, L.; Mu, X.; Nie, J.; Ma, G. Preparation and characterization of core-shell nanofibers by electrospinning combined with in situ UV photopolymerization. *J. Ind. Eng. Chem.* **2016**, *34*, 337–343.
  221. Kalaoglu-Altan, O.I.; Verbraeken, B.; Lava, K.; Gevrek, T.N.; Sanyal, R.; Dargaville, T.; De Clerck, K.; Hoogenboom, R.; Sanyal, A. Multireactive poly (2-oxazoline) nanofibers through electrospinning with crosslinking on the fly. *ACS Macro Lett.* **2016**, *5*, 676–681.
  222. Zhu, X.; Niu, Q.; Xu, Y.; Wu, G.; Li, G.; Nie, J.; Ma, G. From small molecules to polymer fibers: Photopolymerization with electrospinning on the fly. *J. Photochem. Photobiol. A Chem.* **2018**, *353*, 101–107.
  223. Huerta-Angeles, G.; Brandejsová, M.; Knotková, K.; Hermannová, M.; Moravcová, M.; Šmejkalová, D.; Velebný, V. Synthesis of photo-crosslinkable hyaluronan with tailored degree of substitution suitable for production of water resistant nanofibers. *Carbohydr. Polym.* **2016**, *137*, 255–263.
  224. Gupta, P.; Trenor, S.R.; Long, T.E.; Wilkes, G.L. In situ photo-cross-linking of cinnamate functionalized poly (methyl methacrylate-co-2-hydroxyethyl acrylate) fibers during electrospinning. *Macromolecules* **2004**, *37*, 9211–9218.
  225. Zeytuncu, B.; Ürper, M.; Koyuncu, İ.; Tarabara, V. V Photo-crosslinked PVA/PEI electrospun nanofiber membranes: Preparation and preliminary evaluation in virus clearance tests. *Sep. Purif. Technol.* **2018**, *197*, 432–438, doi:<https://doi.org/10.1016/j.seppur.2018.01.002>.
  226. Vitale, A.; Massaglia, G.; Chiodoni, A.; Bongiovanni, R.; Pirri, C.F.; Quaglio, M. Tuning Porosity and Functionality of Electrospun Rubber Nanofiber Mats by Photo-Crosslinking. *ACS Appl. Mater. Interfaces* **2019**, *11*, 24544–24551, doi:10.1021/acsami.9b04599.
  227. Bazbouz, M.B.; Liang, H.; Tronci, G. A UV-cured nanofibrous membrane of vinylbenzylated gelatin-poly( $\epsilon$ -caprolactone) dimethacrylate co-network by scalable free surface electrospinning. *Mater. Sci. Eng. C* **2018**, *91*, 541–555, doi:<https://doi.org/10.1016/j.msec.2018.05.076>.
  228. Kumar, R.; Surendran, P.K.; Thankappan, T.K. Antibacterial activity of shrimp chitosan against Escherichia coli, Salmonella, and Pseudomonas aeruginosa isolated from seafoods. **2006**.
  229. Young, D.H.; Kauss, H. Release of calcium from suspension-cultured Glycine max cells by chitosan, other polycations, and polyamines in relation to effects on membrane permeability. *Plant Physiol.* **1983**, *73*, 698–702.
  230. Raafat, D.; Von Barga, K.; Haas, A.; Sahl, H.-G. Insights into the mode of action of chitosan as an antibacterial compound. *Appl. Environ. Microbiol.* **2008**, *74*, 3764–3773.
  231. Sebti, I.; Martial-Gros, A.; Carnet-Pantiez, A.; Grelier, S.; Coma, V. Chitosan polymer as bioactive coating and film against Aspergillus niger contamination. *J. Food Sci.* **2005**, *70*,

M100–M104.

232. Cuero, R.G.; Osuji, G.; Washington, A. N-carboxymethylchitosan inhibition of aflatoxin production: role of zinc. *Biotechnol. Lett.* **1991**, *13*, 441–444.
233. Roller, S.; Covill, N. The antifungal properties of chitosan in laboratory media and apple juice. *Int. J. Food Microbiol.* **1999**, *47*, 67–77.
234. Másson, M.; Holappa, J.; Hjálmarsdóttir, M.; Rúnarsson, Ö. V.; Nevalainen, T.; Järvinen, T. Antimicrobial activity of piperazine derivatives of chitosan. *Carbohydr. Polym.* **2008**, *74*, 566–571.
235. Pillai, C.K.S.; Paul, W.; Sharma, C.P. Chitin and chitosan polymers: Chemistry, solubility and fiber formation. *Prog. Polym. Sci.* **2009**, *34*, 641–678.
236. Ahsan, S.M.; Thomas, M.; Reddy, K.K.; Sooraparaju, S.G.; Asthana, A.; Bhatnagar, I. Chitosan as biomaterial in drug delivery and tissue engineering. *Int. J. Biol. Macromol.* **2018**, *110*, 97–109, doi:10.1016/j.ijbiomac.2017.08.140.
237. Pakravan, M.; Heuzey, M.C.; Ajji, A. A fundamental study of chitosan/PEO electrospinning. *Polymer (Guildf.)* **2011**, *52*, 4813–4824, doi:10.1016/j.polymer.2011.08.034.
238. Tripathi, S.; Mehrotra, G.K.; Dutta, P.K. Physicochemical and bioactivity of cross-linked chitosan–PVA film for food packaging applications. *Int. J. Biol. Macromol.* **2009**, *45*, 372–376.
239. Muxika, A.; Etxabide, A.; Uranga, J.; Guerrero, P.; de la Caba, K. Chitosan as a bioactive polymer: Processing, properties and applications. *Int. J. Biol. Macromol.* **2017**, *105*, 1358–1368, doi:10.1016/j.ijbiomac.2017.07.087.
240. Dash, M.; Chiellini, F.; Ottenbrite, R.M.; Chiellini, E. Chitosan - A versatile semi-synthetic polymer in biomedical applications. *Prog. Polym. Sci.* **2011**, *36*, 981–1014, doi:10.1016/j.progpolymsci.2011.02.001.
241. Yao, K. De; Peng, T.; Feng, H.B.; He, Y.Y. Swelling kinetics and release characteristic of crosslinked chitosan: polyether polymer network (semi-IPN) hydrogels. *J. Polym. Sci. Part A Polym. Chem.* **1994**, *32*, 1213–1223.
242. Gupta, K.C.; Kumar, M.N.V.R. Studies on semi-interpenetrating polymer network beads of chitosan–poly (ethylene glycol) for the controlled release of drugs. *J. Appl. Polym. Sci.* **2001**, *80*, 639–649.
243. Dal Pozzo, A.; Vanini, L.; Fagnoni, M.; Guerrini, M.; De Benedittis, A.; Muzzarelli, R.A.A. Preparation and characterization of poly (ethylene glycol)-crosslinked reacylated chitosans. *Carbohydr. Polym.* **2000**, *42*, 201–206.
244. Rao, B.S.; Murthy, K.V.R. Preparation and in vitro evaluation of chitosan matrices cross-linked by formaldehyde vapors. *Drug Dev. Ind. Pharm.* **2000**, *26*, 1085–1090.
245. Martinez, L.; Agnely, F.; Leclerc, B.; Siepmann, J.; Cotte, M.; Geiger, S.; Couarraze, G. Cross-linking of chitosan and chitosan/poly (ethylene oxide) beads: A theoretical treatment. *Eur. J. Pharm. Biopharm.* **2007**, *67*, 339–348.
246. Tsai, W.B.; Chen, Y.R.; Liu, H.L.; Lai, J.Y. Fabrication of UV-crosslinked chitosan scaffolds with conjugation of RGD peptides for bone tissue engineering. *Carbohydr. Polym.* **2011**, *85*, 129–137, doi:10.1016/j.carbpol.2011.02.003.
247. Jin, J.; Song, M. Chitosan and chitosan–PEO blend membranes crosslinked by genipin for drug release. *J. Appl. Polym. Sci.* **2006**, *102*, 436–444.
248. Mi, F.-L.; Sung, H.-W.; Shyu, S.-S. Drug release from chitosan–alginate complex beads reinforced by a naturally occurring cross-linking agent. *Carbohydr. Polym.* **2002**, *48*, 61–

- 72.
249. Duan, B.; Yuan, X.; Zhu, Y.; Zhang, Y.; Li, X.; Zhang, Y.; Yao, K. A nanofibrous composite membrane of PLGA–chitosan/PVA prepared by electrospinning. *Eur. Polym. J.* **2006**, *42*, 2013–2022.
  250. Desai, K.; Kit, K.; Li, J.; Zivanovic, S. Morphological and surface properties of electrospun chitosan nanofibers. *Biomacromolecules* **2008**, *9*, 1000–1006.
  251. Geng, X.; Kwon, O.-H.; Jang, J. Electrospinning of chitosan dissolved in concentrated acetic acid solution. *Biomaterials* **2005**, *26*, 5427–5432.
  252. Ohkawa, K.; Cha, D.; Kim, H.; Nishida, A.; Yamamoto, H. Electrospinning of chitosan. *Macromol. Rapid Commun.* **2004**, *25*, 1600–1605, doi:10.1002/marc.200400253.
  253. Bhattarai, N.; Edmondson, D.; Veiseh, O.; Matsen, F.A.; Zhang, M. Electrospun chitosan-based nanofibers and their cellular compatibility. *Biomaterials* **2005**, *26*, 6176–6184.
  254. Bösiger, P.; Richard, I.M.T.; Le Gat, L.; Michen, B.; Schubert, M.; Rossi, R.M.; Fortunato, G. Application of response surface methodology to tailor the surface chemistry of electrospun chitosan-poly (ethylene oxide) fibers. *Carbohydr. Polym.* **2018**, *186*, 122–131.
  255. Zhang, Y.Z.; Su, B.; Ramakrishna, S.; Lim, C.T. Chitosan nanofibers from an easily electrospinnable UHMWPEO-doped chitosan solution system. *Biomacromolecules* **2008**, *9*, 136–141, doi:10.1021/bm701130e.
  256. Thompson, M.S.; Vadala, T.P.; Vadala, M.L.; Lin, Y.; Riffle, J.S. Synthesis and applications of heterobifunctional poly(ethylene oxide) oligomers. *Polymer (Guildf)*. **2008**, *49*, 345–373, doi:10.1016/j.polymer.2007.10.029.
  257. Padmavathi, N.C.; Chatterji, P.R. Structural characteristics and swelling behavior of poly (ethylene glycol) diacrylate hydrogels. *Macromolecules* **1996**, *29*, 1976–1979.
  258. Perloni, P.; Magistris, A.; Chioldelli, G.; Faucitano, A.; Buttafava, A. Effects of gamma-radiation on polymer electrolytes: PEO and PEO20-LiClO4. *Int. J. Radiat. Appl. Instrumentation. Part C. Radiat. Phys. Chem.* **1991**, *37*, 615–621.
  259. Villain, F.L.; Parel, J.-M.A.; Lee, W.G.; Simon, G. Injectable polyethylene oxide gel implant and method for production 1997.
  260. Emami, S.H.; Salovey, R. Crosslinked Poly ( ethylene oxide ) Hydrogels. **2002**.
  261. Zhou, C.; Wang, Q.; Wu, Q. UV-initiated crosslinking of electrospun poly (ethylene oxide) nanofibers with pentaerythritol triacrylate: Effect of irradiation time and incorporated cellulose nanocrystals. *Carbohydr. Polym.* **2012**, *87*, 1779–1786.
  262. Şimşek, M.; Çakmak, S.; Gümüşderelioğlu, M. Insoluble poly(ethylene oxide) nanofibrous coating materials: effects of crosslinking conditions on the matrix stability. *J. Polym. Res.* **2016**, *23*, doi:10.1007/s10965-016-1127-x.
  263. Teixeira, R.S.P.; Correa, R.J.; Belvino, A.; Nascimento, R.S.V. UV irradiation-induced crosslinking of aqueous solution of poly(ethylene oxide) with benzophenone as initiator. *J. Appl. Polym. Sci.* **2013**, *130*, 2458–2467, doi:10.1002/app.39381.
  264. Bösiger, P.; Richard, I.M.T.; Le Gat, L.; Michen, B.; Schubert, M.; Rossi, R.M.; Fortunato, G. Application of response surface methodology to tailor the surface chemistry of electrospun chitosan-poly(ethylene oxide) fibers. *Carbohydr. Polym.* **2018**, *186*, 122–131, doi:10.1016/j.carbpol.2018.01.038.
  265. Tsou, S.Y.; Lin, H.S.; Wang, C. Studies on the electrospun Nylon 6 nanofibers from polyelectrolyte solutions: 1. Effects of solution concentration and temperature. *Polymer (Guildf)*. **2011**, *52*, 3127–3136, doi:10.1016/j.polymer.2011.05.010.
  266. Zong, X.; Kim, K.; Fang, D.; Ran, S.; Hsiao, B.S.; Chu, B. Structure and process



- relationship of electrospun bioabsorbable nanofiber membranes. *Polymer (Guildf)*. **2002**, *43*, 4403–4412.
267. Qasim, S.B.; Zafar, M.S.; Najeeb, S.; Khurshid, Z.; Shah, A.H.; Husain, S.; Rehman, I.U. Electrospinning of chitosan-based solutions for tissue engineering and regenerative medicine. *Int. J. Mol. Sci.* **2018**, *19*, doi:10.3390/ijms19020407.
  268. Rusu, M.C.; Block, C.; Van Assche, G.; Van Mele, B. Influence of temperature and UV intensity on photo-polymerization reaction studied by photo-DSC. *J. Therm. Anal. Calorim.* **2012**, *110*, 287–294, doi:10.1007/s10973-012-2465-5.
  269. Sionkowska, A.; Kaczmarek, H.; Wisniewski, M.; Skopinska, J.; Lazare, S.; Tokarev, V. The influence of UV irradiation on the surface of chitosan films. *Surf. Sci.* **2006**, *600*, 3775–3779.
  270. Kowalonek, J. Surface and thermal properties of UV-irradiated chitosan/poly(ethylene oxide) blends. *J. Photochem. Photobiol. A Chem.* **2017**, *348*, 209–218, doi:10.1016/j.jphotochem.2017.08.035.
  271. Mucha, M.; Pawlak, A. Complex study on chitosan degradability. *Polimery* **2002**, *47*, 509–516.
  272. Jin, Y.; Yang, D.; Zhou, Y.; Ma, G.; Nie, J. Photocrosslinked electrospun chitosan-based biocompatible nanofibers. *J. Appl. Polym. Sci.* **2008**, *109*, 3337–3343.
  273. Fredi, G.; Kianfar, P.; Dalle Vacche, S.; Pegoretti, A.; Vitale, A. Electrospun Shape-Stabilized Phase Change Materials Based on Photo-Crosslinked Polyethylene Oxide. *Polym.* **2021**, *13*.
  274. Harris, J.M. *Poly (ethylene glycol) chemistry: biotechnical and biomedical applications*; Springer Science & Business Media, 2013; ISBN 1489907033.
  275. Bailey, F.E.J. *Poly (ethylene oxide)*; Elsevier, 2012; ISBN 032316059X.
  276. Xu, F.; Gough, I.; Dorogin, J.; Sheardown, H.; Hoare, T. Nanostructured Degradable Macroporous Hydrogel Scaffolds with Controllable Internal Morphologies via Reactive Electrospinning. *Acta Biomater.* **2020**.
  277. Rajam, S.; Ho, C.-C. Graft coupling of PEO to mixed cellulose esters microfiltration membranes by UV irradiation. *J. Memb. Sci.* **2006**, *281*, 211–218.
  278. Aqil, A.; Vasseur, S.; Duguet, E.; Passirani, C.; Benoît, J.-P.; Roch, A.; Müller, R.; Jérôme, R.; Jérôme, C. PEO coated magnetic nanoparticles for biomedical application. *Eur. Polym. J.* **2008**, *44*, 3191–3199.
  279. Fusco, S.; Borzacchiello, A.; Netti, P.A. Perspectives on: PEO-PPO-PEO triblock copolymers and their biomedical applications. *J. Bioact. Compat. Polym.* **2006**, *21*, 149–164.
  280. Apicella, A.; Cappello, B.; Del Nobile, M.A.; La Rotonda, M.I.; Mensitieri, G.; Nicolais, L. Poly (ethylene oxide)(PEO) and different molecular weight PEO blends monolithic devices for drug release. *Biomaterials* **1993**, *14*, 83–90.
  281. Patanaik, A.; Jacobs, V.; Anandjiwala, R.D. Performance evaluation of electrospun nanofibrous membrane. *J. Memb. Sci.* **2010**, *352*, 136–142.
  282. Liu, S.L.; Shao, L.; Chua, M.L.; Lau, C.H.; Wang, H.; Quan, S. Recent progress in the design of advanced PEO-containing membranes for CO<sub>2</sub> removal. *Prog. Polym. Sci.* **2013**, *38*, 1089–1120.
  283. Stringer, J.L.; Peppas, N.A. Diffusion of small molecular weight drugs in radiation-crosslinked poly(ethylene oxide) hydrogels. *J. Control. Release* **1996**, *42*, 195–202, doi:10.1016/0168-3659(96)01457-5.

284. Pielichowska, K.; Głowinkowski, S.; Lekki, J.; Biniś, D.; Pielichowski, K.; Jencyk, J. PEO/fatty acid blends for thermal energy storage materials. Structural/morphological features and hydrogen interactions. *Eur. Polym. J.* **2008**, *44*, 3344–3360.
285. Deng, F.; Wang, X.; He, D.; Hu, J.; Gong, C.; Ye, Y.S.; Xie, X.; Xue, Z. Microporous polymer electrolyte based on PVDF/PEO star polymer blends for lithium ion batteries. *J. Memb. Sci.* **2015**, *491*, 82–89.
286. Zhong, S.P.; Zhang, Y.Z.; Lim, C.T. Tissue scaffolds for skin wound healing and dermal reconstruction. *Wiley Interdiscip. Rev. Nanomedicine Nanobiotechnology* **2010**, *2*, 510–525.
287. Rieger, K.A.; Birch, N.P.; Schiffman, J.D. Designing electrospun nanofiber mats to promote wound healing—a review. *J. Mater. Chem. B* **2013**, *1*, 4531–4541.
288. Sill, T.J.; von Recum, H.A. Electrospinning: applications in drug delivery and tissue engineering. *Biomaterials* **2008**, *29*, 1989–2006.
289. King, P.A. Ionizing radiation of water solution of polyalkylene oxide and product thereof 1966.
290. Emami, S.H.; Salovey, R. Crosslinked poly (ethylene oxide) hydrogels. *J. Appl. Polym. Sci.* **2003**, *88*, 1451–1455.
291. Sloop, S.E.; Lerner, M.M.; Stephens, T.S.; Tipton, A.L.; Paull, D.G.; Stenger-Smith, J.D. Cross-linking poly (ethylene oxide) and poly [oxymethylene-oligo (oxyethylene)] with ultraviolet radiation. *J. Appl. Polym. Sci.* **1994**, *53*, 1563–1572.
292. Doytcheva, M.; Dotcheva, D.; Stamenova, R.; Orahovats, A.; Tsvetanov, C.; Leder, J. Ultraviolet-induced crosslinking of solid poly(ethylene oxide). *J. Appl. Polym. Sci.* **1997**, *64*, 2299–2307, doi:10.1002/(SICI)1097-4628(19970620)64:12<2299::AID-APP5>3.0.CO;2-G.
293. Kalakkunnath, S.; Kalika, D.S.; Lin, H.; Raharjo, R.D.; Freeman, B.D. Molecular relaxation in cross-linked poly(ethylene glycol) and poly(propylene glycol) diacrylate networks by dielectric spectroscopy. *Polymer (Guildf)*. **2007**, *48*, 579–589, doi:10.1016/j.polymer.2006.11.046.
294. Kianfar, P.; Vitale, A.; Dalle Vacche, S.; Bongiovanni, R. Photo-crosslinking of chitosan/poly(ethylene oxide) electrospun nanofibers. *Carbohydr. Polym.* **2019**, *217*, 144–151, doi:10.1016/j.carbpol.2019.04.062.
295. Tonda-Turo, C.; Ruini, F.; Ramella, M.; Boccafocchi, F.; Gentile, P.; Gioffredi, E.; Falvo D'Urso Labate, G.; Ciardelli, G. Non-covalently crosslinked chitosan nanofibrous mats prepared by electrospinning as substrates for soft tissue regeneration. *Carbohydr. Polym.* **2017**, *162*, 82–92, doi:https://doi.org/10.1016/j.carbpol.2017.01.050.
296. Bonino, C.A.; Krebs, M.D.; Saquing, C.D.; Jeong, S.I.; Shearer, K.L.; Alsberg, E.; Khan, S.A. Electrospinning alginate-based nanofibers: From blends to crosslinked low molecular weight alginate-only systems. *Carbohydr. Polym.* **2011**, *85*, 111–119, doi:https://doi.org/10.1016/j.carbpol.2011.02.002.
297. Gutierrez-Gonzalez, J.; Garcia-Cela, E.; Magan, N.; Rahatekar, S.S. Electrospinning alginate/polyethylene oxide and curcumin composite nanofibers. *Mater. Lett.* **2020**, *270*, 127662, doi:https://doi.org/10.1016/j.matlet.2020.127662.
298. Gao, J.; Guo, H.; Zhao, L.; Zhao, X.; Wang, L. Water-stability and biological behavior of electrospun collagen/PEO fibers by environmental friendly crosslinking. *Fibers Polym.* **2017**, *18*, 1496–1503.
299. Liu, Y.; Yu, X.; Li, J.; Fan, J.; Wang, M.; Lei, T.-D.; Liu, J.; Huang, D. Fabrication and

- properties of high-content keratin/poly (ethylene oxide) blend nanofibers using two-step cross-linking process. *J. Nanomater.* **2015**, 2015.
300. Anneaux, B.L.; Ballard, R.; Garner, D.P. Electrospinning of PTFE with high viscosity materials 2012.
  301. Zhou, C.; Wang, Q.; Wu, Q. UV-initiated crosslinking of electrospun poly(ethylene oxide) nanofibers with pentaerythritol triacrylate: Effect of irradiation time and incorporated cellulose nanocrystals. *Carbohydr. Polym.* **2012**, 87, 1779–1786, doi:10.1016/j.carbpol.2011.09.095.
  302. Şimşek, M.; Çakmak, S.; Gümüşderelioğlu, M. Insoluble poly (ethylene oxide) nanofibrous coating materials: effects of crosslinking conditions on the matrix stability. *J. Polym. Res.* **2016**, 23, 236.
  303. Şimşek, M.; Aldemir, S.D.; Gümüşderelioğlu, M. Anticellular PEO coatings on titanium surfaces by sequential electrospinning and crosslinking processes. *Emergent Mater.* **2019**, 2, 169–179.
  304. Fredi, G.; Dorigato, A.; Fambri, L.; Pegoretti, A. Multifunctional structural composites for thermal energy storage. *Multifunct. Mater.* **2020**, 3, 42001.
  305. Farid, M.M.; Khudhair, A.M.; Razack, S.A.K.; Al-Hallaj, S. A review on phase change energy storage: materials and applications. *Energy Convers. Manag.* **2004**, 45, 1597–1615.
  306. Fredi, G.; Dorigato, A.; Fambri, L.; Pegoretti, A. Detailed experimental and theoretical investigation of the thermomechanical properties of epoxy composites containing paraffin microcapsules for thermal management. *Polym. Eng. Sci.* **2020**, 60, 1202–1220.
  307. Royo, P.; Ferreira, V.J.; Ure, Z.; Gledhill, S.; López-Sabirón, A.M.; Ferreira, G. Multiple-Criteria Decision Analysis and characterisation of phase change materials for waste heat recovery at high temperature for sustainable energy-intensive industry. *Mater. Des.* **2020**, 186, 108215.
  308. Sudheer, R.; Prabhu, K.N. A Computer Aided Cooling Curve Analysis method to study phase change materials for thermal energy storage applications. *Mater. Des.* **2016**, 95, 198–203.
  309. Su, J.-F.; Wang, X.-Y.; Wang, S.-B.; Zhao, Y.-H.; Huang, Z. Fabrication and properties of microencapsulated-paraffin/gypsum-matrix building materials for thermal energy storage. *Energy Convers. Manag.* **2012**, 55, 101–107.
  310. Singh, S.; Gaikwad, K.K.; Lee, Y.S. Phase change materials for advanced cooling packaging. *Environ. Chem. Lett.* **2018**, 16, 845–859.
  311. Ren, Q.; Guo, P.; Zhu, J. Thermal management of electronic devices using pin-fin based cascade microencapsulated PCM/expanded graphite composite. *Int. J. Heat Mass Transf.* **2020**, 149, 119199.
  312. Ruiz-Calleja, T.; Bonet-Aracil, M.; Gisbert-Payá, J.; Bou-Belda, E. Analysis of the influence of graphene and phase change microcapsules on thermal behavior of cellulosic fabrics. *Mater. Today Commun.* **2020**, 25, 101557.
  313. Cui, Y.; Liu, X. Soft-logic: design and thermal-comfort evaluation of smart thermoregulatory fabric with pneumatic actuators. *J. Text. Inst.* **2020**, 1–12.
  314. Lu, Y.; Xiao, X.; Fu, J.; Huan, C.; Qi, S.; Zhan, Y.; Zhu, Y.; Xu, G. Novel smart textile with phase change materials encapsulated core-sheath structure fabricated by coaxial electrospinning. *Chem. Eng. J.* **2019**, 355, 532–539.
  315. Zhang, Q.; He, Z.; Fang, X.; Zhang, X.; Zhang, Z. Experimental and numerical investigations on a flexible paraffin/fiber composite phase change material for thermal

- therapy mask. *Energy Storage Mater.* **2017**, *6*, 36–45.
316. Alehosseini, E.; Jafari, S.M. Nanoencapsulation of phase change materials (PCMs) and their applications in various fields for energy storage and management. *Adv. Colloid Interface Sci.* **2020**, 102226.
  317. Sundararajan, S.; Kumar, A.; Chakraborty, B.C.; Samui, A.B.; Kulkarni, P.S. Poly (ethylene glycol)(PEG)-modified epoxy phase-change polymer with dual properties of thermal storage and vibration damping. *Sustain. Energy Fuels* **2018**, *2*, 688–697.
  318. Yang, L.; Jin, X.; Zhang, Y.; Du, K. Recent development on heat transfer and various applications of phase-change materials. *J. Clean. Prod.* **2020**, 124432.
  319. Liu, C.; Rao, Z.; Zhao, J.; Huo, Y.; Li, Y. Review on nanoencapsulated phase change materials: preparation, characterization and heat transfer enhancement. *Nano Energy* **2015**, *13*, 814–826.
  320. Kalaiselvam, S. Bifunctional nanoencapsulated eutectic phase change material core with SiO<sub>2</sub>/SnO<sub>2</sub> nanosphere shell for thermal and electrical energy storage. *Mater. Des.* **2018**, *154*, 291–301.
  321. Pielichowska, K.; Pielichowski, K. Biodegradable PEO/cellulose-based solid–solid phase change materials. *Polym. Adv. Technol.* **2011**, *22*, 1633–1641.
  322. Dorigato, A.; Fredi, G.; Pegoretti, A. Thermo-mechanical behavior of novel wood laminae-thermoplastic starch biodegradable composites with thermal energy storage/release capability. *Front. Mater.* **2019**, *6*, 76.
  323. Jiang, Y.; Ding, E.; Li, G. Study on transition characteristics of PEG/CDA solid–solid phase change materials. *Polymer (Guildf)*. **2002**, *43*, 117–122.
  324. Li, W.-D.; Ding, E.-Y. Preparation and characterization of cross-linking PEG/MDI/PE copolymer as solid–solid phase change heat storage material. *Sol. Energy Mater. Sol. Cells* **2007**, *91*, 764–768.
  325. Li, Z.; He, W.; Xu, J.; Jiang, M. Preparation and characterization of in situ grafted/crosslinked polyethylene glycol/polyvinyl alcohol composite thermal regulating fiber. *Sol. Energy Mater. Sol. Cells* **2015**, *140*, 193–201.
  326. Sundararajan, S.; Samui, A.B.; Kulkarni, P.S. Versatility of polyethylene glycol (PEG) in designing solid–solid phase change materials (PCMs) for thermal management and their application to innovative technologies. *J. Mater. Chem. A* **2017**, *5*, 18379–18396.
  327. Semnani Rahbar, R.; Maleki, H.; Kalantari, B. Fabrication of electrospun nanofibre yarn based on nylon 6/microencapsulated phase change materials. *J. Exp. Nanosci.* **2016**, *11*, 1402–1415.
  328. Wu, Y.; Chen, C.; Jia, Y.; Wu, J.; Huang, Y.; Wang, L. Review on electrospun ultrafine phase change fibers (PCFs) for thermal energy storage. *Appl. Energy* **2018**, *210*, 167–181.
  329. Prajapati, D.G.; Kandasubramanian, B. A review on polymeric-based phase change material for thermo-regulating fabric application. *Polym. Rev.* **2020**, *60*, 389–419.
  330. Cherif, C.; Tran, N.H.A.; Kirsten, M.; Bruenig, H.; Vogel, R. Environmentally friendly and highly productive bi-component melt spinning of thermoregulated smart polymer fibres with high latent heat capacity. *Express Polym. Lett.* **2018**, *12*.
  331. Hoang, H.M.; Leducq, D.; Pérez-Masia, R.; Lagaron, J.M.; Gogou, E.; Taoukis, P.; Alvarez, G. Heat transfer study of submicro-encapsulated PCM plate for food packaging application. *Int. J. Refrig.* **2015**, *52*, 151–160.
  332. Xue, J.; Zhu, C.; Li, J.; Li, H.; Xia, Y. Integration of phase-change materials with electrospun fibers for promoting neurite outgrowth under controlled release. *Adv. Funct.*

- Mater.* **2018**, *28*, 1705563.
333. Darzi, M.E.; Golestaneh, S.I.; Kamali, M.; Karimi, G. Thermal and electrical performance analysis of co-electrospun-electrosprayed PCM nanofiber composites in the presence of graphene and carbon fiber powder. *Renew. Energy* **2019**, *135*, 719–728.
  334. Hu, W.; Yu, X. Encapsulation of bio-based PCM with coaxial electrospun ultrafine fibers. *Rsc Adv.* **2012**, *2*, 5580–5584.
  335. Golestaneh, S.I.; Mosallanejad, A.; Karimi, G.; Khorram, M.; Khashi, M. Fabrication and characterization of phase change material composite fibers with wide phase-transition temperature range by co-electrospinning method. *Appl. Energy* **2016**, *182*, 409–417.
  336. Andrzejewska, E. Photopolymerization kinetics of multifunctional monomers. *Prog. Polym. Sci.* **2001**, *26*, 605–665, doi:10.1016/S0079-6700(01)00004-1.
  337. Hotaling, N.A.; Bharti, K.; Kriel, H.; Simon Jr, C.G. DiameterJ: A validated open source nanofiber diameter measurement tool. *Biomaterials* **2015**, *61*, 327–338.
  338. Yoshihara, T.; Tadokoro, H.; Murahashi, S. Normal vibrations of the polymer molecules of helical conformation. IV. Polyethylene oxide and polyethylene-d4 oxide. *J. Chem. Phys.* **1964**, *41*, 2902–2911, doi:10.1063/1.1726373.
  339. Pucić, I.; Jurkin, T. FTIR assessment of poly(ethylene oxide) irradiated in solid state, melt and aqueous solution. *Radiat. Phys. Chem.* **2012**, *81*, 1426–1429, doi:10.1016/j.radphyschem.2011.12.005.
  340. Zardalidis, G.; Mars, J.; Allgaier, J.; Mezger, M.; Richter, D.; Floudas, G. Influence of chain topology on polymer crystallization: poly(ethylene oxide)(PEO) rings vs. linear chains. *Soft Matter* **2016**, *12*, 8124–8134.
  341. ASTM, A. E96/E96M-16 Standard Test Methods for Water Vapor Transmission of Materials West Conshohocken 2016.
  342. McAvoy, K.; Jones, D.; Thakur, R.R.S. Synthesis and Characterisation of Photocrosslinked poly(ethylene glycol) diacrylate Implants for Sustained Ocular Drug Delivery. *Pharm. Res.* **2018**, *35*, doi:10.1007/s11095-017-2298-9.
  343. Üzüüm, Ö.B.; Karadağ, E. Swelling characterization of poly(acrylamide-co-N-vinylimidazole) hydrogels crosslinked by TMPTA and semi-IPN's with PEG. *J. Polym. Res.* **2007**, *14*, 483–488, doi:10.1007/s10965-007-9132-8.
  344. Karadağ, E.; Saraydin, D. Swelling studies of super water retainer acrylamide/crotonic acid hydrogels crosslinked by trimethylolpropane triacrylate and 1,4-butanediol dimethacrylate. *Polym. Bull.* **2002**, *48*, 299–307, doi:10.1007/s00289-002-0029-8.
  345. Xu, Q.; Liu, H.; Zhong, X.; Jiang, B.; Ma, Z. Permeable Weldable Elastic Fiber Conductors for Wearable Electronics. *ACS Appl. Mater. Interfaces* **2020**, *12*, 36609–36619.
  346. Wang, X.; Meng, S.; Tebyetekerwa, M.; Weng, W.; Pionteck, J.; Sun, B.; Qin, Z.; Zhu, M. Nanostructured polyaniline/poly(styrene-butadiene-styrene) composite fiber for use as highly sensitive and flexible ammonia sensor. *Synth. Met.* **2017**, *233*, 86–93.
  347. Teixeira, J.; Horta-Romaris, L.; Abad, M.-J.; Costa, P.; Lanceros-Méndez, S. Piezoresistive response of extruded polyaniline/(styrene-butadiene-styrene) polymer blends for force and deformation sensors. *Mater. Des.* **2018**, *141*, 1–8.
  348. Duong, H.C.; Chuai, D.; Woo, Y.C.; Shon, H.K.; Nghiem, L.D.; Sencadas, V. A novel electrospun, hydrophobic, and elastomeric styrene-butadiene-styrene membrane for membrane distillation applications. *J. Memb. Sci.* **2018**, *549*, 420–427.
  349. Beshkar, F.; Salavati-Niasari, M.; Amiri, O. Superhydrophobic–superoleophilic copper–graphite/styrene–butadiene–styrene based cotton filter for efficient separation of oil

- derivatives from aqueous mixtures. *Cellulose* **2020**, *27*, 4691–4705.
350. Isozumi, H.; Horiba, T.; Kubota, K.; Hida, K.; Matsuyama, T.; Yasuno, S.; Komaba, S. Application of modified styrene-butadiene-rubber-based latex binder to high-voltage operating LiCoO<sub>2</sub> composite electrodes for lithium-ion batteries. *J. Power Sources* **2020**, *468*, 228332.
  351. Fong, H.; Reneker, D.H. Elastomeric nanofibers of styrene-butadiene-styrene triblock copolymer. *J. Polym. Sci. Part B Polym. Phys.* **1999**, *37*, 3488–3493.
  352. Hao, X.; Zhang, X. Syndiotactic 1, 2-polybutadiene fibers produced by electrospinning. *Mater. Lett.* **2007**, *61*, 1319–1322.
  353. Kerr-Phillips, T.E.; Woehling, V.; Agniel, R.; Nguyen, G.T.M.; Vidal, F.; Kilmartin, P.; Plesse, C.; Travas-Sejdic, J. Electrospun rubber fibre mats with electrochemically controllable pore sizes. *J. Mater. Chem. B* **2015**, *3*, 4249–4258.
  354. Zhang, X.; Chase, G.G. Electrospun elastic acrylonitrile butadiene copolymer fibers. *Polymer (Guildf)*. **2016**, *97*, 440–448.
  355. Wang, X.; Nie, H.; Liu, D.; He, A. Retardation of cold flow in immiscible rubber blends by tailoring their microstructures. *Polym. Int.* **2017**, *66*, 1473–1479.
  356. Valentini, L.; Lopez-Manchado, M.A. Classification of rubbers and components for harsh environmental systems. In *High-Performance Elastomeric Materials Reinforced by Nanocarbons*; Elsevier, 2020; pp. 1–14.
  357. Vitale, A.; Massaglia, G.; Chiodoni, A.; Bongiovanni, R.; Pirri, C.F.; Quaglio, M. Tuning Porosity and Functionality of Electrospun Rubber Nanofiber Mats by Photo-Crosslinking. *ACS Appl. Mater. Interfaces* **2019**, *11*, 24544–24551.
  358. Bussière, P.O.; Gardette, J.L.; Lacoste, J.; Baba, M. Characterization of photodegradation of polybutadiene and polyisoprene: Chronology of crosslinking and chain-scission. *Polym. Degrad. Stab.* **2005**, *88*, 182–188, doi:10.1016/j.polymdegradstab.2004.02.013.
  359. Kagiya, V.T.; Takemoto, K. Crosslinking and Oxidation of 1, 2-Polybutadiene by UV Irradiation. *J. Macromol. Sci. Part A - Chem.* **1976**, *10*, 795–810, doi:10.1080/00222337608061218.
  360. Hoyle, C.E.; Bowman, C.N. Thiol-ene click chemistry. *Angew. Chemie - Int. Ed.* **2010**, *49*, 1540–1573, doi:10.1002/anie.200903924.
  361. Ten Brummelhuis, N.; Diehl, C.; Schlaad, H. Thiol-ene modification of 1, 2-polybutadiene using UV light or sunlight. *Macromolecules* **2008**, *41*, 9946–9947.
  362. Decker, C.; Viet, T.N.T. Photocrosslinking of functionalized rubbers, 7. Styrene-butadiene block copolymers. *Macromol. Chem. Phys.* **1999**, *200*, 358–367.
  363. Kim, S.-S.; Lau, C.M.; Lillie, L.M.; Tolman, W.B.; Reineke, T.M.; Ellison, C.J. Degradable Thermoset Fibers from Carbohydrate-Derived Diols via Thiol-Ene Photopolymerization. *ACS Appl. Polym. Mater.* **2019**, *1*, 2933–2942.
  364. Shanmuganathan, K.; Elliot, S.M.; Lane, A.P.; Ellison, C.J. Highly Stretchable Thermoset Fibers and Nonwovens Using Thiol-ene Photopolymerization. *ACS Appl. Mater. Interfaces* **2014**, *6*, 14259–14265.
  365. Li, G.-Y.; Koenig, J.L. A review of rubber oxidation. *Rubber Chem. Technol.* **2005**, *78*, 355–390.
  366. Chen, L.-W.; Nemoto, T.; Kumanotani, J. Oxidative Polymerization of Polybutadiene and Its Derivatives. *Bull. Chem. Soc. Jpn.* **1967**, *40*, 747–751.
  367. Mehrabzadeh, M.; Kasaei, S.; Khosravi, M. Modification of fast-cure ethylene-propylene diene terpolymer rubber by maleic anhydride and effect of electron donor. *J. Appl. Polym.*

- Sci.* **1998**, *70*, 1–5.
368. Nelson, P.A.; Kutty, S.K.N. Cure characteristics and mechanical properties of maleic anhydride grafted reclaimed rubber/styrene butadiene rubber blends. *Polym. Plast. Technol. Eng.* **2004**, *43*, 245–260.
  369. Yoon, J.; Lee, J.; Hur, J. Stretchable supercapacitors based on carbon nanotubes-deposited rubber polymer nanofibers electrodes with high tolerance against strain. *Nanomaterials* **2018**, *8*, 541.
  370. Thielke, M.W.; Bruckner, E.P.; Wong, D.L.; Theato, P. Thiol-ene modification of electrospun polybutadiene fibers crosslinked by UV irradiation. *Polymer (Guildf)*. **2014**, *55*, 5596–5599.
  371. Agarwal, S.; Greiner, A. On the way to clean and safe electrospinning-green electrospinning: Emulsion and suspension electrospinning. *Polym. Adv. Technol.* **2011**, *22*, 372–378, doi:10.1002/pat.1883.
  372. Stoiljkovic, A.; Ishaque, M.; Justus, U.; Hamel, L.; Klimov, E.; Heckmann, W.; Eckhardt, B.; Wendorff, J.H.; Greiner, A. Preparation of water-stable submicron fibers from aqueous latex dispersion of water-insoluble polymers by electrospinning. *Polymer (Guildf)*. **2007**, *48*, 3974–3981, doi:10.1016/j.polymer.2007.04.050.
  373. Kagiya, V.T.; Takemoto, K. Crosslinking and oxidation of 1, 2-Polybutadiene by UV irradiation. *J. Macromol. Sci.* **1976**, *10*, 795–810.
  374. GOLUB, M.A.; GEMMER, R. V; ROSENBERG, M.L. Spectroscopic Study of Photosensitized Oxidation of 1,4-Polybutadiene. In *Stabilization and Degradation of Polymers*; Advances in Chemistry; AMERICAN CHEMICAL SOCIETY, 1978; Vol. 169, pp. 2–11 ISBN 9780841203815.
  375. Lee, J.; Moon, B. Synthesis of telechelic anthraquinone-functionalized polybutadiene via ROMP and study of its photo-oxidation and UV crosslinking behaviors. *J. Polym. Sci. Part A Polym. Chem.* **2018**, *56*, 1249–1258.
  376. Bussière, P.-O.; Gardette, J.-L.; Lacoste, J.; Baba, M. Characterization of photodegradation of polybutadiene and polyisoprene: chronology of crosslinking and chain-scission. *Polym. Degrad. Stab.* **2005**, *88*, 182–188.
  377. Schopov, I.; Kassabova, N.; Kossmehl, G. Oxidation of cis-1, 4-polybutadiene by singlet oxygen. *Polym. Degrad. Stab.* **1989**, *25*, 31–38.
  378. Nezarati, R.M.; Eifert, M.B.; Cosgriff-Hernandez, E. Effects of humidity and solution viscosity on electrospun fiber morphology. *Tissue Eng. - Part C Methods* **2013**, *19*, 810–819, doi:10.1089/ten.tec.2012.0671.
  379. Nayak, R.; Padhye, R.; Kyratzis, I.L.; Truong, Y.B.; Arnold, L. Effect of viscosity and electrical conductivity on the morphology and fiber diameter in melt electrospinning of polypropylene. *Text. Res. J.* **2013**, *83*, 606–617, doi:10.1177/0040517512458347.
  380. Zhiyuan, C.; He, J.; Fengwen, Z.; Yuexing, L.; Yong, L.; Huilin, Y. Effect of polar additives on melt electrospinning of nonpolar polypropylene. *J. Serbian Chem. Soc.* **2014**, *79*, 587–596.
  381. Decker, C.; Nguyen Thi Viet, T. High-speed photocrosslinking of thermoplastic styrene-butadiene elastomers. *J. Appl. Polym. Sci.* **2000**, *77*, 1902–1912.
  382. Liu, X.; Zhou, T.; Liu, Y.; Zhang, A.; Yuan, C.; Zhang, W. Cross-linking process of cis-polybutadiene rubber with peroxides studied by two-dimensional infrared correlation spectroscopy: a detailed tracking. *RSC Adv.* **2015**, *5*, 10231–10242.
  383. Decker, C.; Viet, T.N.T. Photocrosslinking of functionalized rubbers IX. Thiol-ene

polymerization of styrene-butadiene-block-copolymers. *Polymer (Guildf)*. **2000**, *41*, 3905–3912.



# Appendix A

## Abbreviations/Acronyms

AA	Acetic Acid
ATR-FTIR	Attenuated Total reflection – Fourier transform Infra-red
BP	Benzophenone
CCD	Charge-coupled device
CS	Chitosan
DAROCUR	2-Hydroxy-2-methylpropiophenone
DMF	Dimethylformamide
DMTA	Dynamic Mechanical Tensile Analysis
DSC	Differential Scanning Calorimetry
DTGA	Derivative Thermal Gravimetric Analysis
EO	Ethylene Oxide
ES	Electrospinning
FDA	Food and Drug Administration
FE-SEM	Field-emission scanning electron microscopy
FTIR	Fourier transform Infra-red
FWHM	Full width at half maximum
HCA	Hexadecane contact angle
ISC	Intersystem crossing
L- M- H-	Low- Medium- High-
MA	Maleic Anhydride
MCT	mercury–cadmium–telluride
Mw	Molecular weight
Nylon-6	Polyamide 6
OA	Oleic Acid
PAA	polyacrylic acid
PAN	Polyacrylonitrile
PANi	Polyaniline
PB	Polybutadiene
PCL	Polycaprolactone
PCM	Phase change material
PE	Polyethylene
PEDOT: PSS	Poly(3,4-ethylenedioxythiophene) polystyrene sulfonate
PEGDA	Polyethylene glycol diacrylate
PEG	Polyethylene glycol
PEO	Polyethylene oxide
PEI	Polyethyleneimine
PET	Polyethylene terephthalate
Photo-DSC	Photo-Differential Scanning Calorimetry
PI	Photoinitiator
PLA	Poly lactide acid

PP	Polypropylene
PPy	Polypyrrole
PVP	Polyvinylpyrrolidone
PS	Polystyrene
PTFE	polytetrafluoroethylene
PU	Polyurethane
PVA	Polyvinyl alcohol
PVC	Polyvinyl chloride
PVDF	Polyvinylidene fluoride
RH	Relative Humidity
SBR	Styrene Butadiene Rubbers
T <sub>g</sub>	Glass transition temperature
T <sub>d</sub>	Decomposition Temperature
T <sub>m</sub>	Melting Temperature
TGA	Thermal Gravimetical Analysis
THF	Tetrahydrofuran
TMPTA	Trimethylol propane triacrylate
TPO	Diphenyl(2,4,6-trimethylbenzoyl)phosphine oxide
TRIS	Trimethylolpropane tris-(3-mercaptopropionate)
UTS	Ultimate tensile strength
UV	Ultra-Violate
Vis	Visible light
WCA	Water Contact Angle
wt.%	Weight percent
WT	Water treatment
WVT	Water Vapor Transmission

## Chapter 4

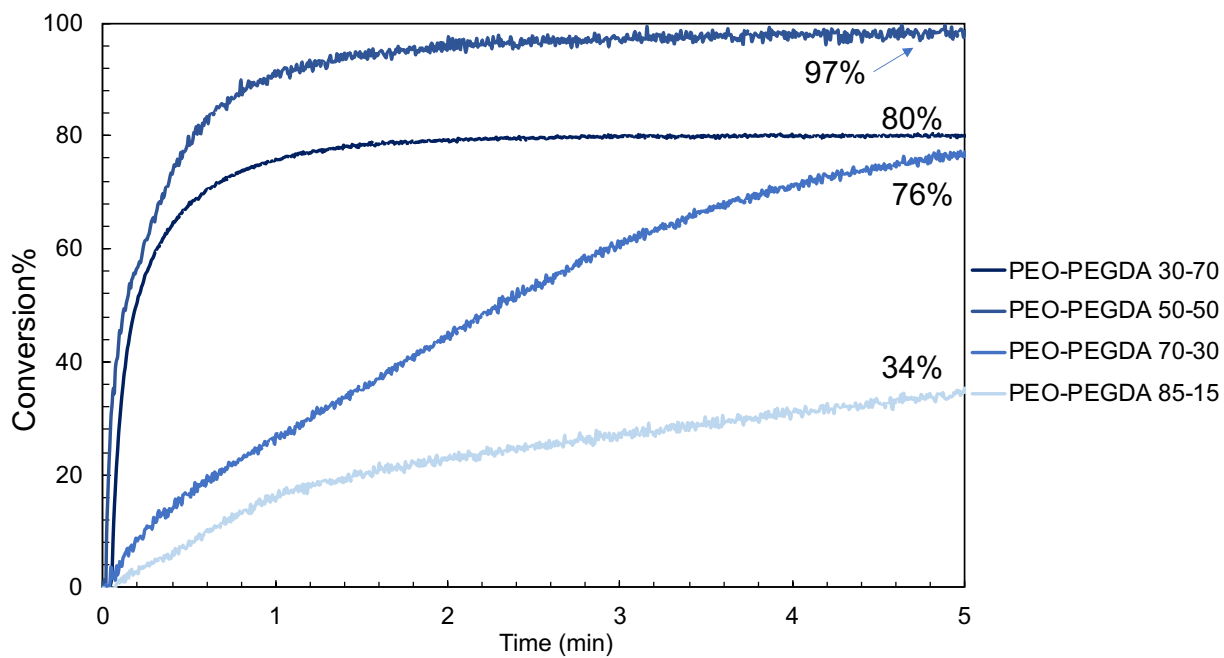


Figure A-1 The C=C conversion obtained through real-time FTIR, the cast film (on the silicon wafer as substrate) of the formulations were subjected to UV irradiation while the silicon wafer and cast film covered by PP transparent layer (initially the background spectrum was collected in presence of the silicon wafer and the PP layer)

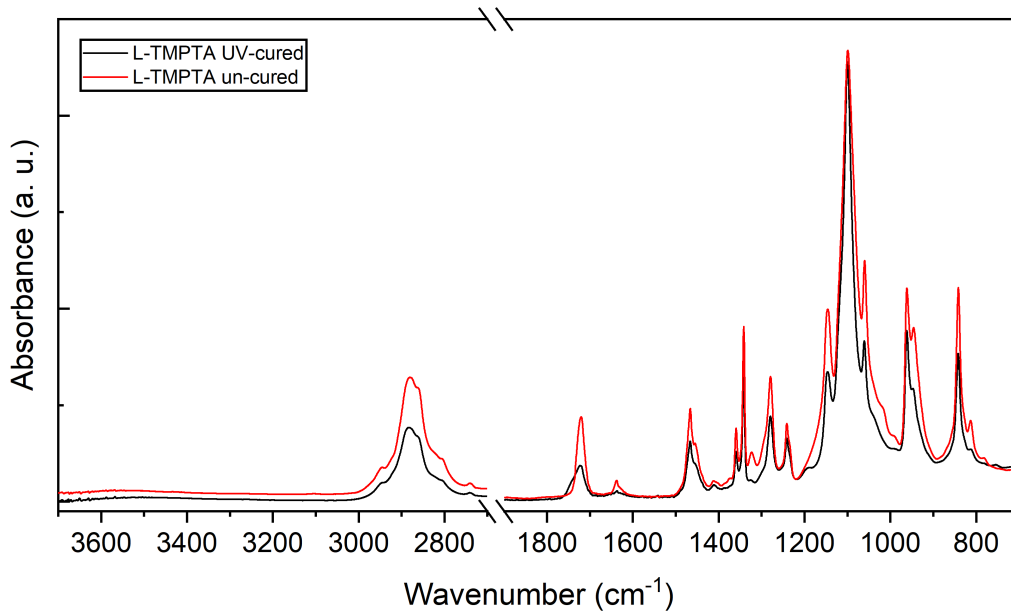


Figure A-2 FTIR-ATR spectra of the L-TMPTA fibers prior and after UV irradiation, the consumption of the C=C can be observed

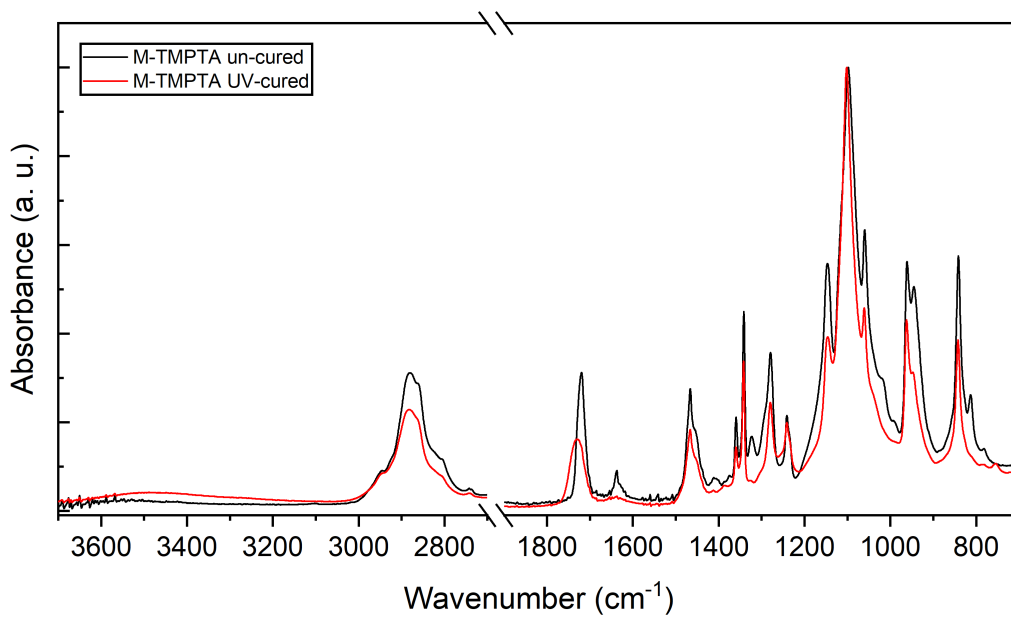


Figure A-3 FTIR-ATR spectra of the M-TMPTA fibers prior and after UV irradiation, the consumption of the C=C can be observed

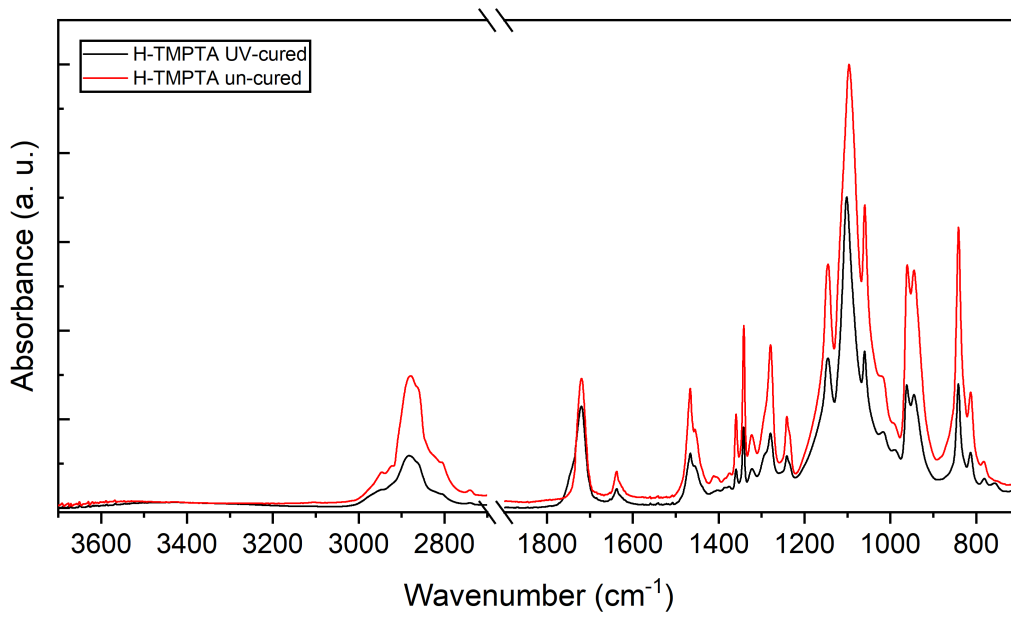


Figure A-4 FTIR-ATR spectra of the H-TMPTA fibers prior and after UV irradiation, the consumption of the C=C can be observed

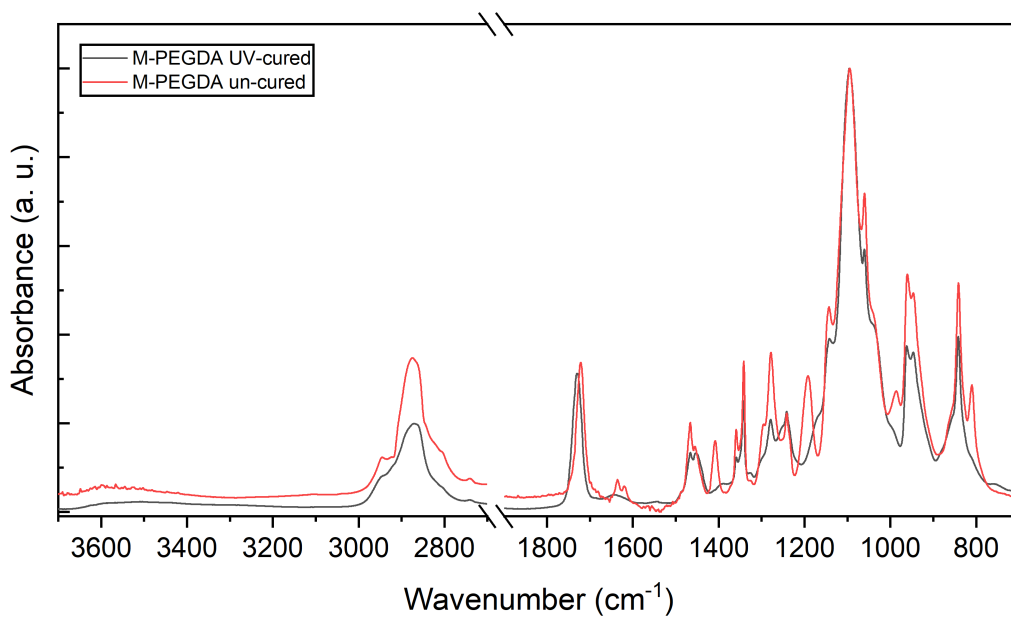


Figure A-5 FTIR-ATR spectra of the M-PEGDA fibers prior and after UV irradiation, the consumption of the C=C can be observed

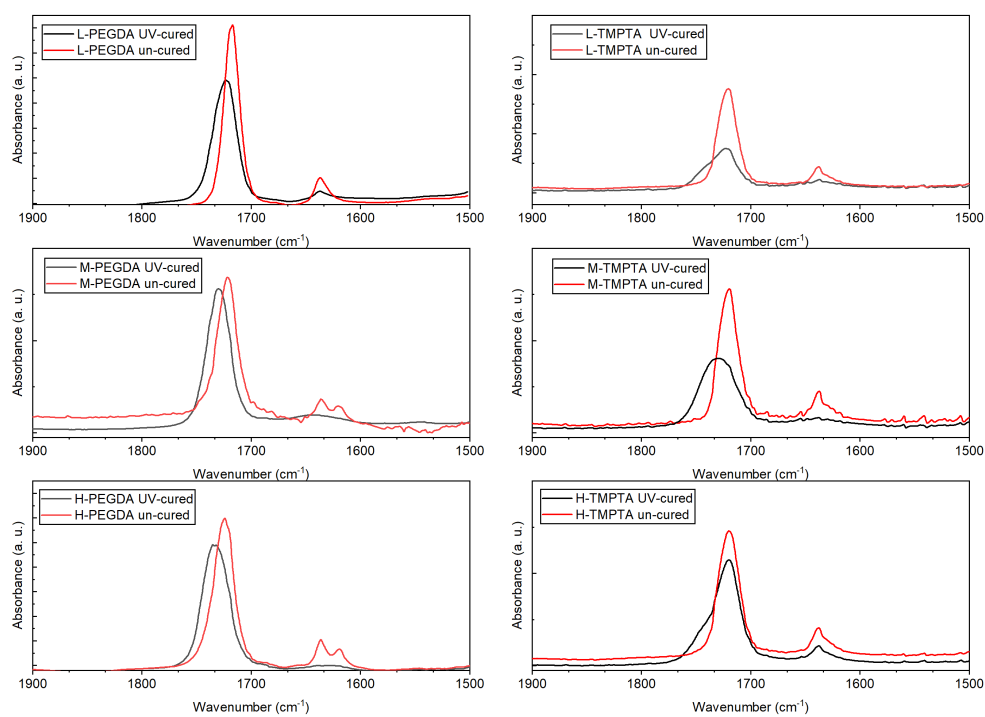


Figure A-6 The FTIR spectra of L-PEGDA, M-PEGDA, H-PEGDA, L-TMPTA, M-TMPTA and H-TMPTA fibers prior and after UV-irradiation. The C=C conversion can be obtained by tracking the band at  $1640\text{ cm}^{-1}$  by considering the peak of C=O as a reference at wave number  $1720\text{ cm}^{-1}$ .

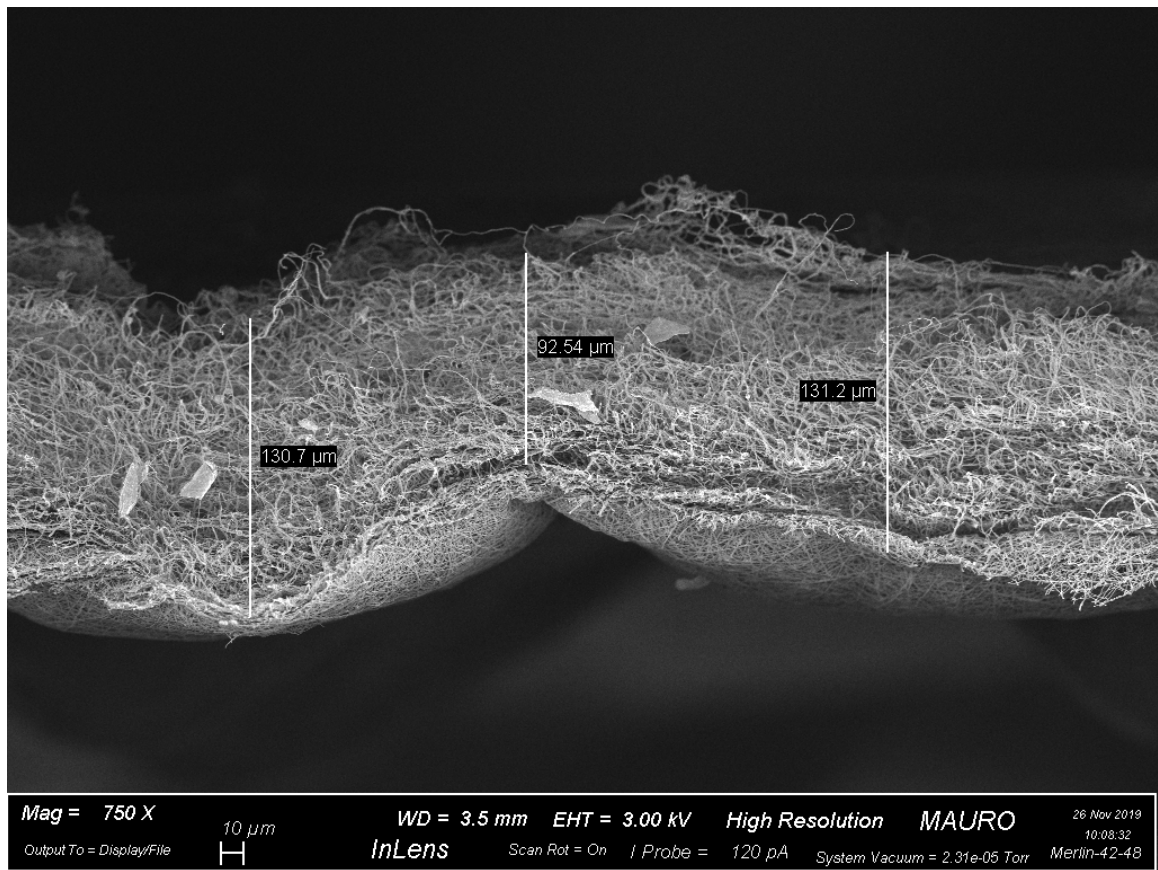


Figure A-7 FE-SEM image of the cross-section of a H-TMPTA electrospun sample. The fibers along the thickness show a homogenous structure.

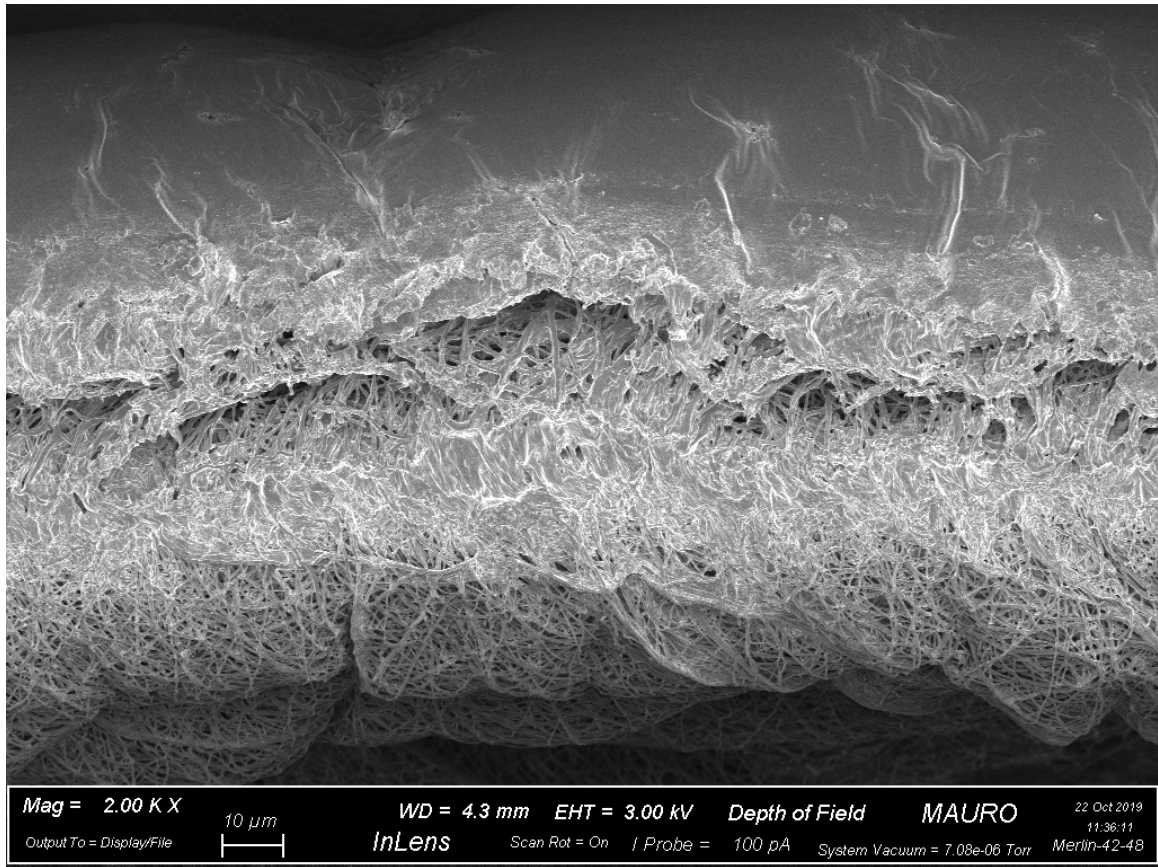


Figure A-8 FE-SEM image of cross-section of H-PEGDA samples, the film formation on backside of the fibers can be seen



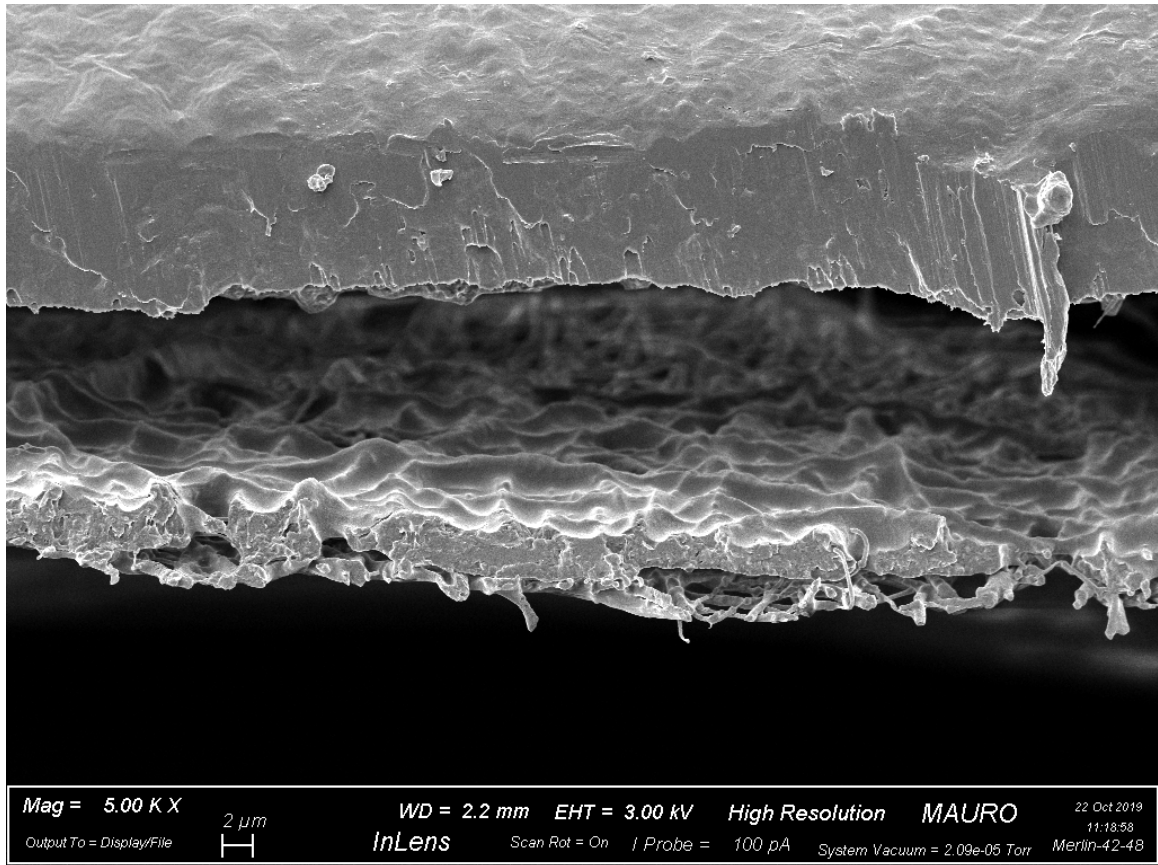


Figure A-9 FE-SEM image of cross-section of the thick H-PEGDA samples, the film formation on the side near the aluminum foil (the substrate) can be observed

## Chapter 5

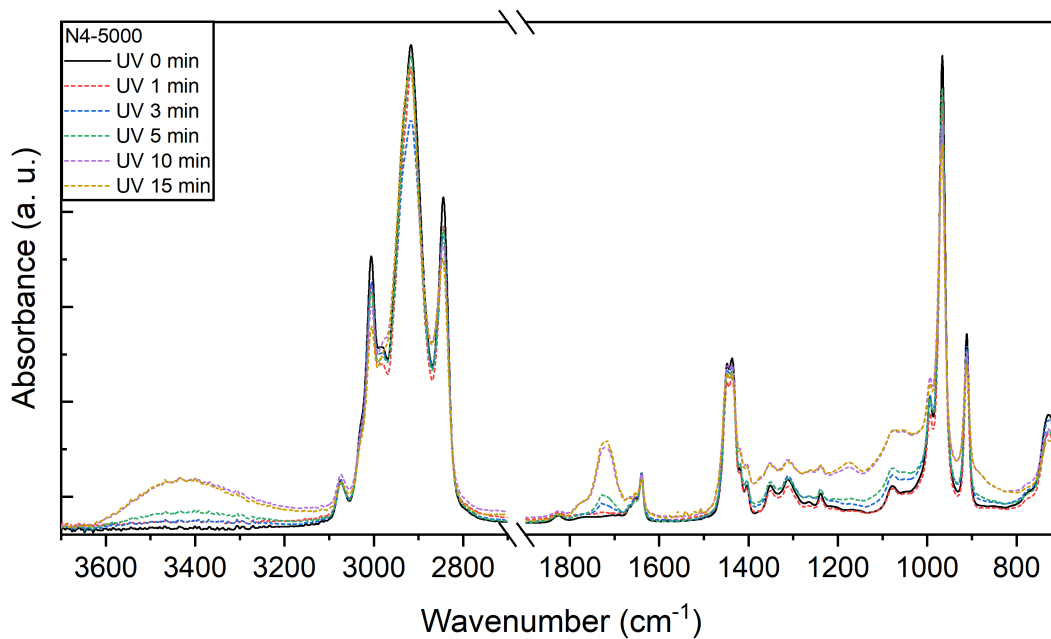


Figure A-10 FTIR spectra of N4-5000 during the UV irradiation at different time intervals.

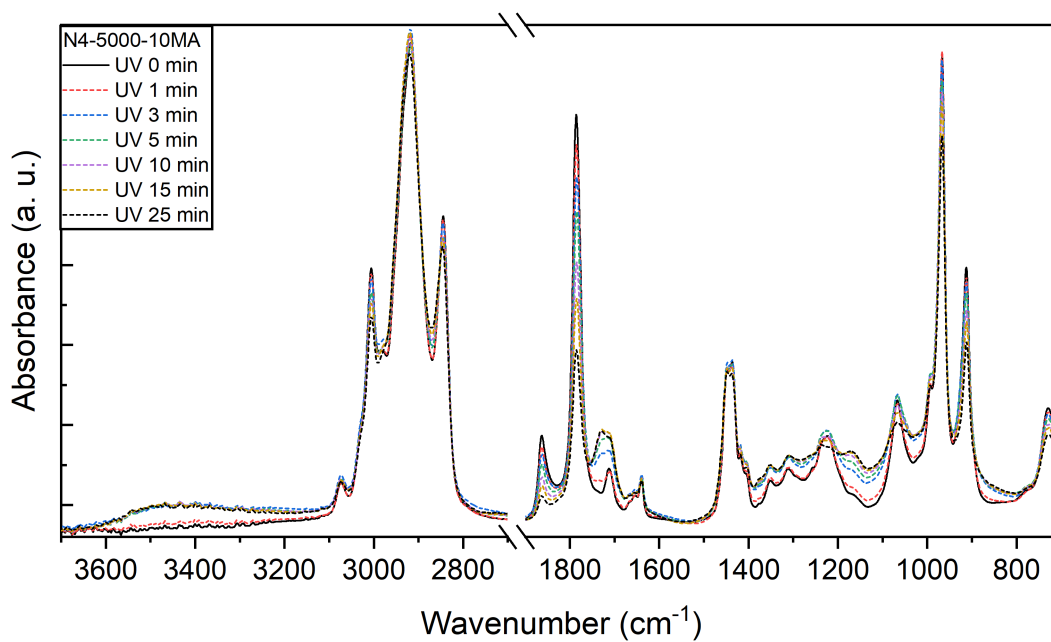


Figure A-11 FTIR spectra of N4-5000-10MA during the UV irradiation at different time intervals.

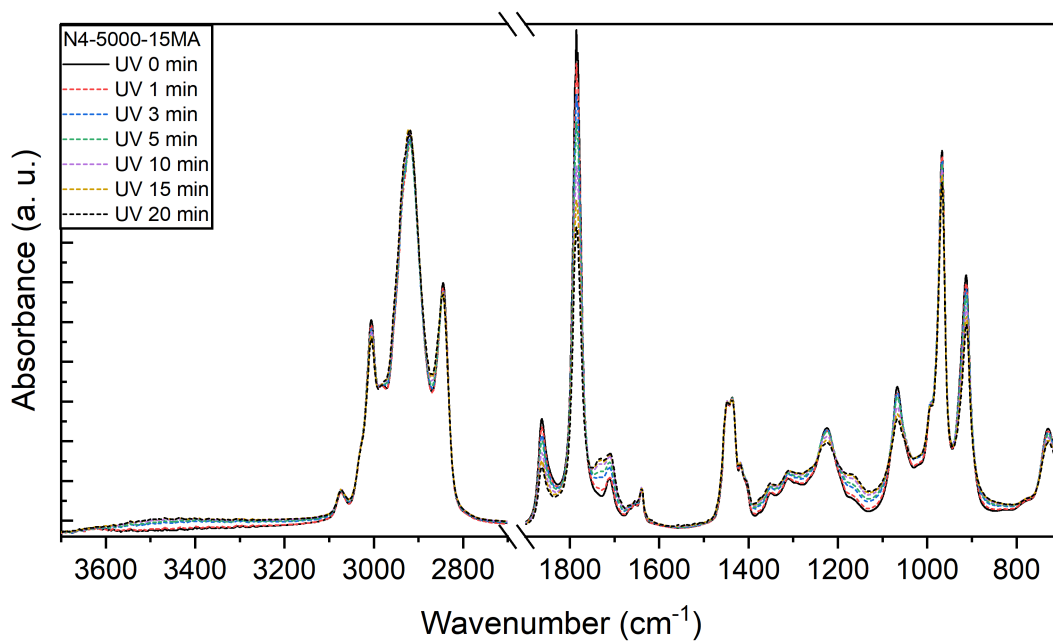


Figure A-12 FTIR spectra of N4-5000-15MA during the UV irradiation at different time intervals.

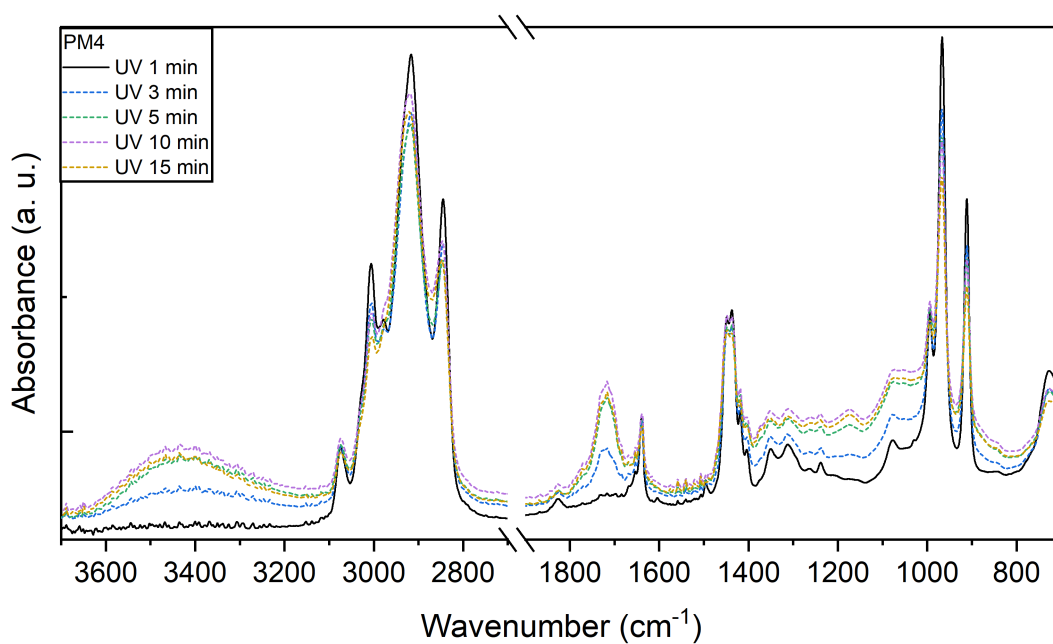


Figure A-13 FTIR spectra of PM4 during the UV irradiation at different time intervals.

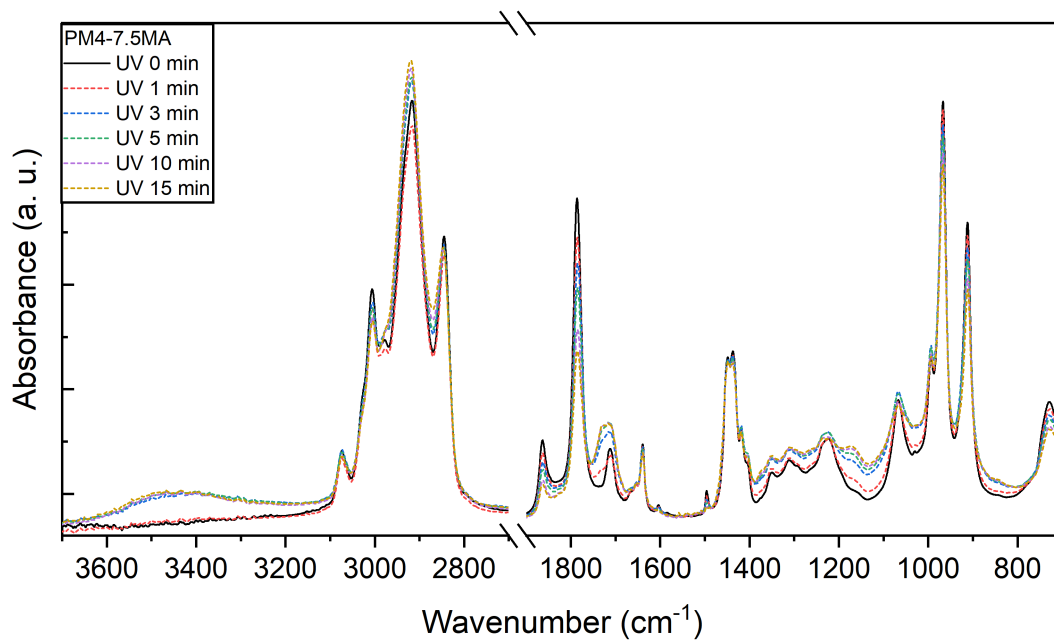


Figure A-14 FTIR spectra of PM4-7.5MA during the UV irradiation at different time intervals.

# Appendix B

## List of publication

### Publication

[1] **Kianfar, P.**, Nguyen Trieu, Q., Dalle Vacche, S., Tsantilis, L., Bongiovanni, R. and Vitale, A., Green electrospinning of liquid polybutadienes and their in-situ photocuring (2021), *Polymer Chemistry*, (under revision)

[2] **Kianfar, P.**, Bongiovanni, R., Ameduri, B., and Vitale, A. (2021) Electrospinning of Fluorinated Polymers: Current State-of the-art on Processes and Applications. *Polymers Review* (under revision)

[3] **Kianfar, P.**, Vitale, A., Dalle Vacche, S., and Bongiovanni, R. (2021) Enhancing properties and water resistance of PEO-based electrospun nanofibrous membranes by photo-crosslinking. *Journal of Materials Science*, 56(2), 1879-1896. DOI: 10.1007/s10853-020-05346-3

[4] Fredi, G., **Kianfar, P.**, Dalle Vacche, S., Pegoretti, and A., Vitale, A. (2021) Electrospun Shape-Stabilized Phase Change Materials Based on Photo-Crosslinked Polyethylene Oxide. *Polymers*, 13(17), 2979. DOI: 10.3390/polym13172979

[5] **Kianfar, P.**, Abate, M.T., Trovato, V., Rosace, G., Ferri, A., Bongiovanni, R. and Vitale A., (2020) Surface Functionalization of Cotton Fabrics by Photo-Grafting for pH Sensing Applications. *Front. Mater.* 7:39. DOI: 10.3389/fmats.2020.00039

[6] **Kianfar, P.**, Vitale, A., Dalle Vacche, S. and Bongiovanni, R. (2019) Photo-crosslinking of chitosan/poly (ethylene oxide) electrospun nanofibers. *Carbohydrate polymers*, 217, pp.144-151. DOI: 10.1016/j.carbpol.2019.04.062

### Conferences

[1] **P. Kianfar**, R. Bongiovanni, and A. Vitale, “Shape stable nanofibrous materials by electrospinning and photo-induced crosslinking”, MNE2021 - 47th international conference on Micro and Nano Engineering, 2021, 20-23 Sep., Turin, Italy. (poster contribution)

[2] **P. Kianfar**, S. Dalle Vacche, R. Bongiovanni, and A. Vitale, “Form stable and solvent resistant PEO-based electrospun mats by photo-induced crosslinking”, Vesps 2021, June 2021 (oral presentation)

[3] **P. Kianfar**, A. Vitale, R. Bongiovanni, “Modification of bio-based chitosan electrospun fibrous membranes by photo-crosslinking”, Polymer EPF summer school, May 2021 (poster contribution)

[4] **P. Kianfar**, A. Vitale, S. Dalle Vacche, R. Bongiovanni, “Photo-crosslinked PEO-based electrospun membranes”, ACS Spring 2021, Virtual meeting, 5-16 April 2021. (oral presentation)

[5] **P. Kianfar**, A. Vitale, T. Soulestin, B. Ameduri, R. Bongiovanni “Electrospinning of PVDF-based copolymers”, 5th International Bio-inspiration NICE2020, October 2020, Nice, France. (oral presentation)

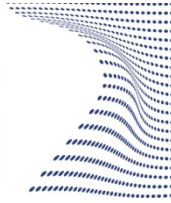
[6] **P. Kianfar**, A. Vitale, S. Dalle Vacche, R. Bongiovanni “Electrospinning and photo-crosslinking of PEO-based nanofibrous membranes”, Macrogiovani2020, June 2020, Genoa, Italy (oral presentation)

[7] **P. Kianfar**, A. Vitale, S. Dalle Vacche, R. Bongiovanni “Preparation of Photo-crosslinked Chitosan/Polyethylene oxide Nanofibrous Mats” EUPOC 2019 Electrospinning and related techniques: From design to production of advanced polymer materials and devices May 2019, Como, Italy. (oral presentation)



ScuDo

Scuola di Dottorato ~ Doctoral School  
WHAT YOU ARE, TAKES YOU FAR



Doctoral Dissertation  
Doctoral Program in Materials Science and Technology (34<sup>th</sup> Cycle)

# Nanofibrous polymeric membranes by coupling electrospinning and photo- induced crosslinking

**Parnian Kianfar**

\* \* \* \* \*

## Supervisors

Prof. Roberta Bongiovanni, Supervisor  
Dr. Alessandra Vitale, Co-Supervisor

## Doctoral Examination Committee:

Dr. Maila Castellano , Referee, University of Genoa  
Dr. Sandra Schlögl, Referee, Polymer Competence Center Leoben

Politecnico di Torino  
February 12, 2022